

UNIVERSITAT POLITÈCNICA DE VALÈNCIA

**INSTITUTO INTERUNIVERSITARIO DE INVESTIGACIÓN DE
RECONOCIMIENTO MOLECULAR Y DESARROLLO TECNOLÓGICO**



**Neurotransmitters recognition based on gold
nanoparticles and mesoporous silica
nanoparticles for sensing and controlled release
applications**

PhD THESIS

Submitted by

Tania Mariel Godoy Reyes

PhD Supervisors:

**Prof. Ramón Martínez Máñez
Prof. Pablo Gaviña Costero**

Valencia, September 2020



UNIVERSITAT
POLITÈCNICA
DE VALÈNCIA

RAMÓN MARTÍNEZ MÁÑEZ, PhD in Chemistry and Professor at the *Universitat Politècnica de València*, and PABLO GAVIÑA COSTERO, PhD in Chemistry and Professor at the *Universitat de València*.

CERTIFY:

That the work ***“Neurotransmitters recognition based on gold nanoparticles and mesoporous silica nanoparticles for sensing and controlled release applications”*** has been developed by Tania Mariel Godoy Reyes under their supervision in the Instituto Interuniversitario de Investigación de Reconocimiento Molecular y Desarrollo Tecnológico (IDM) of the *Universitat Politècnica de València*, as a Thesis Project in order to obtain the degree of PhD in Chemistry at the *Universitat Politècnica de València*.

Valencia, September 10th 2020.

Prof. Ramón Martínez Máñez

Prof. Pablo Gaviña Costero

*A mi familia,
por su apoyo incondicional*

“La ciencia es un gran juego. Es inspiradora y refrescante, y el campo de juego es el universo entero.”

Isidor Isaac Rabi

“Nothing in life is to be feared, it is only to be understood. Now is the time to understand more, so that we may fear less.”

Marie Curie

“Comienza haciendo lo necesario; luego haz lo posible y de repente estarás haciendo lo imposible.”

San Francisco de Asis

“Mira que te mando que te esfuerces y seas valiente; no temas ni desmayes, porque Jehová tu Dios estará contigo en dondequiera que vayas.”

Josue 1:9

Agradecimientos

En primer lugar, me gustaría dar las gracias a mis directores de tesis los Profesores Ramón y Pablo por darme la oportunidad de realizar mi tesis doctoral en el IDM. Gracias por haber confiado en mí y apoyarme en todo este proceso de aprendizaje.

Además, quiero dar las gracias a la Prof. Ana María Costero por haberme dado la oportunidad de trabajar en su grupo de investigación, por todos sus consejos y estar siempre allí para ayudarme en todo lo que necesitaba, realmente ha sido un enorme placer estar en su grupo. También agradecer al Prof. Pablo Gaviña, por toda la ayuda brindada a lo largo de este proceso, por estar siempre dispuesto a ayudarme y guiarme, gracias por las horas invertidas en el arduo proceso de contestar a los referees y escribir los artículos, realmente ha valido la pena y estoy enormemente agradecida. Dar las gracias también a los Profesores Boro y Marga por su disposición a ayudarme siempre que les necesité.

Además, quiero darle las gracias al Prof. Felix Sancenón, por su infinita ayuda desde el momento que llegué al Intituto, por sus consejos y amabilidad en todo lo que necesitaba.

Quiero agradecer, a mis compañeros del laboratorio de Burjassot Estefania, Carlos, Dani, Elena, Samuel, Silvia y todos aquellos que año tras año me acompañaron en este proceso. Muchas gracias por todos los buenos

momentos que vivimos juntos en el laboratorio, por los ánimos, consejos y chistes que hacían que el ambiente en el laboratorio fuera muy ameno, gracias también por enseñarme todo lo relacionado a la cultura española, la verdad que me ha sido de gran ayuda.

También quiero agradecer a mis compañeros, profesores y administrativos del laboratorio 2.6 de la UPV, por todos los buenos momentos que compartí y por estar dispuestos a ayudarme en todo lo que fuese necesario: Toni, Angela, Lorena, Bea Lozano, Alba, Andy, Luis Pla, Adrian, Amelia, Carmen, Santi, Manoharan, Mutu, Mónica, Maria Elena, Luis Villaescusa, Andy, Arianna, Hazem, Xente, Ismael, Bea de Luis, Eva G., Marta, María A. Andrea B. Paula, Borja, Juan Fran, Araceli, Gema, Alejandra, Irene, Serena, Elena L. Elisa, Angy, Andrea E. Elena A. Loles, Eva Brun, Quique, Pablo, Arantxa, y a todos aquellos que me haya dejado muchas gracias.

Gracias a mi prima Diana, por el apoyo en cada momento. También a mis compañeros del teatro “The Crow” por los buenos momentos compartidos.

Quiero dar las gracias a todos mis maestros de Honduras, a mi profesora de Octavo grado de Ciencias Naturales Lideny Robles, por ser la persona que con su carisma para enseñar sembró en mí esa semilla de la curiosidad y de querer saber el porqué de todo, lo que hizo que decidiera incursionar en el maravilloso mundo de las ciencias. A mis profesores de la carrera de Ciencias Naturales, mil gracias por todas sus enseñanzas y por confiar en mí y animarme a seguir siempre adelante.

A mis amigos y amigas de Tegucigalpa: Ana Carbajal, Doña Gris y Luis Enrique, por todo su apoyo durante este tiempo y por sus ánimos a la distancia.

Y de forma especial quiero agradecer a mis maravillosos padres Norma y Marvin y mi hermano Marvin Rubén por su apoyo y amor incondicional, por animarme a cruzar el océano en busca de mis sueños, por creer y confiar en mí, mil gracias porque aún a la distancia los he sentido tan cerca en cada momento y por ser el motor que me impulsa a seguir adelante cada día. También quiero dar las gracias a todos mis tíos en especial a mi tío José Rubén y a mis abuelos Rubén y Andrea y en especial a mi abuela Argentina, por todo su amor y aunque ya no esté en este mundo sé que estaría muy orgullosa de ver todo lo que he podido realizar.

También quiero agradecer a Toni, por ser ese pilar fundamental en cada etapa de este proceso, mil gracias por todo el amor, comprensión, por los consejos y por animarme a seguir adelante y perseverar, haciéndome ver lo positivo de cada momento, gracias porque con tu apoyo todo ha sido mucho más fácil. Además, quiero agradecer enormemente a Tere Lorente, Toni Llopis, Tere Llopis y Jordi Llopis por el gran apoyo que me habéis brindado durante todo este tiempo, mil gracias por acogerme en vuestro hogar y hacerme sentir en familia, gracias por todos los ánimos y los buenos momentos compartidos.

Resumen

La presente tesis doctoral titulada “*Reconocimiento de neurotransmisores basado en nanopartículas de oro y de sílice mesoporosa para aplicaciones de detección y liberación controlada*” es una tesis realizada por compendio de artículos la cual se centra en el diseño, preparación, caracterización y evaluación de distintos nanodispositivos para la detección colorimétrica de neurotransmisores y sistemas de liberación controlada que responden a neurotransmisores basados en nanopartículas de oro y nanopartículas de sílice mesoporosa, equipadas con ligandos orgánicos, efectores enzimáticos, puertas moleculares y especies cromofluorogénicas o medicamentos.

En el primer capítulo se introduce una visión general de lo que son los neurotransmisores, sus principales características y el importante papel que éstos desempeñan en el funcionamiento de nuestro organismo. Además, se presenta una descripción general de las propiedades y potenciales aplicaciones de las nanopartículas de oro funcionalizadas con ligandos orgánicos como sistemas de detección y las nanopartículas mesoporosas de sílice funcionalizadas con puertas moleculares como sistemas de liberación controlada.

A continuación, en el segundo capítulo se presentan los objetivos generales que son abordados en los siguientes capítulos experimentales.

En el tercer capítulo, se presentan tres sistemas de detección colorimétrica de neurotransmisores basados en la agregación de nanopartículas de oro doblemente funcionalizadas con ligandos orgánicos. El primer sistema es un sensor capaz de detectar de forma selectiva el neurotransmisor serotonina, utilizando nanopartículas de oro funcionalizadas con ditio-bis(propionato de succinimidilo) y N-Acetil-L-Cisteína. El segundo sistema consiste en un sensor para la detección selectiva del neurotransmisor norepinefrina diseñado a partir de nanopartículas de oro funcionalizadas con 4-(liponiloxi)benzaldehído y ácido 4-mercato fenilborónico. El tercer sistema está compuesto por nanopartículas de oro funcionalizadas con 4-(liponiloxi)benzaldehído y N-Acetil-L-Cisteína, para la

detección de normetanefrina, un importante biomarcador del tumor feocromocitoma. Todos estos sistemas se evalúan en medios competitivos como suero sanguíneo u orina.

En el cuarto capítulo se muestran dos sistemas de liberación controlados enzimáticamente basados en la apertura de puertas moleculares. El primer sistema de liberación controlada responde a la presencia del neurotransmisor acetilcolina. En concreto, se utilizan nanopartículas de sílice mesoporosa funcionalizadas en su superficie con grupos de ácido fenilborónico y tapadas con la enzima acetilcolinesterasa mediante la formación de ésteres cíclicos de ácido fenilborónico entre las cadenas de oligosacáridos de la enzima y los grupos fenilborónicos de la superficie de las nanopartículas. En este caso la reacción enzimática produce ácido acético que da lugar a la hidrólisis de los ésteres borónicos, destapando los poros y liberando la carga contenida en el interior. Además, se evalúa la capacidad del dispositivo diseñado para liberar el citotóxico doxorubicina en células cancerosas en presencia de acetilcolina.

El segundo sistema consiste en un nanodispositivo para la liberación controlada en respuesta al neurotransmisor L-glutamato. Para esto se utilizan nanopartículas tipo Janus de oro-sílice mesoporosa funcionalizadas con la enzima L-glutamato oxidasa en la parte del oro y con una puerta molecular autoinmolante de arilboronato en la superficie de la sílice. La liberación controlada se basa en el reconocimiento del L-glutamato por la enzima L-glutamato oxidasa y la posterior formación de peróxido de hidrogeno, que es la especie que induce la escisión de la puerta autoinmolante y la subsecuente apertura de los poros. Finalmente se muestra que el sistema diseñado es capaz de liberar un fármaco citotóxico en células de cáncer de cerebro tras detectar la presencia de L-glutamato.

Como conclusión general, los estudios realizados muestran que la utilización de nanopartículas inorgánicas equipadas con componentes orgánicos o enzimáticos permiten el reconocimiento de neurotransmisores con alta selectividad dando lugar al diseño de sistemas versátiles de detección y liberación controlada.

Resum

La present tesi doctoral titulada "Reconeixement de neurotransmissors basat en nanopartícules d'or i de sílice mesoporosa per a aplicacions de detecció i alliberació controlada" és una tesi realitzada per compendi d'articles la qual se centra en el disseny, preparació, caracterització i avaluació de diferents nanodispositius per a la detecció colorimètrica de neurotransmissors i sistemes d'alliberació controlada que responen a neurotransmissors basats en nanopartícules d'or i nanopartícules de sílice mesoporosa equipades amb lligands orgànics, efectors enzimàtics, portes moleculars i espècies cromofluorogénics o medicaments.

En el primer capítol s'introdueix una visió general del que són els neurotransmissors, les seves principals característiques i l'important paper que aquests tenen en el funcionament del nostre organisme. A més es presenta una descripció general de les propietats i potencials aplicacions de les nanopartícules d'or funcionalitzades amb lligands orgànics com a sistemes de detecció, i de les nanopartícules mesoporoses de sílice funcionalitzades amb portes moleculars com a sistemes d'alliberament controlat.

A continuació, en el segon capítol es presenten els objectius generals que són abordats en els següents capítols experimentals.

En el tercer capítol, es presenten tres sistemes de detecció colorimètrica de neurotransmissors basats en l'agregació de nanopartícules d'or doblement funcionalitzades amb lligands orgànics. El primer sistema és un sensor capaç de detectar de forma selectiva el neurotransmissor serotonina, utilitzant nanopartícules d'or funcionalitzades amb ditiobis (propionat de succinimidilo) i N acetil-L-cisteïna. El segon sistema consisteix en un sensor per a la detecció selectiva de neurotransmissor norepinefrina dissenyat a partir de nanopartícules d'or funcionalitzades amb 4- (liponiloxi) benzaldehyd i Àcid 4-mercatofenilborònic. El tercer sistema està compost per nanopartícules d'or funcionalitzades amb 4- (liponiloxi) benzaldehyd i N acetil-L-cisteïna, per a la detecció de normatanefrina

un important biomarcador del tumor feocromocitoma. Tots aquests sistemes s'avaluen en mitjans competitiu com sèrum sanguini u orina.

En el quart capítol es mostren dos sistemes d'alliberament controlats enzimàticament basats en l'obertura de portes moleculars. El primer sistema d'alliberament controlat respon a la presència del neurotransmissor acetilcolina. En concret, s'utilitzen nanopartícules de sílice mesoporosa funcionalitzades en la seva superfície amb grups d'àcid fenilborònic i tapades amb l'enzim acetilcolina esterasa mitjançant la formació d'èsters cíclics d'àcid fenilborònic entre les cadenes d'oligosacàrids de l'enzim i els grups fenilborònics de la superfície de les nanopartícules. En aquest cas, la reacció enzimàtica produeix àcid acètic que dona lloc a la hidròlisi dels èsters borònics, destapant els porus i alliberant la càrrega continguda a l'interior. A més, s'avalua la capacitat del dispositiu dissenyat per alliberar el citotòxic doxorubicina en cèl·lules canceroses en presència d'acetilcolina.

El segon sistema consisteix en un nanodispositiu per alliberació controlada en resposta al neurotransmissor L-glutamat, per al que s'utilitzen nanopartícules tipus Janus d'or-sílice mesoporosa funcionalitzades amb l'enzim L-glutamat oxidasa en la part de l'or i amb una porta molecular autoimmolant d'arilboronat a la superfície de la sílice. La alliberació controlada es basa en el reconeixement de L-glutamat per l'enzim L-glutamat oxidasa i la posterior formació de peròxid d'hidrogen, que és l'espècie que indueix l'escissió de la porta autoimmolant i la subseqüent obertura dels porus. Finalment es mostra que el sistema dissenyat és capaç d'alliberar un fàrmac citotòxic en cèl·lules de càncer de cervell després de detectar la presència de L-glutamat.

Com a conclusió general, els estudis realitzats mostren que la utilització de nanopartícules inorgàniques equipades amb components orgànics o enzimàtics permet el reconeixement de neurotransmissors amb alta selectivitat donant lloc a el disseny de sistemes versàtils de detecció i alliberació controlada.

Abstract

This doctoral thesis entitled “Neurotransmitters recognition based on gold and mesoporous silica nanoparticles for sensing and controlled release applications” is a thesis carried out by compendium of articles, which is focused on the design, preparation, characterization and evaluation of nanodevices for the colorimetric sensing of neurotransmitters and controlled delivery systems responsive to neurotransmitters, based on gold nanoparticles and mesoporous silica nanoparticles equipped with organic ligands, enzymatic effectors, molecular gates and chromo-fluorogenic species or drugs.

The first chapter introduces an overview about what neurotransmitters are, their main characteristics and the important role they play in the functioning of our body. In addition, a general description of the properties and potential applications of gold nanoparticles functionalized with organic ligands as detection systems and mesoporous silica nanoparticles functionalized with molecular gates as controlled delivery systems is presented.

In the second chapter, the general objectives that are addressed in the following experimental chapters are presented.

In the third chapter, three colorimetric detection systems of neurotransmitters based on the aggregation of gold nanoparticles doubly functionalized with organic ligands are presented. The first system is a sensor capable of selectively detecting the neurotransmitter serotonin, using gold nanoparticles functionalized with dithio-bis(succinimidyl propionate) and N acetyl-L-cysteine. The second system consists of a sensor for the selective detection of the neurotransmitter norepinephrine designed from gold nanoparticles functionalized with 4-(liponyloxy)benzaldehyde and 4-mercaptophenylboronic acid. The third system is composed of gold nanoparticles functionalized with 4-(liponyloxy)benzaldehyde and N-Acetyl-L-Cysteine, for the detection of normetanephrine, an important biomarker of the pheochromocytoma tumor. All these systems are evaluated in competitive media such as blood serum or urine.

In the fourth chapter, two enzymatic controlled delivery systems based on the opening of molecular gates are developed. The first controlled delivery system responds to the presence of the neurotransmitter acetylcholine. Specifically, it consists of mesoporous silica nanoparticles functionalized on their surface with phenylboronic acid groups and capped with the enzyme acetylcholinesterase, via the formation of cyclic phenylboronic acid esters between the oligosaccharide chains of the enzyme and the phenylboronic groups on the nanoparticles surface. In this case, the enzymatic reaction produces acetic acid that induces the hydrolysis of the boronic esters, uncapping the pores and releasing the entrapped payload. In addition, the ability of the nanodevice to release the cytotoxic doxorubicin in cancer cells in the presence of acetylthiocholine is evaluated.

The second delivery system consists of a nanodevice responsive to the neurotransmitter L-glutamate. It is based on Janus gold-silica mesoporous nanoparticles functionalized with the enzyme L-glutamate oxidase in the gold part and with a self-immolative arylboronate molecular gate on the surface of the silica. Controlled delivery is based on the recognition of L-glutamate by the enzyme L-glutamate oxidase and the subsequent formation of hydrogen peroxide, which results in the cleavage of the self-immolative gate and the uncapping of the pores. Finally, it is shown that the designed system is capable of releasing a cytotoxic drug in brain cancer cells after detecting the presence of L-glutamate.

As a general conclusion, the studies carried out show that the use of inorganic nanoparticles equipped with organic or enzymatic components allows the recognition of neurotransmitters with high selectivity, giving rise to the design of versatile detection and controlled release systems.

Publications

Work carried out in this PhD Thesis has resulted in the following scientific publications:

- **Godoy-Reyes, T. M.**, Llopis-Lorente, A., Costero, A. M., Sancenón, F., Gaviña, P., Martínez-Máñez, R. “Selective and sensitive colorimetric detection of the neurotransmitter serotonin based on the aggregation of bifunctionalised gold nanoparticles”. *Sensors and Actuators B: Chemical*, **2018**, 258, 829-835.
- **Godoy-Reyes, T. M.**, Costero, A. M., Gaviña, P., Martínez-Máñez, R., Sancenón, F. “A Colorimetric Probe for the Selective Detection of Norepinephrine Based on a Double Molecular Recognition with Functionalized Gold Nanoparticles”. *ACS Applied Nano Materials*, **2019**, 2, 1367-1373.
- **Godoy-Reyes, T. M.**, Costero, A. M., Gaviña, P., Martínez-Máñez, R., Sancenón, F. “Colorimetric detection of normetanephrine, a pheochromocytoma biomarker, using bifunctionalised gold nanoparticles”. *Analytica chimica acta*, **2019**, 1056, 146-152.
- **Godoy-Reyes, T. M.**, Llopis-Lorente, A., García-Fernández, A., Gaviña, P., Costero, A. M., Martínez-Máñez, R., Sancenón, F. “Acetylcholine-responsive cargo release using acetylcholinesterase-capped nanomaterials”. *Chemical Communications*, **2019**, 55, 5785-5788.
- **Godoy-Reyes, T. M.**, Llopis-Lorente, A., García-Fernández, A., Gaviña, P., Costero, A. M., Villalonga, R., Martínez-Máñez, R. “A l-glutamate-responsive delivery system based on enzyme-controlled self-immolative arylboronate-gated nanoparticles”. *Organic Chemistry Frontiers*, **2019**, 6, 1058-1063.

Abbreviations and Acronyms

¹¹B-NMR	Boron-11 nuclear magnetic resonance
¹³C-NMR	Carbon-13 nuclear magnetic resonance
¹H-NMR	Hydrogen-1 nuclear magnetic resonance
5-HIAA	5-hydroxyindoleacetic acid
5-HT	5-hydroxytryptamine
AA	Aspartic acid
ABTS	2,2'-azino-bis(3-ethylbenzothiazoline-6-sulfonic acid)diammonium salt
ACh	Acetylcholine
AChE	Acetylcholinesterase
APB	3-aminophenylboronic acid
APTES	(3-Aminopropyl)triethoxysilane
ATP	Adenosine triphosphate
AuNPs	Gold Nanoparticles
BET	Brunauer-Emmet-Teller
BJH	Barret-Joyner-Halenda
CE	Capillary Electrophoresis
C_{max}	Maximum Supersaturation
C_{min}	Minimum Supersaturation
CNS	Central Nervous System
C_s	solubility concentration of nanocrystals
CSF	Cerebral Spinal Fluid
CTABr	Cetyltrimethylammonium bromide
Cys	Cysteine
DA	Dopamine
DCC	N,N'- dicyclohexylcarbodiimide
DCNP	Diethylcyanophosphonate
DFP	Diisopropyl fluorophosphate
D-Glu	D-glutamate
DLS	Dynamic light scattering
DMAP	4-dimethylaminopyridine
DMEM	Dulbecco's Modified Eagle's Medium
DMF	Dimethyl Formamide
DOX	Doxorubicin

DSP	Dithiobis (succinimidylpropionate)
DTNB	5,5'-dithiobis(2-nitrobenzoic acid)
DTT	Dithiothreitol
E	Epinephrine
EA	Elemental analysis
EDC	N-(3-dimethylaminopropyl)-Nl-ethylcarbodiimide
EDX	Energy dispersive X-ray spectroscopy
ELISA	Enzyme-linked immunosorbent assay
Epi	Epinephrine
FBS	Fetal Bovine Serum
FDA	Food and Drug Administration
FTIR	Fourier transform infrared spectroscopy
GA	Glutamic acid
GABA	Gamma-Aminobutyric acid
GIT	Gastrointestinal tract
Glc	Glucose
Gly	Glycine
GNP1	Gold Nanoparticles Probe 1
GOx	Glucose oxidase
GSH	Glutathione
HPLC	High performance liquid chromatography
HPLC-ED	High performance liquid chromatography fluorogenic detection
HPLC-FD	High performance liquid chromatography with electrochemical detection
HPLC-MS	High performance liquid chromatography with tandem mass spectrometry
HRMS	High Resolution Mass Spectrometry
HRP	Horseadish peroxidase
HVA	Homovanillic acid
Hys	Histamine
ICP-MS	Inductively coupled plasma mass spectrometry
IR	Infrared
IUPAC	International Union of Pure and Applied Chemistry
L-Asp	L-aspartate
LC	Liquid chromatography
L-Cys	L-cysteine
L-Glu	L-glutamate
L-GluOx	L-glutamate oxidase

LOD	Limit of detection
L-Tyr	L-tyrosine
MBA	4-mercatophenylboronic acid
MCM	Mobil Composition of Matter
MSNs	Mesoporous silica nanoparticles
NALC	N-Acetyl-L-cysteine
NE	Norepinephrine
NMN	Normetanephrine
OA	Oxalic acid
PBS	Dulbecco's Phosphate Buffered Saline
PDCA	2,6-Pyridinedicarboxylic acid
PMOs	Periodic Mesoporous Organosilicas
PNS	Peripheral nervous system
PPGL	Pheochromocytomas and paragangliomas
PVA	Polyvinyl alcohol
PVP	Polyvinylpyrrolidone
SBS	Simulated blood serum
SIMs	Self-immolative molecules
SPRB	Surface plasmón resonance band
STEM-EDX	Scanning transmission electron microscopy coupled with energy dispersive X-ray spectroscopy
THF	Tetrahydrofuran
TNB²⁻	2-Nitro-5-thiobenzoate
TNT	2,4,6-Trinitrotoluene
TOAB	Tetraoctylammonium bromide
UA	Uric acid

Table of Contents

Chapter 1: General introduction	3
1.1 Neurotransmitters.....	5
1.2 Nanotechnology	11
1.3 Gold Nanoparticles	14
1.4 Mesoporous silica nanoparticles	32
1.5 Stimuli-responsive gated materials.....	43
1.6 References.....	56
Chapter 2: Objectives	63
Chapter 3: Colorimetric detection of neurotransmitters based on the aggregation of bifunctionalized gold nanoparticles	67
3.1 Introduction	69
3.2 References.....	73
Part 1: Selective and sensitive colorimetric detection of the neurotransmitter serotonin based on the aggregation of bifunctionalised gold nanoparticles	75
Part 2: A Colorimetric Probe for the Selective Detection of Norepinephrine Based on a Double Molecular Recognition with Functionalized Gold Nanoparticles	105
Part 3: Colorimetric detection of normetanephrine, a pheochromocytoma biomarker, using bifunctionalised gold nanoparticles.....	143
Chapter 4: Design of mesoporous nanodevices for controlled cargo release triggered by neurotransmitters	171
4.1 Introduction	173
4.2 References.....	176
Part 1: Acetylcholine-responsive cargo release using acetylcholinesterase-capped nanomaterials.....	179
Part 2: L-Glutamate-Responsive Delivery System Based on Enzyme-Controlled Self-Immolative Arylboronate-Gated Nanoparticles	215
Chapter 5: Conclusions	247

Chapter 1:

General introduction

1.1 Neurotransmitters

Neurotransmitters are chemical messengers that enable neurotransmission. They cross the synaptic cleft to transmit impulses from a neuron to another neuron, glandular cell, or muscle cell.¹ In other words, neurotransmitters are used to send signals from one part of the body to another. These endogenous chemicals are integral in shaping everyday life and functions, activating responses by effector organs (such as contraction in muscles or hormone release from endocrine glands).

Neurotransmitters perform many vital functions in the body. For example, they regulate heartbeat, tell the lungs when to breathe, determine the set point for weight, stimulate thirst, affect mood, and control digestion.² Many neurotransmitters are synthesized from simple and plentiful precursors such as amino acids, which are readily available from the diet and only require a small number of biosynthetic steps for conversion. Their exact numbers are unknown, but more than 100 chemical messengers have been identified.³

Until the early 20th century, scientists assumed that majority of synaptic communication in the brain was electrical. However, through the careful histological examinations made by Ramón y Cajal, a 20 to 40 nm gap between neurons, known today as the synaptic cleft, was discovered.⁴ The presence of such a gap suggested communication via chemical messengers traversing the synaptic cleft and in 1921 Otto Loewi confirmed that neurons can communicate by releasing chemicals. Furthermore, Otto Loewi and Henry Hallett Dale were credited with discovering acetylcholine (ACh) the first known neurotransmitter.⁵

Criteria for Neurotransmitter identification

Neurotransmitters are usually considered to be endogenous substances that are released from neurons, act on receptor sites that are typically present on membranes of postsynaptic cells and produce a functional change in the properties of the target cell. Over the years, general agreement evolved that several criteria should be met for a substance to be designated a neurotransmitter:⁶

- (I) **Neurotransmitters must be synthesized by and released from neurons.** Thus, the presynaptic neuron should contain both the transmitter and the appropriate enzymes needed to synthesize that neurotransmitter.
- (II) **Neurotransmitters should be released from nerve terminals** in a chemically or pharmacologically identifiable form, being possible to isolate the neurotransmitter and characterize its structure.
- (III) **The same response must be obtained** when the neurotransmitter is exogenously placed on the synapse near to the target neuron.
- (IV) **There should be active mechanisms to inactivate the action of the neurotransmitter.** Among such mechanisms are uptake of the transmitter by the presynaptic neurons or glial cells through specific transporter molecules and enzymatic inactivation of the chemical messenger.

Chemical neurotransmission process

Neurotransmission is the fundamental process that drives information transfer between neurons and their targets, this occurs at specialized regions called the synapse.⁷ Chemical neurotransmission is the major mode of neuronal communication carried out by neurotransmitters.

The neurotransmission process begins when the presynaptic neuron is depolarized by an action potential and, as a consequence, synaptic vesicles release the neurotransmitters, which cross via diffusion the small distance (synaptic cleft) between the presynaptic and postsynaptic neuron. When the neurotransmitter binds to a receptor at the postsynaptic neuron, the chemical message has been communicated⁸ (**see figure 1**).

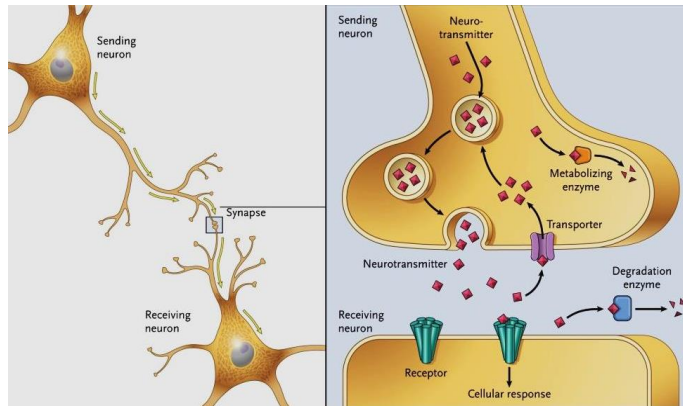


Figure 1. Schematic representation of neurotransmission process. *Reprinted with permission from © TeachMe Series 2020.*

Based on the effect that neurotransmitters produce to the postsynaptic neuron they can be classified as excitatory or inhibitory neurotransmitters:⁹

- **Excitatory neurotransmitter** has excitatory effects on the neuron. This means that they increase the likelihood that the neuron will fire an action potential.
- **Inhibitory neurotransmitter** has inhibitory effects on the neuron. This means that they decrease the probability that the postsynaptic neuron will generate an action potential.

Moreover, depending on the receptor to which the neurotransmitter binds, some of them can produce both excitatory and inhibitory effects; for example, the neurotransmitter acetylcholine is excitatory at the neuromuscular junction in skeletal muscle, causing the muscle to contract. In contrast, it is inhibitory in the heart, where it slows heart rate.

Types of neurotransmitters

There are different ways to classify neurotransmitters. The major methods for categorizing neurotransmitters are:

- **Based on their chemical composition:** esters, amino acids, biogenic amines, peptides, gases, purines and single ions.

- **According to whether they are excitatory or inhibitory:** a neurotransmitter is excitatory or inhibitory depending on its receptor at the postsynaptic neuron.

In the following table is described the major neurotransmitters classified by its chemical composition and excitatory or inhibitory function:¹⁰

Table 1. Neurotransmitters classification based on their chemical composition and their excitatory or inhibitory effect.

Category		Neurotransmitter	Function
Ester		Acetylcholine	Excitatory and inhibitory
Amino acids		Glycine	Inhibitory
		Gamma-aminobutyric acid	Inhibitory
		Glutamate	Excitatory
		Aspartate	Excitatory
Amines	Catecholamines	Epinephrine	Excitatory and Inhibitory
		Norepinephrine	Excitatory and Inhibitory
		Dopamine	Excitatory and Inhibitory
	Indolamines	Serotonin	Excitatory
		Histamine	Excitatory
		Taurine	Inhibitory
Peptides		Endorphins	Excitatory and inhibitory
		Substance P	Excitatory and inhibitory
		Cholecystokinin	Excitatory and inhibitory
		Enkephalins	Excitatory and inhibitory
Gasotransmitters		Nitric oxide	Excitatory and inhibitory
		Carbon monoxide	Excitatory
		Hydrogen sulfide	Excitatory
Purines		ATP	Excitatory
Single ions		Zinc	Excitatory and inhibitory

Although classifying neurotransmitters can be a complicated task as there are over 100 different ones, fortunately, the seven “small molecule” neurotransmitters (**acetylcholine, dopamine, gamma-aminobutyric acid, glutamate, histamine, norepinephrine and serotonin**) regulate majority of the human body functions. Therefore, an imbalance in the concentration of these neurotransmitters can be related to the apparition of different pathologies.

Neurotransmitters functions and related disorders

Neurotransmitters play a remarkable role in the control and regulation of a wide variety of processes including emotions, fear, pleasure, joy, anger, mood, memory, cognition, attention, concentration, alertness, energy, appetite, cravings, sleep and the perception of pain.¹¹ Additionally, neurotransmitters chemically link the brain and spinal cord with the rest of the body: muscles, organs, and glands. In addition, because neurotransmitters are functionally integrated with the immune system and the endocrine system (including the adrenal glands), they affect every cell, tissue, and system in the body.

Any alteration in the production, release, reception, breakdown, or reuptake of neurotransmitters can cause neurologic or psychiatric diseases.¹² In fact, imbalances in certain neurotransmitters can cause widespread health problems such as:

Brain fog: loss of mental focus, attention deficit hyperactivity disorder, impaired memory, poor decision making; **Insomnia:** difficulty falling asleep, staying asleep, or both; **Pain:** migraines, fibromyalgia; **Obesity:** metabolic syndrome, insulin resistance and diabetes; **Mood disorders:** depression, mood swings, irritability; **Anxiety:** panic, obsessions, posttraumatic stress disorder; **Behavioural disturbances:** addictions, binge eating, compulsions, impulsivity, gambling, autism; and **Hormonal imbalances:** estrogen dominance, low testosterone, hypothyroidism.

Moreover, several studies have confirmed that abnormal levels of neurotransmitters or its metabolites concentrations in urine and blood are directly related to the appearance of pathologies such as Parkinson, Alzheimer, Huntington's disease, myasthenia gravis, epilepsy, schizophrenia, and depression and also with the apparition of certain tumours like pheochromocytoma and carcinoid tumours.¹³

In recent years different approaches have been developed for the reliable determination of neurotransmitters *in vivo* and *in vitro*. A widely-adopted analytical strategy is 'separation and detection' such as liquid chromatography (LC), capillary electrophoresis (CE), capillary electro-chromatography coupled with UV detection, flow immunoassay, native fluorescence detection, and electrochemical detection.¹⁴ However, there are increasing demands for new experimental methods since elucidation of the neurotransmitter metabolisms and their functions, the critical information in understanding neuroscience, requires further improvement of the analysis tools in this field to overcome the limitations of the current methods.

On the other hand, in order to correct the neurotransmitters imbalance produced as a consequence of the above mentioned pathologies, different drugs have been administrated. Some of the drugs used acts as neurotransmitters precursors being able to cross the blood-brain barrier, leading an increase in the neurotransmitter synthesis. Other drugs act as an antagonist or agonist of neurotransmitters leading an increase or decrease of the effect of the neurotransmitter.

However, although these drugs can help in the treatment of neurotransmitters imbalance pathologies, side-effects such as dyskinesia, falls, cognitive impairment, excessive daytime sleepiness, pedal edema, hallucinations and impulse control disorders have been reported.¹⁵ Some of these side-effects are produced due to the dissemination of the drug to others body parts where they are not needed.¹

1.2 Nanotechnology

Human dreams and the desire to manipulate matter on a small scale often give rise to new science and technology. Nanotechnology, a 21st-century frontier, was born out of such dreams. Nanotechnology is the study, design, synthesis, and application of materials and devices at dimensions between 1 and 100 nm, where unique phenomena enable novel applications.¹⁷ A nanometer (nm, 10^{-9} m) is equivalent to a distance 100000 times smaller than the diameter of a human hair (see Figure 2).

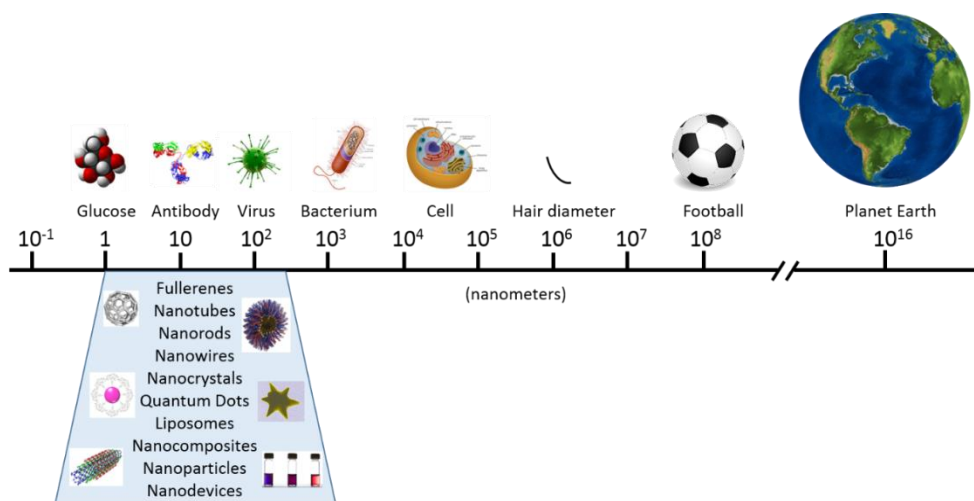


Figure 2. Scheme to compare the range of sizes of nanomaterials, cells and other items. *Reprinted with permission A. Llopis-Lorente PhD Thesis, 2019.*

However, it was not until the talk entitled “There’s Plenty of Room at the Bottom” by physicist and Nobel Prize winner Richard Feynman, in which he introduced the concept of manipulating matter at the atomic level, that the ideas and concepts behind nanoscience and nanotechnology started. This novel idea demonstrated new ways of thinking and Feynman’s hypotheses have since then been proven correct. It is for these reasons that he is considered the father of nanotechnology.¹⁸

A decade later, in his explorations of ultra-precision machining, Professor Norio Taniguchi coined the term nanotechnology. It was not until 1981, with the development of the scanning tunneling microscope that could "see" individual atoms that modern nanotechnology began.

Mechanical, electrical, thermodynamic, and other types of properties are strongly modified as the physical dimensions of a material enters the nanoscale, and researchers in the field are just beginning to catalog and understand these property modifications in this fuzzy area between the classical (bulk) and quantum domains. For example, when the gold atoms that are part of yellow shining gold bullion are rearranged to form small nanoparticles, they have red or blue color acquiring new physical and chemical properties.¹⁹

One of the most remarkable properties of nanomaterials is their high surface-to-volume ratio since as their volume decreases, their surface-to-volume ratio increases. This can be advantageous for some applications such as to catalyze reactions on their surface or for functionalization with a high percentage of biomolecules in order to develop more sensitive biosensors. Moreover, the small size of the nanoparticles allows them to penetrate inside cells to perform certain functions such as the delivery of a drug or a localized heating upon application of an external light.

The main areas of research and application of nanotechnology include medicine, electronics, the design of new materials, and energy production among others.²⁰ Regarding nanomedicine, developments based on nanotechnology have already begun, especially for diagnostic and therapeutic applications. Regarding diagnostic technologies, devices to identify the presence of a certain pathogen or cancer cells and determine their quantity are being developed. In relation to therapeutic technologies, new controlled drug release systems have been designed. The idea is to use functional "nanostructures" able to transport the drug to the damaged area and, once there, instead of releasing it in bulk and "indiscriminately" as with conventional drugs, release the drug at a continuous rate during more time and in a localized way, avoiding their strong side effects. This release is achieved in

response to a certain stimulus, which can be an increase in temperature, light, change in pH, etc. Nanotechnology allows the release of the drug to be minimally invasive and increases its effectiveness by precisely controlling the required dose, as well as the release site. Although there are already more than 50 nanomedicines approved by the FDA,²¹ it is important to be aware that introduction of nanotechnology in the actual medical practice will be slow due to the complexities and regulations involved.

In electronics, current research is focused on the development of smallest and efficient electronic devices. Nanomaterials with improved mechanical, optical and electronic properties are being developed for technological applications.²² Furthermore, nanotechnology holds also great potential in the development of solar cells and more efficient catalysts for the removal of toxic emissions.²³ Nanomaterials are already applied in a number of commercial products such as tennis rackets and bicycles with improved lightness and resistance thanks to carbon nanotubes, sun creams with titanium dioxide nanoparticles able to filter the UV-radiation, paints and deodorants with antibacterial nanoparticles, television screen with quantum dots, car bodyworks with nanocomposites, and so on.²⁴

Nowadays nanotechnology is an ongoing field of research and although remarkable advancements have been made in the last decades, there is still much progress to be made. In order to translate nanotechnology from the lab bench to our daily life will be crucial a better understanding of the properties of nanomaterials, the improvement of the preparation processes, the development of more advanced nanodevices and the collaboration between researchers from different fields and between academics and industry.

1.3 Gold Nanoparticles

Gold was one of the first metals to be discovered, its study and application spans at least several thousand years. Unlike bulk or molecular scale, nanoscale gold (gold nanoparticles) can exhibit unique optical and electronic properties, which have aroused the interest from chemists, physicists, and biomedical. Two physical effects are known to be responsible for these unique properties: one is the quantization of the electronic states, relevant to the optical and magnetic features that are significantly size-dependent, and are more apparent in nanomaterials; and the other is the higher surface to volume ratio compared to bulk materials, very important to the behavior of nanomaterials in terms of thermal, mechanical and chemical properties.²⁵

If they are present in suspensions, the nanomaterials tend to form colloids (by definition, a system composed of one solid or liquid phase in which a second liquid phase is in suspension). Colloids are especially attractive in research and applied science because of their intrinsic properties, such as the above-mentioned high surface to volume ratio. With a higher area of contact between the nanoparticle and the surrounding medium, the interactions are facilitated and, consequently, the ability to catalyze reactions via those interactions increases. Their optical properties, i.e., relevant extinction efficiency in the 300–1000 nm region of the light spectrum, are also suitable for biomedical and chemical protocols.²⁶

Colloidal gold has been used since ancient times as a method of staining glass. In 1676, Johann Kunckel, assumed that the pink color of colloidal gold came from small particles of metallic gold, not visible to human eyes. In 1842, John Herschel invented a photographic process called chrysotype (from the Greek χρῦσός meaning "gold") that used colloidal gold to record images on paper.

Modern scientific evaluation of colloidal gold did not begin until Michael Faraday's work in the 1850s. Faraday further investigated the optical properties of colloidal gold. He recognized that the color was actually due to the miniature size of the

gold particles. He noted the light scattering properties of suspended gold microparticles, which is now called Faraday-Tyndall effect.²⁷

In the last century, the studies on gold nanoparticles have been accelerated as a consequence of the advances in various analytical technologies. Advanced microscopy methods, such as Atomic Force Microscopy and Scanning Electron Microscopy, have contributed the most to nanoparticle research. As a result of extensive studies during the last few decades, it has come out that gold nanoparticles can be used successfully for a variety of applications in the fields of therapeutics,²⁸ biolabeling,²⁹ drug delivery,³⁰ chemical and biological sensing,³¹ imaging,³² nonlinear optics,³³ photovoltaics³⁴ and catalysis³⁵.

Moreover, in the last years various types of gold nanostructures with different shapes and sizes have been synthesized and studied, including nanospheres, nanorods, nanoshells, nanostars and nanocages, for a wide variety of applications. **Figure 3** illustrates some of the morphologies that are featured by gold nanoparticles.

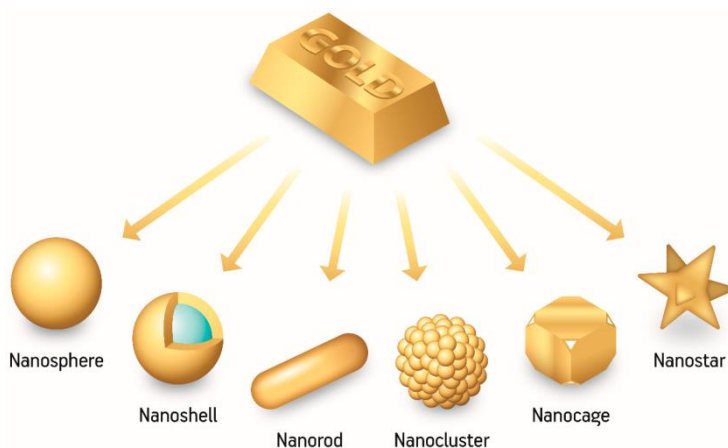


Figure 3. Representative scheme of the most common gold nanoparticle assemblies and morphologies. *Reprinted with permission from Nanomaterials 2018, 8, 939.*

Synthesis of AuNPs

In order to synthesize spherical gold nanoparticles (AuNPs), two basic strategies based on “**Top-down**” and “**Bottom-up**” approaches have been developed. The “**Top-down**” method produces AuNPs by shattering from bulk gold. The application of this method involves physical techniques such as ion sputtering,³⁶ laser ablation,³⁷ arc discharge,³⁸ UV and IR radiation,³⁹ aerosol technology,⁴⁰ etc. On the other hand, the “**Bottom-up**” method involves assembly of atoms, producing the desired AuNPs by chemical reduction of gold ions from a solution. **Figure 4** illustrates the two approaches for the synthesis of AuNPs.

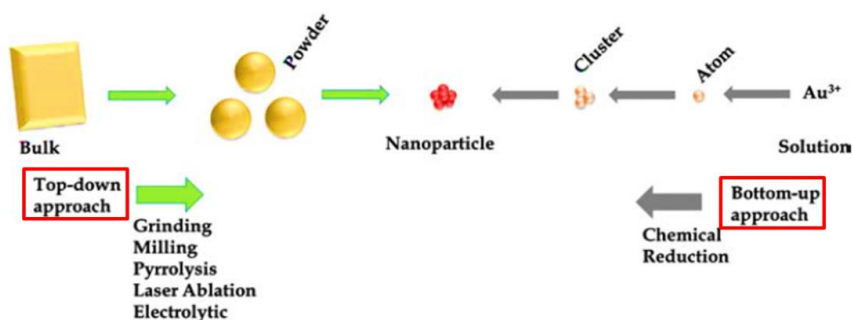


Figure 4. Representative scheme of the **Top-down** and **Bottom-up** approaches for the synthesis of AuNPs. Reprinted with permission from *J. Nanosci. Nanotechnol.*, 2015, 15, 1869-1894.

While both methods can generate AuNPs of desired shape and size, the “**Bottom-up**” methods are more commonly used at least for two reasons: they are more energy efficient and they can be used to produce AuNPs using standard apparatus available in a laboratory.

Broadly, the synthesis of AuNPs via chemical reduction (Bottom-up approach) requires the participation of three important agents:

- (i) **Gold precursor**, which provides the Au ions, the most widely used is the metallic salt of tetrachloroauric acid (HAuCl₄).
- (ii) **Reducing agent**, which reduces the Au (III) ions from the gold salt solution, to produce Au(0). Thus, suitable reducing agents such as citrate, borohydrides and ascorbic acid are commonly used. Moreover, some

studies have suggested the use of different types of amines as reducing agents.

(iii) **Capping or stabilization agent**, which prevents aggregation of the particles by electrostatic or steric stabilization, such as citrate, alkane thiols or polymers (PVA and PVP).

The type of gold precursor, reducing and capping agents selected, their ratio and chemical concentration, among other factors (pH, temperature, solvent) will determine the size and dispersity of the synthesized AuNPs. Regarding the mechanism of AuNPs formation, several experimental studies of nanocrystal growth and size have suggested LaMer-Dinegar⁴¹ mechanism, Ostwald⁴² ripening, or their combination as possible mechanisms of AuNPs formation. LaMer-Dinegar mechanism proposes that nucleation is temporally confined to an early burst period. Meanwhile, in Ostwald ripening, larger nanocrystals grow at the expense of smaller nanocrystals, which are progressively dissolved. Moreover, other experimental mechanistic studies have identified the participation of nanocrystal aggregation and coalescence in growth processes.

Figure 5 illustrates, LaMer-Dinegar curve, which describes the classical nucleation and growth process summarized into three stages⁴³:

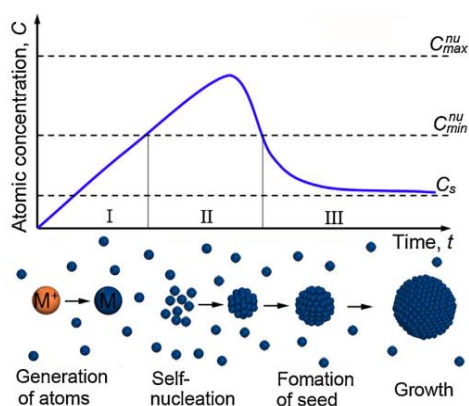


Figure 5. LaMer curve describing three stages of metal nanocrystal formation in solution system. Stage I: atom producing, stage II: nucleation, and stage III: seed formation and growth. *Reprinted with permission from Nano Today, 2016, 11, 145-167.*

- **Stage I:** atoms production is carried out by the reduction of metallic ions with reducing reagents, until the atomic concentration reaches the maximum point of supersaturation (C_{\max}).
- **Stage II:** via self or homogeneous nucleation, the atoms start to aggregate in order to produce stable small clusters. Consequently, the concentration of atoms quickly drops below the minimum supersaturation (C_{\min}) level and no additional nucleation events occur.
- **Stage III:** seed formation takes place by the increase of the nuclei size, which upon reaching a critical size point become locked into a well-defined structure. This seed further grows to form the final nanocrystal through the addition of metal atoms until the concentration decreases to C_s (solubility concentration of nanocrystals).

In the past decades, several theories beyond the different stages of the LaMer curve have been developed in order to describe the process of nucleation and growth of nanoparticles. Among the most recently, mechanism proposed is the one that includes the classic nucleation and growth processes proposed by LaMer (C), aggregate nucleation and growth processes (A) and the processes of maturation described by Ostwald (OR). **Figure 6** illustrates how the three processes can overlap temporarily.⁴⁴

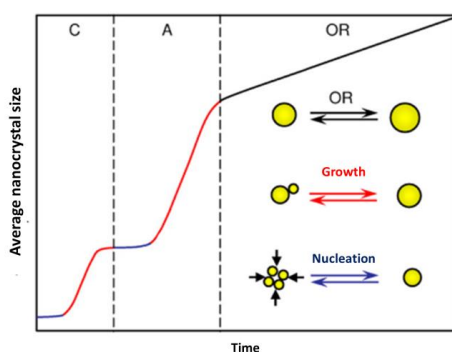


Figure 6. Schematic representation of the nanocrystal formation process including 3 stages. Reprinted with permission from *Chem. Mater.* 2014, 26, 1, 5-21.

In order to prepare AuNPs with different sizes, the two most commonly used methods are the **Turkevich-Frens method** for nanoparticles between 10 and 150 nm and the **Brust-Schiffrin method** for smaller nanoparticles, between 1 and 5 nm.

- **Citrate reduction method (Turkevich-Frens Method)**

One of the most common methods, used for the synthesis of monodisperse spherical AuNPs of around 10–150 nm in diameter, is based on the reduction of Tetrachloroauric(III) acid (HAuCl_4) in water using trisodium citrate (see **Figure 7**).

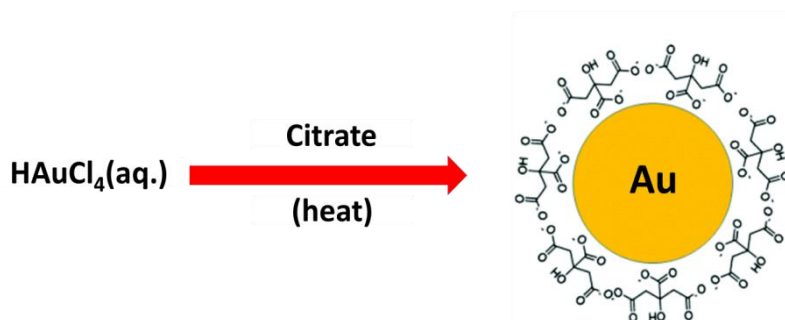


Figure 7. Schematic representation of Citrate Reduction Method (Turkevich-Frens Method) for the synthesis of AuNPs.

This method was reported by Turkevich in 1951⁴⁵ and optimized later in 1973 by Frens⁴⁶. To carry out this method, an aqueous solution of HAuCl_4 is boiled and then a solution of trisodium citrate dihydrate is quickly added under vigorous stirring. After a few minutes, a wine-red colloidal suspension of gold is obtained. In this method, trisodium citrate acts as a **reducing agent**, by producing the reduction of Au^{3+} to Au^+ , then the Au^+ dismutated to Au and Au^{3+} , consequently sodium citrate is oxidized to 3-oxoglutaric acid. **Stabilizing agent** covering the surface of the as-produced AuNPs creating repulsive forces among nanoparticles, which prevent further aggregation. Moreover, the gold nanoparticles size and shape can be tuned by the proper control of different factors like, stabilizing agents, pH, chemical concentrations, temperature, etc. The particle size can also be controlled by changing the Au^{3+} /citrate ratio. Therefore, as the concentration

of citrate increases, the AuNPs particle sizes decrease as a consequence of the stabilizing process of the citrate. On the other hand, at lower concentrations of citrate, the coverage of citrate on AuNPs is incomplete and the aggregation process leads to form larger particles. However, nanoparticles bigger than 20 nm synthesized by this method, have higher polydispersion than AuNPs of smaller sizes.

- **Brust-Schiffrin method**

A two-phase reduction method for the preparation of narrow dispersity small nanoparticles (1–5 nm) stabilized by a monolayer of alkanethiols, was reported by Brust and Schiffrin in 1994⁴⁷ (see Figure 8).

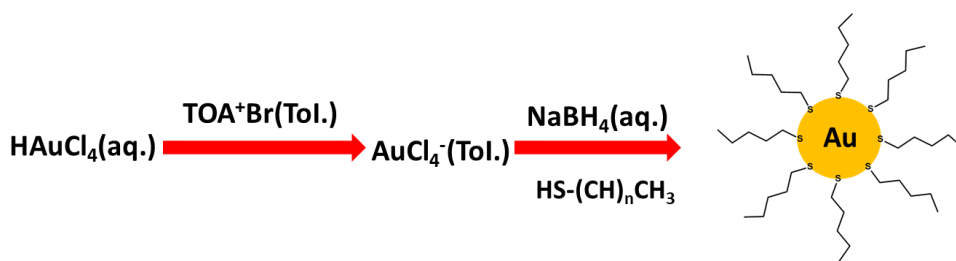


Figure 8. Schematic representation of Brust-Schiffrin Method for the synthesis of spherical gold nanoparticles.

This method involves a simple procedure based on fast chemical reduction of gold ions by borohydride at room temperature in a two-phase system (water-toluene), immediately followed by adsorption of alkanethiols. In this method, an aqueous solution of gold precursor HAuCl_4 is transferred to toluene (organic phase) using as the phase-transfer catalyst the surfactant tetraoctylammonium bromide (TOAB). After adding the stabilizing agent dodecanethiol to the organic phase, an aqueous solution of the reducing agent, sodium borohydride (NaBH_4) is added in order to reduce the Au^{3+} ions. On addition of NaBH_4 , a quick color change from orange to deep brown takes place in organic phase. These thiol-protected AuNPs show a high stability due to the strong thiol-gold interaction and they can be easily handled, characterized and functionalized. Moreover, these thiol-protected AuNPs can be thoroughly dried and then re-dispersed in organic solvents without any aggregation or decomposition process observed. Like citrate-capped AuNPs

the size of these thiol-protected AuNPs can be tuned by controlling various reaction conditions such as gold/thiol ratio, temperature and reduction rate.

- **Other methods for the synthesis of AuNPs**

Over the years, other alternative methods for the synthesis of spherical AuNPs have been developed. Some of them, like the Turkevich-Frens method, use a single reagent as the reducing/stabilizing agent such as Chitosan⁴⁸ or multifunctional peptides containing a gold synthesizing/binding domain.⁴⁹ Others methods consist in the application of electrosynthesis⁵⁰ and solid phase mechanochemical techniques.⁵¹ In the electrosynthesis technique, a metallic gold wire or sheet is taken as the anode in an electrolytic cell, in the presence of suitable stabilizers like tetraalkyl ammonium salts or citrate salts. Regarding the solid phase mechanochemical process, AuNPs can be synthesized by high-speed vibration milling of a gold precursor, KAuCl_4 using sodium borohydride as the reducing agent in the presence of PVP as a stabilizing agent. Moreover Rak et al. have developed an efficient solvent-free mechanochemical methodology for the rapid synthesis of amine-stabilized ultra-small AuNPs.⁵²

Stabilizing agents and functionalization of AuNPs

Aggregation is a major issue in the stabilization and functionalization of AuNPs, therefore, the use of stabilizing agents play a key role in the stabilization of AuNPs, preventing their aggregation by keeping them apart from each other. In general, the stabilizing agents form a monolayer around the gold nanoparticles surface and confer a large number of properties such as stability against aggregation, improved solubility, controlled shape and orderly assembly of nanoparticles, improved electron-transfer efficiency and provide a platform for the sensing of specific molecules or ions⁵³.

Stabilizing agents can be classified, on the basis of their donor group, as anionic and neutral. The anionic stabilizing agents include carboxylates, phosphonates, sulfonates, alkoxides, and thiolates and neutral stabilizing agents include amines, phosphines, alcohols, amides, ethers, thiols and disulfides. The hydrocarbon

shell, which can be achieved either directly during synthesis⁵⁴ or by place-exchange reactions.⁵⁵

- As second component, the stabilizing agent should possess a charged group or be composed by large polymeric chains which prevent the aggregation either electrostatic or steric repulsion.

The stabilization of the gold nanoparticles can be achieved by using mechanisms of charge stabilization or steric stabilization. *Charge stabilization mechanism* is achieved by adsorbing charged ligands like citrate, on the surface of the nanoparticle. Thus, by acquiring a charge on the nanoparticle surface, they repel each other from becoming aggregates. *The steric stabilization* is achieved by coating the gold nanoparticles surface with large molecules like polymers such as poly(N-vinyl-2-pyrrolidone), poly(acrylonitrile), and poly(mercaptomethylstyrene-co-N-vinyl-2 pyrrolidone).⁵⁶

In addition, with the aim of improving the stability and provide new properties or functionality to the gold nanoparticles, the molecules that act as stabilizing agents on the AuNPs surface can be exchanged by others via ligand exchange method. This method consists in the replacement, of the original capping molecules from the AuNPs surface for other ligand molecules with higher affinity for gold.⁵⁷

For instance, gold nanoparticles synthesized by citrate reduction method can exchange their citrate layer by ligands with stronger binding to the particle surface; popular examples include sulfonated phosphines or mercaptocarboxylic acids. In general, thiol groups are considered to show the highest affinity to noble metal surfaces, in particular to gold (approx. 200 kJ mol^{-1}).⁵⁸

Moreover, synthesis of aptamer-conjugated AuNPs generally involves chemical synthesis of AuNPs in the presence of reducing and stabilizing agents, and subsequent ligand exchange with the aptamers.

Optical properties of AuNPs

AuNPs exhibit unique optical properties, which allow its applications in different areas like sensing, imaging, labelling etc. The solutions of AuNPs show different colors depending upon the size and shape of the nanoparticles. The origin of the color is attributed to the collective oscillation of the free electrons from the conduction band induced by an interacting electromagnetic field, a phenomenon known as **surface plasmon resonance** (SPR). As a consequence of the SPR, a strong and broad **surface plasmon resonance band** (SPRB) is observed in the UV-visible spectrum for metallic NPs bigger than 2 nm.

In 1908, Mie first elucidated the origin of the SPR phenomenon by solving Maxwell's electromagnetic equation for small homogeneous spherical particles interacting with an electromagnetic field.⁵⁹ In metals, the quasi-free electrons are not bound to a single atom but are detached from the core and can move freely through the crystalline structure of the metal. The mechanical oscillation of these electron charges can couple with the oscillations of the electric field of electromagnetic wave and gives rise to the SPR (see **Figure 10**).

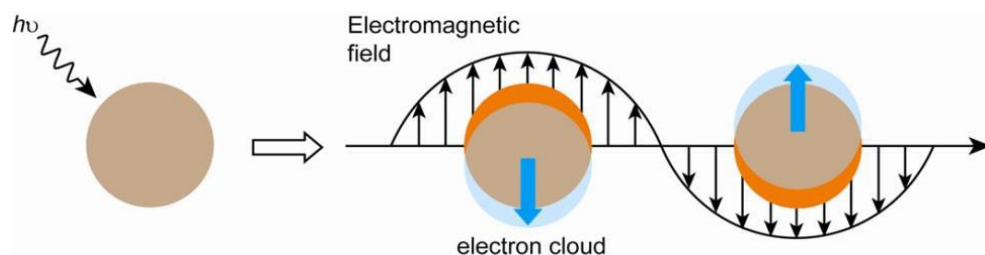


Figure 10. Schematic representation of the oscillation of conduction electrons across the nanoparticle in the electromagnetic field of the incident light. *Reprinted with permission from Nanoscale, 2012, 4, 1871-1880*

For AuNPs, the resonance condition is satisfied at visible wavelengths, which explains its intense color. The SPRB is influenced not only by size and shape but also by solvent, ligand, interparticle distance and temperature. Importantly, as noted before, the SPRB frequency is sensitive to the proximity of other nanoparticles. Therefore, the aggregation of nanoparticles results in significant red-shifting (from ~ 520 to ~ 650 nm) and broadening in the SPRB, changing the

solution color from red to blue due to the interparticle plasmon coupling. This phenomenon has made AuNPs attractive candidates for the development of colorimetric sensors.

In order to determine AuNPs concentration, Liu et al. reported a linear relationship between logarithms of molar extinction coefficient (ϵ) and the core diameter (d) of the gold nanoparticles, independently of the capping ligands on the particle surface and the solvents used to dissolve the nanoparticles. This linear relation can be used as a calibration curve to determine the concentration or average size of an unknown nanoparticle or nanoparticle–biomolecule conjugate sample (see Figure 11).⁶⁰ This finding also agrees with Mie's theory, as well as the study reported by El-Sayed and his team.⁶¹

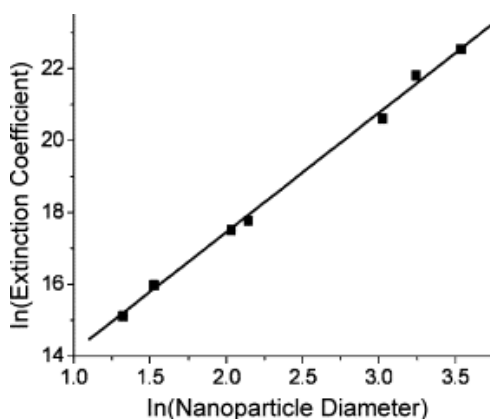


Figure 11. Linear fitting curve of natural logarithm of extinction coefficients vs. logarithm of average nanoparticle core diameters. Reprinted with permission from *Colloids and Surfaces B: Biointerfaces*, 2007, 58, 3-7.

This relationship can be expressed as:

$$\ln \epsilon = k \cdot \ln d + c \quad (1)$$

Where $k = 3.32$ and $c = 10.8$ ($\lambda = 506$ nm). Therefore, the nanoparticles concentrations can be readily deduced from the Beer-Lambert law once the nanoparticle size is known (from TEM). According to equation (1), it is estimated

that AuNP of 20 nm diameter have a molar excitation coefficient of $1 \cdot 10^9 \text{ M}^{-1} \text{ cm}^{-1}$. This value is at least three orders higher than that of common organic dyes (10^4 - $10^6 \text{ M}^{-1} \text{ cm}^{-1}$), indicating that AuNPs may serve as excellent light collectors.

AuNPs as colorimetric sensors

The unique optical properties presented by AuNPs make them excellent materials for the fabrication of novel chemical and biological sensors. Therefore, one of the most important applications of AuNPs is their use as sensors for the detection of analytes with clinical or environmental interest. In addition to their optical properties, AuNPs hold several attributes that make them an ideal sensing platform, including:

- (i) Ease of synthesis;
- (ii) Chemical stability, photostability and biocompatibility;
- (iii) High surface-to-volume ratio, to enhance the sensitivity since the detection events between the analyte and the receptors occur on the particle surface;
- (iv) Ease of functionalization of the surface with multiple organic and biological ligands to allow the interaction with the target analyte;
- (v) Large extinction cross-sections, allowing single AuNP sensors or single-molecule assay in the best cases.

A typical sensor must satisfy the following two requirements:

- (i) It should show a measurable change of some property during the recognition event. Regarding AuNPs, changes in parameters like size, shape or their environment can result in any detectable response signal.
- (ii) It should have a ligand or receptor that selectively interacts with the analyte. When the sensor designed is based on AuNPs, the ligand selected must be able to produce the change of the selected property, only in the presence of the target analyte.

The intense absorption of AuNPs in the visible region with very high extinction coefficients and the strong dependence of SPRB peaks on the immediate environment, make AuNPs attractive candidates to be used as colorimetric sensors. The colorimetric sensing based on AuNPs is a promising analytical method that provides a simple, rapid and inexpensive method for the detection and measurement of analytes. Most often, this method gives signaling of the targeted analyte through a color change that allows detection by the naked eye.

The aggregation of AuNPs of appropriate sizes ($d > 3.5$ nm) induces interparticle surface plasmon coupling, resulting in a visible color change from red to blue at nanomolar concentrations.⁶² The color change during AuNP aggregation (or redispersion of an aggregate) provides a practical platform for absorption-based colorimetric sensing of any target analyte that directly or indirectly triggers the AuNP aggregation or redispersion⁶³ (see Figure 12).

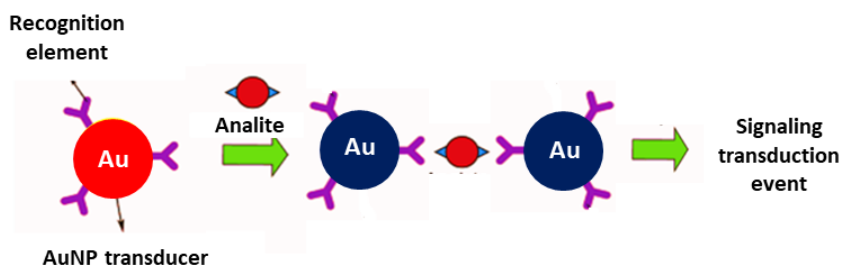


Figure 12. Schematic representation of the AuNPs sensing paradigm, which consists of the aggregation by the presence of the targeting analyte.

Detection of metal ions

The typical strategy of AuNPs based colorimetric sensing for metal ions involves the functionalization of the nanoparticle surface with suitable chelating agents that selectively attach the analyte metal ions and thereby induce aggregation. This causes a red shift in the absorption band due to the interparticle distance sensitivity of SPRB, resulting in a color change from red to blue.

❖ Alkali and alkaline earth metal ions

A colorimetric selective detection of potassium ions in aqueous solution using AuNPs functionalized with crown ether was demonstrated by Lin et al. (see **Figure 13**). Crown ethers are well known for their capacity of forming stable complexes with alkali metals and their selectivity to ions can be tuned by the ring size. In this study, AuNPs were functionalized with thiolated 15-crown-5 ether. The recognition process consists on the aggregation of the AuNPs via formation of a 2:1 sandwich complex between 15-crown-5 moiety and K^+ , which produce a decrease in the absorbance at 528 nm with a concomitant rise of an absorption peak around 710 nm resulting in an immediate color change from red to blue. This sensor system showed micromolar recognition and colorimetric response toward K^+ even in the presence of physiologically important cations, such as Li^+ , Cs^+ , NH_4^+ , Mg^{2+} , Ca^{2+} , and excess Na^+ . In a similar fashion, analogous detection system based on AuNPs functionalized with thiolated crown ethers were fabricated for the detection of Na^+ and Li^+ . Moreover, AuNPs functionalized with lactose has been developed for the detection of Ca^{2+} through metal ion-mediated carbohydrate-carbohydrate interactions.⁶⁴

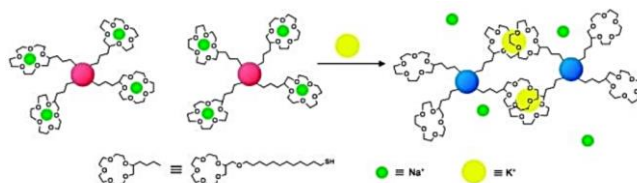


Figure 13. Schematic representation of red to blue color colorimetric sensing of metal ions using AuNPs functionalized with chelating ligands. *Reprinted with permission from Anal. Chem.* 2002, 74, 2, 330-335

❖ Detection of toxic metal ions

The selective and sensitive determinations of various valuable and toxic metal ions are of great importance in different fields such as environmental monitoring, wastewater treatment and food industry. Therefore, several studies have been done in order to develop colorimetric sensors for the selective detection of toxic metal ions.

For instance, citrate synthesized AuNPs, functionalized with glutathione (GSH), dithiothreitol (DTT) and cysteine (Cys) in one set and the chelating agent 2,6-pyridinedicarboxylic acid (PDCA) in another set were also demonstrated to be useful for As^{3+} detection.⁶⁵ PDCA was used to avoid interference from Hg^{2+} ions. DTT assists in the conversion of As^{5+} to As^{3+} , that then binds to the AuNPs leading to aggregation and corresponding change in colour and shift in SPRB peak. A colorimetric sensor for Hg^{2+} was developed by Lai and co-workers⁶⁶ by functionalizing AuNPs using papain (a protein with seven cysteine residues and 212 amino acid residues, which can combine with Hg^{2+}) and PDCA which has a strong affinity for Hg^{2+} . Selectivity measurements reveal that the sensor is specific for Hg^{2+} even with interference by high concentrations of other metal ions (see **Figure 14**).

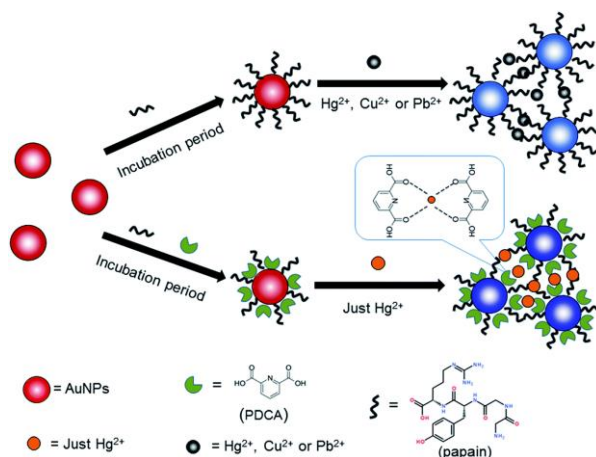


Figure 14. Schematic representation of red to blue colour colorimetric sensing of toxic metal ions using AuNPs functionalized with chelating ligands. *Reprinted with permission from RSC Adv., 2016, 6, 3259-3266.*

❖ Detection of anions

Several studies have been carried out in order to design sensing systems for anionic species. Designing sensing systems for anion recognition is challenging due to their lower charge to radius ratio, pH sensitivity, wide range of geometries and solvent dependent binding affinity and selectivity. Keeping this into account, colorimetric sensing of hydrophilic anions (e.g., dihydrogen phosphate) has been

achieved in dichloromethane using AuNPs with phenyl urea anion binders.⁶⁷ AuNPs coated with ethylene glycol-appended isothiuronium units were used to detect F^- in water using 3-nitrophenylboronic acid as a mediator at pH 5.5.⁶⁸ Han et al. reported a colorimetric detection method for cyanide anions in aqueous solution employing adenosine triphosphate-stabilized AuNPs and a Cu^{2+} phenanthroline complex as the receptor unit.⁶⁹ In the sensing ensemble, exposure of CN^- to Cu^{2+} phenanthroline complex induced a decomplexation process to generate free phenanthroline, which subsequently caused the ATP-stabilized AuNPs to aggregate resulting in colour change. Moreover, Martí et al. reported AuNPs functionalized with thiourea moieties for the colorimetric detection of succinate versus other aliphatic dicarboxylates. The detection process is based on the interparticle aggregation triggered by coordination of the end carboxylates to the thiourea moieties of two different nanoparticles⁷⁰ (see Figure 15).

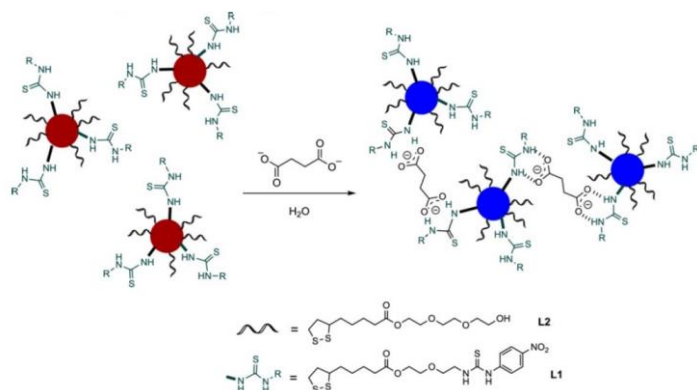


Figure 15. Schematic representation of red to blue colour colorimetric sensing of anions using AuNPs functionalized with chelating ligands. Reprinted with permission from *ChemistrySelect*, 2016, 1, 1057-1060.

Detection of small organic molecules

Regarding small organic molecules detection, Martí et al. reported a selective colorimetric systems for $NO(g)$ detection based on the use of modified AuNPs using click chemistry.⁷¹ The recognition method is based on the aggregation of modified AuNPs through a Cu^+ catalyzed click reaction promoted by the *in situ* reduction of Cu^{2+} by NO . Moreover, AuNPs functionalized with a triarylcarbinol derivative have been used as colorimetric molecular probes for the naked-eye

detection of the nerve agent simulants Diethyl cyanophosphonate (DCNP) and Diisopropyl fluorophosphates (DFP).⁷² The detection process is based on the compensation of charges at the surface of the nanoparticles, which triggers their aggregation in solution with the resulting change in their plasmon band. Sensing probes based on AuNPs have demonstrated their sensing capability through the detection of the explosive trinitrotoluene (TNT), in which AuNPs functionalized with cysteamine aggregated in presence of TNT due to the donor–acceptor (D-A) interaction between TNT and cysteamine⁷³ (see Figure 16).

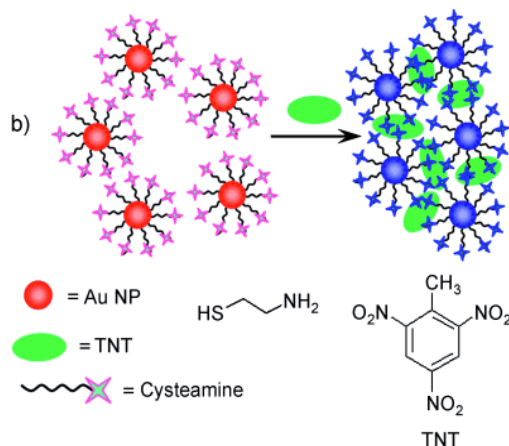


Figure 16. Schematic representation for direct colorimetric visualization of TNT based on the D-A interaction between TNT and cysteamine at the AuNP solution interface. *Reprinted with permission from Angewandte Chemie International Edition, 2008, 47, 8601-8604.*

1.4 Mesoporous silica nanoparticles

As defined by the IUPAC, porous materials are classified according to their pore diameter in microporous (< 2 nm), mesoporous (2-50 nm) and macroporous (> 50 nm) materials. In the last years, mesoporous silica nanoparticles (MSNs) have gained wide popularity in the scientific community. This fact is due to their exceptional properties such as mechanical strength, chemical stability, biocompatibility and synthetic versatility.⁷⁴ These MSNs are constituted by a silica matrix and are characterized by the presence of pores with a diameter between 2 and 30 nm.⁷⁵ This singularity provides to these MSNs two differentiated domains: an external surface and an inner surface in the pores that can be independently functionalized. The main characteristics of MSNs are:⁷⁶

- Large specific surface area (500-1000 m²/g).
- High pore volume and loading capacity.
- Ordered and uniform pore distribution.
- Tunable pore size from 2-30 nm.
- Preparation in the form of micrometric particles or nanoparticles with tunable size through changes in the synthetic parameters.
- Their synthesis requires inexpensive and non-hazardous chemicals and can be produced in large scale.
- Thermal stability, chemical inertness and easy handling.
- Easy functionalization with trialkoxysilane derivatives.
- Biocompatibility.

Based on these characteristics, MSNs have attracted considerable attention for applications such as catalysis,⁷⁷ adsorption of gases and chemicals,⁷⁸ filtration and separation,⁷⁹ chemical/biochemical sensing,⁸⁰ enzyme immobilization,⁸¹ tissue regeneration⁸² and drug delivery.⁸³

The preparation of MSNs from surfactants as structure- directing agents for the self-assembly and condensation of inorganic precursors, was communicated for the first time by scientists from the Mobil Research and Development Corporation

in 1992, under the aim of finding materials with larger pores than those presented by zeolites (whose pores size had technological limitations).⁸⁴ The new MSNs known as Mobil Composition of Matter (MCM) represented a real revolution in the field of mesoporous materials.⁸⁵

Among the most popular MSNs that are keenly studied by researchers are (see **Figure 17**):

- **Mobil Composition of Matter No. 41 (MCM-41):** with a pore diameter of 1.5 to 8 nm and hexagonal arrangement of mesopores (like a honeycomb). MCM-41 is one of the most widely explored materials especially for drug delivery.
- **Mobil Composition of Matter No. 48 (MCM-48):** with a pore diameter of 2 to 5 nm and cubic arrangement of mesopores.
- **Mobil Composition of Matter No. 50 (MCM-50):** with a pore diameter of 2 to 5 nm and lamella-like arrangement.

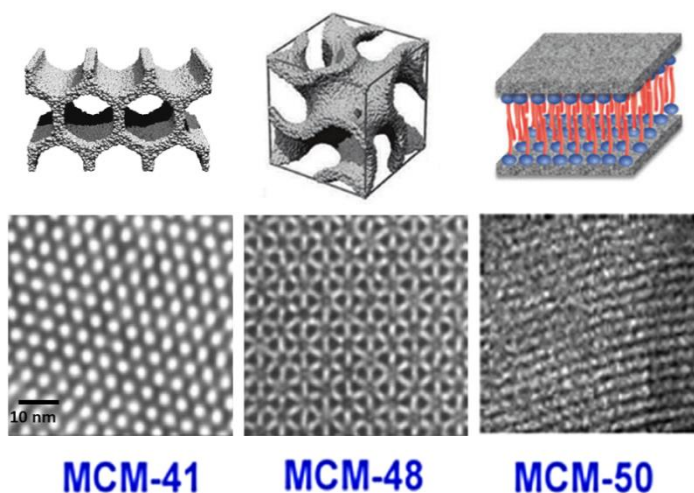


Figure 17. Schematic representation of different types of MCM materials. *Reprinted with permission from Chemical Society Reviews 2013, 42, 3663-3670.*

Furthermore, in 1998 researchers from Santa Barbara University reported the so-called SBA materials which are a family of MSNs which have been designated as SBA-11 (cubic), SBA-12 (3-d hexagonal), SBA-15 (hexagonal) and SBA-16 (cubic cage-structured) based on the symmetry of the mesoporous structure and the triblock polymers used.⁸⁶ They are different from MCM in that they possess larger pores of 4.6–30 nm and thicker silica walls.

Synthesis of mesoporous silica nanoparticles

Generally, the synthesis of inorganic MSNs is accomplished by the use of a **template** that acts as a structure-directing agent, and the use of a **polymeric precursor**, which has to self-organize around the template and, upon polymerization, build up the final rigid structure.

The synthesis methodology is based on the condensation of a silica precursor (for instance tetraethyl orthosilicate, sodium silicate or tetramethylammonium silicate) in the presence of cationic surfactants under basic conditions.⁸⁷ This is similar to the method described by Stöber in 1968 for obtaining silica nanoparticles, but performed in the presence of surfactants. It is considered a sol-gel process, which means that involves the conversion of monomers in solution (sol) into an integrated solid network (gel).

The use of cationic surfactants allows obtaining ordered and monodisperse structures through the formation of supermicelles (supramolecular self-assemblies of individual micelles) over which the precursors molecules condensate. The structure of supermicelles depends on the selected conditions such as temperature, pH, ionic force and surfactant nature and concentration.

The standard procedure for the synthesis of MCM-41-type MSNs consists of mixing a silicate precursor, usually tetraethylorthosilicate (TEOS), with a cationic surfactant, being the most widely used cetyltrimethylammonium bromide (CTAB), at a temperature of 80 °C in basic medium (pH = 11). The nanoparticles are formed by the sol-gel process catalyzed in basic medium, according two key reactions, i.e. hydrolysis and condensation. **(See Figure 18)**

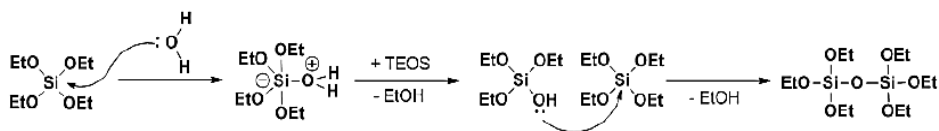


Figure 18. Mechanism of TEOS hydrolysis and condensation.

The first stage of the process consists of the hydrolysis of the tetraethylorthosilicate, followed by condensation of the corresponding silanol with another TEOS molecule forming a siloxane bond (Si-O-Si). After several hydrolysis and condensation reactions, a colloidal suspension containing particles smaller than 100 nm is obtained, while silanol groups (Si-OH) are formed and the corresponding alcohol is released. Then, the silanol groups polymerize by condensation, forming three-dimensional structures linked by siloxane bonds with elimination of water or alcohol.

In this second stage of condensation, a gel more or less compact and dense is formed. The presence in this phase of micelles, formed by the surfactant, is critical since they act as a template and will give rise to the formation of the pores. The structure of the pores in the final material (hexagonal in the case of MCM-41) is the result of the arrangement of the surfactant's micelles. Thus, the cationic surfactant attracts the negative charges of the silica species, which are concentrated around the micelles forming a tubular silica structure. The nanoparticle increases in size until the negative net charge, introduced by the silica species, is so high that it stops growing. It is worth mentioning that the size, shape and regularity of the nanoparticles depend on various variables such as temperature, rate of addition, stirring and the ratio of catalyst to TEOS used. The progressive formation of the silica material can be observed with the naked eye by the appearance of a white turbidity.

Later, the surfactant is removed by an extraction process under reflux in acidic media or by calcination (heating of the solid in a muffle furnace at high temperatures for several hours). These treatments facilitate the elimination of the

surfactant inside the mesoporous and the final formation of the MCM-41-type MSNs (see Figure 19).

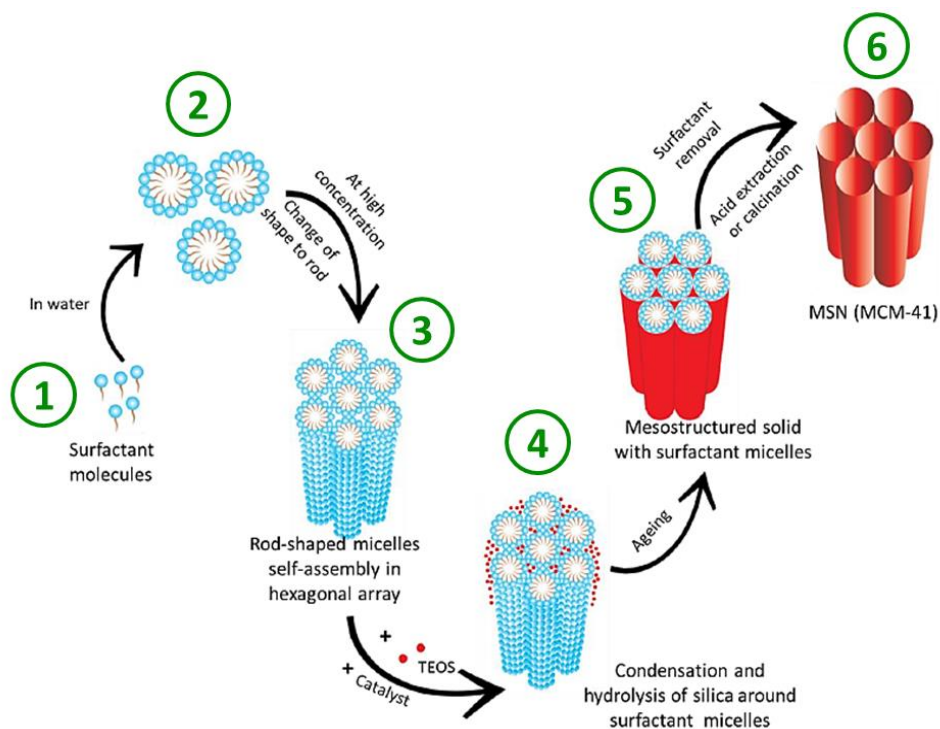


Figure 19. Schematic of synthetic procedure for MCM-41-type MSNs. Adapted from *Pharmaceutics* 2018, 10, 118.

Functionalization of mesoporous silica nanoparticles

The combination of organic and inorganic materials properties in order to build hybrid organic-inorganic materials is particularly attractive due to the possibility of combining the enormous functional variation of organic chemistry with the advantages of a thermally stable and robust inorganic substrate. As a result of this symbiosis, it is possible to obtain materials whose properties can differ significantly from those of the single, isolated components.

The surface functionalization of MSNs via incorporation of organic components leads to the production of hybrid organic-inorganic materials, where the inorganic and organic components are linked via certain interactions.

Hybrid organic-inorganic materials play a major role in the development of advanced functional nanomaterials. These hybrid materials combine the high surface area, stability and easy handling of the inorganic scaffold with a high number of localized functional organic moieties, resulting in new highly adaptive support for a wide range of applications such as chromatography, sensing, catalysis, etc.

Three general pathways are available for the synthesis of mesoporous hybrid materials based on organosilica units:

- (i) **Grafting**, a post-synthetic method that allows by silanization process the incorporation of organosilica precursors to the surface of the as-synthesized inorganic materials.
- (ii) **Co-condensation**, a direct synthetic method, in which the simultaneous condensation of corresponding silica and organosilica precursors is produced.
- (iii) **Periodic mesoporous organosilicas**, the incorporation of organic groups as bridging components directly and specifically into the pore walls by the use of bisilylated single-source organosilica precursors.

▪ **Functionalization by grafting procedure:**

The grafting procedure consists of a subsequent functionalization with organic groups of the previously synthesized MSNs. This method takes advantage of the high concentration of free silanol groups (Si-OH) located in the surfaces of the MSNs, which act as reactive points to anchor organosilanes containing the desired organic moiety.⁸⁸

As part of this process, the free silanol group can react with different types of organosilanes, being trialkoxysilanes with structures $(R'O)_3\text{-Si-R}$ (where R is an organic group) the most common and widely used, and less frequently silazanes $\text{HN}(\text{SiR}_3)_2$ or chlorosilanes ClSiR_3 . In principle, functionalization with a variety of

organic groups can be realized in this way by variation of the organic residue R (see Figure 20).

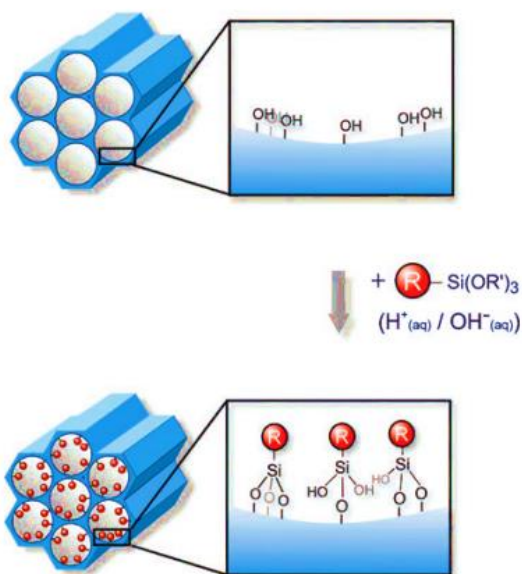


Figure 20. Schematic representation of mesoporous silica nanoparticles functionalized by grafting procedure. Reprinted with permission from *Chem. Soc. Rev.*, 2011, 40, 608-620

This method of functionalization has the advantage that, under the synthetic conditions used; the mesostructure of the silica phase, as well as the morphology of the MSNs, is usually retained. On the other hand, when final MSNs (after the template removal) are functionalized by grafting, the external surface is more accessible and is functionalized predominantly over the internal mesopore surface. This fact can in turn lead to a non-homogeneous distribution of the organic groups on the material surface, and a lower degree of occupation within the pores. Moreover, in cases when the grafting species are very bulky, the preferential external functionalization of the material can lead to complete closure of the pores.

Furthermore, it is possible to achieve a regioselective functionalization of the MSNs by anchoring different groups on the external and internal surface. For this, an appealing strategy is to use the as-synthesised MSNs (with pores occupied by

the surfactant molecules) and treat it with an organosilane that will be attached to the outer surface. Then, the surfactant is removed by extraction (with a refluxing solution of HCl in ethanol) and the resulting surfactant-free scaffold is further functionalized in its internal surface with a different organosilane. The suitability of these methods depends on the properties of the grafting species (size, reactivity, etc.).

▪ **Functionalization by co-condensation procedure:**

This second approach, used for the direct synthesis of hybrid MSNs, makes use of the versatility of the sol–gel process. In the so-called co-condensation method, the hydrolysis and co-condensation of tetraalkoxysilanes $[(RO)_4Si]$ (TEOS or TMOS) with terminal trialkoxy organosilanes of the type $(R'O)_3SiR$ is carried out in a single reaction mixture ('one-pot') in the presence of a directing agents leading to materials with organic residues anchored covalently to the pore walls⁸⁹ (see **Figure 21**).

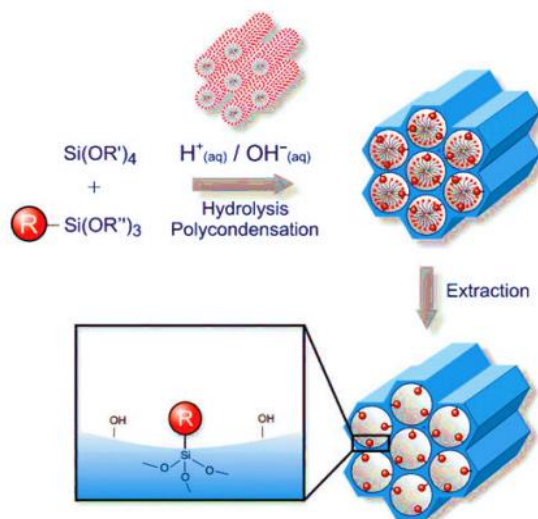


Figure 21. Schematic representation of MSNs functionalized by co-condensation procedure. Reprinted with permission from *Chem. Soc. Rev.*, 2011, 40, 608-620

This method has as advantage that the organic units are generally more homogeneously distributed both on the external and internal surfaces than in

materials synthesized with the grafting process. In this case, the surfactant must be removed by extraction since calcination would spoil the organic functional groups. However, it is also important to point out that the introduction of functional groups will affect the interactions with the surfactant as well as the structure stability and the particle morphology. In some cases, if the amount of added organosilane is too high, it can even prevent the formation of the mesoporous structure. Therefore, although some procedure for incorporating specific and common trialkoxysilanes can be found in the literature, this method is less versatile since the procedure should be optimized in each particular case.

- **Periodic mesoporous organosilicas**

Another strategy less employed for incorporating organic compounds onto MSNs is the production of Periodic Mesoporous Organosilicas (PMOs). In contrast to the organically functionalized MSNs, which are obtained by postsynthetic or direct synthesis, the organic units, in this case, are incorporated in the three-dimensional network structure of the silica matrix through two covalent bonds and thus distributed totally homogeneously in the pore walls⁹⁰.

In this method, silsesquioxane precursors are used. These compounds have molecular structures of the type $(R'O)_3Si-R-Si(OR')_3$, being R the organic functional group to be introduced on the material. They are also called “single-source” precursors since they act as the precursor of the inorganic network and, at the same time, incorporate the organic functionality. These materials, which are obtained as porous aerogel and xerogels, can have large inner surface areas of up to $1800\text{m}^2/\text{g}$ as well as high thermal stability but generally, exhibit completely disordered pore systems with a relatively wide distribution of pore radius. (see **Figure 22**).

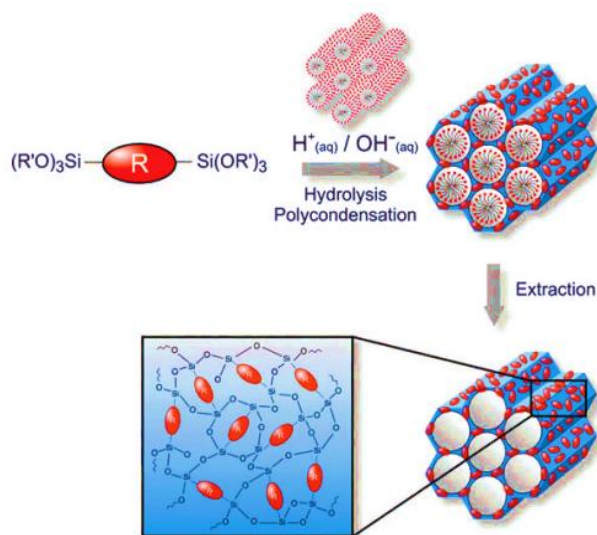


Figure 22. Schematic representation of MSNs functionalized by the synthesis of periodic mesoporous organosilica. *Reprinted with permission from Chem. Soc. Rev., 2011, 40, 608-620.*

Post-functionalization of mesoporous silica nanoparticles

In order to confer greater complexity to the MSNs and improve their functionality, different post-functionalization protocols have been described. The aim of these protocols is to allow that practically any functional group, macromolecule and even other nanoparticles are incorporated into the mesoporous silica matrix. These protocols can be divided into two types:

- (i) **Formation of covalent bonds**, once the MSNs have been functionalized by grafting or co-condensation, it is possible to decorate them with molecules or biomolecules of interest using some interesting coupling strategies such as the formation of amides, thioureas or triazols (through cycloaddition of Huisgen), etc.
- (ii) **Electrostatic interactions**, the elaboration of complex systems that provide functionality to the MSNs can be benefited by the application of supramolecular chemistry concepts. In particular, all types of weak interactions (hydrogen bonds, formation of metal complexes and ion pairs, among others) or associations between macromolecules (polymers

and biomolecules) can be used. A relevant example of biological application is the coating of MSNs positively charged on its surface with quaternized amines and coated with anionic DNA chains.

Common biological and chemical groups that have been conjugated to mesoporous silica nanoparticles are listed in **Figure 23**⁹¹

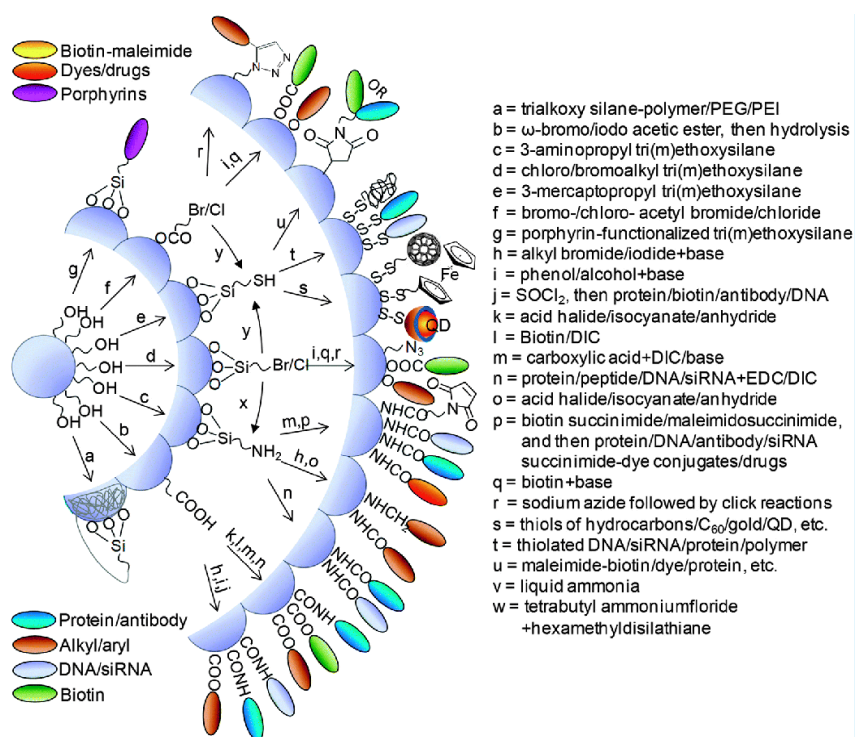


Figure 23. Schematic representation of the different routes that can be followed in order to functionalized silica mesoporous materials with molecules. *Reprinted with permission from J. Nanomed. Nanotechnol, 2018, 3, 1-10.*

1.5 Stimuli-responsive gated materials

The development of hybrid inorganic-organic materials by grafting organic (bio) molecules or supramolecules onto selected inorganic scaffolds (with different sizes and shapes) has promoted the design and preparation of smart nanodevices with applications in several scientific fields.⁹²

Within the realm of smart nanodevices, the design of stimuli-responsive gated materials is an appealing concept. The purpose of these materials is to control the release of chemical species from the voids of porous supports to a solution in response to an external stimulus.⁹³

These nanodevices are generally composed of two subunits (**see Figure 24**):

- (i) **A mesoporous inorganic scaffold:** into which a chemical species (cargo) is entrapped.
- (ii) **Molecular gates:** selected molecular and/or supramolecular entities, which are grafted onto the external surface of the inorganic scaffold. These molecular gates control mass transport from the pores to the solution in response to a certain stimulus.

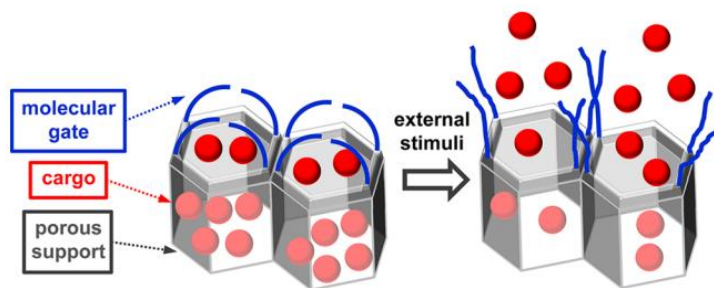


Figure 24. Schematic representation of the general subunits, which compose the stimuli-responsive gated nanodevices. *Reprinted with permission from Chem. Rev. 2016, 116, 2, 561-718.*

Gated materials have attracted great attention due to their potential applications for the controlled release of chemicals, which is highly appealing in the biomedical field,⁹⁴ and also in the development of new sensing/recognition paradigms.⁹⁵

A variety of gated materials that respond to different stimuli such as light, temperature, magnetic fields, redox species, small molecules and biomolecules have been reported. In this regard, one of the most widely used inorganic supports has been mesoporous silica nanoparticles. Additionally, other employed supports include mesoporous silica microparticles,⁹⁶ core-shell nanoparticles with different cores (like gold, magnetite, platinum and upconversion particles) surrounded by a mesoporous silica shell,⁹⁷ anodic alumina⁹⁸ and bioactive glasses.⁹⁹ The gating mechanisms usually take advantage of electrostatic or supramolecular interactions, the rupture/formation of covalent bonds, or changes in the physical properties of molecules or macromolecules. Different kinds of gatekeepers have been used such as polymers, supramolecular ensembles, inorganic nanoparticles, and biomacromolecules.

Extensive reviews about gated materials have been published in recent years and give a comprehensive landscape of the work done so far.¹⁰⁰ As examples, some designs of gated materials classified according to the triggering stimuli are shown below.

❖ Temperature stimuli-responsive nanodevices

Several nanodevices based on molecular gates able to produce a cargo release after a temperature-dependent phase transition have been reported. The majority of them use as molecular gates thermosensitive species able to cap the pores of the materials and respond to the change of temperature. Among the most used strategies for the fabrication of temperature stimuli-responsive gated materials are:

- (i) The use of thermosensitive polymers as molecular gates, which reduce its volume in response to the change in temperature.
- (ii) Pore uncapping due to the hybridization of double stranded DNA sequences induced by temperature.

(iii) Functionalization with melting organic caps such as paraffin.

As an example of the use of temperature stimuli-responsive nanodevices, de la Torre and co-workers reported a temperature stimuli-responsive delivery system based in the conformational transformation of peptide sequences from α -helix to a disordered state induced by an increase in temperature (see Figure 25).¹⁰¹ MSNs were loaded with safranin O and functionalized on the external surface with (azidopropyl)triethoxysilane. Then, a peptide of 17 amino acids with a terminal pentynoic group was linked to azide groups on the silica surface by click reaction. The peptide was specifically designed to adopt α -helix conformation at room temperature. This self-aggregation of the peptide in the form of α -helix bundles inhibited cargo release. When the temperature increased above 50 °C, the peptide structure changes to a disordered conformation, which reduced the steric crowding on the pores outlets and resulted in cargo release.

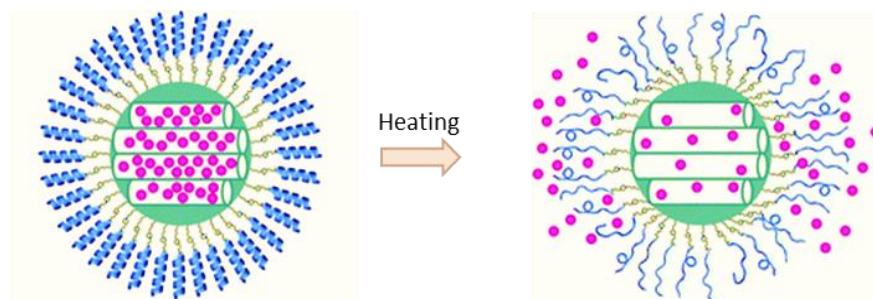


Figure 25. Schematic representation of a temperature stimuli responsive nanodevice. The release of the loaded safranin O dye was achieved by a progressive α -helix-to-disordered transformation when temperature was increased. Reprinted with permission from *Chem. Commun.*, 2014,50, 3184-3186.

❖ Ultrasound and Alternating Magnetic Field stimuli-responsive nanodevices

Ultrasound and magnetic fields are also physical stimuli used for opening up molecular gates with the subsequent controlled delivery of an entrapped cargo. These physical stimuli allow a pulsatile delivery of the cargo, they are non-invasive, can penetrate depth in tissues, and can be carefully controlled by

changing frequency, power, cycles, and time of application. Moreover, magnetically triggered systems have the advantage of having an extra control and possibility of guidance of the gated support, for example, to accumulate in a selected tumor area (for biomedical purposes, where also tracking by MRI is possible) or even in industrial applications where separation and recovery of the gated particles could be of crucial interest. Several examples of capped materials that were opened upon application of these stimuli have been described.

As an illustrative example, in a collaboration between Stroeve's and Martínez-Mañez's groups, the magnetic-responsive delivery system depicted in **Figure 26** was developed.¹⁰² MSNs with supermagnetic iron oxide cores were loaded with methylene blue and capped with (S)-1,2-dioleoyl glycerol-3-phosphocholine by the formation of lipid bilayers around the nanoparticles. Cargo release was observed when aqueous suspensions of the nanoparticles were exposed to an alternating magnetic field (50 Hz, 1570 G), whereas payload delivery was negligible in the absence of it. The response was ascribed to an increase in the permeability of the lipid bilayer due to the vibration of the particles upon application of the alternating magnetic field as well as to an increase of the nanoparticles temperature that partially disrupted the bilayer. The temperature effect was confirmed by studying the release of nanoparticles suspensions at 50 °C, which resulted in a massive delivery at short times.

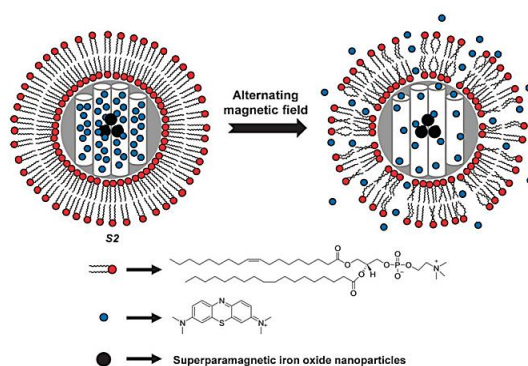


Figure 26. Schematic drawing of the core-shell MSNs capped with a lipid bilayer for controlled delivery triggered by an external magnetic field. *Reprinted with permission from Chem. Commun., 2012, 48, 5647-5649.*

❖ Light stimuli-responsive nanodevices

The use of light as stimuli for controlling open/closed protocols in mesoporous systems have allowed the development of light-driven gated systems, where cargo release can, in principle, be controlled spatially and temporally by fine-tuning the area and time of the light stimulus. Light has the advantage of being applicable from outside of the patient in a non-invasive manner, and it is easily focusable in selected areas, avoiding irradiation of the surrounding tissue. Light-driven molecular gates can be classified into four main paradigms: **(i)** photodimerization **(ii)** cis-trans photoisomerization **(iii)** direct photocleavage of chemical bonds or assisted by photosensitizers and **(iv)** photoinduced heating of gold nanostructures.

A simple and illustrative example of a light-driven molecular gate is depicted in **Figure 27**, here the authors prepared MSNs loaded with $[\text{Ru}(\text{bipy})_3]\text{Cl}_2$ and capped with a photo-cleavable bulky o-methoxybenzylamine derivative that contained two-tert-butyl moieties in its structure. The bulky two-tert-butyl subunits of the o-methoxybenzylamine derivative impeded the release of the entrapped cargo in aqueous media. In contrast, upon irradiation with UV light (250 nm), the bulky group was cleaved which decreased the steric hindrance of the pores outlets and allowed the diffusion of the dye to the solution.¹⁰³

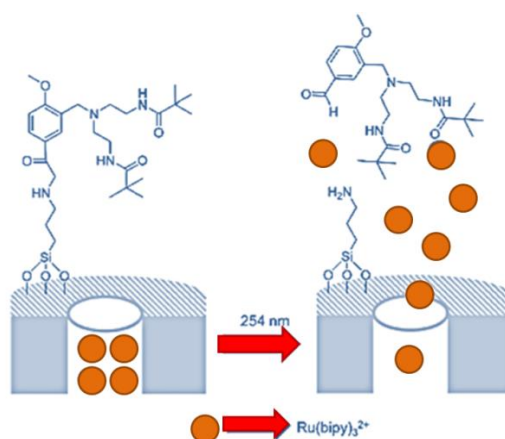


Figure 27. Schematic representation of a gated equipped with a photo-driven uncapping mechanism. *Reprinted with permission from Chem. Rev. 2016, 116, 2, 561-718.*

❖ pH stimuli-responsive nanodevices

A pH change is the most popular stimulus used to develop gated materials. The open/close mechanism in these systems is controlled by the change of conformation, rupture or attraction/repulsion interactions between the gating ensemble components, caused as a consequence of the addition or abstraction of protons. In addition, pH stimuli responsive systems offer the advantage of being totally autonomous, not requiring any extra equipment, and in most cases, the closing and opening mechanism is reversible.

In order to fabricate these pH-stimuli responsible nanodevices, researchers have reported the use of a wide variety of MSNs capping agents such as amines, metallic complexes, macrocycles, different polymers, supramolecular ensembles such as layer-by-layer coatings, biomolecules as DNA, proteins, lipid bilayers, and even inorganic nanoparticles to control the release of selected cargos.

As an example, Yang and co-workers used MSNs that were first functionalized with 2-bromoisobutryl bromide (BIBB) in order to attach poly(2-dimethylaminoethyl methacrylate) brushes (PDMAEMA) by peroxidase mimetic catalytic atom transfer radical polymerization (ATRP).¹⁰⁴ Before to attach the PDMAEMA molecular gate the system was loaded with rhodamine (Rh) 6G. PBS suspensions of the nanoparticles at pH 7.4 showed a moderate Rh 6G release. However, marked dye delivery was observed upon lowering the solution pH to 2.0. The release was ascribed to electrostatic repulsions between the positively charged polymer chains that adopted an extended conformation with subsequent pore opening (see Figure 28).

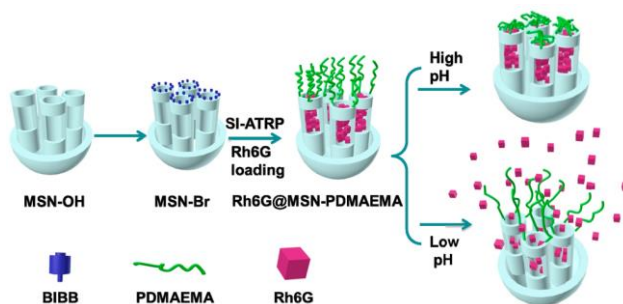


Figure 28. Schematic representation of a pH-driven gated solid based on the protonation of polymer brushes. *Reprinted with permission from Polymers 2016, 8, 277*

Furthermore, the use of self-immolative gates has recently been implemented in the development of gated materials. Juarez et al. reported new MSNs capped with self-immolative gate and loaded with sulforhodamine B dye. Controlled release occurs as a function of pH conditions. Under acidic and neutral conditions, a low level of dye release is detected. However, at slightly basic pH, significant dye release occurs owing to deprotonation of the phenol moiety in the capping molecule, which results in its disassembly¹⁰⁵ (see Figure 29).

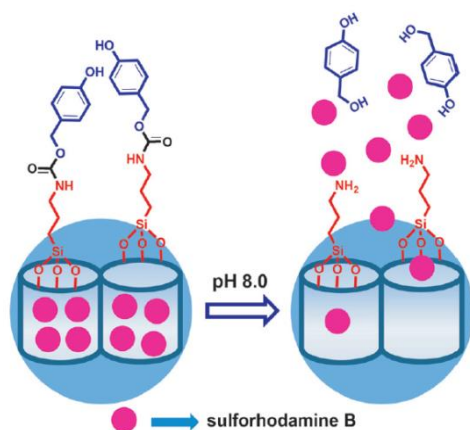


Figure 29. Schematic representation of the cargo release in a pH-stimuli responsive nanodevice controlled by a self-immolative gate. Reprinted with permission from *Chem.Eur.J.* 2016, 22, 14126–14130.

❖ Redox stimuli-responsive nanodevices

Based on the biological relevance of redox agents and redox reactions, the fabrication of redox-stimuli responsive nanodevices has been widely explored. Most of the reported systems can be classified into two main categories:

- (i) Those based on rotaxanes and pseudorotaxanes where supramolecular ensembles between macrocycles (like cyclophanes, cucurbiturils or cyclodextrins) and an organic chain anchored to the external surface of the porous scaffold control the open/close state of the gate;
- (ii) Those based on disulphide-linked capping agents (eg. polymers or inorganic nanoparticles) that are detached by reducing agents like

glutathione or dithiothreitol. Interestingly, some of these systems are reversible which means that the gate can be opened and closed repeatedly by changing the redox conditions of the environment.

In 2004 Nobel Laureate James Fraser Stoddart and co-workers reported one of the first examples of a reversible redox-driven molecular gate.¹⁰⁶ In order to develop that system they synthesized a bistable[2]rotaxane that consisted of the macrocycle cyclobis(paraquat-p-phenylene) (CBPQT4+), a tetrathiafulvalene (TTF) station and a dioxynaphthalene (DNP) station separated by an oligoethylene glycol chain, and a terminal rigid terphenylene as the stopper. In a further step the material was loaded with an iridium complex or rhodamine B and the rotaxane was anchored via the formation of a carbamate bond with isocyanate moieties on the silica surface. In this supramolecular ensemble, the oxidation of TTF using $\text{Fe}(\text{ClO}_4)_3$ to give a TTF^{2+} promoted the movement of the CBPQT4+ ring to the DNP station and resulted in the blocking of the pores. Upon addition of ascorbic acid, the TTF^{2+} unit was reduced back to the neutral TTF, which induced the movement of the macrocycle ring to the TTF station (due to its higher affinity compared to the complex with DNP). Since the TTF station was further away from the silica surface, the movement of the macrocycle unblocked the pores and resulted in the release of the cargo (see Figure 30).

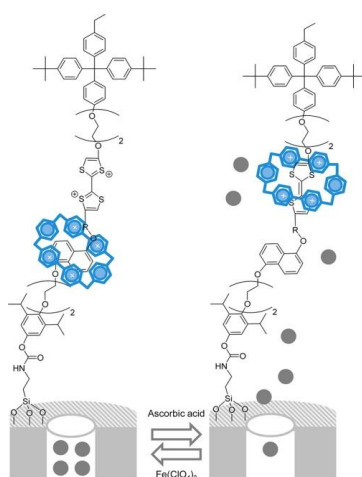


Figure 30. Schematic representation of a reversible redox-driven molecular gate. *Reprinted with permission from Chem. Rev. 2016, 116, 2, 561-718.*

Recently Elsayed et al. have reported an example of redox-driven materials based on the reduction of disulfide bonds.¹⁰⁷ The system based on MSNs were loaded in a first step with safranin O and then, capped with disulfide-containing oligo(ethylene glycol) chains. The uncapping mechanism was attributed to a selective reduction of the disulfide bond carried out by the presence of glutathione (GSH) that allowed the release of the dye entrapped in the porous network of the inorganic scaffold (**see Figure 31**). The observed response was highly selective toward GSH whereas similar sulfur-containing derivatives, such as cysteine, homocysteine and HS^- , were unable to uncage the gated material to a significant extent. The system was able to detect GSH down to concentrations of $0.1 \mu\text{M}$.

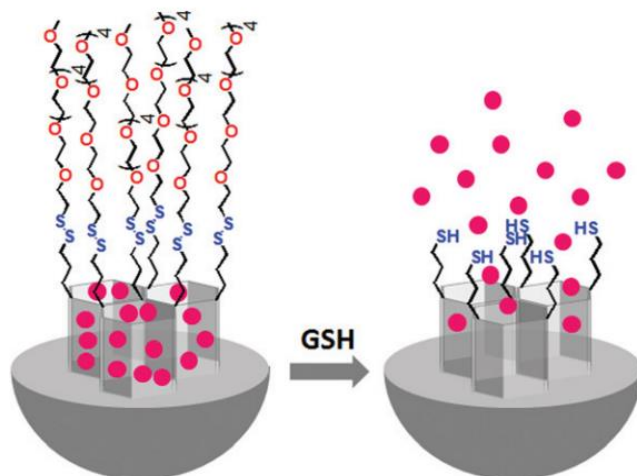


Figure 31. Schematic representation of a gated material in which cargo release is controlled by GSH. Reprinted with permission from *Chem Org. Biomol. Chem.*, 2015, 13, 1017-1021.

❖ Molecules and Biomolecules stimuli-responsive nanodevices

The design of gated materials able to respond to specific molecules or biomolecules has opened the possibility of creating highly selective systems, able to release the encapsulated cargo only in the presence of the selected triggering molecule or biomolecule.

In recent years, various examples of gated materials that respond to anions, cations, neutral molecules and biomolecules have been reported. Most reported examples can be classified into the following main categories:

- (i) Oligonucleotides for recognizing complementary strands or certain analytes (using aptamers and DNAzymes).
- (ii) Supramolecular ensembles responsive to small molecules (mainly anions and cations).
- (iii) Peptide sequences or organic groups that are hydrolyzed by certain enzymes.

In 2013 Martínez-Mañez's group published the first example of an oligonucleotide-gated material.¹⁰⁸ The system consisted of MSNs loaded with a fluorescent cargo (fluorescein) and its external surface functionalized with 3-aminopropyltriethoxysilane (APTES). The end aminopropyl groups have positive charge at neutral pH and its interaction with a 21-bases oligonucleotide (negatively charged) resulted in the capping of the porous material. The opening mechanism was based in the displacement of the capping oligonucleotide by hybridization with its complementary strand (see **Figure 32**). The same researchers reported later the use of a similar system for the detection of *Mycoplasma* genomic DNA.¹⁰⁹ Additionally, other examples of oligonucleotide-capped materials include, for instance, the use of specific aptamers for detection of selected analytes such as thrombin,¹¹⁰ ochratoxine,¹¹¹ and As³⁺.¹¹²

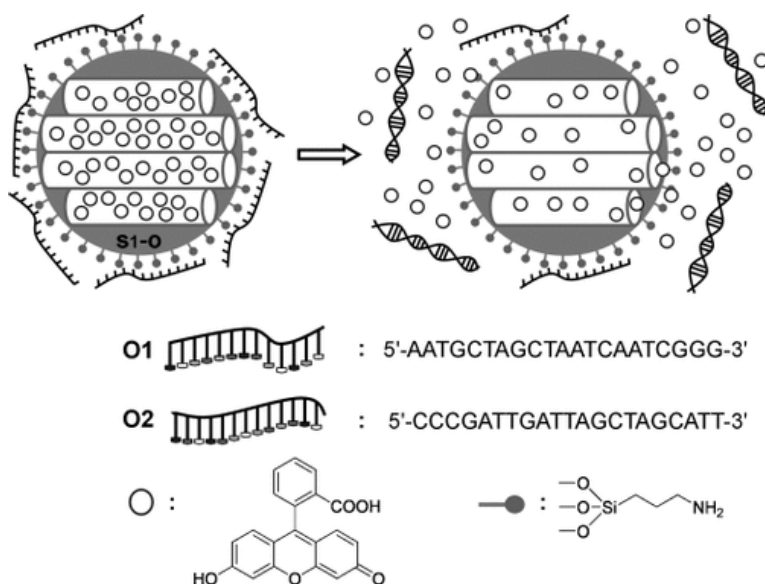


Figure 32. Representation of a gated material functionalized with APTES and capped with single-stranded oligonucleotide O1 for cargo release triggered by the complementary strand O2. *Reprinted with permission from Angew. Chem. Int. Ed.* 2013, 24, 7281-7283.

Regarding supramolecular ensembles responsive to small molecules such as cations and anions, S. El Sayed and co-workers reported an illustrative example of MSNs capped with a supramolecular complex for detection of cyanide (see **Figure 33**).¹¹³ In order to develop this gated material, MSNs were loaded with $[\text{Ru}(\text{bpy})_3]\text{Cl}_2$, functionalized with a macrocyclic Ni^{2+} complex subunit, and capped with a sterically hindering anion (hexametaphosphate) by electrostatic interactions with the Ni^{2+} complex. In the absence of cyanide, the release was negligible due to the blockage of the pore outlets by the bulky supramolecular ensemble. In contrast, addition of cyanide induced demetallation of Ni^{2+} complexes and the removal of the capping hexametaphosphate from the silica surface, allowing the release of the dye and the subsequent increase in fluorescence signal.

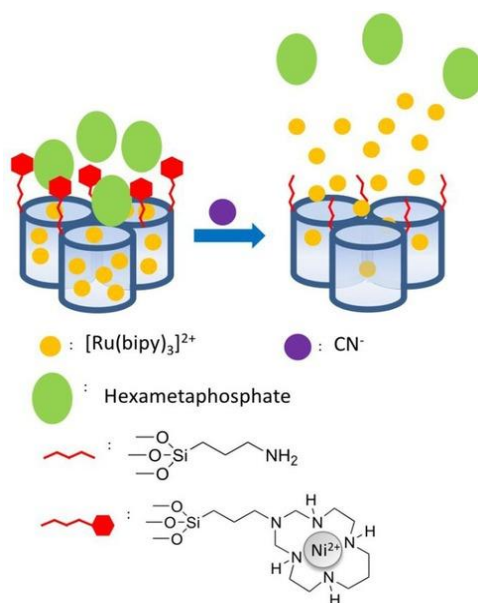


Figure 33. Schematic representation of a gated material for cyanide recognition using a supramolecular complex as the gating ensemble. *Reprinted with permission from Chem. Asian J. 2017, 18, 2670-2674.*

Regarding the design of enzyme-responsive delivery system, the strategy is usually based on capping the particles with a peptide sequence or organic groups that are hydrolyzed by the target enzyme.¹¹⁴ As an example, Martínez-Mañez and co-workers prepared a gated material based on MSNs capped with a peptide and loaded with a safranin O. This systems was able to produce a release of the cargo triggered by the enzyme caspase 3 (C3) (see **Figure 34**).¹¹⁵ The peptide (KKGDEVKKARDEVDK) contained two repeats of a target sequence that is hydrolyzed by C3 (DEVK). First, the MSNs were functionalized with 3-(azido-propyl)triethoxysilane, loaded with the dye and then the alkyne-containing peptidic sequence was attached by click reaction with the amino groups on the silica surface. In the absence of C3, the system showed negligible release whereas in the presence of the enzyme, a remarkable cargo release was found due to hydrolysis of the peptidic sequence. The prepared MSNs were introduced in HeLa cells by electroporation in order to avoid endocytosis taking into account the cytoplasmatic location of C3. Cells were treated or not with staurosporin which

induces apoptosis with the consequent activation of C3 in the cytosol. Safranin O delivery in the cells was observed only when C3 was activated.

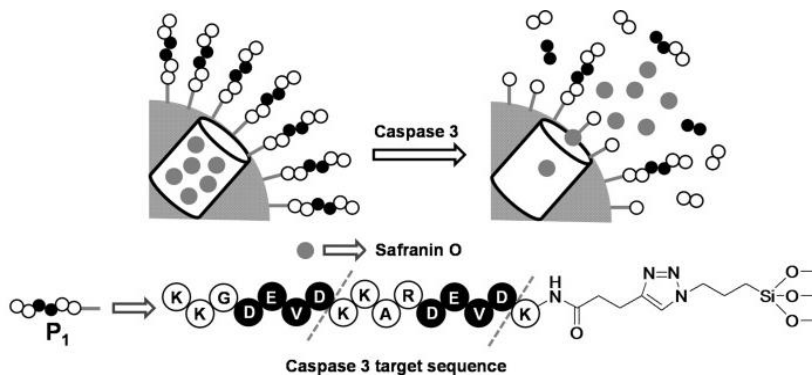


Figure 34. Example of a peptide-capped gated material for controlled delivery triggered by the enzyme caspase 3. Reprinted with permission from *Chem. Eur. J.*, 2015, 21, 15506-15510.

Furthermore, Martínez-Mañez and co-workers reported an ethylene glycol-capped hybrid material capable of producing a cargo release in the presence of esterase enzyme.¹¹⁶ Firstly, the porous of the MSNs were loaded with $[\text{Ru}(\text{bipy})_3]\text{Cl}_2$ complex, and then, in the second step, the pore outlets were functionalized with glycol ester moieties that acted as molecular caps. In the absence of esterase enzyme, the release of the complex from aqueous suspensions is inhibited due to the steric hindrance imposed by the bulky glycol ester moieties. Upon addition of esterase enzyme, delivery of the ruthenium complex was observed due to enzymatic hydrolysis of the ester bond in the anchored ester glycol derivative, inducing the release of oligo(ethylene glycol) fragments. Hydrolysis of the ester bond results in size reduction of the appended group, therefore allowing delivery of the entrapped cargo (see **Figure 35**). The system designed was not toxic for cells, as demonstrated by cell viability assays with HeLa and MCF-7 cell lines.

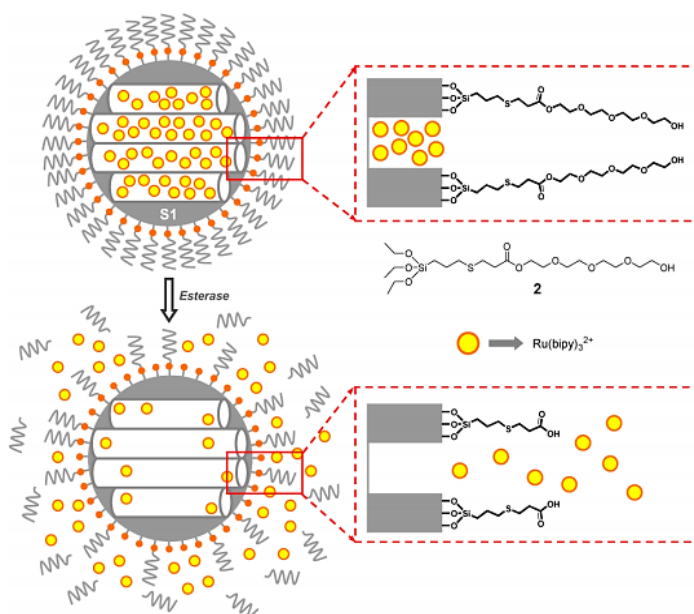


Figure 35. Esterase-induced controlled release of a [Ru(bipy)₃]Cl₂ complex from mesoporous nanoparticles functionalized with glycol ester moieties. Reprinted with permission from *Langmuir*, 2012, 28, 14766–14776.

1.6 References

1. P. J. Magistretti, *Diabetes Metab.*, **1988**, 14, 237-246.
2. M. Levite, *Curr. Opin. Pharmacol.*, **2008**, 8, 460-471.
3. B. V. Beaver, Equine Behavior of Sensory and Neural Origin. In *Equine Behavioral Medicine*, *Academic Press*, **2019**, Pages 31-64
4. R. Rapport, R. L. Rapport, Nerve endings: the discovery of the synapse. WW Norton & Company. **2005**.
5. E. M. Tansey, *CR. Biol.*, **2006**, 329, 419-425.
6. L. Squire, D. Berg, F. E. Bloom, S. du Lac, A. Ghosh, N. C. Spitzer Neurotransmitters. In *Fundamental Neuroscience*, Elsevier, **2013**, 117–138.
7. S., Sankaranarayanan, T. A. Ryan, Neuronal Exocytosis. In *Protein Trafficking in Neurons*, Elsevier, **2007**. p. 97-124.
8. J. Cuevas, Neurotransmission, Reference Module in Biomedical Sciences, Elsevier, **2014**.
9. M. K. Jetha, S. J. Segalowitz, Structural brain development in late childhood, adolescence and early adulthood. *Adolescent Brain Development: Implications for Behavior*, **2012**, 1-18.

- 10 J. W. Baynes, M. H. Dominiczak, *Neurotransmitters in Medical Biochemistry* Fourth Edition, Saunders Elsevier, **2014**.
- 11 Z. M. Sheffler, L. S. Pillarisetty, *Physiology, Neurotransmitters, StatPearls Publishing, 2019*.
- 12 P. L. Pearl, T. R. Hartka, J. Taylor, *Curr Treat Options Neurol*, **2006**, 8, 441-450.
- 13 a) G. Eisenhofer, H. Keiser, P. Friberg, E. Mezey, T.T. Huynh, B. Hiremagalur, T. Ellingson, S. Duddempudi, A. Eijsbouts, J.W. Lenders, *J. Clin. Endocrinol. Metab.*, **1998**, 83, 2175-2185 b) J.M. Zuetenhorst, B.G. Taal, *Oncologist*, **2005**, 10 123-131
- 14 T. Pradhan, H. S. Jung, J. H. Jang, T. W. Kim, C. Kang, J. S. Kim, *Chem. Soc. Rev.*, **2014**, 43, 4684-4713.
- 15 a) W. Jang, H. H. Park, K. Y. Lee, Y. J. Lee, H. T., Kim, and S. H. Koh, *Mol. Neurobiol.*, **2015**, 51, 558; b) J. L. Rudolph, M. J. Salow, M. C. Angelini, R. E. McGlinchey, *Arch. Intern. Med.*, **2008**, 168, 508.effects
- 16 M. García-Escrig, F. Bermejo-Pareja, *Rev. Neurol.*, **1999**, 28, 799
- 17 J. A. Martín-Gago, C. Briones, E. Casero, P. A. Serena, *El nanomundo en tus manos: Las claves de la nanociencia y la nanotecnología*, Editorial Critica, **2014**.
- 18 M. F. Hochella Jr, *Geochim. Cosmochim. Acta*, **2002**, 66, 735-743.
- 19 J. E. Hulla, S. C. Sahu, A. W. Hayes, *Hum. Exp. Toxic.*, **2015**, 34, 1318-1321.
- 20 N. Kumar, S. Kumbhat, *J. Nanosci. Nanotechnol.*, Wiley, **2016**.
- 21 D. Bobo, K. J. Robinson, J. Islam, K. Thurecht, *S. R. Corrie, Pharm. Res.* **2016**, 33, 2373-2387.
- 22 I. Khan, K. Saeed, I. Khan, *Arab. J. Chem.*, **2019**, 12, 908-931.
- 23 a) I. Iavicoli, V. Leso, W. Ricciardi, L. L. Hodson, M. D. Hoover, *J. Environ. Health*, **2014**, 13, 78. b) F. D. Guerra, M. F. Attia, D. C. Whitehead, F. Alexis, *Molecules*, **2018**, 23, 1760.
- 24 S. Murty, P. Shankar, B. Raj, B. B. Rath, J. Murday, *Textbook of nanoscience and nanotechnology. Springer Science & Business Media*, **2013**.
- 25 M. Homberger, U. Simon, *Philos. Trans. R. Soc. A*, **2010**, 368, 1405–1453.
- 26 L. Freitas de Freitas, G. H. C. Varca, J. G. dos Santos Batista, A. Benévolo Lugaõ, *Nanomaterials*, **2018**, 8, 939.
- 27 M. Sharon, *History of nanotechnology From Pre-Historyc to modern times*, Wiley, **2019**
- 28 P. Singh, S. Pandit, V. R. S. S. Mokkalpati, A. Garg, V. Ravikumar, I. Mijakovic, *Int. J. Mol.*, **2018**, 19, 1979.

- 29 M. A. Habeeb Muhammed, P. K. Verma, S. K. Pal, A. Retnakumari, M. Koyakutty, S. Nair, T. Pradeep, *Chem.: Eur. J.*, **2010**, 16, 10103-10112.
- 30 P. Ghosh, G. Han, M. De, C. K. Kim, V. M. Rotello, *Adv. Drug Deliv. Rev.*, **2008**, 60, 1307-1315.
- 31 P. Baptista, E. Pereira, P. Eaton, G. Doria, A. M. Gomes, P. Quaresma, R. Franco, *Anal Bioanal Chem.*, **2008**, 391, 943.
- 32 E. Boisselier, D. Astruc, *Chem. Soc. Rev.*, **2009**, 38, 1759-1782.
- 33 M. Danckwerts, L. Novotny, *Phys. Rev. Lett.*, **2007**, 98, 026104.
- 34 K. S. Tan, M. K. Chuang, F. C. Chen, C. S. Hsu, *ACS Appl. Mater. Interfaces*, **2013**, 5, 12419-12424.
- 35 M. Stratakis, H. Garcia, *Chem. Rev.*, **2012**, 112, 4469-4506.
- 36 R. C. Birtcher, S. E. Donnelly, and S. Schlutig, *Nucl. Instr. Meth. Phys. Res. B.*, **2004**, 215, 69.
- 37 B. Tangeysh, K. M. Tibbetts, J. H. Ochner, B. B. Wayland, and R. J. Levis, *J. Phys. Chem. C.* **2013**, 117, 18719.
- 38 J. Lung, J. Huang, D. Tien, C. Liao, K. Tseng, T. Tsung, W. Kao, T. Tsai, C. Jwo, H. Lin, and L. Stobinski, *J. Alloys Compd.*, **2007**, 434–435, 655.
- 39 M. Sakamoto, M. Fujistuka, and T. Majima, *J. Photochem. Photobiol. C*, **2009**, 10, 33
- 40 T. J. Krinke, K. Deppert, M. H. Magnusson, F. Schmidt, and H. Fissan, *J. Aerosol Sci.* **2002**, 33, 1341.
- 41 V. K. LaMer, R. H. Dinegar, *J. Am. Chem. Soc.* **1950**, 72, 4847–4854.
- 42 I. M. Lifshitz, V. V. Slyozov, *J. Phys. Chem. Solids*, **1961**, 19, 35–50.
- 43 H. You, J. Fang, *Nano Today*, **2016**, 11, 145-167.
- 44 F. Wang, V. N. Richards, S. P. Shields, W. E. Buhro, *Chem. Mater.*, **2013**, 26, 5-21.
- 45 J. Turkevitch, P. C. Stevenson, and J. Hillier, *Discuss. Faraday Soc.* **1951**, 11, 55
- 46 G. Frens, *Nature Phys. Sci.* **1973**, 241, 20
- 47 M. Brust, M. Walker, D. Bethell, D. J. Schiffrin, and R. Whyman, *J. Chem. Soc., Chem. Commun.* **1973**, 801
- 48 Y. Du, X. L. Luo, J. J. Xu, H. Y. Chen, *Bioelectrochemistry*, **2007**, 70, 342-347.
- 49 J. M. Slocik, M. O. Stone, R. R. Naik, *Small*, **2005**, 1, 1048-1052.
- 50 N. Cioffi, L. Colaianni, E. Ieva, R. Pilolli, N. Ditaranto, M. D. Angione, S. Cotrone, K. Buchholt, A. L. Spetz, L. Sabbatini, and L. Torsi, *Electrochim. Acta*, **2011**, 56, 3713.
- 51 D. Debnath, S. H. Kim, and K. E. Geckeler, *J. Mater. Chem.* **2009**, 19, 8810.
- 52 M. J. Rak, N. K. Saade, T. Friscic, and A. Moores, *Green Chem.* **2014**, 16, 86.

- 53 S. Alex, A. Tiwari, *J. Nanosci. Nanotechnol.*, **2015**, 15, 1869-1894.
- 54 K. G. Thomas and P. V. Kamat, *Acc. Chem. Res.* **2003**, 36, 888
- 55 A. C. Templeton, W. P. Wuelfing, and R. W. Murray, *Acc. Chem. Res.* **2000**, 33, 27.
- 56 R. A., Sperling, W. J. Parak, *Philos. Trans. Royal Soc. A*, **2010**, 368, 1333-1383.
- 57 J. W., Park, J. S. Shumaker-Parry, *ACS nano*, **2015**, 9, 1665-1682.
- 58 J. C. Love, L. A. Estroff, J. K. Kriebel, R. G. Nuzzo, G. M. Whitesides, *Chem. Rev.* **2005**, 105, 1103-1169.
- 59 G. Mie, *Ann Phys*, **1908**, 25, 377.
- 60 X. Liu, M. Atwater, J. Wang, Q. Huo, *Colloids Surf B Biointerfaces*, **2007**, 58, 3-7.
- 61 S. Link, M. A. El-Sayed, *J. Phys. Chem. B*, **1999**, 103, 8410-8426
- 62 S. Srivastava, B. L. Frankamp, V. M. Rotello, *Chem. Mater.* **2005**, 17, 487.
- 63 Y. Jiang, H. Zhao, Y. Q. Lin, N. N. Zhu, Y. R. Ma, L. Q. Mao, *Angew. Chem. Int. Ed.* **2010**, 49, 4800.
- 64 S. Y. Lin, S. W. Liu, C. M. Lin, C. H. Chen, *Anal. Chem.*, **2002**, 74, 330-335.
- 65 J. R. Kalluri, T. Arbneshi, S. Afrin Khan, A. Neely, P. Candice, B. Varisli, M. Washington, S. McAfee, B. Robinson, S. Banerjee, A. K. Singh, D. Senapati, P. C. Ray, *Angew. Chem. Int. Ed.* **2009**, 48, 9668-9671.
- 66 C. Lai, L. Qin, G. Zeng, Y. Liu, D. Huang, C., Zhang, X. Piao, C. Min, X. Qin, M. Wang, *RSC Adv*, **2016**, 6, 3259-3266.
- 67 S. Kado, A. Furui, Y. Akiyama, Y. Nakahara, K. Kimura, *Anal. Sci.* **2009**, 25, 261.
- 68 T. Minami, K. Kaneko, T. Nagasaki, Y. Kubo, *Tetrahedron Lett.* **2008**, 49, 432.
- 69 M. H. Kim, S. Kim, H. H. Jang, S. Yi, S. H. Seo, M. S. Han, *Tetrahedron Lett.* **2010**, 51, 4712.
- 70 A. Martí, A. M. Costero, P. Gavina, M. Parra, *ChemistrySelect*, **2016**, 1, 1057-1060.
- 71 A. Martí, A. M. Costero, P. Gaviña, M. Parra, *Chem. Comm*, **2015**, 51, 3077-3079.
- 72 A. Martí, A. M. Costero, P. Gaviña, M. Parra, *Tetrahedron Lett.*, **2014**, 55, 3093-3096.
- 73 Y. Jiang, H. Zhao, N. Zhu, Y. Lin, P. Yu, L. Mao, *Angew. Chem.*, **2008**, 120, 8729-8732.
- 74 V. Mamaeva, C. Sahlgren, M. Linden, *Adv. Drug Deliv. Rev.*, **2013**, 65, 689-702,
- 75 J. M. Rosenholm, C. Sahlgren, M. Lind, *Nanoscale*, **2010**, 2, 1870-1883
- 76 J. G. Croissant, Y. Fatieiev, A. Almalik, N. M. Khashab, *Adv. Healthcare Mater.* **2018**, 7, 1700831.

- 77 C. Perego, R. Millini, *Chem. Soc. Rev.* **2013**, 42, 3956-3976.
- 78 K. M. Thomas, *Catal. Today*, **2007**, 120, 389-398.
- 79 X. Liu, Y. Du, Z. Guo, S. Gunasekaran, C.-B. Ching, Y. Chen, S. S. J. Leong, Y. Yang, *Micropor. Mesopor. Mater.* **2009**, 122, 114-120.
- 80 D. J. Wales, J. Grand, V. P. Ting, R. D. Burke, K. J. Edler, C. R. Bowen, S. Mintova, A. D. Burrows, *Chemical Society Reviews*, **2015**, 44, 4290.
- 81 C. Ispas, I. Sokolov, S. Andreescu, *Anal. Bioanal. Chem.* **2009**, 393, 543-554.
- 82 M. Vallet-Regí, M. Colilla, I. J. Izquierdo-Barba, *Biomed. Nanotechnol.* **2008**, 4, 1.
- 83 I. I. Slowing, B. G. Trewyn, S. Giri, V. S.-Y. Lin, *Adv. Funct. Mater.* **2007**, 17, 1225-1236.
- 84 J. S. Beck, J. C. Vartuli, W. J. Roth, M. E. Leonowicz, C. T. Kresge, K. D. Schmitt, C. T. W. Chu, D. H. Olson, E. W. Sheppard, S. B. McCullen, J. B. Higgins, J. L. Schlenker, *J. Am. Chem. Soc.* **1992**, 114, 10834-10843.
- 85 C. T. Kresge, W. J. Roth, *Chem. Soc. Rev.* **2013**, 42, 3663-3670.
- 86 D. Zhao, J. Feng, Q. Huo, N. Melosh, G. H. Fredrickson, B. F. Chmelka, G. D. Stucky, *Science*, **1998**, 279, 548-552.
- 87 M. C. Llinàs, D. Sánchez-García, *Afinidad LXXI*, **2014**, 565, 20-31.
- 88 I. I. Slowing, J. L. Vivero-Escoto, C. W. Wu, V. S. Y. Lin, *Adv. Drug Deliv. Rev.*, **2008**, 60, 1278-1288.
- 89 S. Huh, J. W. Wiench, J. C. Yoo, M. Pruski, V. S. Y. Lin, *Chem. Mater.*, **2003**, 15, 4247-4256.
- 90 F. Hoffmann, M. Fröba, *Chem. Soc. Rev.*, **2011**, 40, 608-620.
- 91 I. Manavitehrani, A. Schindeler, M. Parviz, *J. Nanomed. Nanotechnol*, **2018**, 3, 1-10.
- 92 **a)** Q. Zhang, E. Uchaker, S. L. Candelariaza, G. Gao, *Chem. Soc. Rev.* **2013**, 42, 3127-3171; **b)** N. Linares, A. M. Silvestre-Albero, E. Serrano, J. Silvestre-Albero, J. García-Martínez, *Chem. Soc. Rev.*, **2014**, 43, 7681-7717; **c)** T. Wagner, S. Haffer, C. Weinberger, D. Klaus, M. Tiemann, *Chem. Soc. Rev.* **2013**, 42, 4036-4053; **d)** A. E. Garcia-Bennett, *Nanomedicine*, **2011**, 6, 867-877; **e)** A. P. Wight and M. E. Davis, *Chem. Rev.* **2002**, 102, 3589-3614.
- 93 S. Iijima, *Nature*, **1991**, 354, 56-58.
- 94 **a)** Z. Li, J. C. Barnes, A. Bosoy, J. F. Stoddart, J. I. Zink, *Chem. Soc. Rev.* **2012**, 41, 2590-2605; **b)** Y. Wang, Q. Zhao, N. Han, L. Bai, J. Li, J. Liu, E. Che, L. Hu, Q. Zhang, T. Jiang, S. Wang, *Nanomedicine*, **2015**, 11, 313-327; **c)** R. R. Castillo, M. Colilla, M. Vallet-Regí, *Expert. Opin. Drug Deliv.* **2017**, 14, 229-243.

- 95 F. Sancenón, L. Pascual, M. Oroval, E. Aznar, R. Martínez-Máñez, *ChemistryOpen*, **2015**, 4, 418-437.
- 96 **a)** A. Bernardos, A. Aznar, C. Coll, R. Martínez-Máñez, J. M. Barat, M. D. Marcos, F. Sancenón, A. Benito, J. Soto, *J. Control. Release*, **2008**, 131, 181-189; **b)** E. Aznar, M. Dolores Marcos, R. Martínez-Máñez, F. Sancenón, J. Soto, P. Amorós, C. Guillem, *J. Am. Chem. Soc.* **2009**, 131, 6833-6843;
- 97 **a)** S. F. Lee, X. M. Zhu, Y. X. J. Wang, S. H. Xuan, Q. H. You, W. H. Chan, C. H. Wong, F. Wang, J. C. Yu, C. H. Cheng, K. C. Leung, *ACS Appl. Mater. Interfaces*, **2013**, 5, 1566-1574; **b)** W.-P. Li, P.-Y. Liao, C.-H. Su, C.-S. Yeh, *J. Am. Chem. Soc.*, **2014**, 136, 10062-10075; **c)** Z. F. Wang, X. Yang, J. Feng, Y. J. Tang, Y. Y. Jiang, N. Y. He, *Analyst*, **2014**, 139, 6088-6091; **d)** M. L. Yin, E. G. Ju, Z. W. Chen, Z. H. Li, J. S. Ren, X. G. Qu, *Chem. Eur. J.* **2014**, 20, 14012-14017.
- 98 **a)** A. Ribes, E. Xifré-Pérez, E. Aznar, F. Sancenón, T. Pardo, L. F. Marsal, R. Martínez-Máñez, *Sci. Rep.* **2016**, 6, 38649; **b)** L. Pla, E. Xifré-Pérez, A. Ribes, E. Aznar, M. D. Marcos, L. F. Marsal, R. Martínez-Máñez, F. Sancenón, *ChemPlusChem*. **2017**, 82, 337-341.
- 99 L. Polo, N. Gómez-Cerezo, E. Aznar, J.-L. Vivancos, F. Sancenón, D. Arcos, M. Vallet-Regí, R. Martínez-Máñez, *Acta Biomater.* **2017**, 50, 114-126
- 100 **a)** N. Song, Y.-W. Yang, *Chem. Soc. Rev.* **2015**, 44, 3474-3504; **b)** J. Wen, K. Yang, F. Liu, Y. Xiu, S. Sun, *Chem. Soc. Rev.* **2017**, 46, 6024-6045; **c)** J. Zhu, Y. Niu, Y. Li, Y. Gong, H. Shi, Q. Huo, Y. Liu, Q. Xu, *J. Mater. Chem. B.* **2017**, 5, 1339-1352.
- 101 C. de la Torre, A. Agostini, L. Mondragón, M. Orzáez, F. Sancenón, R. Martínez-Máñez, M. D. Marcos, P. Amorós, E. Pérez-Payá, *Chem. Commun.* **2014**, 50, 3184-3186.
- 102 E. Bringas, O. Koysuren, D. V. Quach, M. Mahmoudi, E. Aznar, J. D. Roehling, M. D.; Marcos, R. Martínez-Máñez, P. Stroeve, *Chem. Commun.* **2012**, 48, 5647-5649.
- 103 A. Agostini, F. Sancenón, R. Martínez-Máñez, M. D. Marcos, J. Soto, P. Amorós, *A. Chem. Eur. J.*, **2012**, 18, 12218-12221.
- 104 H. Zhou, X. Wang, J. Tang, Y.-W. Yang, *Polymers*, **2016**, 8, 277.
- 105 L. A. Juárez, E. Añón, C. Giménez, F. Sancenón, R. Martínez-Máñez, Costero, A. M. Costero, P. Gaviña, M. Parra, Bernardos, *A. Chem. Eur. J.*, **2016**, 22, 14126-14130.
- 106 T. D. Nguyen, H. R. Tseng, P. C. Celestre, A. H. Flood, Y. Liu, J. F. Stoddart, J. I. Zink, *Proc. Natl. Acad. Sci.* **2005**, 102, 10029-10034.

- 107 S. El Sayed, C. Giménez, E. Aznar, R. Martínez-Máñez, F. Sancenón, M. Licchelli, *Org Biomol Chem*, **2015**, 13, 1017-1021.
- 108 E. Climent, R. Martínez-Máñez, F. Sancenón, M. D. Marcos, J. Soto, A. Maquieira, P. Amorós, *Angew. Chem. Int. Ed.* **2013**, 24, 7281-7283.
- 109 E. Climent, L. Mondragón, R. Martínez-Máñez, F. Sancenón, M. D. Marcos, J. R. Murgía, P. Amorós, K. Rurack, E. Pérez-Payá, *Angew. Chem. Int. Ed.* **2013**, 52, 8938-8942.
- 110 M. Oroval, E. Climent, C. Coll, R. Eritja, A. Aviñó, M. D. Marcos, F. Sancenón, R. Martínez-Máñez, P. Amorós, *Chem. Commun.* **2013**, 49, 5480-5482.
- 111 A. Ribes, S. Santiago-Felipe, A. Bernardos, M. D. Marcos, T. Pardo, F. Sancenón, R. Martínez-Máñez, E. Aznar, *ChemistryOpen*, **2017**, 6, 653-659.
- 112 M. Oroval, C. Coll, A. Bernardos, M. D. Marcos, R. Martínez-Máñez, D. G. Shchukin, F. Sancenón, *ACS Appl. Mater. Interfaces*, **2017**, 9, 11332-11336.
- 113 Elsayed, M. Licchelli, R. Martínez-Máñez, F. Sancenón, *Chem. Asian J.* **2017**, 18, 2670-2674.
- 114 A. Llopis-Lorente, B. Lozano, A. Bernardos, R. Martínez-Máñez, F. Sancenón, *J. Mater. Chem. B*, **2017**, 5, 3069-3083.
- 115 C. de la Torre, L. Mondragón, C. Coll, A. García-Fernández, F. Sancenón, R. Martínez-Máñez, P. Amorós, E. Pérez-Payá, M. Orzáez, *Chem. Eur. J.*, **2015**, 21, 15506-15510.
- 116 A. Agostini, L. Mondragón, L. Pascual, E. Aznar, C. Coll, R. Martínez-Máñez, F. Sancenón, J. Soto, M. D. Marcos, P. Amorós, A. M. Costero, M. Parra, S. Gil, *Langmuir*, **2012**, 28, 14766-14776.

Chapter 2:

General Objectives

Taking into account the increasing interest in developing new tools for the sensing of neurotransmitters and the development of therapies for the treatment of neurotransmitters-related diseases, this PhD thesis has aimed to contribute to filling this need through the development of smart nanodevices based on gold and mesoporous silica nanoparticles.

In particular, we have focused on the design, preparation, characterization and evaluation of nanodevices for the colorimetric sensing of neurotransmitters and controlled delivery systems responsive to neurotransmitters based on gold nanoparticles and mesoporous silica nanoparticles equipped with organic ligands, enzymatic effectors, molecular gates and chromo-fluorogenic species or drugs.

The specific objectives have been:

- To develop and evaluate a colorimetric nanosensor for the selective and sensitive detection of the neurotransmitter serotonin based on the aggregation of bifunctionalized gold nanoparticles.
- To prepare and evaluate a colorimetric probe for the selective detection of the neurotransmitter norepinephrine based on a double molecular recognition with functionalized gold nanoparticles.
- To design and evaluate a nanosensor able to detect the pheochromocytoma biomarker normetanephrine using bifunctionalized gold nanoparticles.
- To design an enzymatic controlled delivery system responsive to the neurotransmitter acetylcholine based on acetylcholinesterase-capped nanomaterials.
- To prepare a novel enzymatic controlled delivery system based on enzyme-controlled self-immolative arylboronate-gated nanoparticles able to respond in presence of the neurotransmitter glutamate.

Chapter 3:

Colorimetric detection of neurotransmitters based on the aggregation of bifunctionalized gold nanoparticles

3.1 Introduction

Neurotransmitters are involved in a variety of regulatory systems taking part in the regulation of the response to stress, psychomotor activity, emotional processes, learning, sleep, and memory and in the control of many processes of metabolism and the immune system.¹

Imbalance in the concentrations of the neurotransmitters in the brain has been shown to relate to various neurological disorders, such as schizophrenia, anxiety, epilepsy, and Alzheimer's and Parkinson's diseases.² NTs, such as dopamine (DA), norepinephrine (NE), epinephrine (E), and serotonin (5-HT) act as neurotransmitters at central and peripheral levels. Schizophrenia and Parkinson's disease have been linked to a deficient DA neurotransmission.³ Moreover a low concentration of NE which is responsible for human cardiovascular control may lead to conditions such as attention deficit hyperactivity disorder (ADHD) and hypotension.⁴ On the other hand, it has been reported that the presence of adrenal tumours such as pheochromocytoma produces an increase in the concentrations of NE and E.⁵ Mood disorders, such as anxiety or depression could be related to 5-HT which is primarily found in the enteric nervous system located in the gastrointestinal tract.⁶ Moreover, a significant increase in the concentrations of 5-HT is registered when a carcinoid tumour is present in the gastrointestinal tract.⁷

Due to the significant contribution of neurotransmitters not only to neurological functioning, but also to endocrinological and immunological actions, doctors and researchers are interested in the function and measurement of neurotransmitters as they have the potential to serve as clinically relevant biomarkers for specific disease states or to monitor treatment efficacy.

The measurement of neurotransmitters is considered as a means to assess functions of organs or tissues and has become the basis for diagnostic or functional indicators in clinical practice. Despite a historical absence of relevant biomarkers in the realm of clinical psychiatry, this format has expanded and

neurotransmitters now serve as a primary target for the development of predictive or correlative biomarkers of nervous system function.⁸

Neurotransmitters can be measured in different body fluids, the most common measurements include:⁹

- ✓ Cerebral Spinal Fluid (CSF).
- ✓ Blood (Plasma/Serum/Platelet).
- ✓ Urine.

The measurements performed on the CSF, may provide the best representation of what is happening in the Central Nervous System. However, sample collection from the spinal tap is highly invasive, which not only creates an inconvenience for the patient, the stress involved also influences the levels of key neurotransmitters including E and NE. Moreover, optimal ranges for the various neurotransmitters have not been established for CSF measurements, thus making results difficult to interpret.

Regarding blood measurements, its performance is less invasive and the optimal range of the neurotransmitters has been established for blood measurements, which makes it one of the most reliable fluids for the neurotransmitters assessment. However, similarly as to CSF measurements, the sample collection could produce a stress associated with venipuncture, which significantly influences the levels of some neurotransmitters.¹⁰

Conversely, to CSF and blood measurements, urinary neurotransmitter testing is the desired method to analyze nervous system function due to its stability, and non-invasiveness. Urinary neurotransmitter testing is frequently used as a marker for pheochromocytoma. Neurotransmitter testing is also being used in the assessment of many psychological disorders.¹¹

Quantitation of neurotransmitters in routine laboratory has triggered an ongoing debate about which technique offers more advantages, taking into account that

some types of neurotransmitters exist in biological samples at extremely low concentrations, which demands highly sensitive and selective bioanalytical methods.

In this scenario, among the approaches developed in order to determine the presence of neurotransmitters are: capillary electrophoresis (CE), liquid chromatography (LC), capillary electro-chromatography coupled with UV detection, flow immunoassay, native fluorescence detection, and electrochemical detection.¹²

However, some of these methods carry significant drawbacks. For instance, the chromatographic method has a long operation time and limited spatial resolution. In addition, selectivity of the electrochemical neurotransmitter sensors may be hampered by the presence of other molecules with the similar redox potentials to that of the target molecule although they can provide millisecond-range responses with micrometer range resolution.

On the last years, fluorescence and colorimetric methods may be valuable to overcome other techniques' weak points since they have fast response time and are simple non-destructive procedures, which allow application to a variety of physiological samples. Moreover, a sensitive analytical method based on a colorimetric or fluorescence probe designed to detect a neurotransmitter selectively may provide fast, reliable and substantial information on the localization and quantity of the target molecule of interest.¹⁰

For instance, Kristen E. Secor et al. reported a fluorescence probe based on boronic acid-containing coumarin aldehyde for the recognition of catecholamines (see **Figure 1**). The sensor binds to dopamine and norepinephrine by forming an iminium ion with the amine as well as a boronate ester with the catechol.¹³

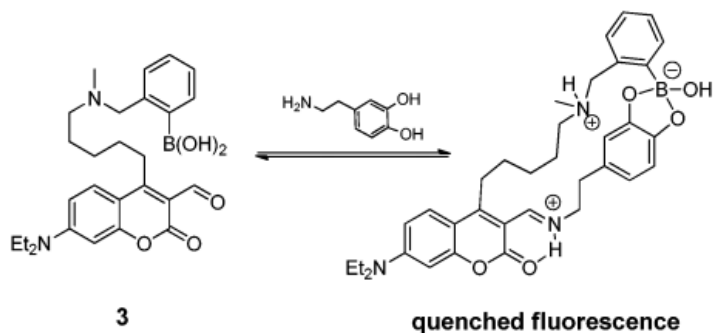


Figure 1. Proposed chemical structure of the fluorescence probe and its conjugate with dopamine. Reprinted with permission from *Org. Lett.*, 2004, 6, 3727-3730.

In recent years, sensing approaches based on the use of nanomaterials have remarkable increase, due to its well-known optical properties, versatile functionalization and stability. A huge variety of sensors based on nanomaterials has been designed for the selective and sensitive detection of different molecules of environmental and clinical interest.¹⁴

However, in the field of neurotransmitters detection there are few examples of sensors based on nanomaterials. One of them uses CdSe–ZnS quantum dots (QDs) and was reported by Ronit Freeman et al. (see **Figure 2**). The dopamine unit of **5** can bind easily with the boronic acid moiety attached to the QD to form a diad system between the QDs and the dye for effective fluorescence resonance energy transfer (FRET). Upon addition of the dopamine analyte, its competitive binding to the boronic acid moiety retards the FRET process in a concentration-dependent manner.¹⁵ However, the main drawback of this method is its lack of selectivity since neurotransmitters with similar molecular structures can be recognized by the same system.

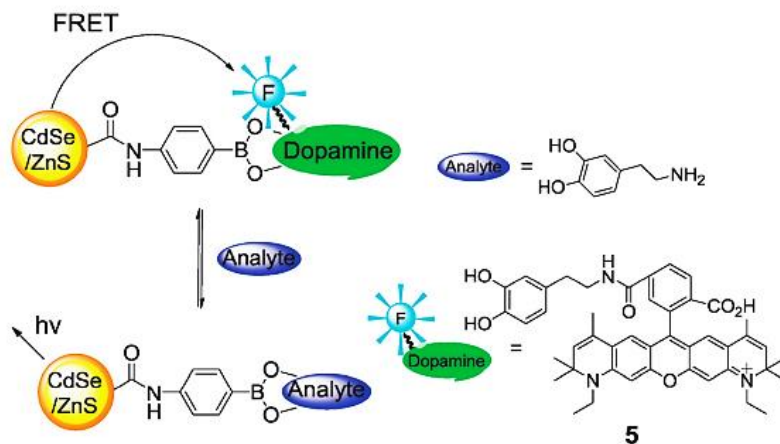


Figure 2. Competitive analysis of dopamine using fluorophore-labeled dopamine 5. Reprinted with permission from *Chem. Comm.*, 2009, 7, 764-766.

Therefore, taking into account: (i) the importance of neurotransmitters as biomarkers for several diseases and their key role in the central nervous system, (ii) the interest in developing new tools for neurotransmitters detection and (iii) the few examples for neurotransmitter sensing based on nanomaterials, this part of the thesis is aimed at designing, preparing and evaluating optical neurotransmitter nanosensors based on the aggregation of functionalized gold nanoparticles.

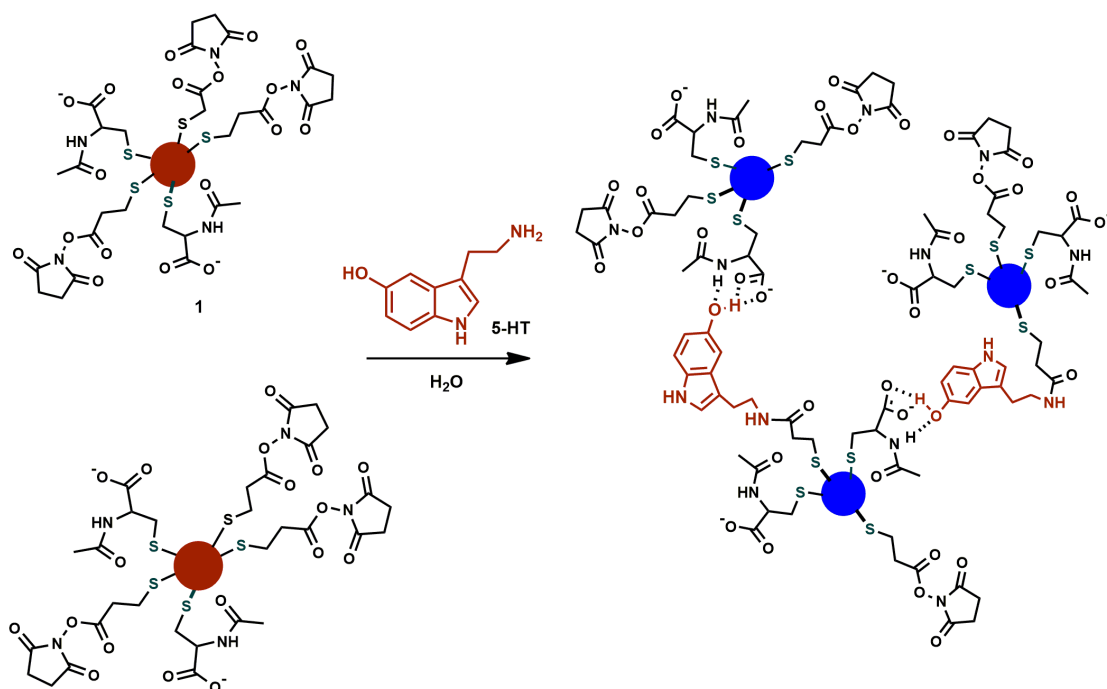
3.2 References

1. J. Bergquist, A. Ściubisz, A. Kaczor, J. Silberring, *J. Neurosci. Methods*, **2002**, 113, 1-13.
2. **a)** K. M. Gill, A. A. Grace, The role of neurotransmitters in schizophrenia. *Schizophrenia and Psychotic Spectrum Disorders*, **2016**, 153-4. **b)** P. Nuss, *Neuropsychiatr Dis Treat*, **2015**, 11, 165. **c)** F. M. Werner, R. Coveñas, *Epilepsy & Behavior*, **2017**, 71, 124-129. **d)** P. T. Francis, *CNS Spectr*, **2005**, 10, 6-9. **e)** P. Barone, *J. Neurol.*, **2010**, 17, 364-376.
3. J. Birtwistle, D. Baldwin, *Br. J. Community Nurs.*, **1998**, 7, 832-841.
4. **a)** N. del Campo, S. R. Chamberlain, B. J. Sahakian, T. W. Robbins, *Biol. Psychiatry*, **2011**, 69, e145-e157. **b)** A. Loavenbruck, P. Sandroni, *Curr Med Res Opin*, **2015**, 31, 2095-2104.

5. V. Kantorovich, K. Pacak, Pheochromocytoma and paraganglioma. *In Progress in brain research*, Elsevier, **2010**, 182, 343-373
6. **a)** K. Martinowich, B. Lu, *Neuropsychopharmacology*, **2008**, 33, 73-83. **b)** III, H. S. Ormsbee J. D. Fondacaro, *Proceedings of the Society for Experimental Biology and Medicine*, **1985**, 178, 333-338.
7. A. C. Rubin de Celis Ferrari, J. Glasberg, R. P. Riechelmann, *Clinics*, **2018**, 73.
8. **a)** Cook, I.A., *Psychiatry*, **2008**, 15, 54–59. **b)** J.H. Wood, *Neurology*, **1980**, 30, 645–651.
9. **a)** D. Svob Strac, D. Muck-Seler, N. Pivac, *Psychiatr Danub*, **2015**, 27, 0-24. **b)** T. Vandenryt, B. Van Grinsven, K. Eersels, P. Cornelis, S. Kholwadia, T. J. Cleij, R. Thoelen, W. D. Ceuninck, M. Peeters, P. Wagner, *Sensors*, **2017**, 17, 2701. **c)** M. Hinz, A. Stein, G. Trachte, T. Uncini, *Open Access J. Urol*, **2010**, 2, 177.
10. V. H. Rice, *Handbook of stress, coping, and health: Implications for nursing research, theory, and practice*, **2011**, Sage Publications.
11. D. T. Marc, J. W. Ailts, D. C. A. Campeau, M. J. Bull, K. L. Olson, *Neurosci. Biobehav. Rev. Reviews*, **2011**, 35, 635-644.
12. **a)** M. Chicharro, A. Sánchez, A. Zapardiel, M. D. Rubianes, G. Rivas, *Anal Chim Acta*, **2004**, 523, 185-191. **b)** E. Johnsen, S. Leknes, S. R. Wilson, E. Lundanes, *Sci. Rep.*, 2015, 5, 1-8. **c)** A. Zapata, V. I. Chefer, T. S. Shippenberg, L. Denoroy, *Curr Protoc Neurosci*, **2009**, 48, 7-4. **d)** X. Huang, X. F. Guo, H. Wang, H. S. Zhang, *Arab. J. Chem.*, **2014**. **e)** R. E. Özel, A. Hayat, S. Andreescu, *Anal. Lett.*, **2015**, 48, 1044-1069.
13. K. E. Secor, T. E. Glass, *Org. Lett.*, **2004**, 6, 3727-3730.
14. **a)** S. Su, W. Wu, J. Gao, J. Lu, C. Fan, *J. Mater. Chem.*, **2012**, 22, 18101-18110. **b)** M. R. Willner, P. J. Vikesland, *J. Nanobiotechnology*, **2018**, 16, 1-16. **c)** M. Pirzada, Z. Altintas, *Sensors*, **2019**, 19, 5311.
15. R. Freeman, L. Bahshi, T. Finder, R. Gill, I. Willner, *Chem. Comm.*, **2009**, 7, 764-766.

Chapter 3: Part 1

Selective and sensitive colorimetric detection of the neurotransmitter serotonin based on the aggregation of bifunctionalised gold nanoparticles



Selective and sensitive colorimetric detection of the neurotransmitter serotonin based on the aggregation of bifunctionalised gold nanoparticles

Tania M. Godoy-Reyes^{a,b,d}, Antoni Llopis-Lorente^{a,b,d}, Ana M. Costero^{a,b,c},
Félix Sancenón^{a,b,d}, Pablo Gaviña^{a,b,c,*} and Ramón Martínez-Mañez^{a,b,d,*}

^a Instituto de Reconocimiento Molecular y Desarrollo Tecnológico (IDM), Universidad Politécnica de Valencia-Universidad de Valencia (Spain).

^b CIBER de Bioingeniería, Biomateriales y Nanomedicina (CIBER-BBN), Spain.

^c Departamento de Química Orgánica, Universitat de València, Doctor Moliner 50, Burjassot, 46100, Valencia, Spain.

^d Departamento de Química, Universitat Politècnica de València, Camino de Vera s/n, 46022, Valencia, Spain.

*Corresponding authors. E-mail addresses: pablo.gavina@uv.es (P. Gaviña), rmaez@qim.upv.es (R. Martínez-Mañez)

Published online: 2 December 2017

(Reprinted with permission from *Sens. Actuators B Chem.*, 2018, 258, 829)

Abstract

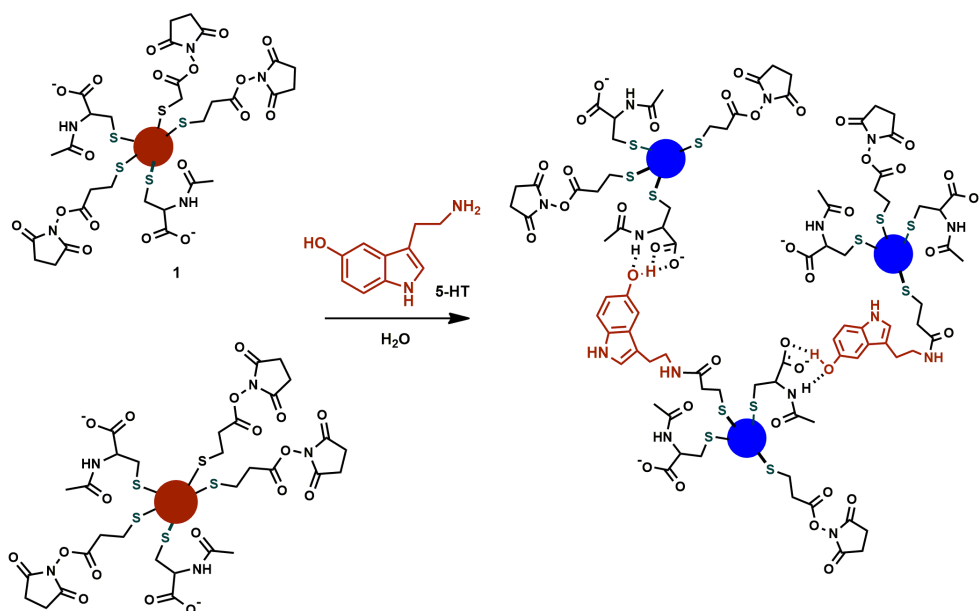
We report a simple, sensitive and selective method for the colorimetric detection of serotonin (5-HT) in aqueous media using bifunctionalized gold nanoparticles (AuNPs). The probe (**1**) consisted of AuNPs functionalised with dithiobis (succinimidylpropionate) (DSP) and N-Acetyl-L-Cysteine (NALC). DSP was chosen to react with the amino group of 5-HT, whereas NALC was chosen to bind the hydroxyl group in 5-HT through hydrogen bonding and electrostatic interactions. A double interaction between nanoparticles and the hydroxyl and the amino group of 5-HT led to interparticle-crosslinking aggregation. This, resulted in a colour change from red to blue that can be observed by the naked-eye. The probe was selective to 5-HT and no colour modulation was observed in the presence of other neurotransmitters (i.e. dopamine, epinephrine, norepinephrine), selected biomolecules (i.e. L-tyrosine, gamma-Aminobutyric acid, L-cysteine, uric acid, oxalic acid, aspartic acid and glutamic acid) and common inorganic species. A limit of detection as low as 0.1 μM was determined in buffered water at pH 7 by UV-vis titrations. Similar response of the probe to 5-HT was observed in simulated blood serum, with a limit of detection of 0.12 μM , and a linear response within the 0-3 μM concentration range, which is within the range of the 5-HT concentrations of clinical interest. Finally, the performance of probe **1** in real human blood samples was evaluated, and showed a remarkable ability to distinguish between normal 5-HT levels and 5-HT levels indicative of disease.

Introduction

Serotonin (5-hydroxytryptamine, 5-HT), commonly known as the molecule of happiness, is an important neurotransmitter that plays a key role in the regulation of various cognitive and behavioural functions such as sleep, mood, pain, anxiety, appetite control, sexual activity and learning ¹. 5-HT is produced in several locations including the brain, to transport information along the central nervous system, and also in the gastrointestinal tract (GIT) to regulate intestinal movement ²⁻³. Abnormal 5-HT levels have been related with a number of disorders like depression, migraines, ADHD, autism and inflammatory syndromes ⁴⁻⁵. Moreover, carcinoid tumours, which usually start in the GI tract, secrete large amounts of 5-HT. This leads to high 5-HT levels in the blood of patients and causes flushing of the skin, diarrhea and breathing problems. In fact, evaluating 5-HT blood levels, together with 5-hydroxyindoleacetic acid (a metabolite of 5-HT), is the principal laboratory test to diagnose carcinoid syndrome ⁶⁻⁷. Although how the serotonergic system operates exactly is still not well-known, scientists are attempting to elucidate the possible hormonal role of 5-HT in neurodegenerative disorders like Parkinson's ⁸⁻⁹ and Alzheimer's disease ¹⁰. All these previous results have suggested the potential use of 5-HT as a biomarker in a number of diseases.

In this scenario, the development of methods to detect 5-HT is a field of interest. Reported methods for 5-HT detection include liquid chromatography ¹¹⁻¹⁷ and electrochemical techniques ¹⁸⁻²⁴. For example, the oxidation/reduction of 5-HT and dopamine using modified glassy carbon electrodes has been reported as a suitable electrochemical approach for 5-HT detection ²³⁻²⁴. Enzymatic ²⁵ and solid surface-room temperature phosphorescence assays have also been reported ²⁶. Other reported methods include fluorometric ²⁷⁻²⁹, flow cytometry ³⁰, immunocytochemical and immunohistochemical ³¹⁻³³ techniques. Although most of these methods can accurately measure 5-HT, they require sophisticated high cost equipment and are time-consuming (especially LC). However, designing simple procedures to detect 5-HT remains a challenge due to the complexity of the molecule and common interference from other neurotransmitters with similar chemical structures such as dopamine and epinephrine.

As an alternative to traditional instrumental methods, chromogenic probes offer certain advantages as they are usually cheap, easy to use, require simple instrumentation or not instrumentation at all, and allow *in situ* and at-site detection³⁴. An appealing approach to develop colorimetric probes is to use gold nanoparticles (AuNPs) given their unique optoelectronic properties³⁵⁻³⁷. When using AuNPs, the detection strategy is usually based on colour changes that arise from interparticle plasmon coupling during analyte-induced aggregation of nanoparticles. It is known that the red colour of dispersed AuNPs of a certain size turns dark blue upon aggregation, and this colour change can usually be observed by the naked eye, even at very low analyte concentrations³⁸⁻⁴³. For instance, Tian and co-workers have reported the use of functionalised AuNPs for the colorimetric detection of dopamine. A double interaction between the nanoparticles and the diol and the amino group of dopamine triggered the aggregation of AuNPs that results in a clear colour modulation⁴⁴. For all the above reasons, and given our current interest in developing probes to detect bio-relevant molecules, we report herein a simple, sensitive and selective method for the colorimetric detection of 5-HT using bifunctionalised AuNPs. The recognition paradigm is shown in **Scheme 1**. Probe **1** consists of AuNPs of ca. 15 nm, which were functionalized dithiobis(succinimidylpropionate) (DSP) and N-Acetyl-L-Cysteine (NALC). DSP was chosen as a suitable group because it is able to react with the amino group in 5-HT⁴⁵, whereas NALC plays a double role: (i) it acts as a stabiliser for AuNPs thanks to its negative charge at a neutral pH; (ii) is also able to bind the hydroxyl group in 5-HT through hydrogen bonding and electrostatic interactions⁴⁶. Whereas, functionalised **AuNPS 1** would not aggregate, we expected the double interaction between 5-HT and **1** to lead to interparticle-crosslinking aggregation, which would result in a colour change from red to blue.



Scheme 1. Sensing paradigm of the colorimetric detection of serotonin (5-HT) based on gold nanoparticles bifunctionalised with NALC and DSP (probe 1).

Results and discussion

In order to prepare probe **1**, the citrate-stabilised AuNPs were firstly obtained following the Turkevich-Frens method, by reducing tetrachloroauric acid with trisodium citrate in boiling water⁴⁸⁻⁵⁰. Then, citrate was displaced from the surface of the nanoparticles in a ligand exchange reaction by the simultaneous addition of NALC and DSP (1:1 molar ratio). Finally, the functionalised **AuNPs 1** were purified by repeated centrifugation and redispersion in water. The resulting bifunctionalised AuNPs were characterised by UV-Vis, transmission electron microscopy (TEM), dynamic light scattering (DLS), Fourier-transform infrared spectroscopy (FTIR) and proton nuclear magnetic resonance spectroscopy (¹H-NMR) studies.

The monodisperse bifunctionalised nanoparticles **1** were obtained with an average size of 15 nm as determined by TEM (**Figure S1**). The aqueous suspensions of **1** were red wine-coloured and showed a SPRB peak at 521 nm, which perfectly agrees with the typical colour and SPRB shown by those AuNPs smaller than 25 nm⁵¹⁻⁵². Typical concentrations of final probe **1** were calculated by

UV-vis spectroscopy to be ca. 8.74×10^{-10} M from an estimated molar extinction coefficient of $\epsilon = 3.97 \times 10^8 \text{ M}^{-1} \cdot \text{cm}^{-1}$ ⁵³. The FTIR studies showed the appearance of absorption bands which were attributed to NALC (C=O stretching at 1649 cm^{-1} , N-H bending at 1543 cm^{-1} and N-H stretching at 3352 cm^{-1}), as reported in other studies⁵⁴, and DSP's C=O stretching also appeared at 1720 cm^{-1} ⁵⁵ (see **Figure S3**). ¹HNMR spectra also showed the appearance of signals, which were attributed to the functionalisation with NALC and DSP. (see **Figure S4**). The red wine-coloured aqueous dispersions of **1** remained stable in the refrigerator for more than 1 month, and no changes were observed on the characteristic plasmon absorption band.

In order to evaluate the sensing capabilities of the prepared nanoparticles, buffered aqueous suspensions of **1** at pH 7.0 (Tris, 50 mM) were studied in the absence and presence of 5-HT (100 μM). Whereas the suspension of the nanoparticles remained red in the absence of 5-HT, addition of 5-HT induced a remarkable shift of the SPRB from 521 nm to 605 nm, which resulted in a colour change from red to blue that could be observed by the naked eye, and indicated aggregation of AuNPs (see **Figure 1**). Aggregation of nanoparticles was not only confirmed by the instantaneous colour change, but also by TEM (see **Figure S1**) and DLS (see **Figure S2**). From the latter, it was found that the hydrodynamic diameter of the nanoparticles increased from 16.5 nm for **1** to 704 nm when 5-HT was added. The zeta potential reduced from -17.8 mV (**1**) to -6.14 mV (**1**+5-HT).

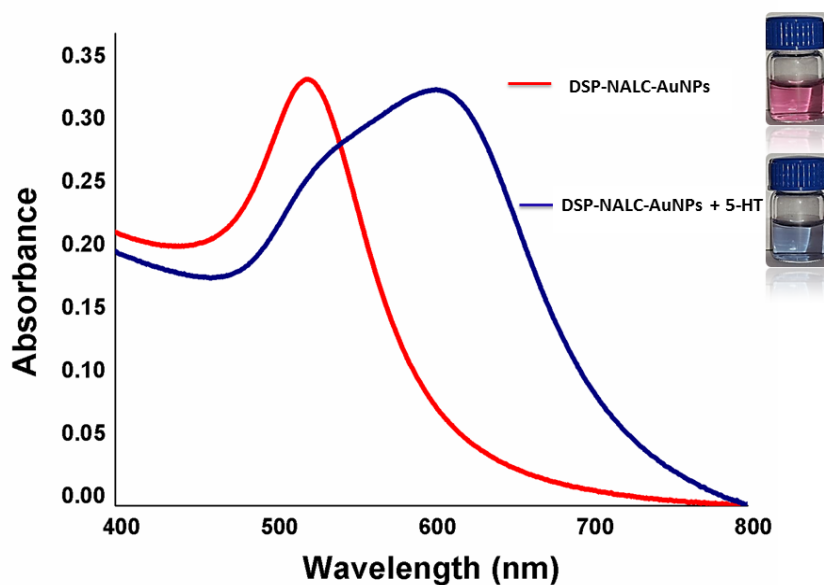


Figure 1. UV-Vis of **1** in the absence (red) and presence of 5-HT (100 μ M) (blue) at pH 7.0 (Tris, 50 mM).

In another step, the selectivity of the prepared functionalised AuNPs towards 5-HT was evaluated. The response of **1** in the presence of other neurotransmitters, e.g., dopamine (DA), epinephrine (Epi) and norepinephrine (NE), and of other biomolecules, e.g., L-tyrosine (L-Tyr, a precursor for stimulatory neurotransmitters), gamma-Aminobutyric acid (GABA, an inhibitory neurotransmitter), L-cysteine (L-Cys), aspartic acid (AA) and glutamic acid (GA) (excitatory amino acids), uric acid (UA, described recently as a potential neurotransmitter) and oxalic acid (OA) was studied. Whereas a remarkable colour change was observed in the presence of 5-HT, negligible colour modulations and negligible changes in the A_{605}/A_{521} ratio (A_{605} = absorbance at 605 nm, A_{521} = absorbance at 521 nm) were observed upon the addition of potential interferents (see **Figure 2a** and **2b** and **Figure S5**).

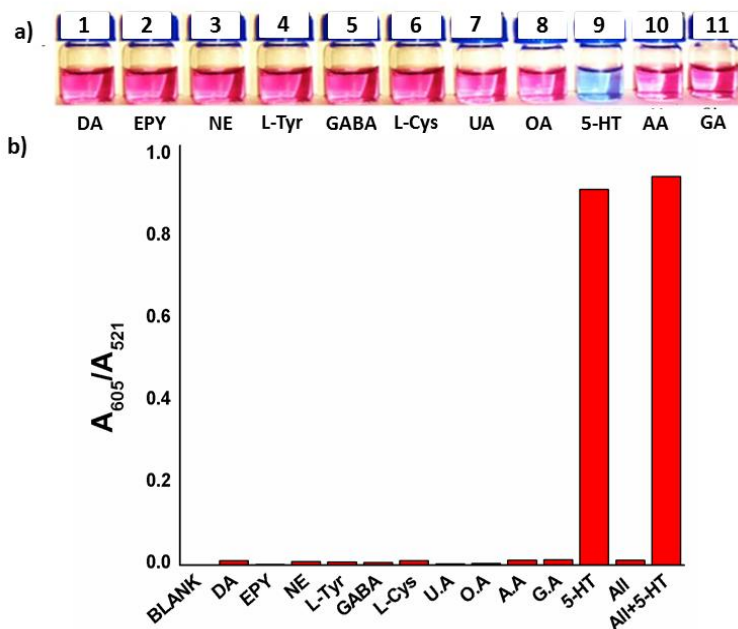


Figure 2. Response of **1** in the presence of different molecules (500 μ M) at pH 7.0 (Tris, 50mM). a) Vials with the different tested molecules. b) Representation of A_{605}/A_{521} for interferences.

In an additional competitive experiment, the response of **1** in a mixture that contained 5-HT and DA, Epi, NE, L-Tyr, GABA, L-Cys, UA, OA, AA and GA (500 μ M of each) was also tested. As seen in **Figure 2b**, the observed response was extremely similar to that found when probe **1** was used alone with 5-HT. All these data indicate that the bifunctionalised **AuNPs 1** are able to selectively detect 5-HT in buffered media, and in the presence of other neurotransmitters and selected biomolecules. One possible explanation for the good selectivity for 5-HT versus catecholamines (DA, Epi and NE) could be the different ionisation equilibria of the biogenic phenolic amines and catecholamines in biological media, with different proportions of zwitterionic species⁵⁵⁻⁵⁶. The selectivity of the probe in the presence of common inorganic cations and anions was also tested. Probe **1** remained stable in the presence of the different species individually and in a mixture that contained them all. Remarkably, the probe retained its capability to recognise 5-HT in the presence of all the inorganic species (see **Figure S6**).

Furthermore, the sensitivity of **1** to 5-HT was evaluated. In this experiment, the colour changes of aqueous suspensions of **1** in the presence of different amounts of 5-HT were studied. As seen in **Figure 3**, a gradual colour modulation from red wine to purple, and finally to blue, which was dependent on the 5-HT concentration, was observed. This change coincides with the proposed sensing protocol that involves the 5-HT-induced aggregation of the bifunctionalised AuNPs. The changes in colour shown in **Figure 3a** agree with changes in the UV-vis bands observed for the different prepared suspensions of **1** in the presence of increasing amounts of 5-HT (see **Figure 3b**). An increase in the aggregation of AuNPs, according to the 5-HT concentration, was confirmed by the TEM studies (see **Figure 3c**).

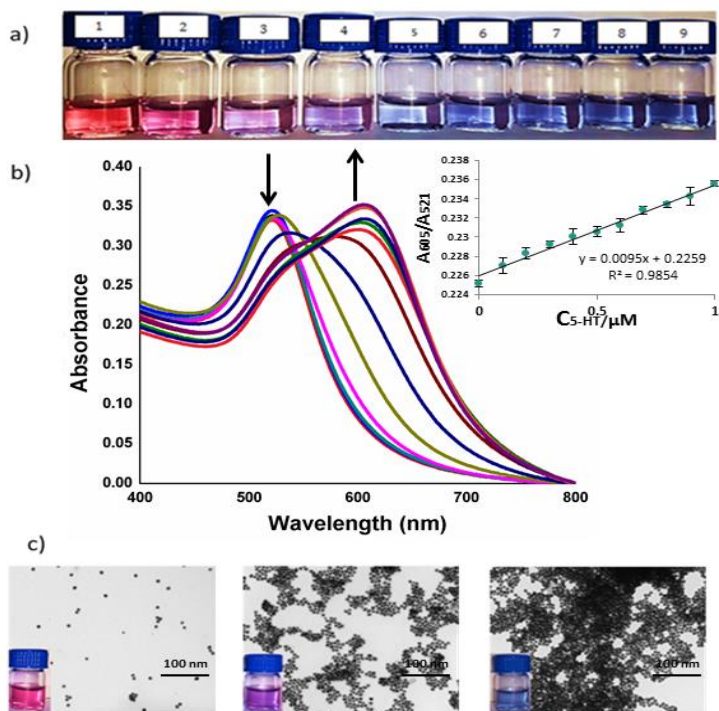


Figure 3. a) Colorimetric visualisation of probe **1** when 5-HT was added at concentrations of 0, 0.9, 10, 20, 30, 40, 50, 70, 100 μM (1-9, respectively). b) Changes in the UV-Vis spectra of probe when 5-HT was added at concentrations of 0, 0.9, 10, 20, 30, 40, 50, 70, 100 μM . Inset: plot of the A_{605}/A_{521} vs. 5-HT concentrations within the 0-1 μM range. c) TEM images of **1** with 0, 40 and 150 μM of 5-HT, respectively. Experiments were performed at a buffered pH 7.0 (Tris, 50 mM).

From the A_{605}/A_{521} vs. 5-HT concentration plot, a linear response within the 0-1 μM 5-HT concentration range was noted. From these studies a limit of detection (LOD) as low as 0.1 μM (17 $\text{ng}\cdot\text{mL}^{-1}$) was determined (see **Figure S7**). The calculated LOD indicates the noteworthy sensitivity of the probe, and confers our system a competitive basis to detect 5-HT at relevant clinical concentrations. In particular, reported studies have determined that 5-HT levels above 500 $\text{ng}\cdot\text{mL}^{-1}$ (2.80 μM) in blood serum can be indicative of carcinoid tumours, while values above 1,000 $\text{ng}\cdot\text{mL}^{-1}$ are indicative of metastasis⁵⁸⁻⁶². Other studies have found that 5-HT rises from a mean value of 767 $\text{ng}\cdot\text{mL}^{-1}$ for those patients with carcinoid tumours to 1,720 $\text{ng}\cdot\text{mL}^{-1}$ for the patients with carcinoid tumours who are also affected by heart disease⁶³. Given the importance of determining the 5-HT concentration in blood serum, further studies into the response of probe **1** in simulated blood serum⁴⁰ were carried out. Probe **1** in simulated serum showed similar behaviour as described above in water when increasing amounts of 5-HT were added (see **Supplementary Data**). From the A_{605}/A_{521} vs 5-HT concentration plots, a linear response in simulated serum within the 0 to 3 μM 5-HT concentration range was observed, and a LOD of 0.12 μM (23 $\text{ng}\cdot\text{mL}^{-1}$) was determined in this medium, which was lower than the normal range for adults of 50-300 $\text{ng}\cdot\text{mL}^{-1}$ (0.28 to 1.70 μM) in blood⁶⁴⁻⁶⁵. Finally, encouraged by these results, we decided to test the performance of nanoparticles **1** in real human blood samples. Samples were taken from a healthy volunteer, and were centrifuged to remove red blood cells and proteins (see the **Experimental section and Figure S13 for details**). Nanoparticles were stable in serum samples and led to a change that was observed by the naked eye when serum was spiked with 1 mM of 5-HT (see **Figure S14-A**). A remarkably significant increase in the A_{605}/A_{521} values was observed from normal serum to serum containing 10 μM of 5-HT (indicative of carcinoid tumours) (see **Figure S14-B**).

Conclusions

In summary, we report herein a new method for the colorimetric detection of 5-HT using 15 nm AuNPs bifunctionalized with dithiobis (succinimidylpropionate) and N-Acetyl-L-Cysteine. The prepared nanoparticles, **1**, selectively detect 5-HT in

water at pH 7 (Tris, 50mM) via the 5-HT-induced aggregation of the bifunctionalised AuNPs which results in a remarkable colour change. The probe is selective to 5-HT and no colour modulation was observed in the presence of other neurotransmitters (i.e. dopamine, epinephrine, norepinephrine) and selected biomolecules (i.e. L-tyrosine, gamma-Aminobutyric acid, L-cysteine, uric acid, oxalic acid, aspartic acid and glutamic acid). A linear response within the 0-1 μM 5-HT concentration range and a LOD as low as 0.1 μM were determined in buffered water at pH 7 (Tris, 50 mM). A similar response of probe **1** to 5-HT was observed in simulated blood serum with a linear response within the 0-3 μM 5-HT concentration range and with a LOD as low as 0.12 μM . Finally, the probe was capable of detecting 5-HT in human blood samples and of distinguishing between normal 5-HT levels and 5-HT levels that are indicative of disease. Given the importance of serotonin in different diseases, we expect that our findings could help to elucidate the role played by serotonin and to develop innovative tools for early point-of-care or personalized diagnosis applications.

Experimental Section

• *Chemicals*

Chloroauric acid ($\text{HAuCl}_4 \cdot 3\text{H}_2\text{O}$), sodium citrate dihydrate, N-Acetyl-L-Cysteine (NALC), dithiobis succinimidyl propionate (DSP), serotonin (5-HT), dopamine (DA), epinephrine (Epi), norepinephrine (NE), L-tyrosine (L-Tyr), gamma-Aminobutyric acid (GABA), uric acid (AU), oxalic acid (AO), aspartic acid (A.A) and glutamic acid (GA) were commercially available, and were used without purification.

• *General Methods*

UV-Vis absorption spectra were recorded using a 1-cm path length quartz cuvette on a Shimadzu UV-2101PC spectrophotometer. All the measurements were taken at room temperature. To verify the serotonin-induced aggregation of the gold nanoparticles probe, high resolution transmission electron microscopy (JEOL-1010 transmission electron microscopy operating at 100 kV) was used. Zeta potential and hydrodynamic diameter values were measured in a Malvern Zetasizer ZS 3 times in 10-25 cycles. Fourier-transform infrared spectroscopy spectra were

recorded with a Cary 630 FT-IR spectrometer within the wavenumber range of 648-4000 cm^{-1} at a resolution of 8 cm^{-1} . Proton nuclear magnetic resonance spectroscopy (^1H NMR) spectra were recorded with a Bruker DRX-500 Spectrometer (500 MHz, 1024 scans).

- ***Synthesis of citrate-capped AuNPs***

Citrate-capped AuNPs with a diameter ca. 15 nm were synthesised as previously reported⁴⁶. Briefly, 5 mL of aqueous 13.61 mM trisodium citrate solution were added to an aqueous boiling solution of HAuCl_4 (95 mL, 0.23 mM) and the resulting solution was allowed to boil for 30 min until a red solution was obtained. The solution was cooled to room temperature. Then the mixture was purified by filtering through a 0.22 μM membrane and the filtrate was stored in a refrigerator at 4°C until it was used.

- ***Functionalisation of AuNPs***

Probe **1** was prepared by modifying the citrate-capped AuNPs by ligand-exchange reaction, which was performed at room temperature by mixing 95 mL of the as-prepared AuNPs with 190 μL of 2 mM aqueous solution of NALC and 190 μL of DSP (2 mM in DMF). Ligands were added simultaneously and the solution was stirred for 1 h with magnetic stirring. To purify **1**, the mixture was centrifuged for 10 min at 11,000 rpm and the supernatants were decanted twice.

- ***Sensing studies***

For the sensing studies, serotonin solutions were freshly prepared in 50 mM Tris buffer, pH 7.0, at room temperature. Next 500 μL of **1** (4.37×10^{-10} M) and 500 μL of the 5-HT solution at an appropriate concentration were placed to obtain a final volume of 1 mL. Samples were incubated for 3 min before taking measurements in the spectrophotometer. The procedure was the same for the interferences. Simulated blood serum (SBS)⁴⁷ was prepared as follows: 8.036 g of NaCl, 0.352 g NaHCO_3 , 0.225 g of KCl, 0.230 g of $\text{K}_2\text{HPO}_4 \cdot 3\text{H}_2\text{O}$, 0.311 g $\text{MgCl}_2 \cdot 6\text{H}_2\text{O}$, 40 mL of HCl 1M, 0.293 g of CaCl_2 , 0.072 g of Na_2SO_4 and 6.063 g of Tris were all dissolved in 1 L

of Milli-Q water and adjusted to pH 7.4. Next 100 mL of this solution and 900 mL of Milli-Q water were used to prepare the corresponding SBS solutions of 5-HT. Then 500 μL of **1** were mixed with 500 μL of SBS solutions of 5-HT at an appropriate concentration, incubated for 3 min, and analysed by UV-vis spectrophotometry. Real human blood samples from a healthy volunteer were obtained thanks to the support of our university health centre. Firstly, red blood cells were separated from serum by centrifugation. Next, serum samples were further centrifuged (15 min, 11000 rpm) using Amicon Ultra-05 centrifugal filters units with Ultracel-10 membranes to remove proteins, and were mixed (1:1) with 50 mM Tris Buffer. Finally, 100 μL of **1** and 100 μL of the resulting serum samples (which either contained spiked 5-HT or did not) were incubated for 3 min and measured in the spectrophotometer (see the illustrated steps in Figure S13).

Acknowledgements

Financial support from the Spanish Government (Projects MAT2015-64139-C4-1-R and MAT2015-64139-C4-4-R) and the Generalitat Valencia (Project PROMETEOII/2014/047) is gratefully acknowledged. T. Godoy-Reyes is grateful to the Generalitat Valenciana for her Santiago Grisolia fellowship. A. Llopis-Lorente thanks “La Caixa” Banking Foundation for his PhD grant. SCSIE (Universitat de València) is gratefully acknowledged for all the equipment employed. NMR was registered at the U26 facility of ICTS “NANBIOSIS” at the Universitat de València. Support from the Juana Portaceli Health Centre of the Universitat Politècnica de València to obtain blood samples from a healthy volunteer is gratefully acknowledged.

References

1. T. Canli, K.P. Lesch, Long story short: the serotonin transporter in emotion regulation and social cognition, *Nat. Neurosci.* 10 (2007) 1103-1109.
2. J. M. Yano, K. Yu, G. P. Donaldson, G. G. Shastri, P. Ann, L. Ma, C. R. Nagler, R. F. Ismagilow, S. K. Mazmanian, E. Y. Hsiao, Indigenous bacteria from the gut microbiota regulate host serotonin biosynthesis, *Cell* 161 (2015) 264-276.
3. M. Camilleri, Serotonin in the gastrointestinal tract, *Curr. Opin. Endocrinol. Diabetes Obes.* 16 (2009) 53-59.

4. J. R. Lacasse, J. Leo, Serotonin and depression: a disconnect between the advertisements and the scientific literature, *PLoS Med.* 2 (2005) e392.
5. E. H. Cook Jr, B. L. Leventhal, The serotonin system in autism, *Curr. Opin. Pediatr.* 8 (1996) 348-354.
6. J. M. Zuetenhorst, B. G. Taal, Neuroendocrine tumors in decompensated liver disease, *Oncologist* 10 (2005) 123-131.
7. J. M. Feldman, Urinary serotonin in the diagnosis of carcinoid tumors, *Clin. Chem.* 32 (1986) 840-844.
8. S. H. Fox, R. Chuang, J. Brotchie, Serotonin and Parkinson's disease: On movement, mood, and madness, *Mov. Disord.* 24 (2009) 1255-1266.
9. M. Politis, F. Niccolini, Serotonin in Parkinson's disease, *Behav. Brain Res.* 277 (2015) 136-145.
10. M. Butzlaff, E. Ponimaskin, The role of serotonin receptors in Alzheimer's disease, *Opera Med. Physiol.*, 2 (2016) 77-86.
11. M. Maillet, S. J. Robert, F. Lezoualc'h, New insights into serotonin 5-HT₄ receptors: a novel therapeutic target for Alzheimer's disease?, *Curr. Alzheimer Res.* 1 (2004) 79-85.
12. C. P. Bearcroft, M. J. G. Farthing, D. Perrett, Determination of 5-hydroxytryptamine, 5-hydroxyindoleacetic acid and tryptophan in plasma and urine by HPLC with fluorimetric detection, *Biomed. Chromatogr.* 9 (1995) 23-27.
13. A. Gironi, G. Seghieri, M. Niccolai, P. Mammini, Simultaneous liquid-chromatographic determination of urinary vanillylmandelic acid, homovanillic acid, and 5-hydroxyindoleacetic acid, *Clin. Chem.* 34 (1998) 2504-2506.
14. O. C. Ingebretsen, A. N. Bakken, M. Farstad, Liquid chromatography of serotonin and adenine nucleotides in blood platelets, illustrated by evaluation of functional integrity of platelet preparations, *Clin. Chem.* 31 (1985) 695-698.
15. P. C. Gunaratna, K. K. Cadle, C. B. Kissinger, An improved liquid chromatographic method with electrochemical detection for direct determination of serotonin in microdialysates from Caudate-putamen and pineal gland regions of rat brain, *J. Neurosci. Methods* 155 (2006) 143-148.
16. B. A. Patel, M. Arundell, K. H. Parker, M. S. Yeoman, D. O'Hare, Simple and rapid determination of serotonin and catecholamines in biological tissue using high-performance liquid chromatography with electrochemical detection, *J. Chromatogr. B* 818 (2005) 269-276.
17. A. Vaarmann, A. Kask, U. Maeorg, Novel and sensitive high-performance liquid chromatographic method based on electrochemical coulometric array

- detection for simultaneous determination of catecholamines, kynurenine and indole derivatives of tryptophan, *J. Chromatogr. B* 769 (2002) 145-153.
18. F. Mashige, Y. Matsushima, C. Miyata, R. Yamada, H. Kanazawa, I. Sakuma, N. Takai, N. Shinozuka, A. Ohkubo, K. Nakahara, Simultaneous determination of catecholamines, their basic metabolites and serotonin in urine by high-performance liquid chromatography using A mixed-mode column and an eight-channel electrochemical detector, *Biomed. Chromatogr.* 9 (1995) 221-225.
 19. K. Wu, J. Fie, S. Hu, Simultaneous determination of dopamine and serotonin on a glassy carbon electrode coated with a film of carbon nanotubes, *Anal. Biochem.* 318 (2003) 100-106.
 20. B. E. K. Swamy, B. J. Venton, Carbon nanotube-modified microelectrodes for simultaneous detection of dopamine and serotonin in vivo, *Analyst* 132 (2007) 876-884.
 21. J. Li, X. Lin, Simultaneous determination of dopamine and serotonin on gold nanocluster/overoxidized-polypyrrole composite modified glassy carbon electrode, *Sens. Actuators B Chem.* 124 (2007) 486-493.
 22. R. N. Goyal, V. K. Gupta, M. Oyama, N. Bacheti, Gold nanoparticles modified indium tin oxide electrode for the simultaneous determination of dopamine and serotonin: Application in pharmaceutical formulations and biological fluids, *Talanta*, 72 (2007) 976-983.
 23. Y. Li, X. Huang, Y. Chen, L. Wang, X. Lin, Simultaneous determination of dopamine and serotonin by use of covalent modification of 5-hydroxytryptophan on glassy carbon electrode, *Microchim. Acta* 164 (2009) 107-112.
 24. Y. Sun, J. Fei, J. Hou, Q. Zhang, Y. Liu, B. Hu, Simultaneous determination of dopamine and serotonin using a carbon nanotubes-ionic liquid gel modified glassy carbon electrode, *Microchim. Acta* 165 (2009) 373-379.
 25. S. K. Kim, S. Jeon, Simultaneous determination of serotonin and dopamine at the PEDOP/MWCNTs–Pd nanoparticle modified glassy carbon electrode, *J. Nanosci. Nanotechnol.* 12 (2012) 1903-1909.
 26. M. I. Nichkiva, H. Huisman, P. M. Wynveen, D. T. Marc, k. L. Olson, G. H. Kellermann, Evaluation of a novel ELISA for serotonin urinary serotonin as potential biomarker for depression, *Anal. Biochem. Chem.* 402 (2012) 1539-1600.
 27. T. Ramon-Marquez, A. Medina-Castillo, A. L. Fernandez-Gutierrez, J. F. Fernandez-Sanchez, A novel optical biosensor for direct and selective determination of serotonin in serum by Solid Surface-Room Temperature Phosphorescence, *Biosens. Bioelectron.* 82 (2016) 217-223.

28. J. H. Thompson, C. A. Spezia, M. Angulo, Fluorometric detection of serotonin using o-phthalaldehyde: an improvement, *Experientia*. 26 (1970) 327-329.
29. P Frattini, M. L. Cucchi, G. Santagostino, G. L. Corona, A sensitive fluorimetric method for determination of platelet-bound and plasma free serotonin, *Clin. Chim. Acta*. 92 (1979) 353-360.
30. R. M. Fleming, W. G. Clark, Single extraction method for the simultaneous fluorometric determination of serotonin, dopamine and norepinephrine in brain, *Anal. Chem*, 37 (1965) 692-696.
31. G. Gobbi, P. Mirandola, P. L. Tazzari, F. Ricci, L. Caimi, A. Cacchioli, M. Vitale, Flow cytometry detection of serotonin content and release in resting and activated platelets. *Br. J. Haematol* 121 (2003) 892-896.
32. Consolazione, C. Milstein, B. Wright, A. C. Cuello, Immunocytochemical Detection of Serotonin with Monoclonal Antibodies, *J. Histochem. Cytochem*, 29 (1981) 1425-1430.
33. C. S. Kim, M. C. McNamara, J. M. Lauder, E. E. Lawson, Immunocytochemical detection of serotonin content in raphe neurons of newborn and young adult rabbits before and after acute hypoxia, *Int. J. Dev. Neurosci* 12 (1994) 499-505.
34. C. Sur, H. Betz, P. Schloss, Immunocytochemical detection of the serotonin transporter in rat brain. *Neuroscience* 73 (1996), 217-231.
35. L. E. Santos-Figueroa, M. E. Moragues, E. Climent, A. Agostini, R. Martínez-Mañez, F. Sancenón, Chromogenic and fluorogenic chemosensors and reagents for anions. A comprehensive review of the years 2010–2011, *Chem. Soc. Rev.* 42 (2013) 3489-3613.
36. K. Saha, S. S. Agasti, C. Kim, X. Li, V. M. Rotello, Gold nanoparticles in chemical and biological sensing, *Chem. Rev.* 112 (2012) 2739-2779.
37. K. M. Mayer, J. H. Hafner, Localized surface plasmon resonance sensors, *Chem. Rev.* 111 (2011) 3828-3857.
38. E. Boisselier, D. Astruc, Gold nanoparticles in nanomedicine: preparations, imaging, diagnostics, therapies and toxicity. *Chem. Rev.* 38 (2009) 1759-1782.
39. K. A. Rawat, J. R. Bhamore, R. K. Singhal, S. K. Kailasa, Microwave assisted synthesis of tyrosine protected gold nanoparticles for dual (colorimetric and fluorimetric) detection of spermine and spermidine in biological samples, *Biosens. Bioelectron.* 88 (2017) 71-77.
40. K. A. Rawat, R. K Singhal, S. K. Kailasa, Colorimetric and fluorescence “turn-on” methods for the sensitive detection of bromelain using carbon dots functionalized gold nanoparticles as a dual probe, *RSC Adv.* 6 (2016) 32025-32036.

41. K. A. Rawat, S. K. Kailasa, 2, 3, 4-Trihydroxy benzophenone as a novel reducing agent for one-step synthesis of size-optimized gold nanoparticles and their application in colorimetric sensing of adenine at nanomolar concentration. *RSC Adv.* 6 (2016) 11099-11108.
42. A. Martí, A. M. Costero, P. Gaviña, M. Parra, Selective colorimetric NO (g) detection based on the use of modified gold nanoparticles using click chemistry, *Chem. Commun.* 51 (2015) 3077-3079.
43. J. V. Rohit, S. K. Kailasa, Simple and selective detection of pendimethalin herbicide in water and food samples based on the aggregation of ractopamine-dithiocarbamate functionalized gold nanoparticles, *Sens Actuators B Chem.* 245 (2017) 541-550.
44. L. Chena, W. Lua, X. Wanga, L. Chen, A highly selective and sensitive colorimetric sensor for iodide detection based on anti-aggregation of gold nanoparticles, *Sens Actuators B Chem.* 182 (2013) 482-488.
45. B. Kong, A. Zhu, Y. Luo, Y. Tian, Y. Yu, G. Shi, Sensitive and selective colorimetric visualization of cerebral dopamine based on double molecular recognition, *Angew. Chem.* 123 (2011) 1877-1880.
46. H. Su, Q. Zheng, H. Li, Colorimetric detection and separation of chiral tyrosine based on N-Acetyl-L-Cysteine modified gold nanoparticles, *J. Mater. Chem.* 22 (2012) 6546-6548.
47. V. A. Turek, M. P. Cecchini, J. Paget, A. R. Kucernak, A. A. Kornyshev, J. B. Edel, Plasmonic ruler at the liquid-liquid interface, *ACS nano* 6 (2012) 7789-7799.
48. A. Oyane, H. M. Kim, T. Furuya, T. Kokubo, T. Miyazaki, T. Nakamura, Preparation and assessment of revised simulated body fluids, *J. Biomed. Mater. Res. Part A* 65 (2003) 188-195.
49. P. Zhao, N. Li, D. Astruc, State of the art in gold nanoparticle synthesis, *Coord. Chem. Rev.* 257 (2013) 638-665.
50. J. A. Turkevich, A study of the nucleation and growth processes in the synthesis of colloidal gold *Discuss. Faraday Soc.* 11 (1951) 55-75.
51. G. Frens, Controlled nucleation for the regulation of the particle size in monodisperse gold suspensions, *Nature* 241 (1973) 20-22.
52. W. Haiss, N. T. K. Thanh, J. Aveyard, D. G. Fernig, Determination of size and concentration of gold nanoparticles from UV-Vis spectra, *Anal. Chem.* 79 (2007) 4215-4221.
53. S.-Y. Lin, Y.-T. Tsai, C.-C. Chen, C.-M. Lin, C.-H. Chen, Two-step functionalization of neutral and positively charged thiols onto citrate-stabilized Au nanoparticles, *J. Phys. Chem. B* 108 (2004) 2134-2139.

54. X. Liu, M. Atwater, J. Wang, Q. Huo, Extinction coefficient of gold nanoparticles with different sizes and different capping ligands, *Colloids Surf. B* 58 (2007) 3-7.
55. Y. Zhang, M. Yan, S. Wang, J. Jiang, P. Gao, G. Zhang, C. Dong, S. Shuang, Facile one-pot synthesis of Au(0)@Au(I)-NAC core-shell nanoclusters with orange-yellow for cancer cell imaging, *RSC Adv.* 6 (2016) 8612-8620.
56. C. S. Stan, C. Albu, A. Coroaba, M. Popa, D. Sutiman, One step synthesis of fluorescent carbon dots through pyrolysis of N-hydroxysuccinimide. *J. Mater. Chem. C* 3 (2015) 789-795.
57. J. Armstrong, R. B. Barlow, The ionization of phenolic amines, including apomorphine, dopamine and catecholamines and an assessment of zwitterion constant, *Br J Pharmacol.* 57(1976) 501-516.
58. G. Rudnick, K. L. Kirk, H. Fishkes, S. Schuldine, Zwitterionic and anionic forms of a serotonin analog as transport substrates, *J. Biol. Chem.*, 264(1989), 14865-14868.
59. P. C. Emson, R. F. Gilbert, H. Martensson, A. Nobin, Elevated concentrations of substance p and 5-HT in plasma in patients with carcinoid tumors, *Cancer* 54 (1984) 715-718.
60. E. Pussard, N. Guigueno, O. Adam, J.-F. Giudicelli, Validation of HPLC-amperometric detection to measure serotonin in plasma, platelets, whole blood, and urine, *Clin. Chem.* 42 (1996) 1086-1091.
61. D. O'Toole, M. Ducreux, G. Bommelaer, J.-L. Wemeau, O. Bouché, F. Catus, J. Blumberg, P. Ruzsniwski, Treatment of carcinoid syndrome, *Cancer* 88 (2000) 770-776.
62. R. H. Resnick, S. J. Gray, Serotonin metabolism and the carcinoid syndrome: a review, *Med. Clin. North Am.*, 44 (1960) 1323-1339.
63. F. V. Plapp, ClinLab Navigator, <http://www.clinlabnavigator.com/carcinoid-syndrome.html>, (accessed March 2017).
64. P. A. Robiolio, V. H. Rigolin, J. S. Wilson, J. K. Harrison, L. L. Sanders, T. M. Bashore, J. M. Feldman, Carcinoid heart disease, *Circulation* 92 (1995) 790-795.
65. Laura J. Martin, MedlinePlus, <https://medlineplus.gov/ency/article/003562.htm>, (accessed July 2017).
66. Mayo Clinic, <http://www.mayomedicallaboratories.com/test-catalog/Clinical+and+Interpretive/84373>, (accessed July 2017).

Supporting Information

- *Transmission Electron Microscopy (TEM)*

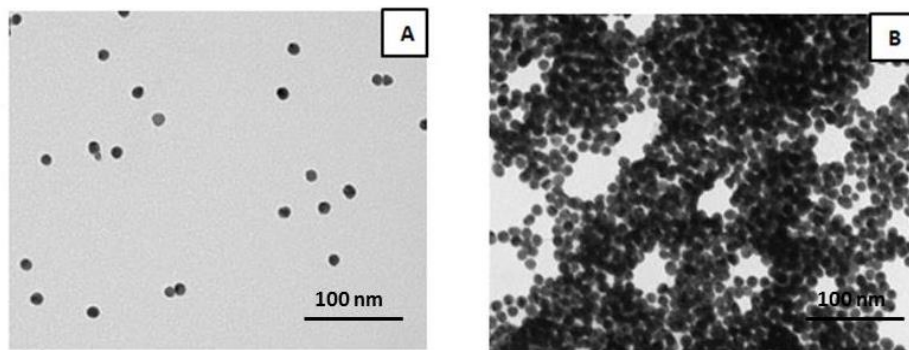


Figure S1. TEM images of probe 1 (A) in the absence and (B) in the presence of 5-HT (150 μM).

- *Dynamic Light Scattering (DLS)*

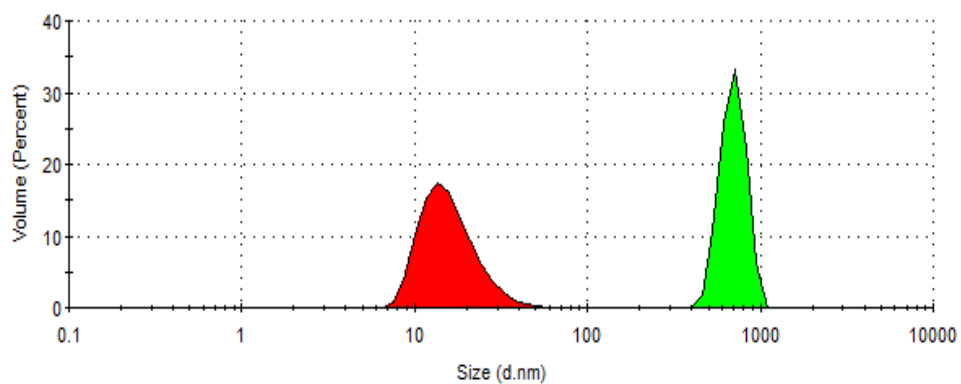


Figure S2. Hydrodynamic diameter of probe 1 in the absence (16.5 nm, red) and in the presence of 5-HT (150 μM) (704 nm, green).

- **Fourier-transform infrared spectroscopy (FTIR)**

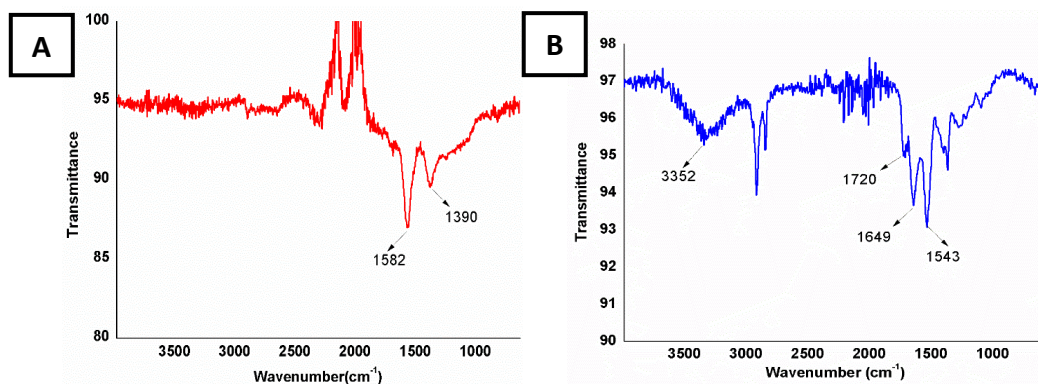


Figure S3. FT-IR spectra of (A) unmodified Au NPs and (B) probe 1. Whereas citrate bands (1390 and 1582 cm⁻¹) are observed in (A), NALC (1543, 1649 and 3352 cm⁻¹) and DSP (3352) characteristic bands are observed in (B).

- **Proton nuclear magnetic resonance spectroscopy (¹H-NMR)**

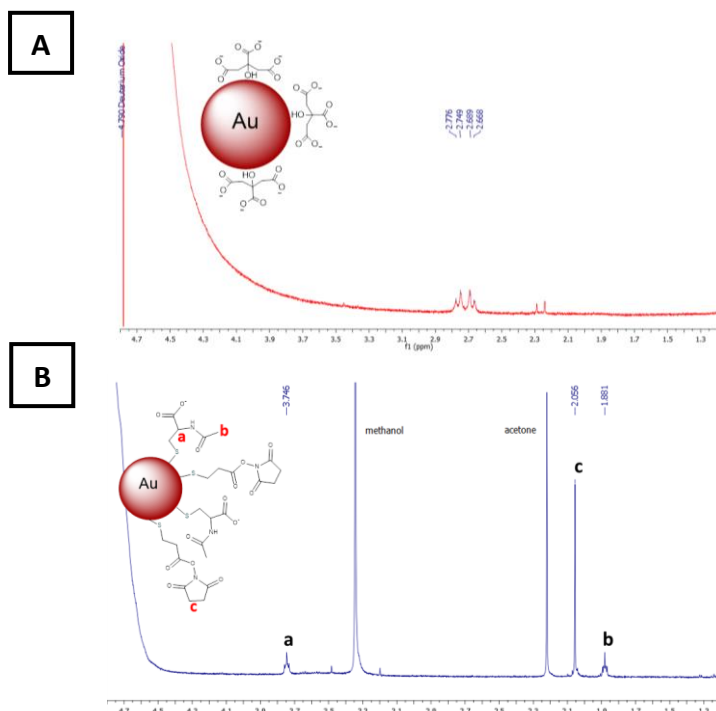


Figure S4. ¹H-NMR spectra of (A) unmodified Au NPs and (B) probe 1.

- *UV-Vis of interferences*

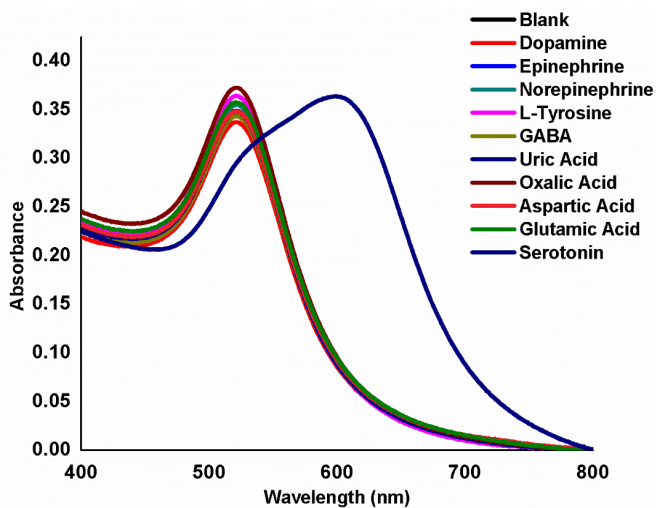


Figure S5. UV-Vis spectra of probe 1 in the presence of 500 μM of different neurotransmitters and biological molecules.

- *Response in the presence of inorganic interferences*

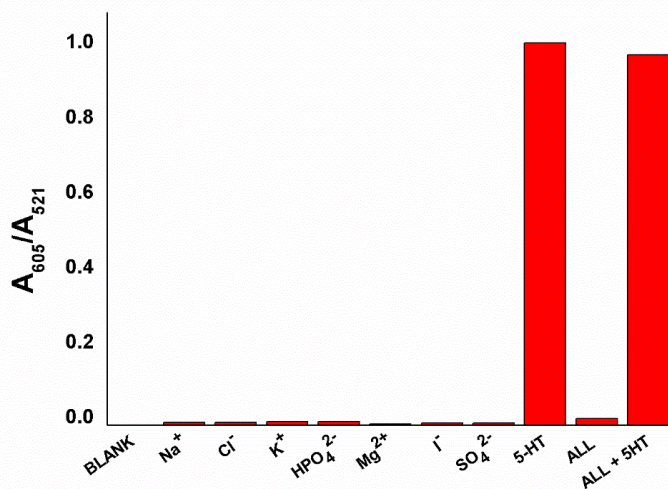


Figure S6. Response of 1 in the presence of different ions (500 μM) at pH 7.0 (Tris, 50mM).

- **Calibration curve in aqueous media**

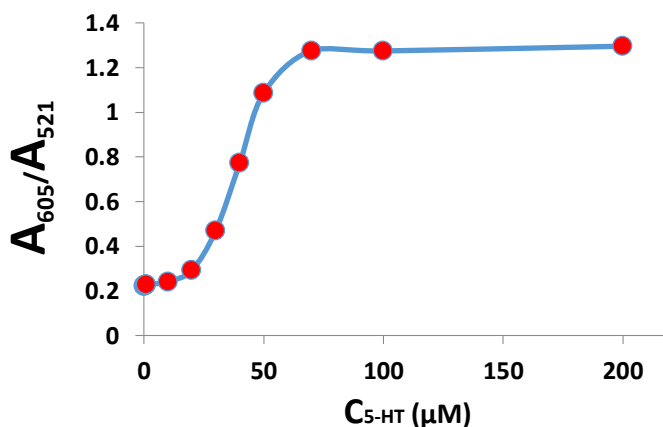


Figure S7. Plot of A_{605}/A_{521} versus 5-HT concentration (0-200 μM) obtained with **1**.

- **Determination of LOD**

The limit of detection for 5-HT was obtained from the plot of the ratio of the absorbance intensities at 521 and 605 nm (A_{605}/A_{521}) versus 5-HT concentration in μM . LOD was calculated by using the equation (1), where $K=3$; S_b is the standard deviation of the blank (0.000354922) and m is the slope of the calibration curve. The resulting LOD was 0.1 μM .

$$LOD = K \cdot \frac{S_b}{m} \quad (1)$$

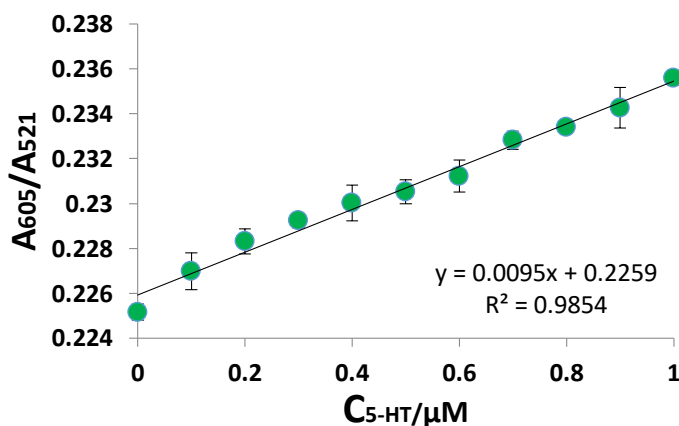


Figure S8. Linear plot of A_{605}/A_{521} versus 5-HT concentration (0-1 μM) obtained with **1**. Error bars expressed as standard deviation for $n=3$.

- **Determination of recovery and accuracy of the method**

Recovery and accuracy of the method were calculated according to reference 39 (K. A. Rawat, R. K Singhal, S. K. Kailasa, *RSC Adv.* 6 (2016) 32025-32036).

KNOWN CONCENTRATION (μM)	FOUND CONCENTRATION (μM)	RECOVERY % ^{A)}	ACCURACY% ^{B)}	PRECISION% ^{C)}
0.1 μM	0.11 μM	113.94 %	13.94 %	0.36 %
0.7 μM	0.72 μM	104.11 %	4.11 %	0.17 %

Table S1. **A)** % recovery (found concentration/known concentration) \times 100, **B)** Accuracy was calculated from (found concentration – known concentration/known concentration) \times 100. **C)** Precision was calculated from standard deviation/mean \times 100.

- **Response in simulated blood serum**

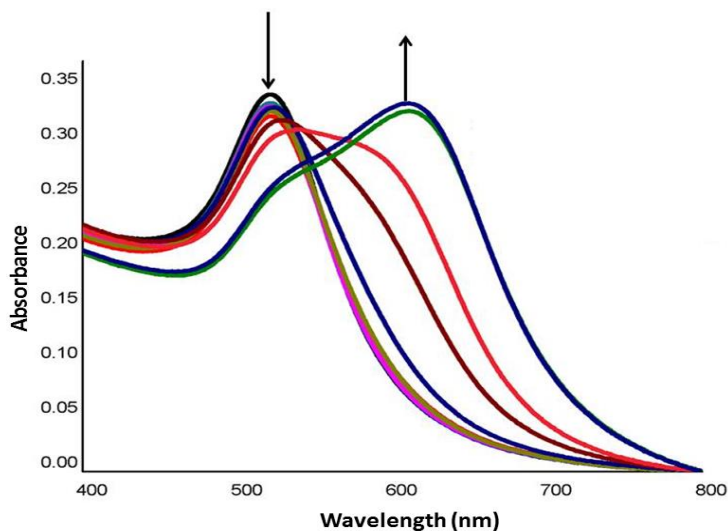


Figure S9. UV-Vis of **1** upon addition of simulated blood serum (pH 7.4) with increasing amounts of 5-HT.

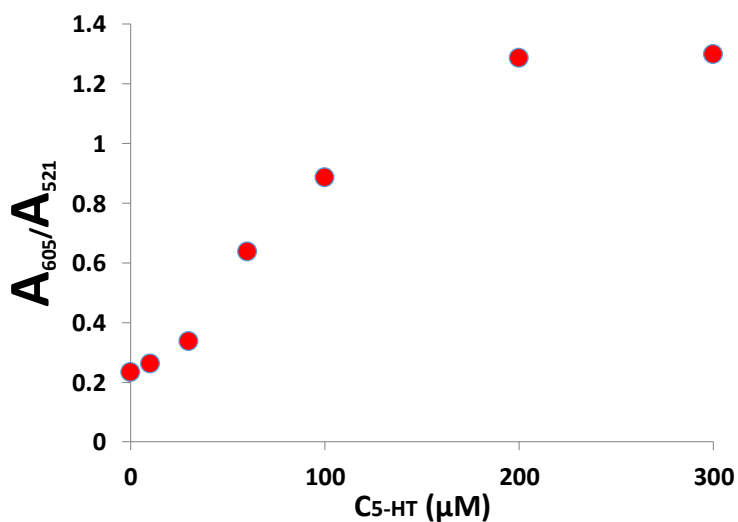


Figure S10. Plot of A_{605}/A_{521} versus 5-HT concentration (0-300 μM) obtained with **1** in simulated blood serum.

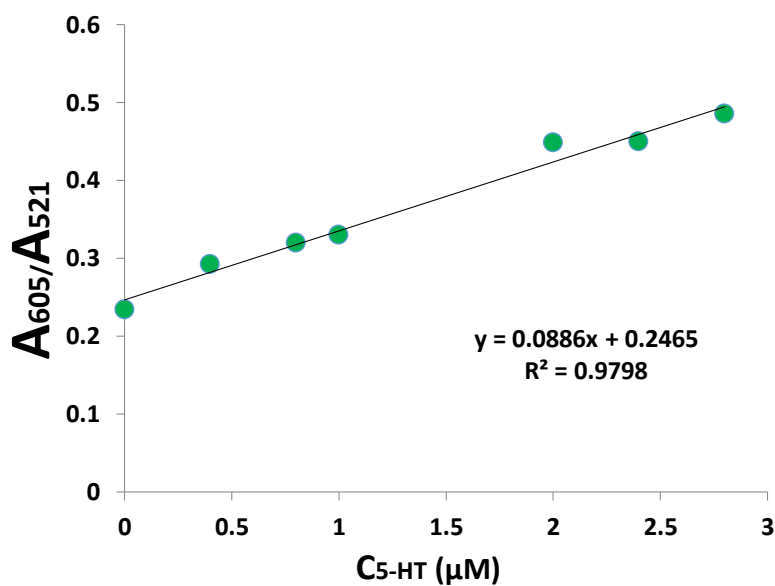


Figure S11. Linear plot of A_{605}/A_{521} versus 5-HT concentration (0-3 μM) obtained with **1** in simulated blood serum.

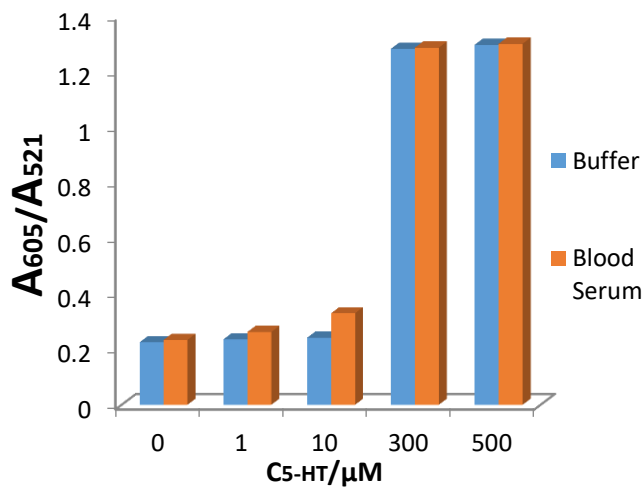


Figure S12. Comparison between 5-HT detection using **1** in aqueous media and simulated blood serum.

- **Response in real human blood samples**



Figure S13. Images illustrating the procedure followed for measuring 5-HT in real human blood as described in the Experimental section. First, blood was centrifuged to separate serum (yellow phase) from red blood cells (**I**). Next, proteins were removed from serum using centrifugal filters giving a colorless solution (**II**). Finally, serum samples were mixed with the probe **1** and measured in the spectrophotometer (**III**).

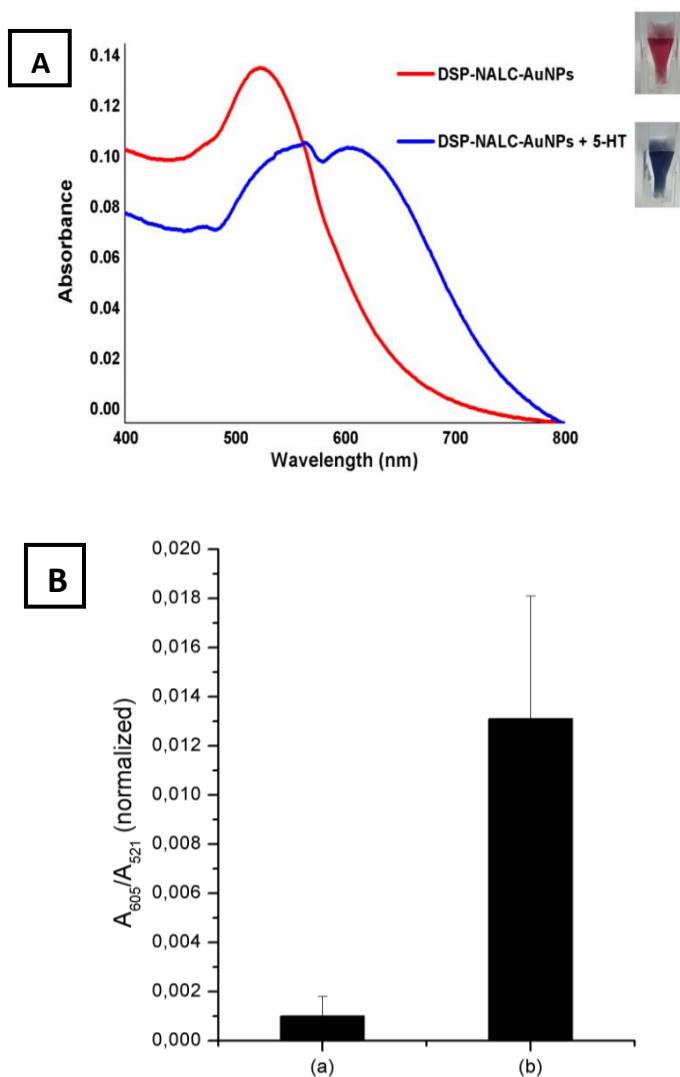
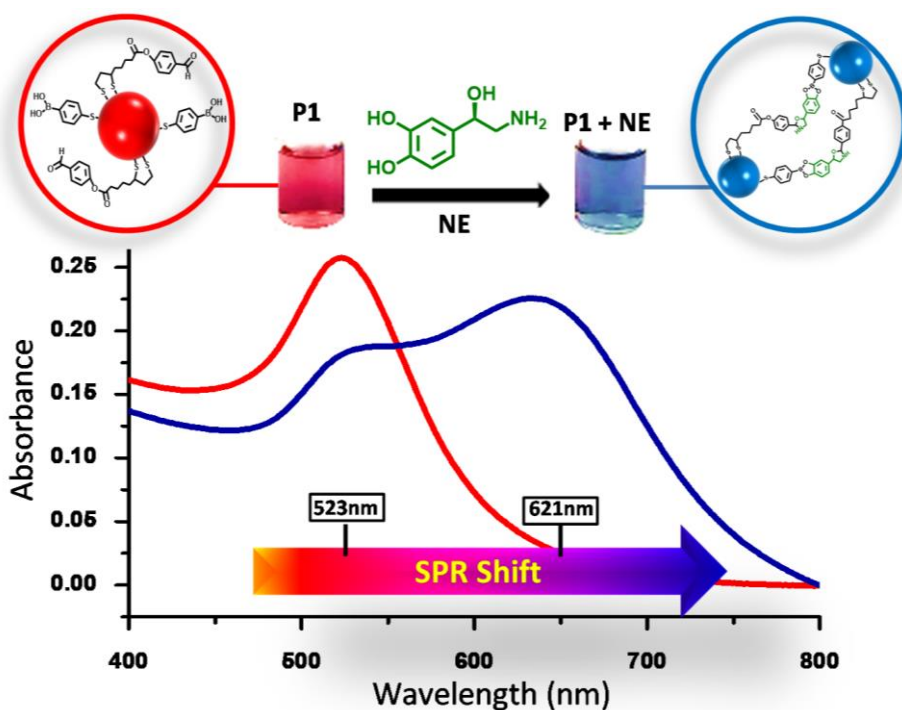


Figure S14. Performance of probe **1** using human blood samples. **A)** UV-Vis of **1** in the absence of spiked 5-HT (red) and in the presence of 5-HT (1 mM) (blue) in human serum samples. **B)** Normalized A_{605}/A_{521} ratio for **1** in samples of human serum from a healthy person (a) and human serum containing 10 μM of 5-HT (indicative of carcinoid tumours). Error bars expressed as standard deviation for $n=3$.

Chapter 3: Part 2

A Colorimetric Probe for the Selective Detection of Norepinephrine Based on a Double Molecular Recognition with Functionalized Gold Nanoparticles



A Colorimetric Probe for the Selective Detection of Norepinephrine Based on a Double Molecular Recognition with Functionalized Gold Nanoparticles

Tania M. Godoy-Reyes,^{†,‡,||} Ana M. Costero,^{†,‡,§} Pablo Gaviña,^{*,†,‡,§} Ramón Martínez-Máñez,^{*,†,‡,||} and Félix Sancenón^{†,‡,||}

[†] Instituto Interuniversitario de Investigación de Reconocimiento Molecular y Desarrollo Tecnológico (IDM), Universitat Politècnica de València, Universitat de València, 46022 Valencia, Spain.

[‡] CIBER de Bioingeniería, Biomateriales y Nanomedicina (CIBER-BBN), 28029 Madrid, Spain.

[§] Departamento de Química Orgánica, Universitat de València, Doctor Moliner 50, Burjassot, 46100, Valencia, Spain.

^{||} Departamento de Química, Universitat Politècnica de València, Camino de Vera s/n, 46022, Valencia, Spain.

Published online: February 8, 2019

(Reprinted with permission from *ACS Appl. Nano Mater.* 2019, 2, 1367)

Abstract

A simple colorimetric probe for the selective and sensitive detection of neurotransmitter norepinephrine (NE), an important biomarker in the detection of tumours such as pheochromocytoma and paraganglioma, is described. The sensing strategy is based on the use of spherical gold nanoparticles functionalized with benzaldehyde and boronic acid-terminated moieties. A double molecular recognition involving on one hand the aromatic aldehyde and the aminoalcohol group of NE, and on the other hand the boronic acid and the catechol moiety of the neurotransmitter, results in analyte triggered aggregation of the gold nanoparticles, leading to a bathochromic shift of the SPRB in the UV-vis spectrum of the probe and a clear change in the color of the solution from red to blue. Probe (**P1**) shows a remarkable selectivity toward NE versus other catecholamine neurotransmitters (dopamine and epinephrine) and selected biomolecules (5-HIAA, L-Tyr, glucose, uric acid, Lys and glutamic acid). Moreover, a linear response to NE in the 0–1 μM concentration range was observed and a limit of detection of 0.07 μM in aqueous media was determined by UV-vis spectroscopy. The sensitivity of the probe toward NE in synthetic urine was also evaluated. In this medium, a limit of detection of 0.09 μM was obtained which falls within the range of clinical interest.

Introduction

Norepinephrine (NE) or noradrenaline, also known as the “hormone of the stress”, is a hormone and a neurotransmitter secreted by noradrenergic neurons in the sympathetic and central nervous system. NE plays important roles in physiological processes such as stress,^{1,2} anxiety,^{3,4} sleep,⁵ and memory.⁶ Additionally, NE is involved in the fight-or-flight response, triggering the release of glucose and increasing heart rate and blood flow to skeletal muscle.⁷

Furthermore, it also regulates the function of certain types of immune cells (e.g., T and NK cells).⁸ Pathologies such as depression,^{9,10} Alzheimer’s disease,¹¹ and Parkinson’s disease are associated with low levels of NE.¹² Conversely, high NE levels are indicative of pheochromocytoma and paraganglioma, two neuroendocrine tumours, which start in the adrenal medulla and extra-adrenal paraganglia, respectively, and secrete large amounts of NE.^{13,14} This increases NE levels in patients’ urine and causes hypertension, fast heart rate, headache, sweating, and chest or abdominal pain.¹⁵ In addition, human immunodeficiency virus-1 (HIV-1) replication is accelerated by NE via protein kinase A dependent effects on cytokine production.¹⁶ Given the importance of NE as biomarker for the early diagnosis of the previously mentioned pathologies, the development of effective and simple methods for the detection and quantitative determination of NE is highly desirable.

In recent years, some analytical methods have been developed for the determination of NE, such as high performance liquid chromatography (HPLC),^{17,18} fluorometric,^{19,20} and electrochemical techniques.²¹⁻²³ Although these reported methods are able to determine correctly the presence of NE, in general, expensive equipment and complicated sample pretreatment is needed. Hence, the development of fast, low cost, sensitive, and selective techniques for the specific and simple detection of NE in biological fluids is of great importance.

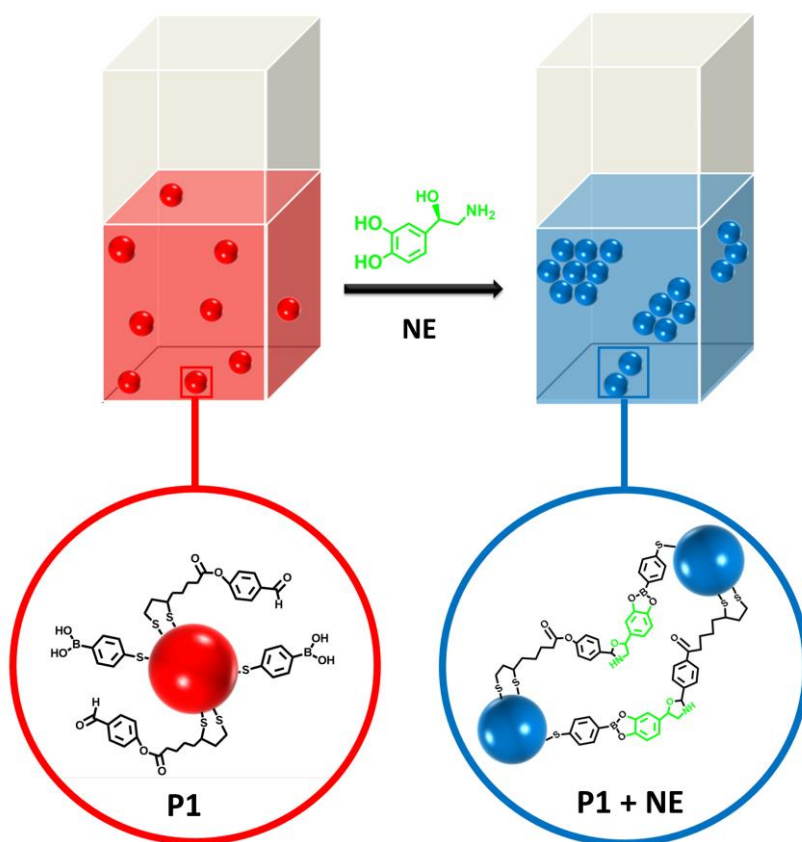
The use of chromogenic sensors and probes is an appealing alternative to overcome some limitations of traditional instrumental methods, because their low cost and operational simplicity, allow on-site detection, and require

simple equipment or no instrumentation at all.²⁴ Remarkably, in spite of them being of much interest, very few colorimetric methods have been developed to detect NE.^{25–30} Moreover, most of these methods are based on the use of catecholamines as reducing agents, which lead to reduced selectivity to NE in the presence of other catecholamines, such as dopamine or epinephrine (**see Table S3 in Supporting Information**).

Gold nanoparticles (AuNPs) are excellent materials and have been successfully applied for the design of colorimetric probes.^{31–33} In general, the detection strategy relies on the observed color changes that arise upon analyte-triggered aggregation or the redispersion of nanoparticles. Colloidal solutions of dispersed AuNPs, with particle size between 5 and 30 nm, exhibit a deep red color and a high molar extinction coefficient due to SPRB. Moreover, AuNPs can be easily functionalized on their surface with a broad range of organic molecules or biological macromolecules, which selectively interact with the target analyte. This interaction triggers the aggregation of AuNPs, resulting in interparticle surface plasmon coupling. This results in an important bathochromic shift of the SPR band and a change in the color of the solution from red to blue, which can be seen with the naked eye at very low analyte concentrations.^{34–37} For instance, the implementation of double-functionalized AuNPs as probes for the selective colorimetric detection of neurotransmitters such as dopamine³⁸ or serotonin³⁹ has been previously reported.

Based on the aforementioned facts, and following our interest in developing colorimetric methods for the fast, simple, and selective detection of biomarkers, we report herein the use of bifunctionalized AuNPs as probes for the colorimetric detection of NE, through the double molecular recognition of the catechol and aminoalcohol moieties. The sensing strategy is sketched in **Scheme 1**. Probe **P1** consists of AuNPs (ca. 14 nm), functionalized on their surface with two different ligands, 4-(liponyloxy)benzaldehyde (L1) and 4-mercatophenylboronic acid (L2). The terminal aldehyde of L1 was chosen to react with the aminoalcohol group of NE to form an oxazolidine,^{40,41} whereas L2 plays a double role: (i) the boronic acid

group is able to react with the catechol moiety in NE to form stable boronate groups;^{42,43} (ii) the ligand also acts as a stabilizer for AuNPs. A double interaction between NE and the dispersed gold nanoparticles was expected to trigger their aggregation leading to a shift of the AuNPs SPR band, with the resulting change in the color of the solution (from red to blue).



Scheme 1. Sensing Strategy for the Colorimetric Detection of Norepinephrine (NE) Using Gold Nanoparticles Functionalized with L1 and L2 (**P1**).

Experimental section

• *Synthesis of Probe P1*

Probe **P1** was synthesized from freshly prepared citrate-stabilized gold nanoparticles of ca. 14 nm diameter (see **Supporting Information**) by a ligand-exchange reaction with L1 and L2, which was performed as follows: First L2 (20 μ L, 0.5 mM in DMF) was added to an aqueous dispersion of the as-prepared citrate-coated AuNPs (10 mL) and the mixture stirred for 1 min at room temperature. Then L1 (20 μ L, 0.5 mM in DMF) was added to the solution and the mixture was stirred at room temperature for 1 h. The resulting suspension of nanoparticles was centrifuged (10 min, 11000 rpm), the supernatant was decanted and the nanoparticles redispersed again in Milli-Q water (18.2 M Ω cm⁻¹). This procedure was repeated twice to yield probe **P1**.

• *Sensing Studies*

NE solutions of different concentrations were freshly prepared at pH 6.5 in 10 mM phosphate buffer at room temperature. Then 200 μ L of the NE solution at the corresponding concentration was added to 200 μ L of the solution of **P1** (8.1×10^{-10} M). The resulting mixture of NE and probe **P1** (400 μ L) was incubated for 5 min and then the corresponding UV-vis spectra was recorded at room temperature. The same protocol was followed in the study of interferences. The assays run with the optimized probe (**OP1**) were performed by adding 20 μ L of NE (500 μ M, final concentration) to 200 μ L of **P1** and incubating for 1 min. Next 180 μ L of the NE problem solution at different concentrations were added resulting in a final volume of 400 μ L. UV-vis measurements were performed after an incubation time of 5 min. In order to ensure that the priming of the probe does not bias the results, 220 μ L of the mother solution of **OP1** plus 180 μ L of phosphate buffer is used as blank (0 added NE) and compared with the signal of the optimized probe upon addition of external NE. This procedure of priming gold nanoparticle-based probes has been carried out based on previously reported studies.³⁸ Surine (synthetic urine negative control) was used for the measurements of NE in urine. To take these measurements, **OP1** (200 μ L) and

200 μL of the NE solutions in 10% of the synthetic urine were mixed, incubated for 5 min, and their UV–vis spectra were recorded.

Results and discussion

Probe **P1**, which is depicted in **Scheme 1**, consists of spherical gold nanoparticles functionalized with 4-(liponyloxy)-benzaldehyde (L1) and 4-mercaptophenyl boronic acid (L2), which are attached to the AuNPs' surface through the formation of stable Au–S bonds. L1 was prepared from lipoic acid and p-hydroxybenzaldehyde in the presence of N,N'-dicyclohexylcarbodiimide (DCC) and 4-dimethylaminopyridine (DMAP) with an overall 86% yield (**Scheme S1**). The bifunctionalized AuNPs were prepared as follows: first citrate-capped AuNPs were synthesized by reduction of chloroauric acid with sodium citrate in boiling water, following the Turkevich-Frens method.^{44–46} Then, citrate was displaced from the surface of the nanoparticles, in a ligand exchange reaction, by the addition of L1 and L2 (1:1 molar ratio). A repeated process of centrifugation, elimination of the supernatants, and redispersion in water yielded probe **P1**.

In order to characterize **P1**, transmission electron microscopy (TEM), dynamic light scattering (DLS), Fourier transform infrared spectroscopy (FTIR), inductively coupled plasma mass spectrometry (ICP-MS), and UV–vis spectroscopy measurements were performed. Monodisperse AuNPs with an average size of 14 ± 2 nm were observed by TEM (**Figure S2**). The hydrodynamic diameter of nanoparticles, determined by DLS, increased from 16.7 nm for the citrate stabilized AuNPs to 20.5 nm for the bifunctionalized AuNPs **P1** (**Figure S3A**). The double molecular functionalization was confirmed by FTIR spectra, which showed the presence of absorption bands corresponding to L1 and L2 (**see Figure S5**). Finally, the amount of ligands L1 and L2 per gold nanoparticle was calculated from ICP-MS studies (Boron and Sulfur) resulting in ca. 1400 and 930 molecules, respectively, corresponding to a L1/L2 molar ratio of 1.5:1 (**Table S1**). The aqueous suspensions of **P1** presented the characteristic red wine color and their UV–vis spectrum showed the presence of an intense SPR peak at 523 nm, typical of AuNPs with an average size smaller than 30 nm.^{47,48} A final concentration of the **P1** nanoparticles of ca. 8.12×10^{-10} M was calculated from their UV–vis spectra,

considering a molar extinction coefficient $\epsilon = 3.15 \times 10^8 \text{ M}^{-1} \text{ cm}^{-1}$.⁴⁹ The suspensions of **P1** were stored in the refrigerator until their use. No changes in the characteristic SPRB or in the color of the solutions were observed after more than 3 weeks, which is evidence of the good stability of **P1**. Before starting the sensing studies with **P1**, a preliminary ^1H NMR study of a mixture of NE and 4-methoxybenzaldehyde in MeOH/H₂O at room temperature confirmed the reaction of the aromatic aldehyde with the aminoalcohol group of NE (see **Figure S17**). The sensing capability of probe **P1** to NE was evaluated in buffered aqueous solution at pH 6.5 (phosphate, 10 mM) because a preliminary screening showed that this pH gave the best results. Thus, when NE (1000 μM) was added to a red-colored suspension of **P1**, a clear color change, from red to blue, was rapidly observed, and indicated the aggregation of the gold nanoparticles. A remarkable shift of the SPRB from 523 to 621 nm was observed in the UV-vis absorption spectrum (see **Figure 1**) due to aggregation-induced interparticle plasmon coupling.

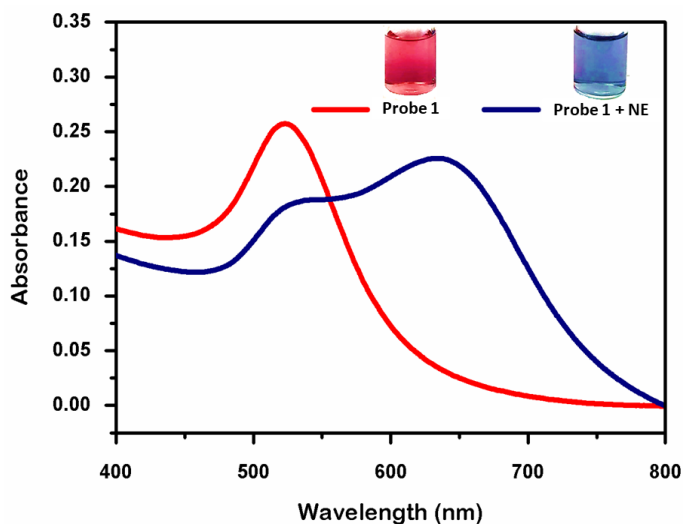


Figure 1. The UV-Vis spectra of **P1** in the absence (red) and in the presence (blue) of NE (1000 μM) (pH 6.5 phosphate buffer, 10 mM).

Aggregation of nanoparticles was also confirmed by TEM (**Figure S2A and B**) and DLS. The DLS studies showed an increase in the hydrodynamic diameter of the nanoparticles from 20.51 nm for **P1** to 658.8 nm after the addition of NE (**Figure**

S3B). Moreover, the zeta potential lowered from -28 mV (**P1**) to -12 mV (**P1+NE**) due to the reaction of the recognition moieties with the neurotransmitter and to the aggregation of the nanoparticles (see **Figure S4**). The kinetic studies showed a marked increase in the absorbance of **P1** at 621 nm after the addition of NE at minute 1, reaching its maximum point in around 5 min (**Figure S6**).

The selectivity of **P1** toward NE versus other similar neurotransmitters, such as dopamine (DA), and epinephrine (Epi), and other biomolecules, e.g., 5-hydroxyindoleacetic acid (5-HIAA, the main metabolite of serotonin in urine), Ltyrosine (L-Tyr, precursor of some stimulatory neurotransmitters), glucose (Glc), uric acid (UA, a potential neurotransmitter), lysine (Lys), and glutamic acid (GA, excitatory amino acid) was also evaluated. Upon the addition of these potential interferences to the suspension of **P1**, negligible changes in the color or in the A_{621}/A_{523} ratio (A_{621} = absorbance at 621 nm, A_{523} = absorbance at 523 nm) of the solutions were observed (**Figures 2 and S7, S8**). Finally, a competitive experiment was performed to evaluate the response of **P1** in a mixture containing NE and DA, Epi, L-Tyr, Glc, UA, Lys, and GA ($1000 \mu\text{M}$ of each). As shown in **Figure 2b**, a similar response to that found for **P1** in the presence of NE alone was observed.

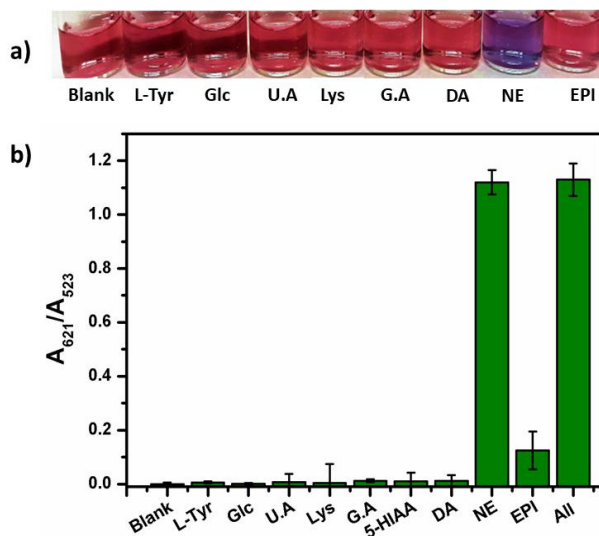


Figure 2. Response of probe **P1** in the presence of relevant biomolecules ($1000 \mu\text{M}$) at pH 6.5 (phosphate buffer, 10 mM). a) Observed colour changes. b) Representation of A_{621}/A_{523} for NE, the interferences and a mixture of all.

The stability of **P1** and its selectivity to NE remained almost unchanged within the 6.5–7.5 pH range (see **Figure S9**). We attribute this higher selectivity of the probe toward NE versus other similar catecholamines such as DA and Epi, to the presence of the aminoalcohol group in NE, which allows the formation of a highly stable oxazolidine upon reaction with the aromatic aldehyde attached to the gold nanoparticles. Imine formation is highly unfavorable in water and this would explain the fact that we did not observe aggregation in the presence of DA, which lacks of the hydroxyl group. On the other hand, the lower response of the probe toward Epi under the tested reaction conditions could be a kinetic effect due to the presence of the methyl group attached to the nitrogen atom. In fact, as observed in **Figure 2**, epinephrine also produces some aggregation of the nanoparticles, although to a much lesser extent.

Additionally, control experiments with citrate-capped AuNPs and with AuNPs modified only with L1 (L1-AuNPs) or with L2 (L2-AuNPs) (see **Supporting Information for details**) were also performed. We observed the aggregation of the citrate-AuNPs in the presence of excess of all the catecholamines (1000 μM),⁵⁰ whereas negligible changes in the color or in the A_{621}/A_{523} ratio of the solutions were observed upon the addition of an excess of NE, EPI, or DA to the suspensions of L1-AuNPs or L2-AuNPs. Finally, the response observed in the A_{621}/A_{523} ratio for an equimolecular mixture of L1-AuNPs and L2-AuNPs in the presence of NE (100 μM) was much lower than that observed in the presence of **P1** (see **Supporting Information, Figure S13**).

In order to evaluate the sensitivity of probe **P1**, UV–vis titration experiments were performed in the presence of increasing amounts of NE. As observed in **Figure 3a**, the addition of NE to an aqueous suspension of **P1** induced a gradual color modulation that went from clear red to purple, and finally to blue. The corresponding bathochromic shift of the SPRB of **P1** with increasing NE concentrations was also observed in the corresponding UV–vis spectra (see **Figure 3b**), and can be attributed to the analyte-induced aggregation of nanoparticles.

From the A_{621}/A_{523} vs the NE concentration plot, a LOD of 1.16 μM was determined (Figure 4b curve 2 and Figure S14).

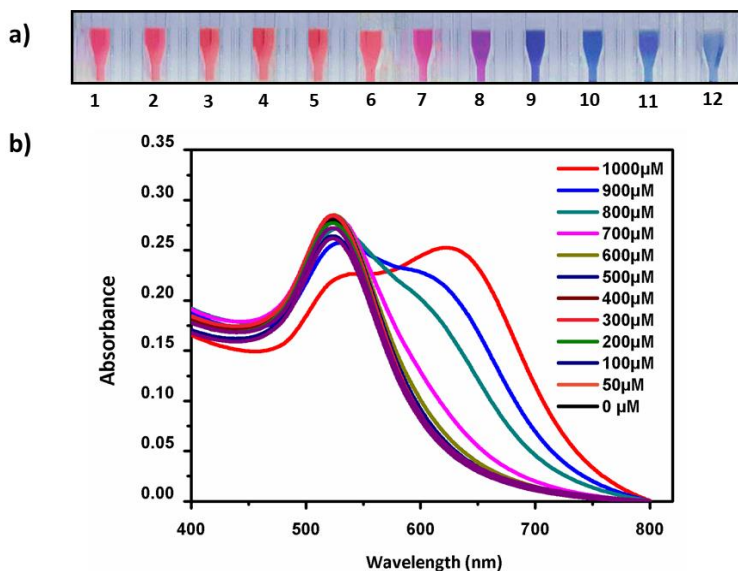


Figure 3. a) Color modulation of P1 when NE was added at the 0, 50, 100, 200, 300, 400, 500, 600, 700, 800, 900 and 1000 μM concentrations (1-12, respectively). b) Changes in the UV-Vis spectra of P1 upon addition of NE at 0, 50, 100, 200, 300, 400, 500, 600, 700, 800, 900 and 1000 μM concentrations at pH 6.5 (phosphate buffer, 10 mM).

As shown in **Figure 4a**, a slight linear increase in the A_{621}/A_{523} ratio with increasing NE concentrations was observed within the 0–500 μM concentration range. Interestingly, a much more marked intensity increase was observed within the 500–1200 μM concentration range. This fact allowed improvement of the sensitivity to NE detection by simply adding a certain fixed amount of NE to the stock solution of **P1** immediately before use.³⁸ Thus, an optimized probe (**OP1**) was prepared by adding 500 μM of NE to the **P1** solution in advance. As observed in the A_{621}/A_{523} vs the NE concentration plot for **OP1** (**Figure 4b**, curve 1), sensitivity is greater than it is for **P1**. From this plot, a LOD of 0.07 μM could be determined (see **Figure S15**). This low LOD of **OP1** is indicative of the remarkable sensitivity of the optimized probe, conferring the system the possibility of detecting NE at relevant clinical concentrations.

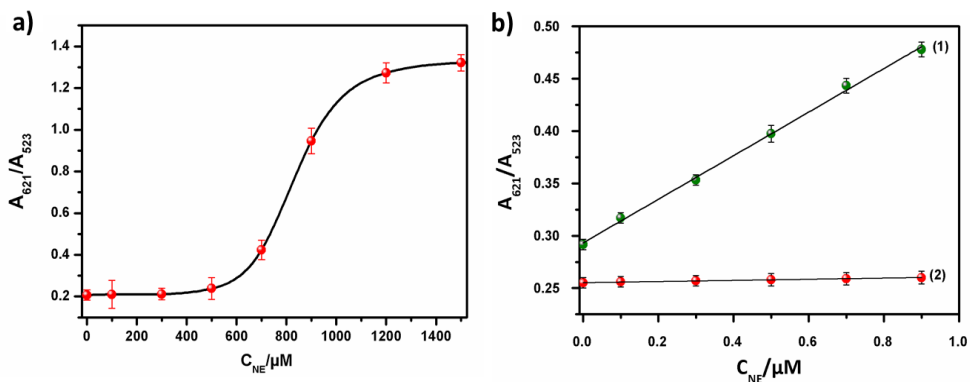


Figure 4. a) Plot of A_{621}/A_{523} versus NE concentration (0-1500 μM) obtained with **P1**. b) Linear plots of A_{621}/A_{523} versus the NE concentration obtained with (1) **OP1** and (2) **P1**.

The normal range for NE in healthy individuals is 0.08 to 0.47 μM in urine. Reported studies determined that higher NE levels could be indicative of pheochromocytoma and paraganglioma tumours.⁵¹ Given the interest in the determination of NE concentration in urine, we decided to test the response of **OP1** in this highly competitive media.⁵² **OP1** in urine showed a similar behavior to that described before in aqueous media upon the addition of increasing concentrations of NE (**See Figure S16**). The plot of A_{621}/A_{523} vs NE concentration in urine shows a linear response within the 0–1 μM concentration range (**see Figure 5**). The determined LOD in this medium was 0.09 μM , which falls within the normal range for adults of 0.08 to 0.4 μM in urine.⁵¹

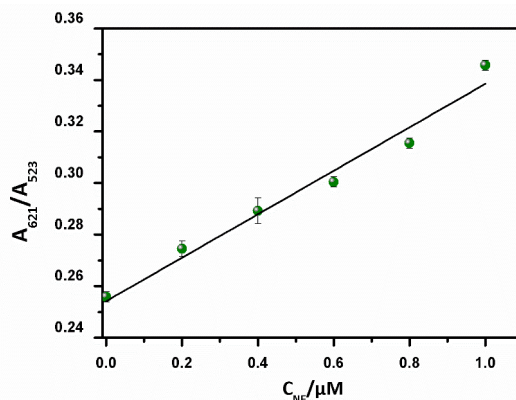


Figure 5. Linear plot of A_{621}/A_{523} versus the NE concentration obtained with **OP1** in urine samples

Conclusions

In short, we have developed a new approach for the selective and sensitive colorimetric detection of NE using bifunctionalized gold nanoparticles based on a double recognition process. Probe **P1**, consisting of AuNPs functionalized with boronic acid and aldehyde-terminated ligands, selectively reacted with the catechol group and the aminoalcohol moiety of NE in aqueous buffered solution, and led to nanoparticle aggregation. This resulted in a remarkable color change in the solution from red to blue, and the appearance of a new absorption band at 621 nm in the UV–vis spectrum. Due to this double interaction, **P1** showed excellent selectivity to NE, whereas almost no response of the probe was observed for similar neurotransmitters (dopamine and epinephrine) or selected biomolecules (5-hydroxyindoleacetic acid, L-tyrosine, glucose, uric acid, lysine, and glutamic acid). An optimized probe (**OP1**) was prepared by adding a certain fixed amount of NE to the probe before using it. **OP1** showed a linear response to NE within the 0–1 μM range in buffered water at pH 6.5, with a calculated LOD of 0.07 μM . A similar response to NE in synthetic urine could be observed, with a LOD in this medium of 0.09 μM . To conclude, our system allows the rapid, cheap, selective, and sensitive detection of NE by overcoming some of the limitations of current methods. We think that our findings could help with early diagnosis of diseases such as pheochromocytoma or paraganglioma for which NE is an important biomarker.

Acknowledgments

Financial support from the Spanish Government (Projects MAT2015-64139-C4-1-R and MAT2015-64139-C4-4-R) and the Generalitat Valencia (Projects PROMETEOII/2014/047 and AICO/2017/093) is gratefully acknowledged. T. Godoy-Reyes is grateful to the Generalitat Valenciana for her Santiago Grisolia fellowship. SCSIE (Universitat de València) is gratefully acknowledged for all the equipment employed.

References

1. Nakane, H.; Shimizu, N.; Hori, T. Stress-Induced Norepinephrine Release in the Rat Prefrontal Cortex Measured by Microdialysis. *Am. J. Physiol. Regul. Integr. Comp. Physiol.* **1994**, *267*, R1559–R1566.
2. Simeon, D.; Knutelska, M.; Smith, L.; Baker, B. R.; Hollander, E. A Preliminary Study of Cortisol and Norepinephrine Reactivity to Psychosocial Stress in Borderline Personality Disorder with high and low Dissociation. *Psychiatry Res.* **2007**, *149*, 177–184.
3. Spivak, B.; Vered, Y.; Graff, E.; Blum, I.; Mester, R.; Weizman, A. Low Platelet-poor Plasma Concentrations of Serotonin in Patients with Combat-related Posttraumatic Stress Disorder. *Biol. Psychiatry* **1999**, *45*, 840–845.
4. Goddard, A. W.; Ball, S. G.; Martinez, J.; Robinson, M. J.; Yang, C. R.; Russell, J. M.; Shekhar, A. Current Perspectives of the Roles of the Central Norepinephrine System in Anxiety and Depression. *Depression Anxiety* **2010**, *27*, 339–350.
5. Hunsley, M. S.; Palmiter, R. D. Norepinephrine-Deficient Mice Exhibit Normal Sleep-wake States but have Shorter Sleep Latency after Mild stress and low Doses of Amphetamine. *Sleep* **2003**, *26*, 521–526.
6. Murchison, C. F.; Zhang, X. Y.; Zhang, W. P.; Ouyang, M.; Lee, A.; Thomas, S. A. A Distinct Role for Norepinephrine in Memory Retrieval. *Cell* **2004**, *117*, 131–143.
7. Jansen, A. S.; Nguyen, X.; Karpitskiy, V.; Mettenleiter, T. C.; Loewy, A. D. Central Command Neurons of the Sympathetic Nervous System: Basis of the Fight-or-Flight Response. *Science* **1995**, *270*, 644–646.
8. Takenaka, M. C.; Araujo, L. P.; Maricato, J. T.; Nascimento, V. M.; Guerreschi, M. G.; Rezende, R. M.; Quintana, F. J.; Basso, A. S. Norepinephrine Controls Effector T Cell Differentiation through β 2- Adrenergic Receptor-Mediated Inhibition of NF- κ B and AP-1 in Dendritic Cells. *J. Immunol.* **2016**, *196*, 637–644.
9. Jobe, P. C.; Dailey, J. W.; Wernicke, J. F. A Noradrenergic and Serotonergic Hypothesis of the Linkage between Epilepsy and Affective Disorders. *Crit. Rev. Neurobiol.* **1999**, *13*, 317–356.
10. Nutt, D. J. The Role of Dopamine and Norepinephrine in Depression and Antidepressant Treatment. *J. Clin Psychiatry* **2006**, *67*, 3–8.
11. Chalermphanupap, T.; Kinkead, B.; Hu, W. T.; Kummer, M. P.; Hammerschmidt, T.; Heneka, M. T.; Weinschenker, D.; Levey, A. I. Targeting

- Norepinephrine in Mild Cognitive Impairment and Alzheimer's Disease. *Alzheimer's Res. Ther.* **2013**, 5, 21–29.
12. Delaville, C.; De Deurwaerdère, P.; Benazzouz, A. Noradrenaline and Parkinson's Disease. *Front. Syst. Neurosci.* **2011**, 5, 31–42.
 13. Higashi, Y.; Sasaki, S.; Nakagawa, K.; Kimura, M.; Sasaki, S.; Noma, K.; Matsuura, H.; Hara, K.; Goto, C.; Oshima, T.; Chayama, K. Excess Norepinephrine Impairs both Endothelium-Dependent and- Independent Vasodilation in Patients with Pheochromocytoma. *Hypertension* **2002**, 39, 513–518.
 14. Kantorovich, V.; Pacak, K. Pheochromocytoma and Paraganglioma. *Prog. Brain Res.* **2010**, 182, 343–373.
 15. Walther, M. M.; Keiser, H. R.; Linehan, W. M. Pheochromocytoma: Evaluation, Diagnosis, and Treatment. *World J. Urol.* **1999**, 17, 35–39.
 16. Cole, S. W.; Korin, Y. D.; Fahey, J. L.; Zack, J. A. Norepinephrine Accelerates HIV Replication via Protein Kinase A-Dependent Effects on Cytokine Production. *J. Immunol.* **1998**, 161, 610–616.
 17. Kanamori, T.; Funatsu, T.; Tsunoda, M. Determination of Catecholamines and Related Compounds in Mouse Urine using Column-Switching HPLC. *Analyst* **2016**, 141, 2568–2573.
 18. Liu, L.; Li, Q.; Li, N.; Ling, J.; Liu, R.; Wang, Y.; Sun, L.; Chen, X. H.; Bi, K. Simultaneous Determination of Catecholamines and their Metabolites Related to Alzheimer's Disease in Human Urine. *J. Sep. Sci.* **2011**, 34, 1198–1204.
 19. Karim, M. M.; Alam, S. M.; Lee, S. H. Spectrofluorimetric Estimation of Norepinephrine using Ethylenediamine Condensation Method. *J. Fluoresc.* **2007**, 17, 427–436.
 20. Wei, F.; Xu, G.; Wu, Y.; Wang, X.; Yang, J.; Liu, L.; Hu, Q. Molecularly Imprinted Polymers on Dual-Color Quantum Dots for Simultaneous Detection of Norepinephrine and Epinephrine. *Sens. Actuators, B* **2016**, 229, 38–46.
 21. Samdani, K. J.; Samdani, J. S.; Kim, N. H.; Lee, J. H. FeMoO₄ based, Enzyme-Free Electrochemical Biosensor for Ultrasensitive Detection of Norepinephrine. *Biosens. Bioelectron.* **2016**, 81, 445–453.
 22. Łuczak, T. Determination of Norepinephrine Alone and in the Presence of Ascorbic and Uric Acids Using a Gold Electrode Modified with Gold Nanoparticles and Self-Assembled Layers of meso-2,3- Dimercaptosuccinic Acid. *Electroanalysis* **2014**, 26, 1461–1470.
 23. Kalimuthu, P.; Abraham John, S. Selective Determination of Norepinephrine in the Presence of Ascorbic and Uric Acids using an Ultrathin Polymer Film Modified Electrode. *Electrochim. Acta* **2011**, 56, 2428–2432.

24. Santos-Figueroa, L. E.; Moragues, M. E.; Climent, E.; Agostini, A.; Martínez-Mañez, R.; Sancenón, F. Chromogenic and Fluorogenic Chemosensors and Reagents for Anions. A Comprehensive Review of the years 2010–2011. *Chem. Soc. Rev.* **2013**, *42*, 3489–3613.
25. Baron, R.; Zayats, M.; Willner, I. Dopamine-, L-DOPA-, Adrenaline-, and Noradrenaline-Induced Growth of Au Nanoparticles: Assays for the Detection of Neurotransmitters and of Tyrosinase Activity. *Anal. Chem.* **2005**, *77*, 1566–1571.
26. Zhu, M.; Huang, X.; Li, J.; Shen, H. Peroxidase-Based Spectrophotometric Methods for the Determination of Ascorbic Acid, Norepinephrine, Epinephrine, Dopamine and Levodopa. *Anal. Chim. Acta* **1997**, *357*, 261–267.
27. Secor, K. E.; Glass, T. E. Selective Amine Recognition: Development of a Chemosensor for Dopamine and Norepinephrine. *Org. Lett.* **2004**, *6*, 3727–3730.
28. Zhu, S.; Yang, J.; Zhao, X. E.; Kong, R.; Wang, H.; You, J. Simple and Fast Determination of Catecholamines in Pharmaceutical Samples using Ag^+ -3,3',5,5'-tetramethylbenzidine as a Colorimetric Probe. *Anal. Methods* **2015**, *7*, 6785–6790.
29. Jafarinejad, S.; Ghazi-Khansari, M.; Ghasemi, F.; Sasanpour, P.; Hormozi-Nezhad, M. R. Colorimetric Fingerprints of Gold Nanorods for Discriminating Catecholamine Neurotransmitters in Urine Samples. *Sci. Rep.* **2017**, *7*, 8266–8273.
30. Menon, S.; Jose, A. R.; Jesny, S.; Kumar, K. G. A colorimetric and Fluorometric Sensor for the Determination of Norepinephrine. *Anal. Methods* **2016**, *8*, 5801–5805.
31. Saha, K.; Agasti, S. S.; Kim, C.; Li, X.; Rotello, V. M. Gold Nanoparticles in Chemical and Biological Sensing. *Chem. Rev.* **2012**, *112*, 2739–2779.
32. Mayer, K. M.; Hafner, J. H. Localized Surface Plasmon Resonance Sensors. *Chem. Rev.* **2011**, *111*, 3828–3857.
33. Wang, R.; Wang, R.; Ge, B.; Jia, X.; Li, Z.; Chang, J. Spectral Method Determination of Kanamycin Sulfate using both Gold Nanoparticles and Quantum Dots. *Anal. Methods* **2013**, *5*, 5302–5308.
34. Rawat, K. A.; Bhamore, J. R.; Singhal, R. K.; Kailasa, S. K. Microwave Assisted Synthesis of Tyrosine Protected Gold Nanoparticles for dual (Colorimetric and Fluorimetric) detection of Spermine and Spermidine in Biological Samples. *Biosens. Bioelectron.* **2017**, *88*, 71–77.

35. Martí, A.; Costero, A. M.; Gaviña, P.; Parra, M. Selective Colorimetric NO (g) Detection based on the use of Modified Gold Nanoparticles using Click Chemistry. *Chem. Commun.* **2015**, 51, 3077–3079.
36. Rohit, J. V.; Kailasa, S. K. Simple and Selective Detection of Pendimethalin Herbicide in Water and Food Samples based on the Aggregation of Ractopamine-Dithiocarbamate Functionalized Gold Nanoparticles. *Sens. Actuators, B* **2017**, 245, 541–550.
37. Chen, L.; Lu, W.; Wang, X.; Chen, L. A Highly Selective and Sensitive Colorimetric Sensor for Iodide Detection based on Anti- Aggregation of Gold Nanoparticles. *Sens. Actuators, B* **2013**, 182, 482–488.
38. Kong, B.; Zhu, A.; Luo, Y.; Tian, Y.; Yu, Y.; Shi, G. Sensitive and Selective Colorimetric Visualization of Cerebral Dopamine based on Double Molecular Recognition. *Angew. Chem.* **2011**, 123, 1877–1880.
39. Godoy-Reyes, T. M.; Llopis-Lorente, A.; Costero, A. M.; Sancenón, F.; Gaviña, P.; Martínez-Máñez, R. Selective and Sensitive Colorimetric Detection of the Neurotransmitter Serotonin based on the Aggregation of Bifunctionalized Gold Nanoparticles. *Sens. Actuators, B* **2018**, 258, 829–835.
40. Agami, C.; Rizk, T. Role of Solvent on the Diastereoselectivity of Oxazolidine Formation from (–)-Ephedrine. *J. Chem. Soc., Chem. Commun.* **1983**, 0, 1485–1486.
41. Juhász, M.; Lázár, L.; Fülöp, F. Substituent Effects in the Ring- Chain Tautomerism of 4-Alkyl 2-aryl substituted Oxazolidines and Tetrahydro-1,3-oxazines. *J. Heterocycl Chem.* **2007**, 44, 1465–1473.
42. Freeman, R.; Elbaz, J.; Gill, R.; Zayats, M.; Willner, I. Analysis of Dopamine and Tyrosinase Activity on Ion-Sensitive Field-Effect Transistor (ISFET) Devices. *Chem. - Eur. J.* **2007**, 13, 7288–7293.
43. Wu, W.; Zhu, H.; Fan, L.; Liu, D.; Renneberg, R.; Yang, S. Sensitive Dopamine Recognition by Boronic Acid Functionalized Multi-Walled Carbon Nanotubes. *Chem. Commun.* **2007**, 23, 2345–2347.
44. Zhao, P.; Li, N.; Astruc, D. State of the Art in Gold Nanoparticle Synthesis. *Coord. Chem. Rev.* **2013**, 257, 638–665.
45. Turkevich, J.; Stevenson, P. C.; Hillier, J. A Study of the Nucleation and Growth Processes in the Synthesis of Colloidal Gold. *Discuss. Faraday Soc.* **1951**, 11, 55–75.
46. Frens, G. Controlled Nucleation for the Regulation of the Particle Size in Monodisperse Gold Suspensions. *Nature, Phys. Sci.* 1973, 241, 20–22.
47. Haiss, W.; Thanh, N. T. K.; Aveyard, J.; Fernig, D. G. Determination of Size and Concentration of Gold Nanoparticles from UV– Vis Spectra. *Anal. Chem.* **2007**, 79, 4215–4221.

48. Lin, S.-Y.; Tsai, Y.-T.; Chen, C.-C.; Lin, C.-M.; Chen, C.-H. Two-step Functionalization of Neutral and Positively Charged Thiols onto Citrate-Stabilized Au Nanoparticles. *J. Phys. Chem. B* **2004**, 108, 2134–2139.
49. Liu, X.; Atwater, M.; Wang, J.; Huo, Q. Extinction Coefficient of Gold Nanoparticles with Different Sizes and Different Capping Ligands. *Colloids Surf., B* **2007**, 58, 3–7.
50. Zhang, Y.; Li, B.; Chen, X. Simple and Sensitive Detection of Dopamine in the presence of High Concentration of Ascorbic Acid using Gold Nanoparticles as Colorimetric Probes. *Microchim. Acta* **2010**, 168, 107–113.
51. Fischbach, F. T.; Dunning, M. B. *A Manual of Laboratory and Diagnostic Tests*, 8th ed.; Walters Kluwer Health/Lippincott Williams & Wilkins, 2009.
52. Cerilliant Analytical Reference Standards, https://www.cerilliant.com/shoponline/Item_Details.aspx?itemno=1cedba31-c7f4-4ab1-ba9f-a02f3328d204&item=S-020 (accessed May 2018).

Supporting Information

• *Chemicals and general procedures*

Chloroauric acid ($\text{HAuCl}_4 \cdot 3\text{H}_2\text{O}$), sodium citrate dihydrate, 4-mercatophenylboronic acid (MBA), (\pm)- α -lipoic acid, 4-hydroxybenzaldehyde, 4-methoxybenzaldehyde, $\text{N,N}'$ -dicyclohexylcarbodiimide (DCC), 4-dimethylaminopyridine (DMAP), DL-norepinephrine hydrochloride (NE), 5-hydroxyindole-3-acetic acid (5-HIAA), L-tyrosine (L-Tyr), glucose (Glc), uric acid (U.A), L-lysine (Lys), glutamic acid (G.A), dopamine (DA), epinephrine (Epi) and SurineTM Negative Urine Control (rugged non-biological urine with constituents that mimic human urine, but without human urine's research impediments) were obtained from Sigma Aldrich, and were used without further purification. All the aqueous solutions were prepared with Milli-Q water ($18.2 \text{ M}\Omega \text{ cm}^{-1}$).

UV-Vis absorption spectra were recorded in a Shimadzu UV-2101PC spectrophotometer using a 1 cm path length quartz cuvette. All measurements were performed at room temperature. High-resolution transmission electron microscopy (JEOL-1010 transmission electron microscopy operating at 100 kV) and dynamic light scattering (Malvern Zetasizer ZS) were used to determine the size, hydrodynamic diameter and zeta potential values of **P1** and confirm the NE induced aggregation of the gold nanoparticles. Inductively coupled plasma mass spectrometry (ICP-MS) was used in order to quantify the amount of L1 and L2 per gold nanoparticle. The equipment employed was an Agilent 7900 ICP-MS with a standard sample introduction system consisting of a MicroMist nebulizer pump and Scott type spray chamber. The FT-IR spectra were recorded with a Cary 630 FT-IR spectrometer within the wavenumber range of $648\text{--}4000 \text{ cm}^{-1}$. ^1H -NMR and ^{13}C -NMR spectra were recorded by a Bruker DRX-300 Spectrometer (300 MHz, 128 scans). Chemical shifts are reported in ppm using tetramethylsilane as an internal standard. High resolution mass spectra were recorded in the positive ion mode using a VG-AutoSpec mass spectrometer.

• Synthesis

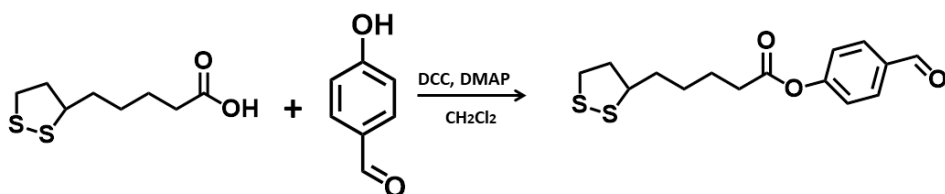
Citrate-capped AuNPs

Citrate-stabilized AuNPs of ca. 14 nm diameter were synthesized by the reduction of chloroauric acid with sodium citrate in boiling water. Briefly, an aqueous solution of trisodium citrate (13.6 mM, 5 mL) was added to an aqueous boiling solution of HAuCl₄ (0.23 mM, 95 mL) and the solution was gently refluxed for 30 min yielding a red solution. This solution of citrate-capped AuNPs was cooled at room temperature, and filtered through a 0.22 μm membrane. The suspension of citrate-capped AuNPs was stored in the fridge at 4°C, in order to keep them at a constant temperature, and remained stable for several weeks.

Synthesis of 4-(liponyloxy)benzaldehyde (L1)

L1 was synthesized in 86 % yield from lipoic acid 0.75 g, 3.63 mmol), 4-hydroxybenzaldehyde (0.44 g, 3.63 mmol), DCC (0.75 g, 3.63 mmol) and a catalytic amount of DMAP in anhydrous CH₂Cl₂ (10 mL) as previously reported¹

¹H NMR (300 MHz, CDCl₃) δ 9.98 (s, 1H), 7.91 (d, J = 9.0, 2H), 7.26 (d, J = 9.0, 2H), 3.61–3.57 (m, 1H), 3.22 – 3.09 (m, 2H), 2.60 (t, J = 7.4 Hz, 2H), 2.51 – 2.42 (m, 1H), 1.97 – 1.88 (m, 1H), 1.84 – 1.67 (m, 4H), 1.63 – 1.52 (m, 2H). ¹³C NMR (75 MHz, CDCl₃) δ 190.96, 171.71, 155.35, 134.39, 131.25, 122.51, 56.53, 40.51, 38.79, 34.94, 34.21, 28.64, 24.77. HRMS (ESI): m/z calcd. for C₁₅H₁₈O₃S₂ ([M+H]⁺): 310.43; 311.07 (100%) (See Figure S1)



Scheme S1. Synthesis of 4-(liponyloxy)benzaldehyde (L1)

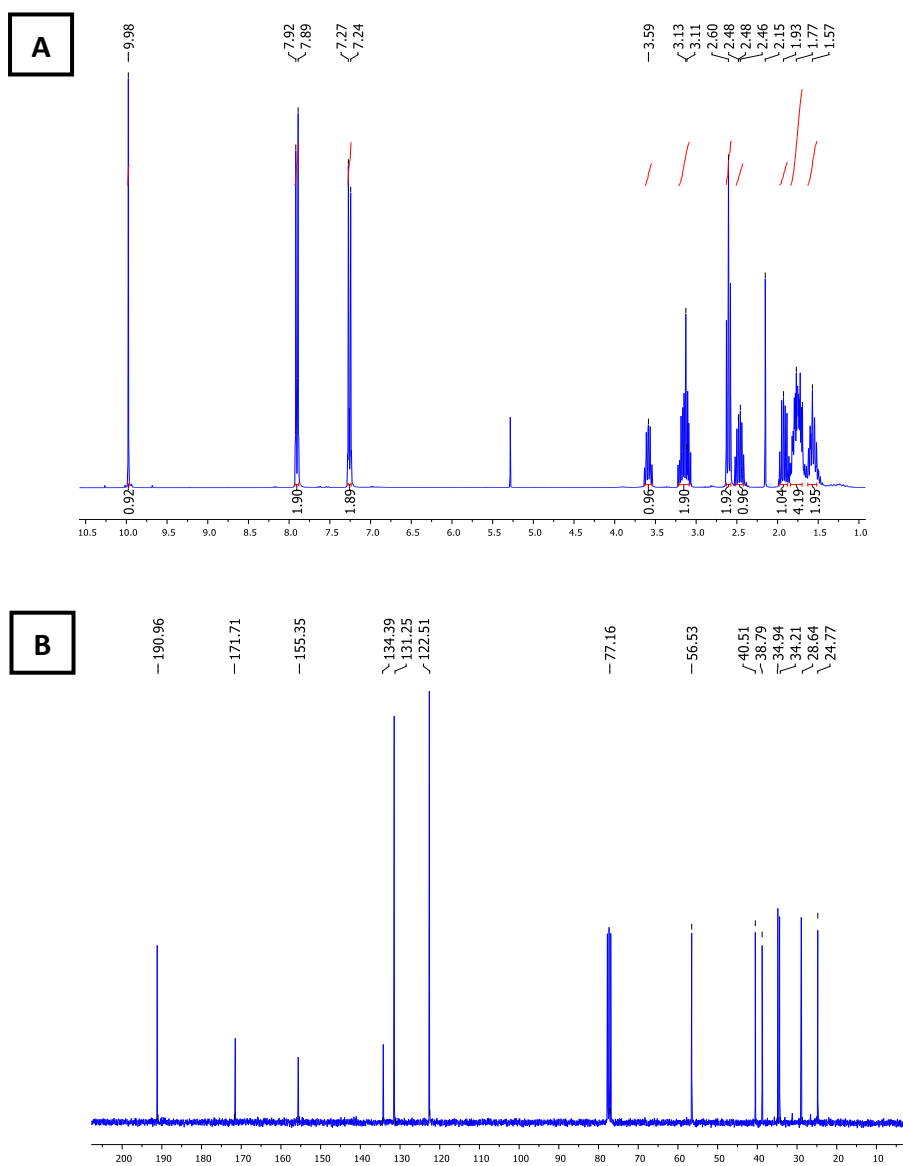


Figure S1: (A) ^1H NMR in CDCl_3 at 300 MHz. (B) ^{13}C NMR spectra of 4-(liponyloxy)benzaldehyde (L1) in CDCl_3 at 300 MHz.

- TEM images

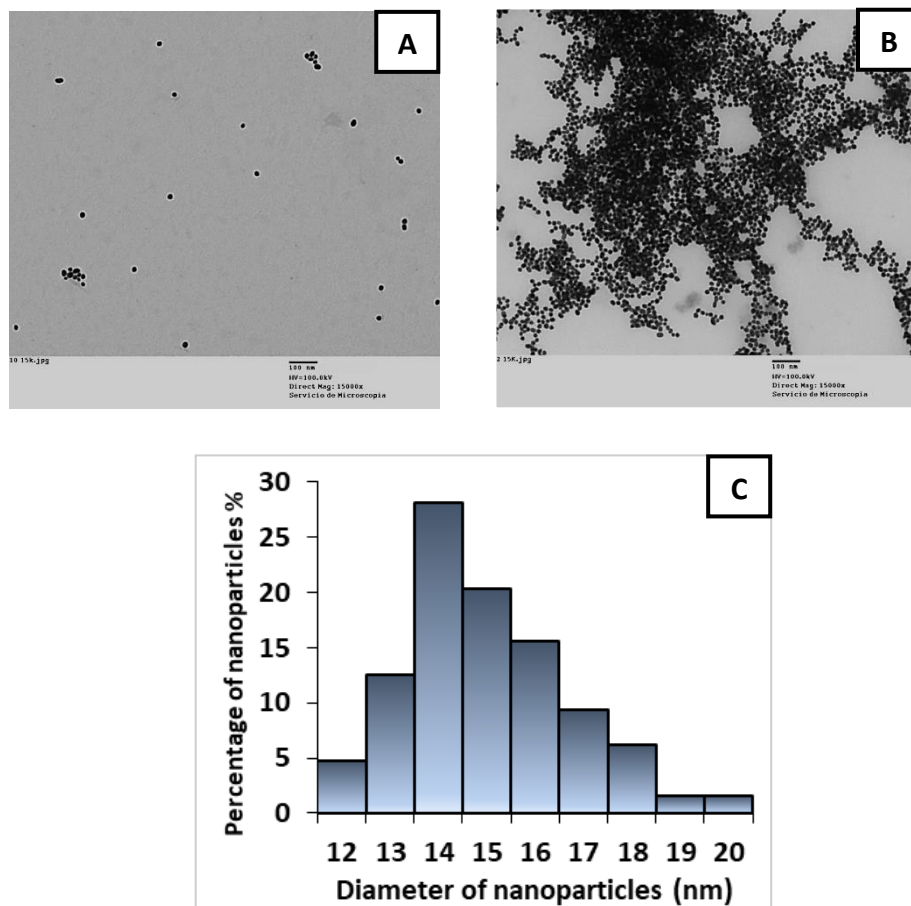


Figure S2. TEM images of **P1** (A) in the absence and (B) in the presence of NE (1000 μM) (C) Size distribution of **P1**. According to the size distribution, the diameter of **P1** is about 14 nm.

- **Dynamic Light Scattering (DLS) and Zeta potential studies**

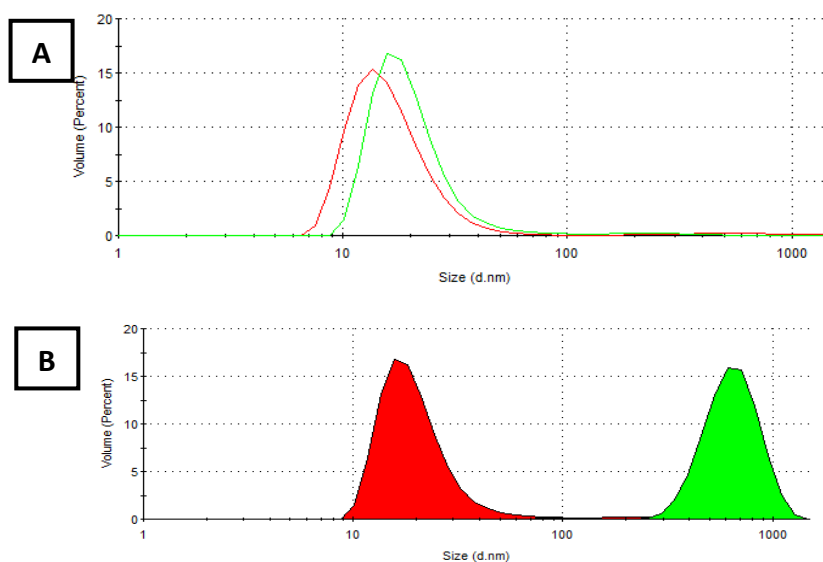


Figure S3. Hydrodynamic diameter of (A) citrate coated AuNPs (red $16.73\text{nm} \pm 7.68\text{ nm}$) and **P1** (green $20.51\text{ nm} \pm 10.56\text{ nm}$) (B) **P1** in the absence (red $20.51\text{ nm} \pm 10.56\text{ nm}$) and in the presence of NE ($1000\text{ }\mu\text{M}$) (green $658.8\text{ nm} \pm 186.6\text{ nm}$).

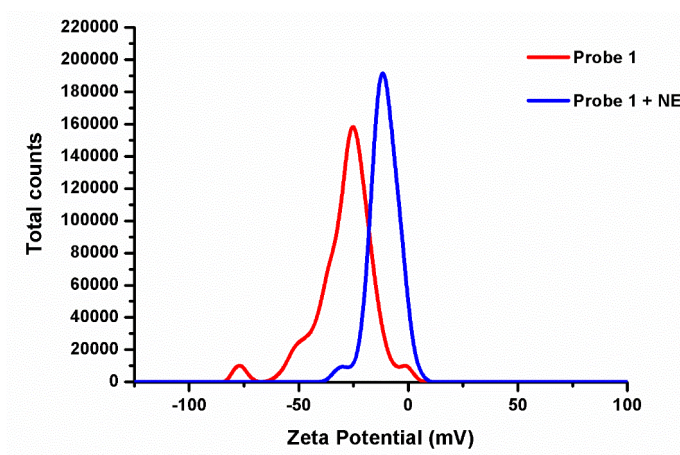


Figure S4. Zeta potential curves for **P1** (red, -28 mV) and **P1 + NE** (blue, -12 mV).

The relatively high zeta potential of the **P1** nanoparticles is clearly associated to the partial deprotonation of the functional boronic acid groups at the working pH conditions. Very low particle hydrodynamic diameters (around 20 nm) together

with a high density of negative charge at the surfaces evidently leads to a high interparticle repulsion. Then, under these conditions, a low aggregation is expected (practically negligible in our case where a certain concordance of particle size is achieved between TEM and DLS measurements) and high zeta potential result. The addition of the NE generates two phenomena that cooperatively lead to the zeta potential decrease: the effective decrease of negative charges as a result of the reaction of the neurotransmitter with the recognition units of **P1** and the aggregation of the original **P1** nanoparticles. In this case, the zeta potential measured for the **P1**+NE is due in a majority way to the residual (non compensated) negative charges of the functional groups in the outer surface of the large aggregates (ca. 659 nm). Lower negative charges and only restricted to the external surface of the large aggregates evidently diminish the zeta potential.

- **Fourier-transform infrared spectroscopy (FTIR)**

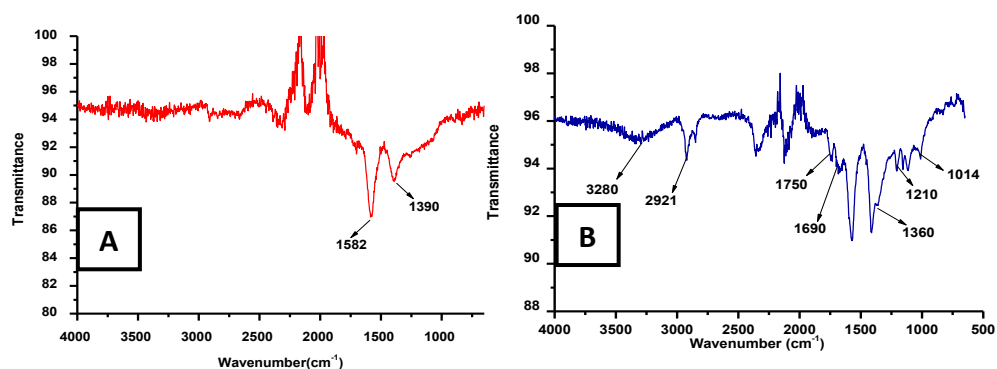


Figure S5. FT-IR spectra of (A) unmodified Au NPs and (B) **P1**. Whereas citrate bands (1390 and 1582 cm⁻¹) are observed in (A), L1 (C=O stretching at 1690 and 1750 cm⁻¹, C-O bending at 1210 cm⁻¹) and L2 (O-H, C-C, B-O and B-C bending at 3280, 2921, 1360, 1014 cm⁻¹ respectively) characteristic bands are observed in (B).

- **Inductively coupled plasma mass spectrometry (ICP-MS)**

Table S1. Determination of Au, B and S contained in $P1$ (6.57×10^{-9} M) by ICP-MS.

Description	Au (mg/L)	B ($\mu\text{g/L}$)	S ($\mu\text{g/L}$)
P1	121.3 ± 0.7	66.3 ± 0.9	806 ± 9

Based on the data obtained from the ICP-MS studies of **P1** (6.57×10^{-9} M), and considering that all B comes from L2 and S comes from L1 and L2, a L1/L2 molar ratio of ca. 1.5:1 was calculated. Given the concentration of the gold nanoparticles from UV-vis measurements, the calculated amount of L1 and L2 per gold nanoparticle was 1400 and 930 molecules respectively.

- **Kinetic studies**

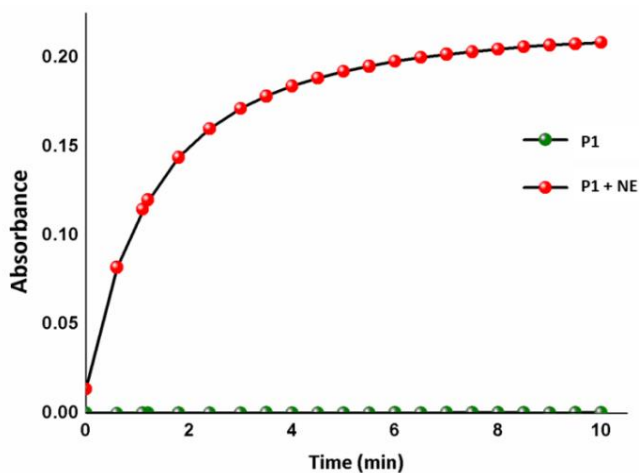


Figure S6. UV-Vis kinetic profiles of **P1** ($\lambda_{\text{Abs}} 621$ nm) in the absence (green) and in the presence of $800 \mu\text{M}$ of NE (red).

- *UV-Vis of interferences*

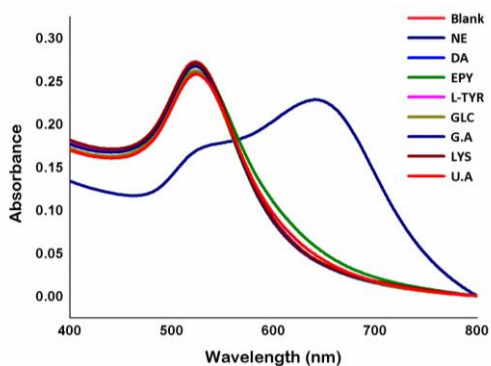


Figure S7. UV-Vis spectra of **P1** in the presence of 1000 μM of different neurotransmitters and biological molecules at pH 6.5 (phosphate buffer, 10 mM).

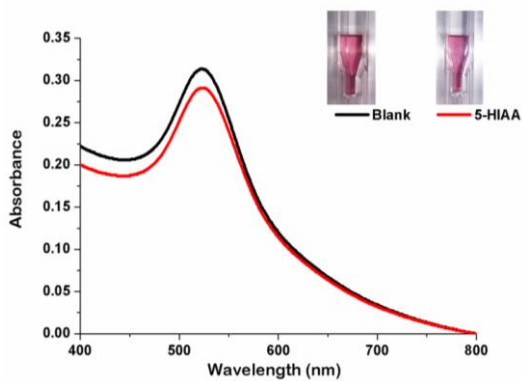


Figure S8. UV-Vis spectra of **P1** in the presence of 1000 μM of 5-HIAA at pH 6.5 (phosphate buffer, 10 mM).

- *pH response*

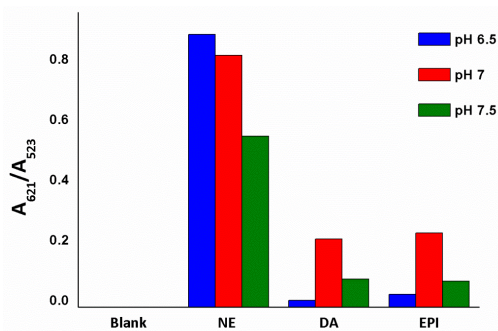


Figure S9. pH response of **P1**, in presence of NE, DA and EPI (500 μM).

• Synthesis of L1-AuNPs and L2-AuNPs

L1-AuNPs and L2-AuNPs were prepared from citrate-capped AuNPs by ligand-exchange reaction with L1 for L1-AuNPs and L2 for L2-AuNPs, which was performed as follows: 20 μL of L1 (0.5 mM in DMF) were added to 10 mL of the as-prepared citrate coated AuNPs and the solution was magnetically stirred for 1 h at room temperature. Then, the mixture was centrifuged for 6 min at 10,500 rpm and the supernatants were decanted and the nanoparticles redispersed in Milli-Q water ($18.2 \text{ M}\Omega \text{ cm}^{-1}$). The same procedure was followed for the preparation of L2-AuNPs from L2 and citrate-capped AuNPs.

• Characterization of L1-AuNPs and L2-AuNPs

Table S2. Characterization of L1-AuNPs and L2-AuNPs by DLS and Zeta Potential

AuNPs	DLS(nm)	ZETA POTENTIAL (mV)
L1-AuNPs	20.24	-23.0
L2-AuNPs	20.74	-25.1

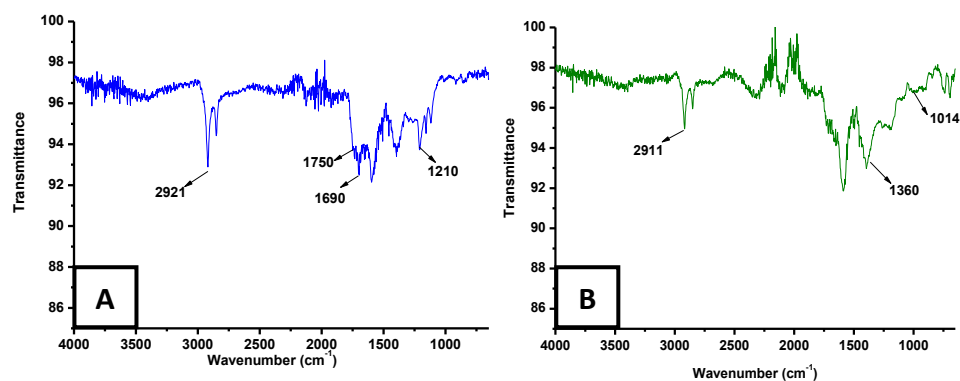


Figure S10. FT-IR spectra of (A) L1-AuNPs (B) L2-AuNPs. Whereas L1-AuNPs bands (C=O at 1690 and 1750 cm^{-1} , C-O bending at 1210 cm^{-1}) are observed in (A), L2-AuNPs (C-C, B-O and B-C bending at 2911, 1360, 1014 cm^{-1} respectively) characteristic bands are observed in (B).

- **Colorimetric response of citrate-capped AuNPs, L1-AuNPs, L2-AuNPs and P1 in the presence of NE, EPI and DA**

Sensing studies with Citrate-AuNPs, L1-AuNPs and L2 in presence of NE, EPI and DA were performed as follow: 200 μL of the solution of **Citrate-AuNPs**, **L1-AuNPs** or **L2-AuNPs** and 200 μL of the corresponding catecholamine (2000 μM) were mixed to obtain a final volume of 400 μL . Samples were incubated for 5 min at room temperature before taking measurements in the spectrophotometer.

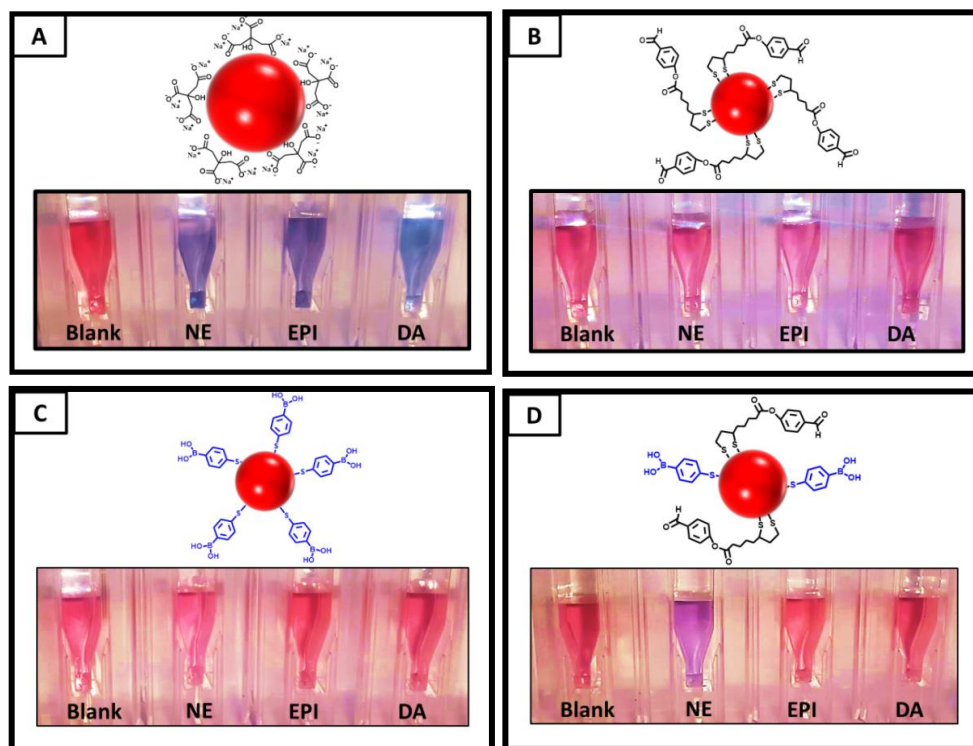


Figure S11. Response of **A.** Citrate-AuNPs, **B.** L1-AuNPs, **C.** L2-AuNPs and **D.** P1 in presence of NE, DA and EPI (1000 μM final concentration) at pH 6.5 (phosphate buffer, 10 mM).

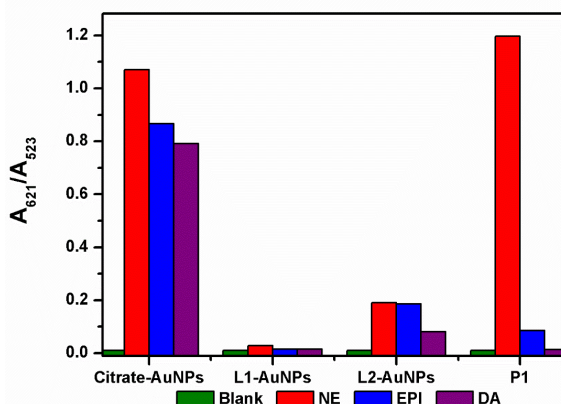


Figure S12. Representation of A_{621}/A_{523} of Citrate-AuNPs, L1-AuNPs, L2-AuNPs and P1 in presence of NE, DA and EPI (1000 μ M final concentration).

- **Determination of NE with a mixture of L1-AuNPs and L2-AuNPs.**

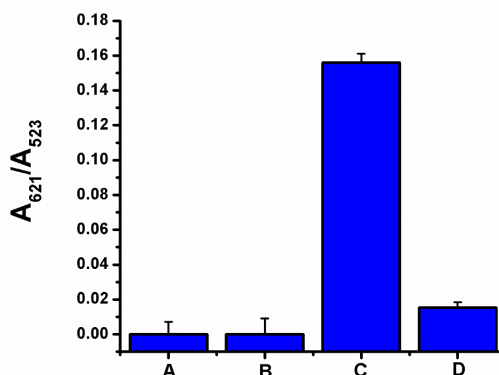


Figure S13. Representation of A_{621}/A_{523} of A) P1 (7.40×10^{-10} M) 200 μ L and 200 μ L of phosphate buffer pH 6.5, B) mixture of L1-AuNPs (100 μ L), L2-AuNPs (100 μ L) and 200 μ L of phosphate buffer pH 6.5, C) P1 (200 μ L) + NE (200 μ L) at 0.1 mM and D) mixture of L1-AuNPs (100 μ L) and L2-AuNPs (100 μ L) + NE (200 μ L) at 0.1 mM.

- **Determination of limit of detection for NE**

The limit of detection (LOD) for NE was obtained from the plot of the ratio of the absorbance intensities at 523 and 621 nm (A_{621}/A_{523}) versus NE concentration in μ M. As observed in **Figures S14 and S15** a good coefficient of determination ($R^2 > 0.99$) was obtained for P1 and OP1 showing a good correlation in the linear regression curve between NE concentration and the ratio of aggregated versus

dispersed nanoparticles. LOD was calculated by using the equation (1), where $K=3$; S_b is the standard deviation of the blank and m is the slope of the calibration curve. The resulting LOD was $1.16 \mu\text{M}$ (P1) and $0.07 \mu\text{M}$ (OP1).

$$LOD = K \cdot \frac{S_b}{m} \quad (1)$$

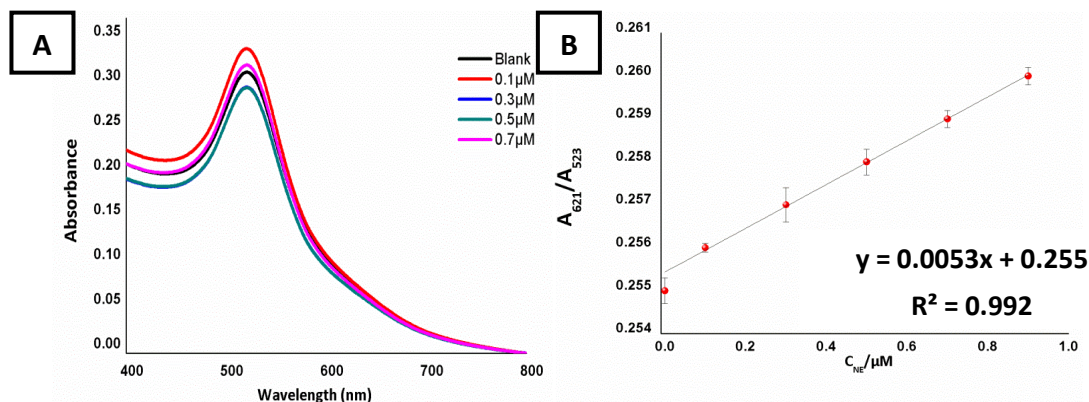


Figure S14. A) UV-Vis spectra of P1 when NE was added at concentrations of 0, 0.1, 0.3, 0.5, 0.7 μM. B) Plot of the A_{621}/A_{523} vs. NE concentrations within the 0-1 μM range.

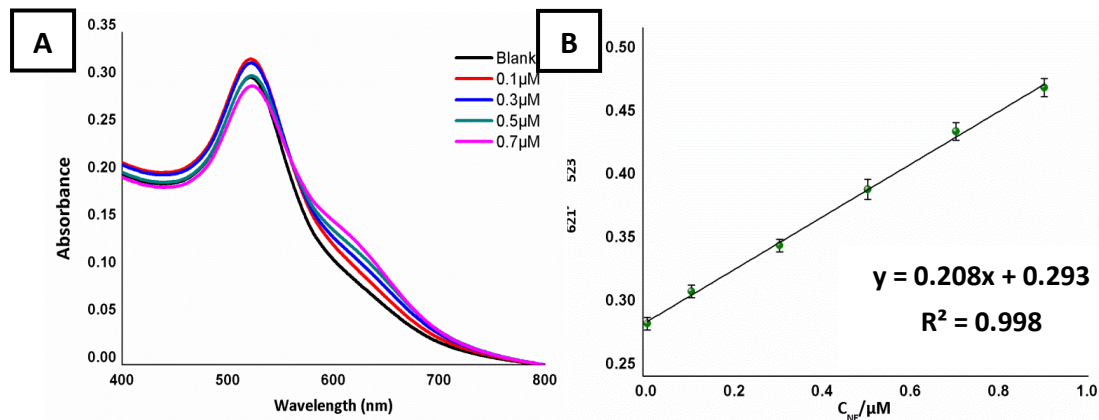


Figure S15. A) UV-Vis spectra of optimized P1 when NE was added at concentrations of 0, 0.1, 0.3, 0.5, 0.7 μM. B) Plot of the A_{621}/A_{523} vs. NE concentrations within the 0-1 μM range.

- **Determination of recovery and accuracy of the method**

Recovery and accuracy of the method were calculated according to Suresh Kumar methods¹

Table S3. OP1 A) % recovery (found concentration/known concentration) × 100, B) Accuracy was calculated from (found concentration – known concentration/known concentration) × 100.

KNOWN CONCENTRATION (μM)	FOUND CONCENTRATION μM	RECOVERY % ^{A)}	ACCURACY% ^{B)}
0.20 μM	0.25 μM	124.64 %	0.25 %
0.40 μM	0.38 μM	96.14 %	-0.04 %
0.60 μM	0.58 μM	97.10 %	-0.02 %

- **Response in urine**

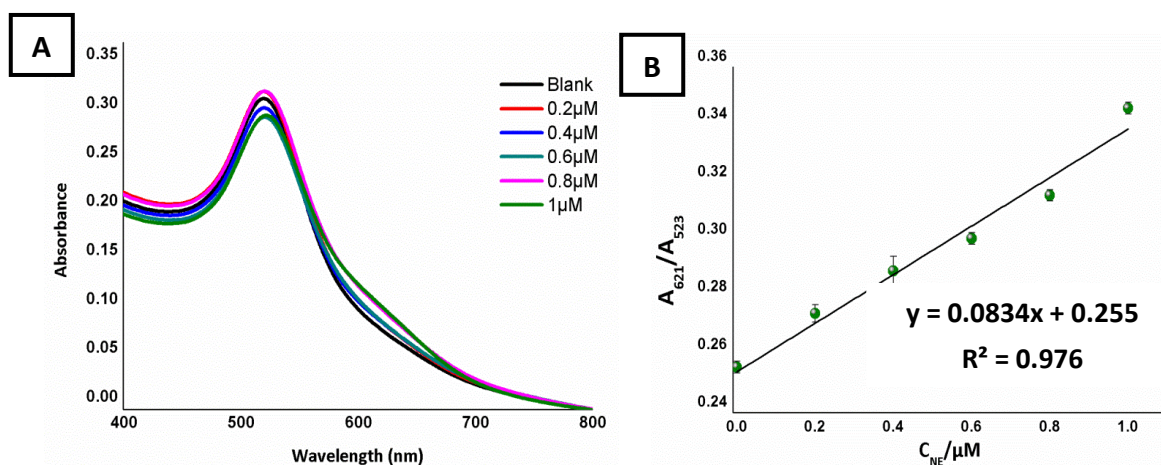


Figure S16. A) UV-Vis spectra of OP1 when NE was added at concentrations of 0, 0.1, 0.3, 0.5, 0.7 μM in Surine Negative Urine Control B) Plot of the A_{621}/A_{523} vs. NE concentrations within the 0-1 μM range.

• **Comparison with other colorimetric methods for detection of Norepinephrine**

Table S4. Comparison with other methods previously reported.

Method	LOD (M)	Interferences by other catecholamines	Selective of NE	Time (min)	Ref
Generation of AuNPs with HAuCl ₄ and cetyltrimethylammonium chloride (CTAC)	2.5×10^{-6}	Yes: Dopamine, L-DOPA and epinephrine	No	2	2
Interference in the formation of the quinoid dye catalyzed by horseradish peroxidase (HRP)	-----	Yes: Dopamine, L-DOPA, epinephrine, and ascorbic	No	15	3
Boronic acid-containing coumarin aldehyde	-----	Yes: Dopamine	No	----- -	4
Reduction of oxidize 3,3',5,5'-tetramethylbenzidine (oxTMB)	1.5×10^{-8}	Yes: Dopamine, epinephrine	No	5	5
Reducing agents, for the formation of silver nanoshell on the surface of gold nanorods (Colorimetric array)	4.8×10^{-6}	Yes: Dopamine, epinephrine	No (only qualitative)	20	6
Double molecular recognition by aggregation of bifunctionalized gold nanoparticles	7×10^{-8}	No interference by other catecholamines	Yes	5	This study

- **Experiment to prove the reactivity of an aromatic aldehyde with the amino alcohol group of NE**

In order to prove the formation of the oxazolidine from the terminal aldehyde and amino-alcohol group of NE, a 1:1 mixture of 4-methoxybenzaldehyde (0.2 mmol) and NE (0.2 mmol) was stirred in MeOH: H₂O (9:1) for 1 h at room temperature. Then, the solvents were evaporated and the resulting oil was dissolved in deuterated methanol for ¹H NMR analysis. We could observe that the reaction led to a mixture of starting materials and the corresponding oxazolidine and/or the imine open form in a ca 30:70 ratio (from the integration of the signals corresponding to the aldehyde and the imine/oxazolidine).

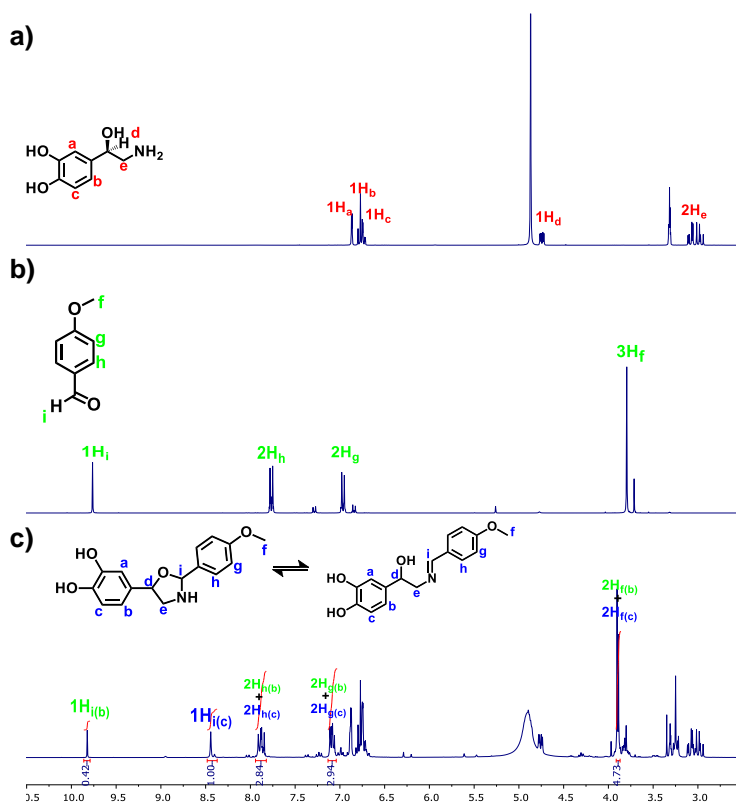


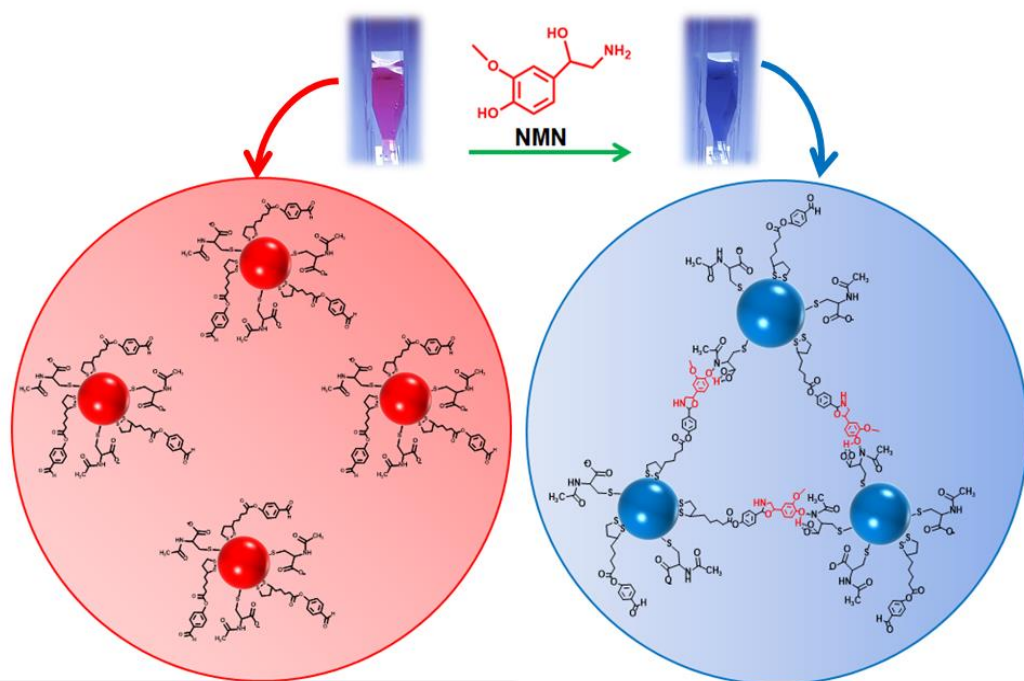
Figure S17. ¹H NMR in CD₃OD at 300 MHz. a) Norepinephrine (NE) b) 4-methoxybenzaldehyde c) oxazolidine/imine open form.

• References

1. Rawat, K. A.; Singhal, R. K.; Kailasa S. K., Colorimetric and Fluorescence “Turn-On” Methods for the Sensitive Detection of Bromelain using Carbon Dots Functionalized Gold Nanoparticles as a Dual Probe. *RSC Adv.* **2016**, 6, 32025-32036.
2. Baron, R.; Zayats, M.; Willner, I., Dopamine-, L-DOPA-, Adrenaline-, and Noradrenaline-Induced Growth of Au Nanoparticles: Assays for the Detection of Neurotransmitters and of Tyrosinase Activity, *Anal. Chem.* **2005**, 77, 1566-1571.
3. Zhu, M.; Huang, X.; Li, J.; Shen, H., Peroxidase-Based Spectrophotometric Methods for the Determination of Ascorbic Acid, Norepinephrine, Epinephrine, Dopamine and Levodopa, *Anal. Chim. Acta.* **1997**, 357, 261-267.
4. Secor, K. E.; Glass, T. E., Selective Amine Recognition: Development of a Chemosensor for Dopamine and Norepinephrine, *Org. Lett.* **2004**, 6, 3727-3730.
5. Zhu, S.; Yang J.; Zhao, X. E.; Kong, R.; Wang, H.; You, J., Simple and Fast Determination of Catecholamines in Pharmaceutical Samples using Ag⁺-3,3',5,5'-tetramethylbenzidine as a Colorimetric Probe, *Anal. Methods* **2015**, 7, 6785-6790.
6. Jafarinejad, S.; Ghazi-Khansari, M.; Ghasemi F.; Sasanpour, P.; Hormozi-Nezhad, M. R., Colorimetric Fingerprints of Gold Nanorods for Discriminating Catecholamine Neurotransmitters in Urine Samples, *Sci. Rep* **2017**, 7, 8266.

Chapter 3: Part 3

Colorimetric detection of normetanephrine, a pheochromocytoma biomarker, using bifunctionalised gold nanoparticles



Colorimetric detection of normetanephrine, a pheochromocytoma biomarker, using bifunctionalised gold nanoparticles

Tania M. Godoy-Reyes^{a, b, d}, Ana M. Costero^{a, b, c}, Pablo Gaviña^{a, b, c, *},
Ramon Martínez-Maez^{a, b, d, **}, Felix Sancenon^{a, b, d}

^a Instituto Interuniversitario de Investigación de Reconocimiento Molecular y Desarrollo Tecnológico (IDM), Universitat Politècnica de València, Universitat de València, Spain

^b CIBER de Bioingeniería, Biomateriales y Nanomedicina (CIBER-BBN), Spain.

^c Departamento de Química Orgánica, Universitat de València, Doctor Moliner 50, Burjassot, 46100, Valencia, Spain.

^d Departamento de Química, Universitat Politècnica de València, Camino de Vera s/n, 46022, Valencia, Spain.

Published online: 8 January, 2019

(Reprinted with permission from *Anal. Chim. Acta*, 2019, 1056, 146)

Abstract

A simple and effective colorimetric method for the detection of normetanephrine (NMN), an O-methylated metabolite of norepinephrine, using functionalised gold nanoparticles is described. This metabolite is an important biomarker in the diagnosis of adrenal tumours such as pheochromocytoma or paraganglioma. The colorimetric probe consists of spherical gold nanoparticles (AuNPs) functionalized with two different ligands, which specifically recognize different functional groups in normetanephrine. Thus, a benzaldehyde-terminated ligand was used for the recognition of the aminoalcohol moiety in NMN, by forming the corresponding oxazolidine. On the other hand, N-Acetyl-Cysteine was chosen for the recognition of the phenolic hydroxyl group through the formation of hydrogen bonds. The selective double molecular recognition between the probe and the hydroxyl and the aminoalcohol moieties of normetanephrine led to interparticle-crosslinking aggregation resulting in a change in the color of the solution, from red to blue, which could be observed by naked eye. The probe was highly selective towards normetanephrine and no color changes were observed in the presence of other neurotransmitter metabolites such as homovanillic acid (HVA) (dopamine metabolite), 5-hydroxyindoleacetic acid (5-HIAA) (serotonin metabolite), or other biomolecules present in urine such as glucose (Glc), uric acid (U.A), and urea. Finally, the probe was evaluated in synthetic urine with constituents that mimic human urine, where a limit of detection of 0.5 μM was achieved.

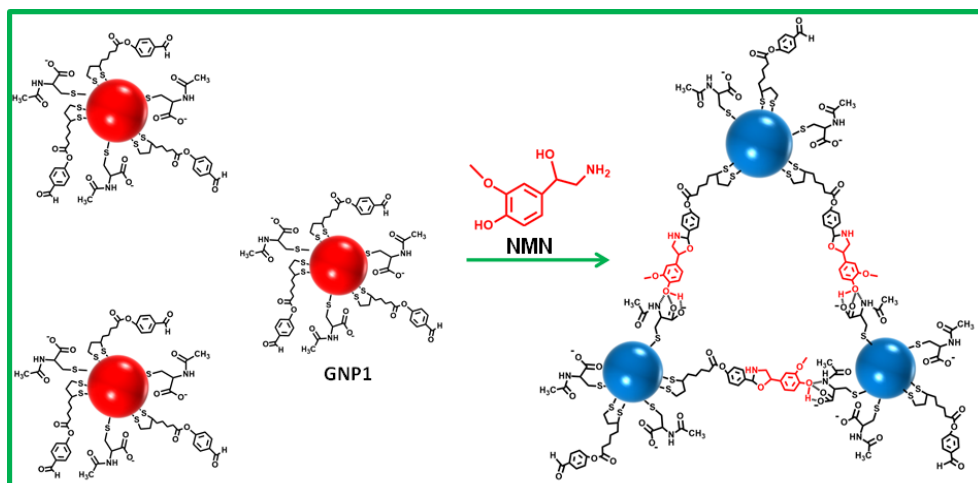
Introduction

Normetanephrine (NMN) is an O-methylated metabolite of norepinephrine produced by the enzyme catechol-O-methyltransferase within tumours. This metabolite is one of the most useful biomarkers for the early diagnostic of neuroendocrine tumours such as pheochromocytomas and paragangliomas (PPGL) ¹⁻³. These tumours, which cause hypertension and occur with headaches, excessive sweating and palpitations, arise from the intra-adrenal and extra-adrenal chromaffin cells, and are characterized by an overproduction of catecholamines, which result in increased levels of their O-methylated metabolites in plasma or urine, being NMN the metabolite found in the highest concentration⁴. Measurements of NMN levels in plasma or urine are recommended for first line biochemical diagnosis of PPGL^{5,6}.

Some analytical methods such as electrochemistry⁷, radioimmunoassays^{8,9}, enzyme-linked immunosorbent assay (ELISA) ¹⁰, high performance liquid chromatography with tandem mass spectrometry (HPLC-MS)¹¹⁻¹⁴ with fluorogenic detection (HPLC-FD)^{15,16} and with electrochemical detection (HPLC-ED)¹⁷⁻¹⁹ have been developed for the quantification of NMN in human plasma and urine. However, the application of these techniques requires of sophisticated and expensive equipment, in addition to their complicated sample-preparation and professional operation. Due to the limitations of the above-mentioned analytical methods and the importance of the determination of NMN for the diagnosis of PPGL, the development of simple analytical techniques that can be readily applied to the measurement of NMN in clinical samples is of high interest. Colorimetric probes are especially appealing as sensing devices because there are few techniques as simple as visual detection and they allow rapid and sensitive determination to the naked eye, on site, without any sample pretreatment. However, to the best of our knowledge, the only colorimetric assay for NMN detection is based on the Pisano colorimetric method, which measures the total content of metanephrines (normetanephrine and metanephrine) in urine, after their conversion into vanillin through oxidation using periodate. This method is non-specific, and involves lengthy separations and sample pretreatment²⁰⁻²².

In recent years, spherical gold nanoparticles have received great attention as platforms in the development of colorimetric sensors and probes. AuNPs have wonderful optoelectronics properties^{23,24}. In particular the SPRB, which can be modified upon the analyte-induced aggregation of the nanoparticles. This modification in the SPRB results in a color change from red (dispersed AuNPs) to blue (aggregated AuNPs) which can be observed by naked eye. Other great advantages are their good biocompatibility and ease of surface functionalisation with different organic molecules. Thus, numerous selective and sensitive colorimetric probes based on functionalised AuNPs, which allow the selective determination of different types of analytes at very low concentrations, have been reported²⁵⁻²⁸.

Taking into account the above mentioned facts, we present herein a novel approach for the fast, simple and selective determination of normetanephrine in water and in simulated urine, based on the use of bifunctionalised gold nanoparticles. Probe **GNP1** consists of spherical gold nanoparticles functionalised with two different moieties: a benzaldehyde-terminated ligand (L1) which can react with the aminoalcohol group of NMN to give the corresponding oxazolidine²⁹, and N-Acetyl-L-Cysteine (L2), which binds the phenolic hydroxyl group through the formation of hydrogen bonds, and is also a good stabilizer of gold nanoparticles due to its carboxylate group^{30,31}. This double molecular interaction with NMN leads to aggregation of the nanoparticles, resulting in a strong bathochromic shift of their SPRB and a color change of the solution from red to blue, visible to the naked eye. The recognition approach is shown in **Scheme 1**.



Scheme 1. Sensing paradigm of the colorimetric detection of normetanephrine (NMN) based on the aggregation of gold nanoparticles (GNP1) bifunctionalised with 4-(liponyloxy)benzaldehyde (L1) and N-acetylcysteine (L2).

Experimental section

• Chemicals

Gold (III) chloride hydrate ($\text{HAuCl}_4 \cdot 3\text{H}_2\text{O}$) 99.995%, sodium citrate dihydrate, N-Acetyl-L-cysteine $\geq 99\%$ (L2), (\pm)- α -lipoic acid $\geq 98.0\%$, 4-hydroxybenzaldehyde 98%, N,N'-dicyclohexylcarbodiimide (DCC) 99%, 4-dimethylaminopyridine (DMAP) $\geq 99\%$, homovanillic acid (HVA) $\geq 99.0\%$, 5-Hydroxyindole-3-acetic acid (5-HIAA) $\geq 98\%$, D-(+)-Glucose (Glc) $\geq 99.5\%$, uric acid (U.A) $\geq 99\%$, urea 98% and surine negative urine, were purchased from Sigma Aldrich and used without further purification. All the aqueous solution were prepared with Milli-Q water ($18.2 \text{ M}\Omega \text{ cm}^{-1}$).

• General Methods

UV-Vis absorption spectra were recorded using a 1 cm path length quartz cuvette on a Shimadzu UV-2101PC spectrophotometer. All measurements were carried out at room temperature. To characterize the induced aggregation of the gold nanoparticles probe in the presence of normetanephrine, high-resolution transmission electron microscopy (JEOL-1010 transmission electron microscopy operating at 100 kV) was used. Zeta potential and DLS values were measured in a

Malvern Zetasizer ZS, for 3 times in 10-25 cycles. To verify the gold nanoparticles functionalization Fourier-transform infrared spectra were recorded with a Cary 630 FT-IR spectrometer within the wavenumber range of 648-4000 cm^{-1} at a resolution of 8 cm^{-1} . To confirm the structure of ligand L1 ^1H -NMR and ^{13}C -NMR spectra were recorded with a Bruker DRX-300 Spectrometer (300 MHz, 128 scans). Chemical shifts are reported in ppm with tetramethylsilane as an internal standard.

- **Synthesis of 4-(liponyloxy)benzaldehyde (L1)**

4-(Liponyloxy)benzaldehyde (L1) was synthesized as previously reported³⁵ from (\pm)- α -lipoic acid (0.75 g, 3.63 mmol), 4-hydroxybenzaldehyde (0.44 g, 3.63 mmol), DCC (0.75 g, 3.63 mmol) and a catalytic amount of DMAP (0.04 g, 0.33 mmol) in anhydrous CH_2Cl_2 (10 mL). L1 was obtained as a yellow oil in 86% yield.

^1H NMR (300 MHz, CDCl_3) δ 9.98 (s, 1H), 7.91 (d, $J = 9.0$, 2H), 7.26 (d, $J = 9.0$, 2H), 3.61–3.57 (m, 1H), 3.22 – 3.09 (m, 2H), 2.60 (t, $J = 7.4$ Hz, 2H), 2.51 – 2.42 (m, 1H), 1.97 – 1.88 (m, 1H), 1.84 – 1.67 (m, 4H), 1.63 – 1.52 (m, 2H). ^{13}C NMR (75 MHz, CDCl_3) δ 190.96, 171.71, 155.35, 134.39, 131.25, 122.51, 56.53, 40.51, 38.79, 34.94, 34.21, 28.64, 24.77.

- **Synthesis of probe GNP1**

First, citrate-coated AuNPs with a diameter ca. 17 nm were synthesized as reported previously³²⁻³⁴. Briefly, 5 mL of 13.6 mM aqueous trisodium citrate solution were added to an aqueous boiling solution of HAuCl_4 (95 mL, 0.23 mM) and the resulting mixture was kept continuously boiling for 30 min until a red solution was obtained. The solution was cooled to room temperature, and then the mixture was purified by filtration through a 0.22 μM membrane and the filtrate was then stored in a refrigerator at 4°C until use. Probe **GNP1** was prepared from the previously synthesized citrate-capped AuNPs (ca. 17 nm) by a stepwise ligand-exchange reaction. Thus, 20 μL of L2 1 mM in DMF were added to 10 mL of the as-prepared citrate-capped AuNPs. After stirring for 1 min at room temperature, 20 μL of L1 1 mM in DMF were added. The solution was stirred 5 h at room temperature. To purify GNP1, the mixture was centrifuged for 10 min at

11,000 rpm, the supernatants were decanted and the nanoparticles redispersed in Milli-Q water (10 mL). This procedure was repeated twice.

- **Synthesis of probe GNP2**

GNP2 nanoparticles were synthesized following the same procedure as **GNP1**. First, citrate-coated AuNPs of ca. 34 nm were prepared, following the process mentioned above, but in this case, using 5 mL of 3.4 mM aqueous trisodium citrate solution. Probe **GNP2** was obtained by the stepwise addition of L2 and L1 to the as-synthesized citrate-capped AuNPs using the same amounts and the same procedure as described above for **GNP1**.

- **Sensing and selectivity studies**

For the UV-vis titration experiments, aqueous solutions of NMN of different concentrations at pH 7 (phosphate buffer 10 mM) were freshly prepared. Then, 200 μL of **GNP1** (8.12×10^{-10} M) and 200 μL of the NMN solution at an appropriate concentration (0–24 mM) were mixed to obtain a final volume of 400 μL . As an example, 400 μL of a solution containing **GNP1** 4.06×10^{-10} M and NMN 5 mM were obtained by mixing 200 μL of **GNP1** and 200 μL of NMN 10 mM. Samples were incubated at room temperature for 6 min before recording the corresponding UV-vis spectra. The same procedure was followed to evaluate the sensing ability of **GNP2** (NMN final concentrations of 1, 6 and 10 mM). The selectivity studies were performed following the same procedure by mixing 200 μL of **GNP1** (8.12×10^{-10} M) and 200 μL of an aqueous buffered solution (pH = 7) of the studied interferent (10 mM). A competitive study was performed by adding 200 μL of an aqueous buffered solution containing a mixture of NMN and all the interferents (10 mM each) to 200 μL of **GNP1**. The titration experiments with optimized probe (**OGNP1**) were conducted as follows: **OGNP1** was freshly prepared by adding 20 μL of NMN 80 mM to 200 μL of the **GNP1** solution, and incubating the mixture for 1 min at room temperature. Then, 180 μL of the NMN sample solution at an appropriate concentration (0–20 μM) were added to the **OGNP1** solution to obtain a final volume of 400 μL . Samples were incubated for 6 min before taking measurements in the spectrophotometer. Measurements in simulated urine were made using SurineTM Negative Urine Control, that is rugged

non-biological urine with constituents that mimic human urine, but without human urine's research impediments. In a typical experiment, 200 μL of **OGNP1** were mixed with 200 μL of NMN solutions in 20% Surine Negative Urine Control, incubated for 6 min, and analysed by UV-vis spectrophotometry.

Results and discussion

• Synthesis and characterization of **GNP1**

Compound L1 was obtained through Steglich esterification of lipoic acid with 4-hydroxybenzaldehyde using as a coupling agent DCC and DMAP as a catalyst³⁵. On the other hand, citrate-capped AuNPs were prepared by the Turkevich-Frens method which consist in the reduction of tetrachloroauric acid with trisodium citrate in boiling water³²⁻³⁴. Addition of L1 and L2 (1:1 molar ratio) to the citrate-stabilized AuNPs led to the formation of probe **GNP1** through ligand exchange reactions, due the highly stable S-Au interactions. The functionalised gold nanoparticles were purified by repeated centrifugation and redispersion in water to yield a red colored solution.

Probe **GNP1** was characterized by UV-vis spectroscopy, transmission electron microscopy (TEM), dynamic light scattering (DLS) and infrared spectroscopy (FTIR). The aqueous dispersions of **GNP1** showed the typical SPRB at 523 nm in the UV-vis spectrum, in accordance with the values observed for dispersed AuNPs with sizes smaller than 25 nm³⁶⁻³⁷. The average size of the nanoparticles turned out to be of 17 nm from TEM measurements (see **Figure S1 C**). Regarding the hydrodynamic diameter of the dispersed nanoparticles DLS showed an increase from 28 nm for citrate-stabilized AuNPs to 30 nm for **GNP1** (see **Figure S2**). The zeta-potential value of the **GNP1** nanoparticles in aqueous solution was -30.6 mV. Finally, the ligand exchange was confirmed by FTIR, showing bands characteristic of L1 and L2 (see **Figure S4**). The concentration of **GNP1** probe solution was calculated to be ca. 6×10^{-10} M by UV-vis spectroscopy considering an estimated molar extinction coefficient of $\epsilon = 6.01 \times 10^8 \text{ M}^{-1} \text{ cm}^{-1}$ ³⁸. The red colored aqueous dispersion of **GNP1** remained stable in the refrigerator for more than a month, with no observable changes in color nor in its SPRB.

- **Sensing ability of GNP1 towards normetanephrine**

GNP1 sensing capabilities were evaluated in the absence and presence of NMN (5 mM) at pH 7 (phosphate buffer, 10 mM). In the absence of NMN the aqueous suspension of **GNP1** remained red with its characteristic SPRB at 523 nm in the UV-vis spectrum. However, in presence of excess NMN the red color changed progressively to blue within minutes, and the corresponding UV-vis spectrum showed a shift in the SPRB from 523 nm to 612 nm, indicating the aggregation of **GNP1** induced by NMN (see **Figure 1**). This aggregation was further confirmed by TEM (see **Figure S1 A and B, corresponding to dispersed and aggregated nanoparticles**) and DLS studies. The latter shows that in the presence of NMN the hydrodynamic radius of the particles increases from 30 nm to 450 nm (see **Figure S3 A and B**). The zeta potential reduced from -30.6 mV (**GNP1**) to -9.35 mV (**GNP1** + NMN). In addition, UV-vis kinetic studies confirmed a significant increase in the absorbance at 612 nm of **GNP1** in the presence of NMN, starting at the first minute, and reaching its maximum point approximately after 6 min (see **Figure S5**).

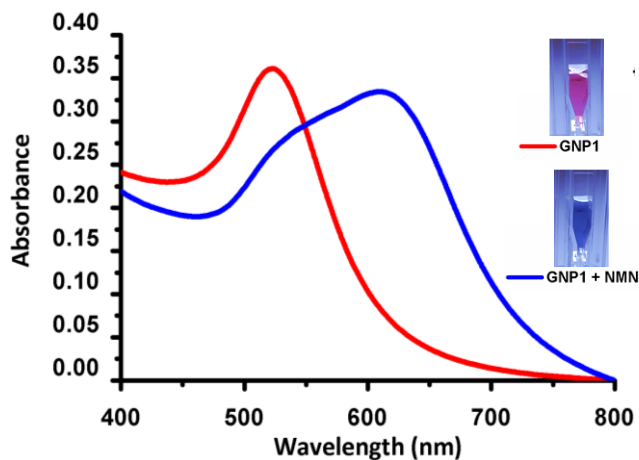


Figure 1. UV-Vis spectra of **GNP1** in the absence (red) and presence of NMN (5 mM) (blue) at pH 7 (phosphate buffer, 10 mM).

- **Selectivity evaluation of GNP1 in the presence of possible interferents**

Selective and sensitive detection of NMN plays a key role in the diagnosis of tumours such as pheochromocytoma. Selectivity features of **GNP1** were evaluated

in presence of other neurotransmitter metabolites such as, homovanillic acid (HVA, a dopamine metabolite) and 5-hydroxyindoleacetic acid (5-HIAA, a serotonin metabolite), and other biomolecules present in urine such as glucose (Glc), uric acid (U.A) and urea. After the addition of excess (5 mM final concentration) of the potential interferents to **GNP1**, negligible changes in the A_{612}/A_{523} ratio (A_{612} = absorbance at 612 nm, A_{523} = absorbance at 523 nm), nor in the color of the solutions were observed (see **Figure 2a** and **2b** and **Figure S6**). Moreover, in a competitive experiment, the addition of a mixture containing NMN and all the interferents (HVA, 5-HIAA, Glc, U.A and urea) to GNP1 led to a response similar to that found when only NMN is added to **GNP1**, (see **Figure 2b**). All these data indicate that GNP1 is able to selectively detect NMN in aqueous media in the presence of other neurotransmitter metabolites and selected biomolecules.

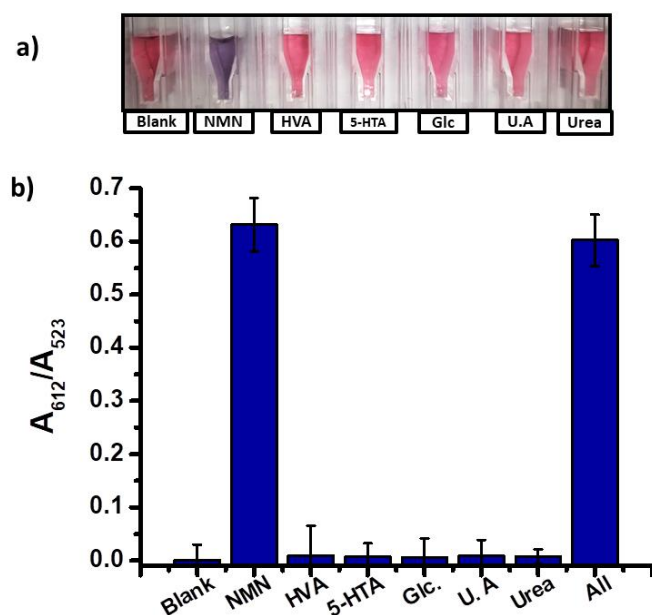


Figure 2. Response of **GNP1** in the presence of different molecules (5 mM) at pH 7 (phosphate buffer, 10 mM). a) Vials with the different tested molecules. b) Representation of A_{612}/A_{523} for NMN and the interferents. Error bars correspond to the s. d. from three independent experiments.

- **Sensitivity studies and optimization of GNP1**

In order to determine the sensitivity of the response of **GNP1** towards NMN, UV-vis titration experiments in the presence of increasing concentrations of NMN (from 0 to 12 mM) were undertaken. As the concentration increased, a gradual change in the color of the nanoparticles is clearly observed, changing from red to purple and finally to blue (see **Figure 3a**). Moreover as the amount of NMN increases a shift in the SPRB from 523 nm (dispersed nanoparticles) to 612 nm (aggregated) was observed by UV-vis (see **Figure 3b**), confirming in this way the sensing protocol based on the NMN-induced aggregation of **GNP1**. As seen in **Figure 4**, a remarkable increase in the A_{612}/A_{523} ratio was observed in the 4–10 mM concentration range, indicating a higher sensitivity of the probe within these NMN concentration values. Consequently, the sensitivity of the probe towards NMN detection could be improved by the addition of certain amount of NMN (to yield a final concentration of 4 mM) to the stock solution of **GNP1** before use³⁹. **Figure 5** shows clearly how the sensitivity towards NMN of this optimized probe (**OGNP1**) increases with respect to the sensitivity of **GNP1** in the 0–10 μM range (see **Figure 5, curves a and b**). The limit of detection (LOD), calculated from the plot of A_{612}/A_{523} vs NMN concentration in this low concentration range, was 4.7 μM for **GNP1**, and as low as 0.2 μM for **OGNP1**. This LOD confers our system a competitive basis for the detection of NMN at relevant clinical concentration. In particular, reported studies have determined that for normotensive patients, NMN levels above the normal range of 0.15 to 3.05 μM in urine can be indicative of pheochromocytoma and paraganglioma tumours⁴⁰.

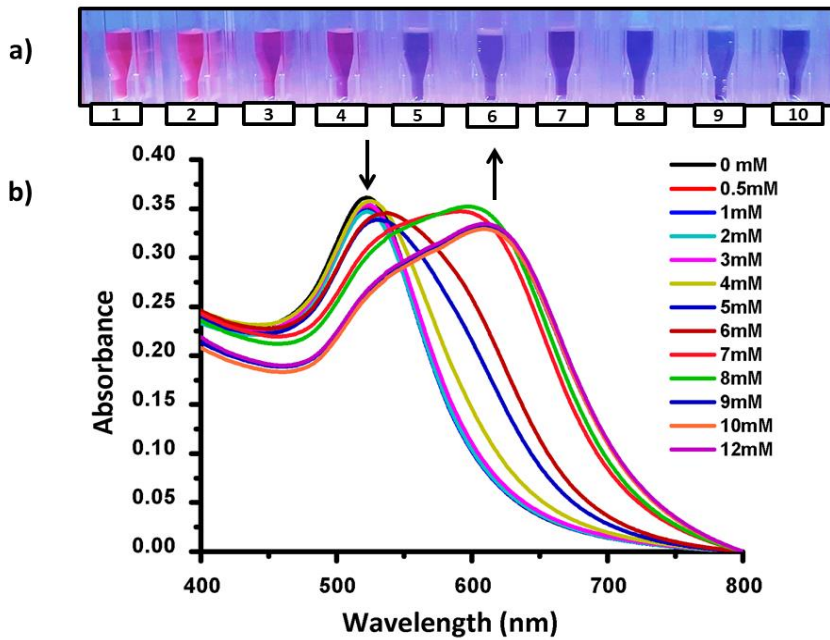


Figure 3. a) Colour modulation of **GNP1** when NMN was added at concentrations of 0, 3, 4, 5, 6, 7, 8, 9, 10, 11 mM (1-10, respectively). b) Changes in the UV-Vis spectra of probe when NMN was added at concentrations of 0, 0.5, 1, 2, 3, 4, 5, 6, 7, 8, 9, 10, 11, 12 Mm.

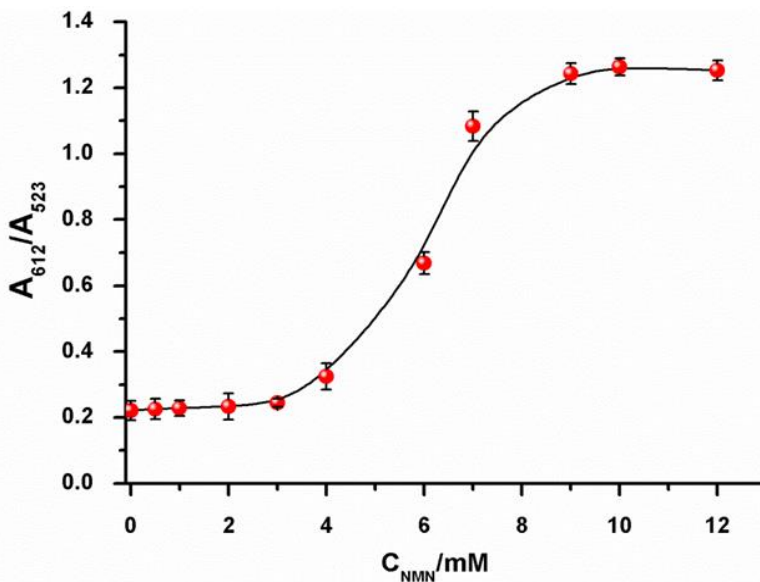


Figure 4. Plot of A_{612}/A_{523} versus NMN concentration (0-12 mM) obtained with **GNP1**. Error bars correspond to the s. d. from three independent experiments.

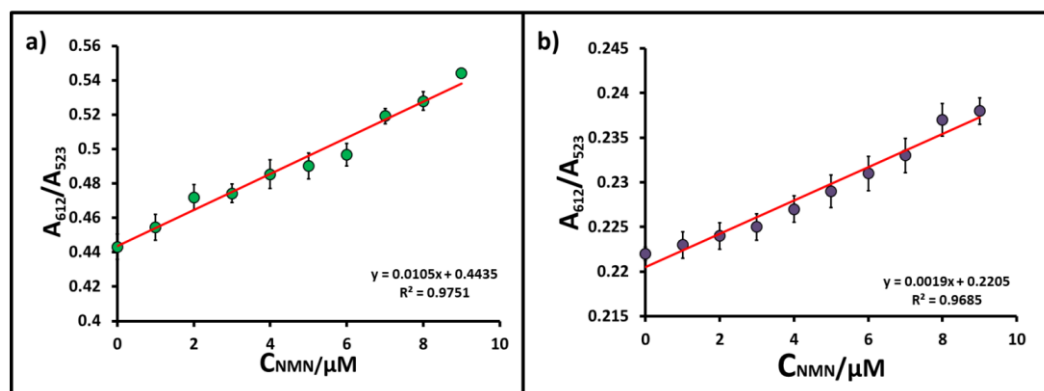


Figure 5. Plots of A_{612}/A_{523} versus NMN concentration within the 0–10 μM range for: a) optimized probe **OGNP1**; and b) **GNP1**. Error bars correspond to the s. d. from three independent experiments.

• Evaluation of **OGNP1** sensitivity in urine

In order to evaluate the sensing capabilities of **GNP1** in real samples, assays in synthetic urine were performed. **OGNP1** present a similar behaviour in urine⁴¹ to that described above in aqueous media when increasing concentrations of NMN were added (see **Figure S7**). From the A_{612}/A_{523} vs NMN concentration plots, a linear response in urine within the 0 to 10 μM NMN concentration range was observed, and a LOD of 0.52 μM was determined in this medium, which was into the normal range for healthy adults in urine (0.15 to 3.05 μM)⁴⁰.

Conclusions

In conclusion, we present herein a simple, fast, selective and sensitive colorimetric method for the detection of normetanephrine, a pheochromocytoma biomarker, using aqueous dispersions of spherical gold nanoparticles bifunctionalised with 4-(liponyloxy)benzaldehyde and N-acetylcysteine (**GNP1**). The presence of NMN induces the aggregation of the nanoparticles due to a double recognition process, which results in a clear colour change of the solution from red to blue, easily observed by naked eye, and a remarkable shift in the SPRB in the UV-vis spectrum. Selectivity essays in presence of other neurotransmitter metabolites such as homovanillic acid (HVA, a major catecholamine metabolite), 5-hydroxyindoleacetic acid (5-HIAA, a serotonin metabolite), and of other biomolecules present in urine such as glucose (Glc), uric acid (U.A), and urea, were

performed. Only in the presence of NMN a remarkable color change and UV-vis response were observed, demonstrating the high selectivity of the system. Regarding the sensitivity of the probe, a linear response within the 0-10 μM NMN concentration range and a LOD as low as 0.2 μM were determined in aqueous media with **OGNP1**. A similar response of the optimized probe to NMN was observed in synthetic urine with a LOD of 0.52 μM . We think that probe **GNP1** can be a simple and effective alternative to determine NMN in aqueous media and urine, contributing to the early diagnosis of pheochromocytoma and paraganglioma tumours.

Acknowledgements

Financial support from the Spanish Government (project MAT2015-64139-C4) and the Generalitat Valencia (Project PROMETEOII/2014/047 and AICO/2017/093) is gratefully acknowledged. T. Godoy-Reyes is grateful to Generalitat Valenciana for her Santiago Grisolfá fellowship. SCSIE (Universitat de València) is gratefully acknowledged for all the equipment employed.

References

1. G. Eisenhofer, J. W. Lenders, W. M. Linehan, M. M. Walther, D. S. Goldstein, and H. R. Keiser, Plasma normetanephrine and metanephrine for detecting pheochromocytoma in von Hippel–Lindau disease and multiple endocrine neoplasia type 2, *N. Engl. J. Med.* 340 (1999) 1872-1879.
2. A. M. Sawka, R. Jaeschke, R. J. Singh, and W. F. Young Jr, A Comparison of Biochemical Tests for Pheochromocytoma: Measurement of Fractionated Plasma Metanephrines Compared with the Combination of 24-Hour Urinary Metanephrines and Catecholamines, *J. Clin. Endocrinol. Metab.* 88 (2003) 553-558.
3. W. F. Young, Paragangliomas, *Ann. N. Y. Acad. Sci.* 1073 (2006) 21-29.
4. G. Eisenhofer, H. Keiser, P. Friberg, E. Mezey, T. T. Huynh, B. Hiremagalur, T. Ellingson, S. Duddempudi, A. Eijsbouts and J. W. Lenders, Plasma Metanephrines Are Markers of Pheochromocytoma Produced by Catechol-O-

- Methyltransferase Within Tumors, *J. Clin. Endocrinol. Metab.* 83 (1998) 2175-2185.
5. R. Därr, C. Pamporaki, M. Peitzsch, K. Miehle, A. Prejbisz, M. Peczkowska, D. Weismann, F. Beuschlein, R. Sinnott, S. R. Bornstein, H.P. Neumann, A. Januszewicz, J. Lenders, G. Eisenhofer. Biochemical diagnosis of pheochromocytoma using plasma-free normetanephrine, metanephrine and methoxytyramine: importance of supine sampling under fasting conditions. *Clin. Endocrinol.* 80 (2014), 478-486.
 6. K. Pacak, W. M. Linehan, G. Eisenhofer, M. M. Walther, and D. S. Goldstein, Recent advances in genetics, diagnosis, localization, and treatment of pheochromocytoma, *Ann. Intern. Med.* 134 (2001) 315-329.
 7. R. El Khamlichi, D. Bouchta, M. B. Atia, M. Choukairi, R. T. Khalid, I. Raissouni, S. Tazi, A. Mohammadi, A. Soussi, K. Draoui, C. Faiza, M.L. Sefian, A novel carbon/chitosan paste electrode for electrochemical detection of normetanephrine in the urine, *J Solid State Electrochem.* 22 (2018) 1-12.
 8. S. Oishi, M. Sasaki, M. Masato, T. Sato, Urinary Normetanephrine and Metanephrine Measured by Radioimmunoassay for the Diagnosis of Pheochromocytoma: Utility of 24-Hour and Random 1-Hour Urine Determinations, *J Clin Endocrinol Metab.* 67 (1988) 614-618.
 9. E. Pussard, A. Chaouch, T. Said, Radioimmunoassay of free plasma metanephrines for the diagnosis of catecholamine-producing tumors, *Clinical chemistry and laboratory medicine.* 52 (2014) 437-444.
 10. B. G. Wolthers, I. P. Kema, M. Volmer, R. Wesemann, J. Westermann, B. Manz. Evaluation of urinary metanephrine and normetanephrine enzyme immunoassay (ELISA) kits by comparison with isotope dilution mass spectrometry, *Clin. Chem.* 43 (1997) 114-120.
 11. M. Y. Cheuk, Y. C. Lo, W. T. Poon, Determination of urine catecholamines and metanephrines by reversed-phase liquid chromatography-tandem mass spectrometry, *Chin. J. Chromatogr.* 35 (2017) 1042-1047.
 12. Zheng, J., Mandal, R., & Wishart, D. S. A sensitive, high-throughput LC-MS/MS method for measuring catecholamines in low volume serum, *Anal. Chim. Acta.* 1037 (2018), 159-167.

13. R. T. Peaston, K. S. Graham, E. Chambers, J. C. van der Molen, S. Ball, Performance of plasma free metanephrines measured by liquid chromatography–tandem mass spectrometry in the diagnosis of pheochromocytoma, *Clin. Chim. Acta.* 411 (2010) 546-552.
14. M. J. Whiting, Simultaneous measurement of urinary metanephrines and catecholamines by liquid chromatography with tandem mass spectrometric detection, *Ann. Clin. Biochem.* 46 (2009) 129-136.
15. E. C. Y. Chan, P. Y. Wee, P. Y. Ho, P. C. Ho, High-performance liquid chromatographic assay for catecholamines and metanephrines using fluorimetric detection with pre-column 9-fluorenylmethyloxycarbonyl chloride derivatization, *J Chromatogr B Biomed Sci Appl.* 749 (2000) 179-189.
16. G. P. Jackman, A simple method for the assay of urinary metanephrines using high performance liquid chromatography with fluorescence detection, *Clin. Chim. Acta*, 120 (1982) 137-142.
17. B. H. Westerink, Determination of Normetanephrine, 3,4-Dihydroxyphenylethyleneglycol (Free and Total), and 3-Methoxy-4-Hydroxyphenylethyleneglycol (Free and Total) in Rat Brain by High-Performance Liquid Chromatography with Electrochemical Detection and Effects of Drugs on Regional Concentrations, *J. Neurochem.* 42 (1984) 934-942.
18. P. Volin, Determination of urinary normetanephrine, metanephrine and 3-methoxytyramine by high-performance liquid chromatography with electrochemical detection: comparison between automated column-switching and manual dual-column sample purification methods, *J Chromatogr B Biomed Sci Appl.* 578 (1992) 165-174.
19. J. J. Willemsen, C. F. Sweep, J. W. Lenders, H. A. Ross, Stability of plasma free metanephrines during collection and storage as assessed by an optimized HPLC method with electrochemical detection, *Clin. Chem.* 49 (2003) 1951.
20. J. J. Pisano. A simple analysis for normetanephrine and metanephrine in urine. *Clin. Chim. Acta* 5 (1960), 406-414.
21. R.N. Gupta, D. Price, P.M. Keane. Modified Pisano method for estimating urinary metanephrines. *Clin. Chem.* 19 (1973), 611–614.

22. J-B. Corcuff, L. Chardon, I. H. Ridah, J. Brossaud. Urinary sampling for 5HIAA and metanephrines determination: revisiting the recommendations. *Endocr. Connect.* 6 (2017), R87-R98.
23. K. Saha, S. S. Agasti, C. Kim, X. Li, V. M. Rotello, Gold nanoparticles in chemical and biological sensing, *Chem. Rev.* 112 (2012) 2739-2779.
24. K. M. Mayer, J. H. Hafner, Localized surface plasmon resonance sensors, *Chem. Rev.* 111 (2011) 3828-3857.
25. K. A. Rawat, J. R. Bhamore, R. K. Singhal, S. K. Kailasa, Microwave assisted synthesis of tyrosine protected gold nanoparticles for dual (colorimetric and fluorimetric) detection of spermine and spermidine in biological samples, *Biosens. Bioelectron.* 88 (2017) 71-77.
26. A. Martí, A. M. Costero, P. Gaviña, M. Parra, Selective colorimetric NO (g) detection based on the use of modified gold nanoparticles using click chemistry, *Chem. Commun.* 51 (2015) 3077-3079.
27. J. V. Rohit, S. K. Kailasa, Simple and selective detection of pendimethalin herbicide in water and food samples based on the aggregation of ractopamine-dithiocarbamate functionalized gold nanoparticles, *Sens. Actuators B Chem.* 245 (2017) 541-550.
28. L. Chen, W. Lu, X. Wang, L. Chen, A highly selective and sensitive colorimetric sensor for iodide detection based on anti-aggregation of gold nanoparticles, *Sens. Actuators B Chem.* 182 (2013) 482-488.
29. C. Agami, T. Rizk, Role of solvent on the diastereoselectivity of oxazolidine formation from (-)-ephedrine, *J. Chem. Soc., Chem. Commun.* 24 (1983) 1485-1486.
30. H. Su, Q. Zheng and H. Li, Colorimetric detection and separation of chiral tyrosine based on N-acetyl-L-cysteine modified gold nanoparticles, *J. Mater. Chem.* 22 (2012) 6546-6548.
31. T. M. Godoy-Reyes, A. Llopis-Lorente, A. M. Costero, F. Sancenón, P. Gaviña, and R. Martínez-Máñez, Selective and sensitive colorimetric detection of the neurotransmitter serotonin based on the aggregation of bifunctionalised gold nanoparticles, *Sens. Actuators B Chem.* 258 (2017) 829-835.
32. P. Zhao, N. Li and D. Astruc, State of the art in gold nanoparticle synthesis, *Coord. Chem. Rev.* 257 (2013) 638-665.

33. J. Turkevich, P. C. Stevenson and J. Hillier, A study of the nucleation and growth processes in the synthesis of colloidal gold, *Discuss. Faraday Soc.* 11 (1951) 55-75
34. G. Frens, Controlled nucleation for the regulation of the particle size in monodisperse gold suspensions, *Nature-Phys Sci.* 241 (1973) 20-22.
35. C. Zhang, G. Shen, Y. Shen, X. Zhang. The development of an electrochemical immunosensor using a thiol aromatic aldehyde and PAMAM-functionalized Fe₃O₄@Au nanoparticles. *Anal. Biochem.* 485 (2015), 66-71.
36. W. Haiss, N. T. K. Thanh, J. Aveyard and D. G. Fernig, Determination of size and concentration of gold nanoparticles from UV- Vis spectra, *Anal. Chem.* 79 (2007) 4215-4221.
37. S.-Y. Lin, Y.-T. Tsai, C.-C. Chen, C.-M. Lin and C.-H. Chen, Two-step functionalization of neutral and positively charged thiols onto citrate-stabilized Au nanoparticles, *J. Phys. Chem. B.* 108 (2004) 2134-2139.
38. X. Liu, M. Atwater, J. Wang and Q. Huo, Extinction coefficient of gold nanoparticles with different sizes and different capping ligands, *Colloids Surf. B.* 58 (2007) 3-7.
39. B. Kong, A. Zhu, Y. Luo, Y. Tian, Y. Yu, G. Shi. Sensitive and selective colorimetric visualization of cerebral dopamine based on double molecular recognition. *Angew. Chem.* 123 (2011) 1877-1880
40. Mayo Clinic. (s.f.). Mayo medical laboratories. <https://www.mayomedicallaboratories.com/testcatalog/Clinical+and+Interpretive/83006> , (accessed December 2017).
41. Cerilliant Analytical Reference Standards, https://www.cerilliant.com/shoponline/Item_Details.aspx?itemno=1cedba31-c7f4-4ab1-ba9f-a02f3328d204&item=S-020, (accessed December 2017).

Supporting Information

• TEM Images

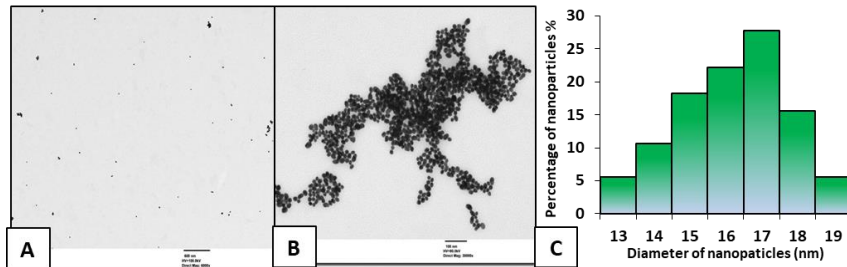


Figure S1. TEM images of **GNP1** (A) in the absence and (B) in the presence of NMN (5 mM) (C) Size distribution of **GNP1**. According to the size distribution the diameter of **GNP1** is ca. 17 nm.

• Dynamic Light Scattering (DLS)

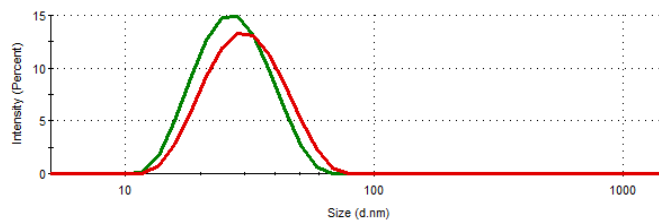


Figure S2. Hydrodynamic diameter of citrate coated AuNPs (28 nm, green) and **GNP1** (30 nm, red).

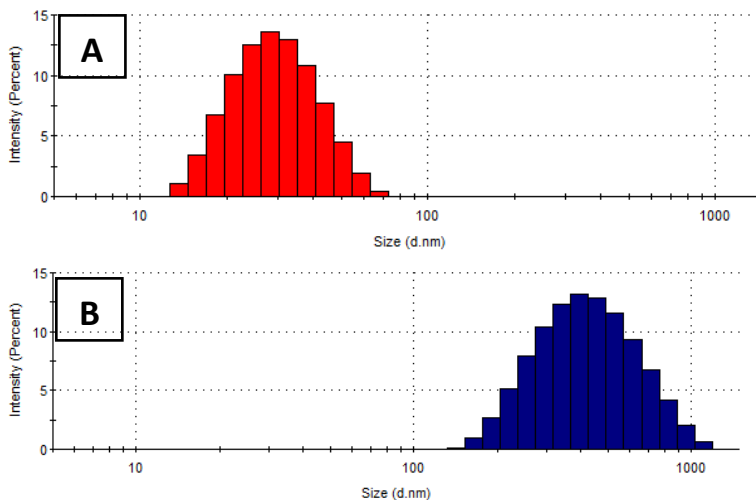


Figure S3. (A) Hydrodynamic diameter of **GNP1** in the absence of NMN (30 nm, red) and (B) in the presence of NMN (5 mM) (450 nm, blue).

- Fourier-transform infrared spectroscopy (FTIR)

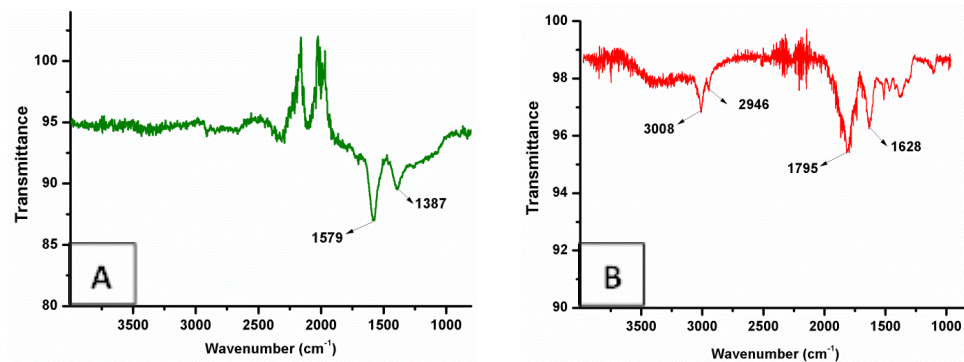


Figure S4. FT-IR spectra of (A) Citrate-capped AuNPs. Citrate shows bands at 1579 and 1387 cm^{-1} , and (B) **GNP1**, showing bands corresponding to both **L1** (3008, 2946 and 1795 cm^{-1}) and **L2** (3370, and 1628).

- Kinetic studies

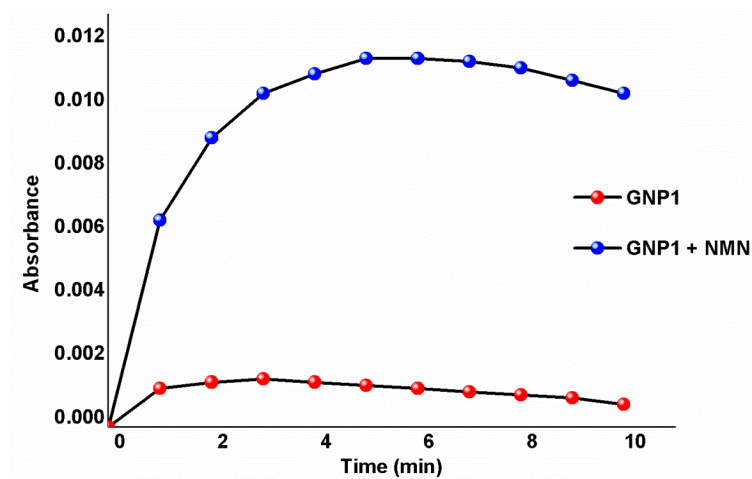


Figure S5. Kinetic profiles of **GNP1** at 612 nm in the absence (red) and in the presence of 5 mM of NMN (blue).

- UV-Vis of interferences

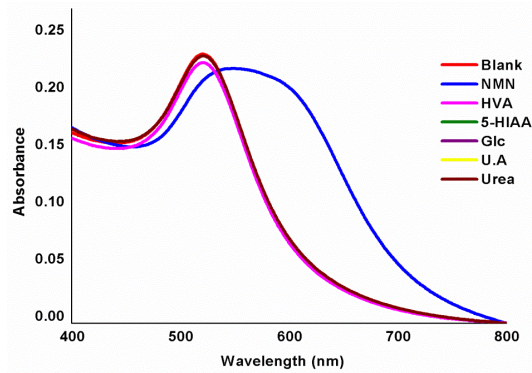


Figure S6. UV-Vis spectra of **GNP1** in the presence of different neurotransmitters metabolites and biological molecules (at 5 mM concentration).

- Determination of LOD

The limit of detection (LOD) for NMN was obtained from the plot of the ratio of the absorbance intensities at 523 and 612 nm (A_{612}/A_{523}) versus NMN concentration in μM . LOD was calculated by using the equation (1), where $K=3$; S_b is the standard deviation of the blank and m is the slope of the calibration curve. The resulting LOD was 4.7 μM (**GNP1**) and 0.2 μM (**OGNP1**).

$$LOD = K \cdot \frac{S_b}{m} \quad (1)$$

- Response in urine

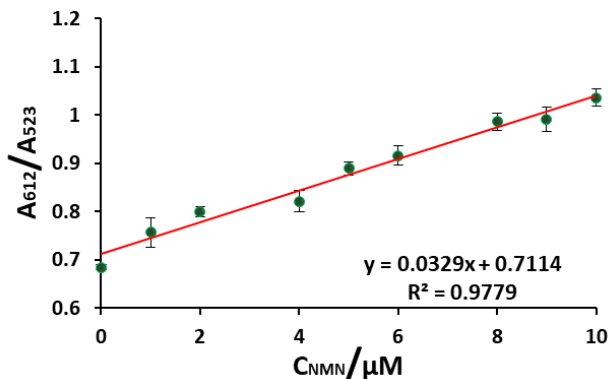


Figure S7. Plot of the A_{612}/A_{523} vs. NE concentrations within the 0-10 μM range

- **Determination of recovery and accuracy of the method**

Recovery and accuracy of the method were calculated according to Suresh Kumar methods¹.

KNOWN CONCENTRATION (μM)	FOUND CONCENTRATION μM	RECOVERY % ^{A)}	ACCURACY% ^{B)}
1 μM	1.5 μM	66%	0.25 %
5 μM	5.4 μM	92%	-0.04 %
9 μM	8.4 μM	107%	-0.02 %

Table S1. OGNP1 in urine **A)** % recovery (found concentration/known concentration) \times 100, **B)** Accuracy was calculated from (found concentration – known concentration/known concentration) \times 100.

- **Comparative experiments with GNP1 and GNP2**

GNP	TEM (nm)	DLS (nm)
GNP1	17 nm	30 nm
GNP2	34 nm	38 nm

Table S2. DLS and TEM of **GNP1** and **GNP2**.

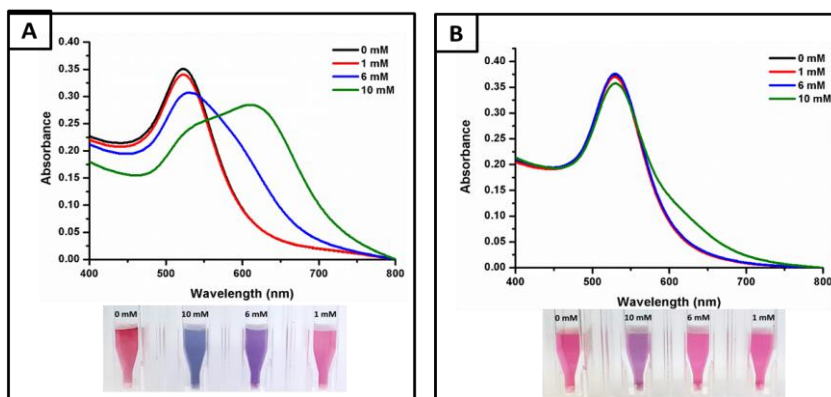


Figure S8. **A.** UV-Vis spectra and vials of **GNP1** in the presence of different concentrations of NMN. **B.** UV-Vis spectra and vials of **GNP2** in the presence of different concentrations of NMN.

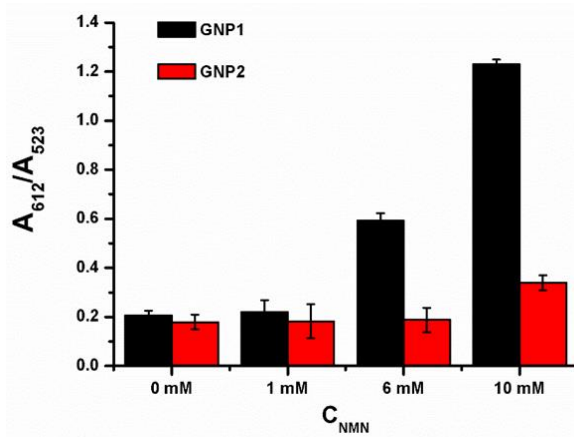


Figure S9. Representation of A_{612}/A_{523} for **GNP1** and **GNP2** in presence of different amounts of NMN. Error bars correspond to the s. d. from three independent experiments.

• References

1. K. A. Rawat, R. K Singhal, S. K. Kailasa, Colorimetric and fluorescence “turn-on” methods for the sensitive detection of bromelain using carbon dots functionalized gold nanoparticles as a dual probe, *RSC Adv.* 6 (2016) 32025-32036.

Chapter 4:

Design of mesoporous nanodevices for controlled cargo release triggered by neurotransmitters

4.1 Introduction

In recent times, advances in nanomedicine have allowed the development of smart delivery systems, based on the use of nanostructures as delivery agents capable of encapsulating drugs and releasing them to target tissues in response to a specific stimulus.¹

In this field, gated materials based on mesoporous silica nanoparticles (MSNs) have been widely used. These nanodevices are generally composed of two subunits: (i) a porous inorganic support, in which a cargo is entrapped; and (ii) selected molecular and/or supramolecular entities, grafted onto the external surface, which control mass transport from the pores to the solution.

Being able to deliver in a selective manner the entrapped cargo in the presence of a specific stimulus is one of the main challenges faced in the development of smart delivery systems. Therefore, the use of enzymes as a functional component of these nanodevices becomes an appealing concept towards the construction of smart devices with advanced capabilities.²

The enzymes can be defined as the “catalysts of the life and nature”. Enzymes accelerate the velocity of reactions that otherwise would take too long or would not take place at all in a biological environment and make them possible in a time short enough to be compatible with life. They are involved in vital processes such as reactions needed to digest food, send nerve signals, contract muscles and many others.³

Enzymes have two extraordinary properties:

- (i) **Very efficient catalysts transforming biomolecules into new products;** enzymes are able to accelerate reactions by as much as 10^{17} -fold and, in some cases, the increase is even higher. For instance, the velocity constant for the hydrolysis of methyl phosphate is $10^{-20} \text{ M}^{-1} \text{ s}^{-1}$ without enzyme and $1.2 \times 10^6 \text{ M}^{-1} \text{ s}^{-1}$ in the presence of alkaline phosphatase.⁴ That

is a 10^{26} -fold increase and means that instead of taking a billion of years, the hydrolysis only takes milliseconds. The extraordinary efficiency of enzymes comes from the reduction of the reaction activation energy via interaction of substrates with the enzyme's active site. Using this property, the incorporation of enzymes as a functional component of the delivery systems allows designing delivery systems that release the cargo as a result of the enzymatic reaction.

(ii) **High selectivity;** enzymes are capable of discriminating between closely related molecules and controlling reactions to yield a single product. Specificity is achieved by binding pockets with complementary shape, charge and hydrophilic/hydrophobic characteristics to the substrates. Enzymes can therefore distinguish between very similar substrate molecules in chemoselective, regioselective and stereospecific manner.⁵ To explain the observed specificity of enzymes, in 1894 Emil Fischer proposed that both the enzyme and the substrate possess specific complementary geometric shapes that fit exactly into one another.⁶ This is often referred to as "the lock and key" model (see Figure 1). Later in 1958, Daniel Koshland suggested a modification of the lock and key model and proposed the "induced fit model", also known as the "glove and hand model".⁷ It takes into account that enzymes are flexible structures and once the substrate interacts with the active site, there is a molding effect that enables the enzyme to perform its catalytic function. This remarkable selectivity described above allows the development of highly selective enzyme controlled delivery systems.

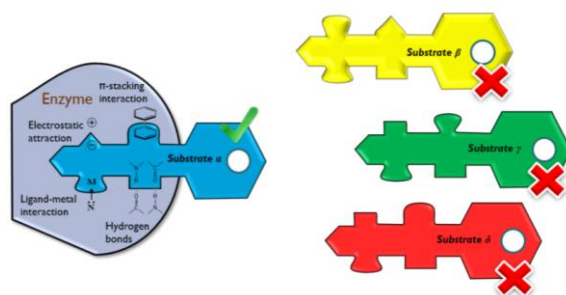


Figure 1. Schematic representation of the "Lock and key model" to explain the observed specificity of enzymes.

Enzymes as components of delivery systems are used as:

- (i) **Recognition element**, due to the selective and sensitive detection of the molecule of interest. Once the enzyme has recognized the analyte, the delivery of the cargo (opening of the pores of the mesoporous nanoparticles) can be produced by a secondary product resulted from the interaction of the enzyme-analyte, the metabolite of the analyte or by a change in the pH of the environment.
- (ii) **Bulky capping units**, owing to their large size enzymes are suitable for capping the pores of the mesoporous nanoparticles. These enzymes can be covalently or electrostatically bonded to the surface of the mesoporous materials. Once the enzyme has interacted with the analyte of interest, this bond can be broken with a subsequent delivery of the entrapped cargo.

In this area Aznar et al. developed a glucose-responsive system,⁸ which uses the enzyme glucose oxidase (GOx). In this system MSNs were loaded with $\text{Ru}(\text{bpy})_3^{2+}$, functionalised with benzimidazole groups and capped with GOx that had been previously modified with β -cyclodextrin (β -CD). The CD groups in CD-GOx formed an inclusion complex with the propylbenzimidazole molecule anchored on the surface of the nanoparticles and capped the pores. In the presence of glucose, the GOx catalysed oxidation of glucose to gluconic acid, which induced the protonation of the benzimidazole group, resulting in CD-GOx displacement and clear cargo delivery (see figure 2).

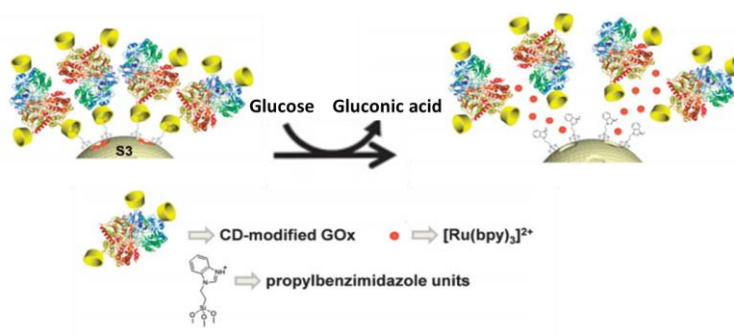


Figure 2. Delivery paradigm of the glucose-responsive system. Reprinted with permission from *Chem comm*, 2013, 49, 6391-6393.

On the other hand Villalonga and co-workers reported a new delivery system based on Janus-type nanoparticles with opposing Au and mesoporous silica faces in which the urease enzyme mediated the conversion of urea to ammonia and the consequent cargo delivery.⁹ In particular, the gold face was functionalised with a thiol-modified urease enzyme. Previously, the mesoporous silica face was loaded with $\text{Ru}(\text{bipy})_3^{2+}$ and functionalised on the external surface with 3-(2-aminoethylamino)propyl trimethoxysilane that acted as a molecular gate. The gate was closed at pH 5.0 due to the protonation of polyamines. In the presence of urea, a clear delivery of the entrapped ruthenium complex took place. The opening mechanism was based on transforming urea into CO_2 and NH_3 by urease, which induced a rise in pH and the subsequent deprotonation of polyamines.

As described above the incorporation of enzymes as functional components of delivery systems make possible the fabrication of versatile nanodevices able to release the cargo as a result of an enzymatic reaction. However, the design and development of systems capable to responds at the presence of neurotransmitter is scarcely explored.

Therefore, taking into account: **(i)** the increasing interest in developing new therapies for the treatment of neurotransmitter related neurological disorders, **(ii)** the lack of delivery systems responsive to neurotransmitters **(iii)** and the interesting properties of the enzymes as a functional component of gated nanodevices; this part of this thesis is aimed at designing, preparing and evaluating different neurotransmitter responsive delivery systems based on mesoporous silica nanoparticles and Janus nanoparticules controlled by enzymes.

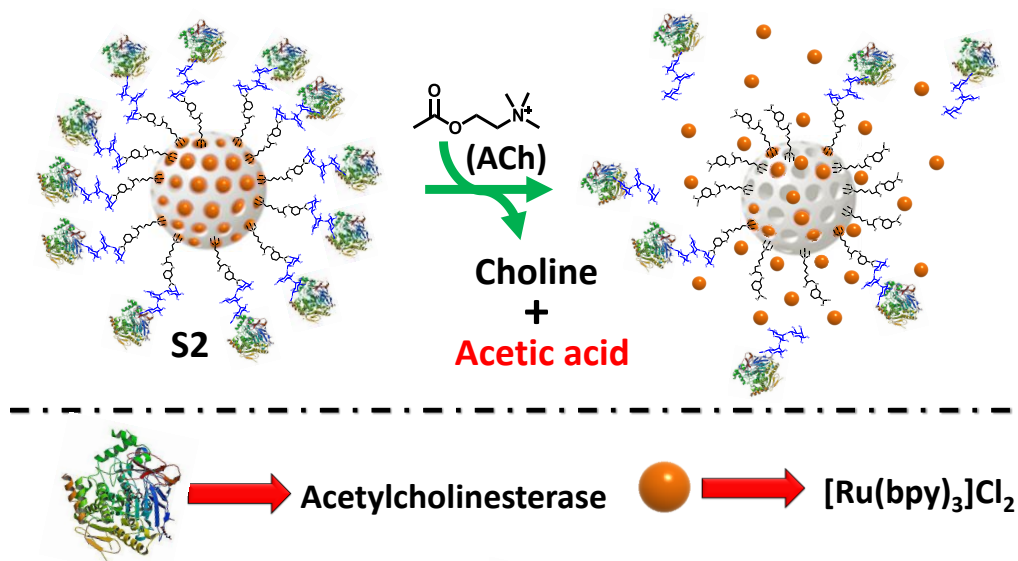
4.2 References

1. **a)** E. R. Balmayor, H. S. Azevedo, R. L. Reis, *Pharm. Res.*, **2011**, 28, 1241-1258. **b)** S. S. Suri, H. Fenniri, B. Singh, *J Occup Med Toxicol.*, **2007**, 2, 16. **c)** J. K. Patra, G. Das, L. F. Fraceto, E. V. R. Campos, M. del Pilar Rodriguez-Torres, L. S. Acosta-Torres, L. A. Diaz-Torres, R. Grillo, M. K. Swamy, S. Sharma, S. Habtemariam, H. S. Shin, *Journal Nanobiotechnology*, **2018**, 16, 71.
2. A. Llopis-Lorente, B. Lozano-Torres, A. Bernardos, R. Martínez-Mañez, F. Sancenón, *J. Mater. Chem. B*, **2017**, 5, 3069-3083.

3. **a)** G. M. Cooper, The central role of enzymes as biological catalysts. *Sinauer Associates*, 2000. **b)** P. K. Robinson, *Essays Biochem*, **2015**, 59, 1-41.
4. F. J. Plou, Las enzimas, *CSIC*, **2016**.
5. L. Hedstrom, Enzyme specificity and selectivity, *e LS*, **2001**.
6. E. Fischer, *Ber. Dtsch. Chem. Ges.* **1895**, 28, 1429-1438.
7. D. E. Koshland, *Proc. Natl. Acad. Sci.*, **1958**, 44, 98-104.
8. E. Aznar, R. Villalonga, C. Giménez, F. Sancenón, M. D. Marcos, R. Martínez-Máñez, P. Díez, J. M. Pingarrón, P. Amorós, *Chem comm*, **2013**, 49, 6391-6393.
9. R. Villalonga, P. Díez, A., Sánchez, E., Aznar, R., Martínez-Máñez, J. M. Pingarrón, *Chemistry—A European Journal*, **2013**, 19, 7889-7894.

Chapter 4: Part 1

Acetylcholine-responsive cargo release using acetylcholinesterase-capped nanomaterials



Acetylcholine-responsive cargo release using acetylcholinesterase-capped nanomaterials

Tania M. Godoy-Reyes^{abc}, Antoni Llopis-Lorente^{abd}, Alba García-Fernández^{abd}, Pablo Gaviña^{abc}, Ana M. Costero^{abc}, Ramón Martínez-Máñez^{*abd} and Félix Sancenón^{abd}

^a Instituto Interuniversitario de Investigación de Reconocimiento Molecular y Desarrollo Tecnológico (IDM), Universitat Politècnica de València, Universitat de València, Spain.

^b CIBER de Bioingeniería, Biomateriales y Nanomedicina (CIBER-BBN), Spain.

^c Departamento de Química Orgánica, Universitat de València, Doctor Moliner 50, Burjassot, 46100, Valencia, Spain. E-mail: ana.costero@uv.es

^d Departamento de Química, Universitat Politècnica de València, Camino de Vera s/n, 46022, Valencia, Spain. E-mail: rmaez@qim.upv.es

Published online: 25th April 2019

(Reprinted with permission from *Chem. Commun.*, 2019, 55, 5785)

Abstract

Mesoporous silica nanoparticles capped with acetylcholinesterase, through boronic ester linkages, selectively release an entrapped cargo in the presence of acetylcholine.

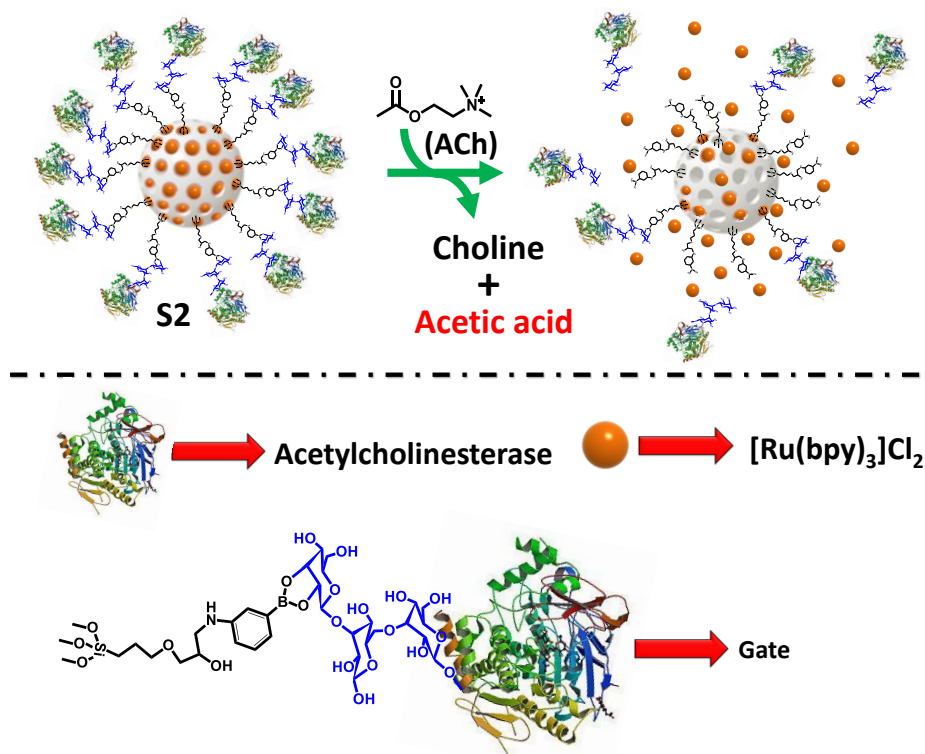
Introduction

Acetylcholine (ACh) is one of the most important neurotransmitters in the central nervous system (CNS) and in the peripheral nervous system (PNS).¹ ACh is synthesized in neuron terminals by acetylation of choline with acetyl coenzyme A in a reaction catalysed by the enzyme choline acetyltransferase.² In the CNS, ACh is responsible for modulating the activity of the neurons which control motivation, excitement and attention.³ It is a key neurotransmitter to maintain memory and promote learning, in addition to favour brain neuroplasticity.⁴ On the other hand in the PNS, ACh is responsible for transmitting signals between motor nerves and muscles, contributing to the contraction of the cardiac, skeletal and smooth muscles.⁵ Low levels of ACh are related to neurodegenerative pathologies such as Alzheimer,⁶ and myasthenia gravis.⁷ In contrast, high levels of ACh are responsible for movement disorders such as dystonia⁸ and Parkinson's disease.⁹ The high concentrations of ACh in the movement disorders are caused by an imbalance between cholinergic and dopaminergic activity, generating a dopamine depletion which blocks the autoinhibition of acetylcholine release through muscarinic autoreceptors, leading to excessive acetylcholine release to the synaptic cleft.¹⁰

From another point of view, the design of smart delivery systems able to release an entrapped cargo in response to a specific stimulus is receiving increasing attention in recent years.¹¹ For the development of these smart delivery systems inorganic scaffolds, liposomes, polymers and metallic nanoparticles are commonly used as nanocarriers.¹² Among them, mesoporous silica nanoparticles (MSNs) offer appealing features such as high loading capacity, uniform pore distribution, biocompatibility, thermal stability, easy synthesis, tuneable size and easy functionalization.¹³ Additionally, the external surface of the loaded MSNs can be functionalized with molecular or supramolecular architectures which change their

shape and/or size upon application of external stimuli.¹⁴ In the absence of stimuli, pores are blocked preventing cargo release whereas in their presence a marked delivery is observed. Gated MSNs that respond to physical and (bio)chemical stimuli have been developed.¹⁵ Notwithstanding, the design of gated materials that respond to small biomolecules remains more challenging and comparatively fewer examples have been reported.¹⁶

Given the relevance of ACh as a key neurotransmitter and our interest in the development of stimuli-responsive gated materials for biomedical applications, we present herein a simple strategy to design ACh-responsive delivery systems based on the use of the enzyme acetylcholinesterase. Acetylcholinesterase is a glycoprotein that catalyses the breakdown of acetylcholine at the synaptic cleft. In our approach, acetylcholinesterase plays the following roles: (i) acts as capping agent, anchored to the external surface of the support through the formation of hydrolysable phenylboronic esters; (ii) acts as recognition unit, capable of detecting ACh; (iii) acts as anticholinergic agent by breaking down ACh, and, finally, (iv) acts as mediator agent, that generates acid molecules which induce the uncapping of the support. As a support, we have used MSNs that are loaded with a fluorescent cargo ($[\text{Ru}(\text{bpy})_3]\text{Cl}_2$) and functionalized with phenylboronic acid residues on the external surface. Oligosaccharide groups of the enzyme are linked to phenylboronic acid residues by the formation of boronic acid cyclic esters, a well-known strategy previously used for the immobilisation of glycoproteins on electrodes and surfaces.¹⁷ Acetylcholinesterase induces the rupture of ACh into choline and acetic acid. The later induces the hydrolysis of acid-sensitive boronic esters and the uncapping of the pores, resulting in cargo release (see **Scheme 1**).



Scheme 1. Representation of the design and performance of the acetylcholinesterase-capped nanodevice **S2** for cargo release in response to ACh.

To prepare the ACh-responsive nanodevice, MSNs were synthesized via a sol-gel template method (solid **S0**). **S0** was suspended in acetonitrile and treated with (3-glycidyloxypropyl)trimethoxysilane for 5.5 h. Then, 3-aminophenylboronic acid was anchored by nucleophilic attack of the amine to the highly reactive epoxide on the silica surface. The pores were loaded with the fluorescent dye $[Ru(bpy)_3]Cl_2$ as a model cargo (**S1**). **S1** was finally capped with acetylcholinesterase, via the formation of cyclic phenylboronic acid esters between the oligosaccharide chains of the glycoenzyme and the phenylboronic groups on the nanoparticles surface, yielding **S2**.

The prepared materials were characterised by different standard techniques. Powder X-ray diffraction (PXRD) of the as-made nanoparticles showed the (100) low-angle reflection Bragg peak at around 2.2° which is characteristic of MCM-41-

type porous materials, with a slight displacement to 2.4 after surfactant removal (see Figure 1A). The presence of this peak in the PXRD pattern of **S1** confirmed that the functionalization and loading processes had not damaged the mesoporous 3-D structure. From N₂ adsorption–desorption isotherms (see Figure 1B), pore volume and pore size of **S0** were determined as 0.715 cm³ g⁻¹ and 2.52 nm, respectively, by applying the BJH model¹⁸ on the absorption branch of the isotherm. The volume of N₂ adsorbed considerably decreased from the empty solid **S0** to the loaded nanoparticles **S1** due to the filling of the pores with the cargo. A large specific surface area of 1141.13 m² g⁻¹ was determined for **S0** according to the BET model,¹⁹ whereas it reduced to 20.46 m² g⁻¹ for **S1**. Transmission electron microscopy (TEM) images of **S0**, **S1** and **S2** confirmed the formation of nanoparticles (average diameter of 92 ± 10 nm) with spherical morphology and porous structure, that was preserved after the functionalization processes (see Figure 1C). Additionally, the surface modification was confirmed by chemical methods such as solid-state ¹³C-NMR, ¹¹B-NMR, FTIR, and UV-visible (see Figure S1–S4). The zeta potential of the starting **S0** nanoparticles was –30.5 mV and decreased to –12.7 mV for **S1** due to its functionalization with phenylboronic acid residues. For the final nanodevice **S2**, the surface charge increased (–24.1 mV) compared to **S1** as a consequence of enzyme capping (see Figure S5). The hydrodynamic diameter of the final nanodevice **S2** was determined to be 152 nm using dynamic light scattering (DLS) measurements (see Figure S6). Besides, the content of grafted aminophenylboronic moiety (53 mg per g of solid) and [Ru(bpy)₃]Cl₂ (270 mg per g of solid) on **S1** were estimated by elemental analysis. The boron and ruthenium content were determined by Inductively coupled plasma mass spectrometry (ICP-MS) and amounted to 5.10 ± 0.03 and 44.7 ± 0.3 mg per g of **S1**, respectively. Moreover, the immobilization of acetylcholinesterase on **S2** was confirmed by a specific enzymatic assay (see Figure S7). Additionally, the amount of protein was quantified as 58.5 mg per g of **S2** according to the Bradford method (see Figure S8). The key role played by the phenylboronic linker in the attachment of the enzyme was confirmed by control experiments using non-functionalized MSNs (see Figure S13 and S14). The total loaded [Ru(bpy)₃]Cl₂ dye in the final nanodevice **S2** was 34 mg g⁻¹ (determined via several extractions of the dye content in water at pH 3, and spectrophotometric measurement).

Finally, **Figure 1D and S9** shows scanning transmission electron microscopy coupled with energy dispersive X-ray spectroscopy (STEM-EDX) mapping of several elements on the final nanodevice **S2** attributed to the different components: Si and O (silica scaffold), C and N (cargo, aminophenylboronic moiety and enzyme), B (boronic ester), and S (cysteine groups of the enzyme).

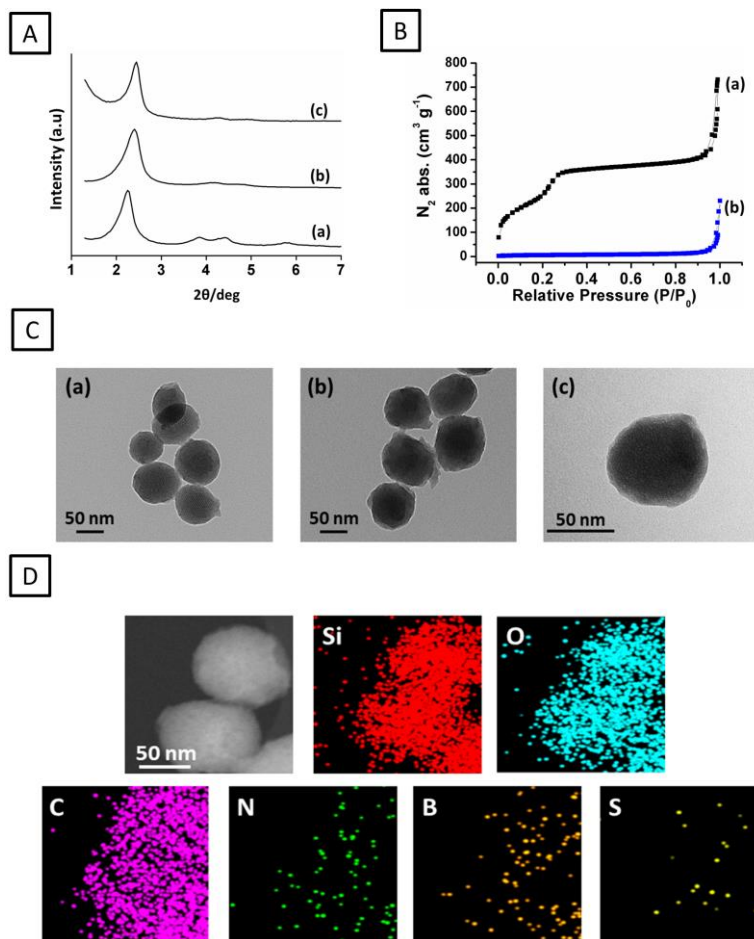


Figure 1 (A) PXRD of (a) as-made MS nanoparticles, (b) calcined support **S0**, and (c) loaded and functionalized nanoparticles **S1**. (B) N_2 adsorption–desorption isotherm for (a) **S0** and (b) **S1** nanoparticles. (C) TEM images of (a) **S0**, (b) **S1**, and (c) final nanodevice **S2**. (D) STEM image and STEM-EDX mapping of different atoms on the final nanodevice **S2**.

Once characterized, cargo release from **S2** was evaluated in aqueous media in the absence and presence of ACh. In a typical release experiment, aqueous (pH 7.5, 20 mM Na₂SO₄) **S2** suspensions (2 mg mL⁻¹) in the absence and in the presence of ACh (1 mM) were shaken at room temperature. Aliquots were taken at different times, centrifuged (to eliminate the nanoparticles), and the amount of cargo released to the solution was assessed by measuring the emission band of [Ru(bpy)₃]Cl₂ at 595 nm ($\lambda_{\text{exc}} = 435$ nm). The obtained delivery kinetics profiles are shown in **Figure 2**. In the absence of ACh, cargo release from **S2** was negligible which confirms the correct capping of the nanoparticles. On the contrary, in the presence of ACh, a remarkable and fast delivery of the payload was observed in less than 5 minutes, which could be appreciated even to the naked eye (see **Figure S11**). This fast and effective response is attributed to the rapid action of acetylcholinesterase (turnover number = $7.4 \times 10^5 \text{ min}^{-1}$)²⁰ which is an enzyme naturally prepared to catalyse very fast in order to regulate muscle contraction and synaptic transmission in the nervous system. ACh is hydrolysed by the enzyme into choline and acetic acid (pKa = 4.75),²¹ which triggers the rupture of the acid-sensitive boronic cyclic esters and results in the detachment of the enzyme and the delivery of the payload.

A reduction in the pH of the solution was observed after release experiment in the presence of ACh, thus confirming the formation of acetic acid (see **Figure S15**). Furthermore, in order to confirm enzyme detachment from the nanoparticles surface, we measured the acetylcholinesterase activity on **S2** after ACh-triggered release and it decreased to 0.4 U mg⁻¹ (4.5 U mg⁻¹ for the control sample) (see **Figure. S12**).

In further control experiments, we confirmed that the release from **S2** is triggered at acidic pH (4.5). However, **S2** remained capped at slightly acidic pH (6.5) such as the one found in tumours and some intracellular compartments (see **Figure S16 and S17**).²² On the other hand, release experiments with **S1** (without the enzyme) in the presence and absence of ACh were also carried out. The obtained results (see **Figure S18**) showed a marked cargo release in both cases. This confirms the key role played by the enzyme on the performance of the nanodevice.

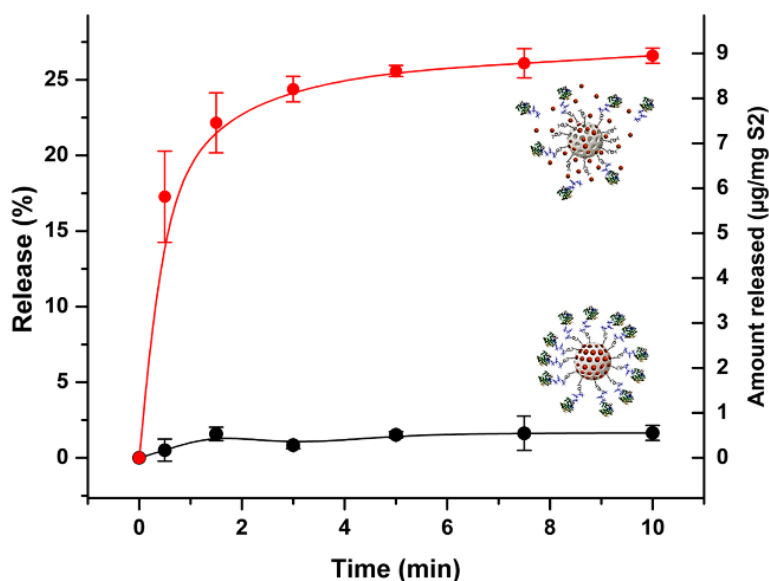


Figure 2 Kinetics of cargo release from **S2** (2 mg mL^{-1}) in aqueous media (pH 7.5) in the presence of ACh (1 mM, red curve) and absence of ACh (black curve) determined by measuring $[\text{Ru}(\text{bpy})_3]\text{Cl}_2$ fluorescence at 595 nm ($\lambda_{\text{exc}} = 453 \text{ nm}$). Error bars correspond to the s.d. from three independent experiments.

In order to assess the selectivity of the nanodevice, we evaluated the response of aqueous suspensions of **S2** (2 mg mL^{-1}) in the presence of other relevant neurotransmitters such as epinephrine (Epi), norepinephrine (NE), dopamine (DA), serotonin (5-HT), gamma-Aminobutyric acid (GABA), glutamate (Glu), aspartate (Asp), and glycine (Gly) at 1 mM concentration. The obtained emission intensities at 595 nm (due to $[\text{Ru}(\text{bpy})_3]\text{Cl}_2$ release) after 10 min are shown in **Figure 3**. As could be seen, **S2** nanodevice remained closed in the presence of these neurotransmitters whereas a selective cargo release occurred only in the presence of ACh, suggesting that **S2** could be used for the selective detection of ACh.

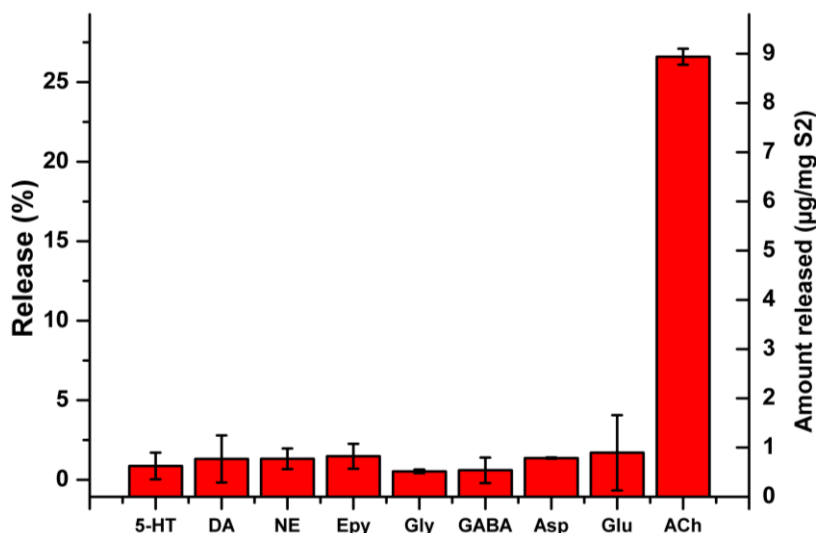


Fig. 3 Cargo release from **S2** (2 mg mL^{-1}) in aqueous media (pH 7.5) in the presence of selected neurotransmitters (1 mM) after 10 min.

In order to evaluate the sensitivity of the nanodevice, **S2** nanoparticles were exposed to different concentrations of ACh and the released cargo at a fixed time (10 min) was measured. As can be observed in **Figure S10**, the amount of cargo release was very low at acetylcholine concentrations below $25 \mu\text{M}$, whereas a significant and proportional increase occurred in the $0.025\text{--}10 \text{ mM}$ concentration range. This indicates that **S2** would remain closed in blood, where the concentration of ACh is around 9 nM .²³ In contrast, in patients suffering from Parkinson's disease the levels of ACh in synaptic vesicles, neuromuscular junctions and synaptic clefts are higher than 100 mM , 3 mM and 0.5 mM respectively,²³ suggesting that **S2** nanoparticles could be able to release the cargo in these target regions.

Finally, we aimed to demonstrate that this delivery system could operate in more complex biological environments. To this end, we prepared **S2_{dox}**, a solid like **S2** but loaded with the cytotoxic drug doxorubicin. The amount of loaded doxorubicin was quantified as 195 mg per g of **S2_{dox}** by spectrophotometry, with a release efficiency of ca. 31% in in vitro release experiments conducted in a similar way as describe above (see **Figure S20**). Next, as a proof of concept, human HeLa cell²⁴ culture media (DMEM supplemented with 10% FBS)²⁵ were treated with 50

$\mu\text{g mL}^{-1}$ of **S2_{dox}** for 30 min, washed to remove non-internalized particles and further incubated for 24 h in the absence or presence of ACh (50 mM). After 24 h of incubation, cell viability was determined by means of the WST-1 cell proliferation reagent. Cell viability remained nearly to 100% in the presence of ACh or in the presence of **S2_{dox}**, whereas it reduced to 72% upon treatment with the equivalent amount of free doxorubicin (**Figure 4A**).

Remarkably, a significant reduction in cell viability (ca. 40%) was observed in the simultaneous presence of both, **S2_{dox}** and ACh, which was ascribed to the recognition of the neurotransmitter by the nanodevice and the subsequent release of the drug. Additionally, release of doxorubicin in cells was directly visualized by means of confocal microscopy imaging. For these experiments, cells were incubated with **S2_{dox}** for 2 h in the absence or presence of ACh, washed to remove non-internalized particles and stained with DNA marker Hoechst 3342 (blue). A clear doxorubicin-associated fluorescence (red) was observed for cells treated with **S2_{dox}** in a culture media containing ACh (**Figure 4B**). These results confirm the ability of the nanodevice to recognise ACh and deliver the payload despite the presence of cellular metabolites and other potential interferences found in cell culture media.

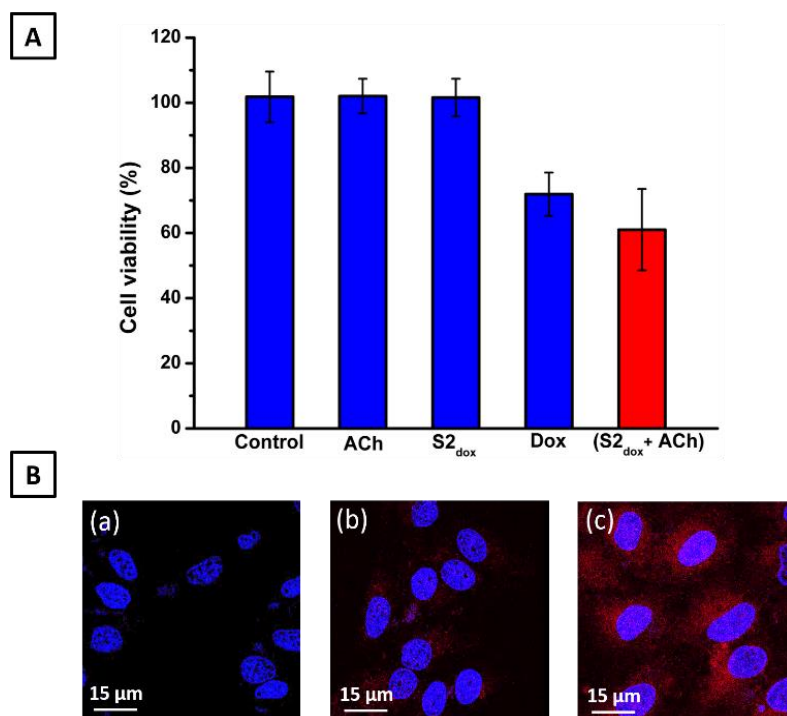


Figure 4 Experiments in cell culture media (DMEM supplemented with 10% FBS). (A) HeLa cell viability for the control experiment (no ACh and no S2_{dox}), incubation with ACh (50 mM), incubation with S2_{dox} (50 μg mL⁻¹), incubation with the equivalent amount of free doxorubicin, and incubation with both ACh and S2_{dox}. Error bars correspond to the s. d. from three independent experiments containing triplicates. (B) Confocal microscopy images of HeLa cells (showing nuclei-marker fluorescence in blue) for: (a) control experiment, (b) cells incubated with S2_{dox}, and (c) cells incubated with S2_{dox} in a medium containing ACh showing doxorubicin-associated fluorescence in red.

In conclusion, we report herein the design, synthesis and characterization of ACh-responsive delivery nanocarriers, based on the use of MSNs capped with the enzyme acetylcholinesterase using boronic ester linkers. In the presence of ACh, the neurotransmitter is detected by acetylcholinesterase and transformed into choline and acetic acid, which leads to the hydrolysis of boronic cyclic esters, the subsequent detachment of the enzyme and the uncapping of pores. The nanoparticles show a remarkable payload delivery in the presence of ACh in less than 5 min, whereas release is negligible in the absence of the neurotransmitter. Moreover, the nanodevice remains closed in the presence of other relevant neurotransmitters and responds selectively to ACh. Cargo release is negligible at

ACh concentrations present in human blood, whereas a significant payload delivery is observed in the 0.025–10 mM range, which coincides with typical concentration of ACh in synaptic vesicles, neuromuscular junctions and synaptic clefts in Parkinson's patients. We also demonstrate that the nanodevice shows an ACh-responsive behaviour in complex biological environments such as HeLa cells. We hope this study could inspire the development of smart nanosensors able to selectively detect ACh and/or nanocarriers for therapies with high effectiveness and minimal side effects for the future treatment of nervous system disorders such as Parkinson's.

Acknowledgment

The authors acknowledge financial support from the Spanish Government (MAT2015-64139-C4-1-R, MAT2015-64139-C4-4-R and AGL2015-70235-C2-2-R) and the Generalitat Valenciana (PROMETEO2018/024). T. Godoy-Reyes is grateful to Generalitat Valenciana for her Santiago Grisolia fellowship. A. García-Fernández is grateful to the Spanish Government for her FPU fellowship.

References

1. L. K. McCorry, *Am. J. Pharm. Educ.*, **2007**, 71, 78
2. W. M. Haschek, C. G. Rousseaux and M. A. Wallig, *Nervous System*, in *Fundamentals of Toxicologic Pathology*, 2nd edn, Academic Press CY, San Diego, **2010**, p. 377.
3. I. Klinkenberg, A. Sambeth and A. Blokland, *Behav. Brain Res.*, **2011**, 221, 430.
4. M. E. Hasselmo, *Curr. Opin. Neurobiol.*, **2006**, 16, 710
5. M. C. An, W. Lin, J. Yang, B. Dominguez, D. Padgett, Y. Sugiura, P. Aryal, T. W. Gould, R. W. Oppenheim, M. E. Hester, B. K. Kaspar, C. P. Ko and K. F. Lee, *Proc. Natl. Acad. Sci. U. S. A.*, **2010**, 107, 10702.
6. G. Ehrenstein, Z. Galdzicki and G. D. Lange, *Biophys. J.*, **1997**, 73, 1276
7. D. M. Fambrough, D. B. Drachman and S. Satyamurti, *Science*, **1973**, 182, 293.
8. D. E. Casey, J. Gerlach and E. Christensson, *Psychopharmacology*, **1980**, 70, 83.
9. A. L. Bartels and K. L. Leenders, *Cortex*, **2009**, 45, 915

10. T. Aosaki, M. Miura, T. Suzuki, K. Nishimura and M. Masuda, *Geriatr. Gerontol. Int.*, **2010**, 10, S148.
11. S. Mura, J. Nicolas and P. Couvreur, *Nat. Mater.*, **2013**, 12, 991.
12. (a) B. S. Pattni, V. V. Chupni and V. P. Torchilin, *Chem. Rev.*, **2015**, 115, 10938; (b) K. Ulbrich, K. Hola', V. Subr, A. Bakandritsos, J. Tucek and R. Zboril, *Chem. Rev.*, **2016**, 116, 5338.
13. F. Tang, L. Li and D. Chen, *Adv. Mater.*, **2012**, 24, 1504
14. N. Song and Y.-W. Yang, *Chem. Soc. Rev.*, **2015**, 44, 3474.
15. E. Aznar, M. Oroval, L. Pascual, J. R. Munguia, R. Martínez-Mañez and F. Sancenón, *Chem. Rev.*, **2016**, 116, 561.
16. F. Sancenón, L. Pascual, M. Oroval, E. Aznar and R. Martínez-Mañez, *ChemistryOpen*, **2015**, 4, 418.
17. (a) J. M. Abad, M. Vélez, C. Santamaría, J. M. Guisán, P. R. Matheus, L. Vázquez, I. Gazaryan, L. Gorton, T. Gibson and V. M. Fernández, *J. Am. Chem. Soc.*, **2002**, 124, 12845; (b) Y. Zhao, B. G. Trewyn, I. I. Slowing and V. S.-Y. Lin, *J. Am. Chem. Soc.*, **2009**, 131, 8398; (c) P. Díez, B. Esteban-Fernandez de Avila, D. E. Ramírez-Herrera, R. Villalonga and J. Wang, *Nanoscale*, **2017**, 9, 14307.
18. E. P. Barrett, L. G. Joyner and P. P. Halenda, *J. Am. Chem. Soc.*, **1951**, 73, 373.
19. S. Brunauer, P. H. Emmett and E. Teller, *J. Am. Chem. Soc.*, **1938**, 60, 309.
20. I. B. Wilson and M. A. Harrison, *J. Biol. Chem.*, **1961**, 236, 2292
21. N. V. Narendranath, K. C. Thomas and W. M. Ingledew, *J. Ind. Microbiol. Biotechnol.*, **2001**, 26, 171.
22. N. Zhang, F. Zhao, Q. Zou, Y. Li, G. Ma and X. Yan, *Small*, **2016**, 12, 5936.
23. (a) C.-I. Wang, W.-T. Chen and H.-T. Chang, *Anal. Chem.*, **2012**, 84, 9706; (b) A. Schena and K. Johnsson, *Angew. Chem., Int. Ed.*, **2014**, 53, 1302; (c) E. S. Vizi, A. Fekete, R. Karoly and A. Mike, *Br. J. Pharmacol.*, **2010**, 160, 785; (d) Y. Zhou, L.-L. Tan, Q.-L. Li, X.-L. Qiu, A.-D. Qi, Y. Tao and Y.-W. Yang, *Chem. – Eur. J.*, **2014**, 20, 2998.
24. W. F. Scherer, J. T. Syverton and G. O. Gey, *J. Exp. Med.*, **1953**, 97, 695.
25. S. Li, Q. Zou, Y. Li, C. Yuan, R. Xing and X. Yan, *J. Am. Chem. Soc.*, **2018**, 140, 10794.

Supporting Information

• Chemicals

Tetraethyl orthosilicate (TEOS), *n*-cetyltrimethylammonium bromide (CTABr), sodium hydroxide (NaOH), tris(2,2'-bipyridyl)dichlororuthenium(II) hexahydrate ($[\text{Ru}(\text{bpy})_3]\text{Cl}_2$), (3-glycidyloxypropyl)trimethoxysilane, 3-aminophenyl boronic acid, acetylcholine esterase from *Electrophorus electricus*, acetylcholine chloride, dopamine hydrochloride, serotonin hydrochloride, glycine, aspartic acid, glutamic acid, gamma-aminobutyric acid, L-norepinephrine hydrochloride, epinephrine hydrochloride, acetylthiocholine iodide, 5,5'-dithiobis(2-nitrobenzoic acid and methyl red were purchased from Sigma-Aldrich and used without purification. Sodium dihydrogen phosphate monohydrate, disodium hydrogen phosphate heptahydrate, sodium sulfate anhydrous and solvents were provided by Scharlau. Bradford dye reagent was provided by Bio-Rad. Deuterium oxide (99.8%) was acquired from Thermo Fisher Scientific. Doxorubicin hydrochloride was purchased from Carbosynth. For cell experiments, HeLa human cervix adenocarcinoma cells were purchased from the German Resource Centre for Biological Materials-DSMZ. Dulbecco's Phosphate Buffered Saline (PBS), Dulbecco's Modified Eagle's Medium (DMEM), Fetal Bovine Serum (FBS), and Hoechst 3342 were purchased from Sigma-Aldrich. WST-1 cell proliferation reagent WST-1 was purchased from Roche Applied Science.

• General methods

Powder X-ray diffraction (PXRD), N_2 adsorption-desorption isotherms, transmission electron microscopy (TEM), solid state nuclear magnetic resonance (NMR), Fourier-transform infrared spectroscopy (FTIR), dynamic light scattering (DLS), elemental analysis, inductively coupled plasma mass spectroscopy (ICP-MS), UV-visible and fluorescence spectrophotometry, and scanning transmission electron microscopy coupled with energy dispersive X-ray spectroscopy (STEM-EDX) were employed for materials characterization. PXRD measurements were performed on a Seifert 3000TT diffractometer using CuK_α radiation. N_2 adsorption-desorption isotherms were recorded on a Micromeritics TriStar II Plus automated

analyser. TEM images were acquired using a JEOL TEM-1010 Electron microscope working at 100 kV. DLS studies were performed using a ZetaSizer Nano ZS (Malvern). Elemental analysis was performed using a CE Instruments CHNS1100 analyser. UV-visible measurements were recorded with a JASCO V-650 Spectrophotometer. Fluorescence measurements were carried out in a JASCO FP-8500 Spectrophotometer. Solid State ^{13}C -NMR and ^{11}B -NMR were performed using a Bruker AV 400 WB Spectrometer. FTIR were performed with a Bruker Platinum ATR. The ICP-MS equipment employed was an Agilent 7900 ICP-MS with a standard sample introduction system consisting of a MicroMist nebulizer pump and Scott type spray chamber. Furthermore, STEM-EDX mapping was performed using a JEOL TEM-2100F microscope. A Bruker DRX-300 Spectrometer (300 MHz) was used for ^1H -NMR experiments. Cell viability was analysed using a Wallac 1420 workstation. Confocal microscopy imaging was performed by means of a Leica TCS SP8 AOBS inverted laser scanning confocal microscope (Leica Microsystems Heidelberg GmbH).

- **Synthesis of Mesoporous silica nanoparticles (S0)**

Firstly, the surfactant n-cetyltrimethylammonium bromide (CTABr) 1.00 g (2.74 mmol) was dissolved in 480 mL of distilled water and heated. Once the temperature reached 40 °C, 2.00 M of NaOH in distilled water (3.5 mL) was added to the CTABr solution, and then the temperature was further increased up to 80 °C. Then, TEOS 5.00 mL (22.4 mmol) were added dropwise. The mixture was kept under stirring for 2 h at 80 °C. The resulting white precipitate was isolated by centrifugation, washed with distilled water several times until pH 7.5 and dried at 70 °C overnight. Finally, the surfactant template was removed by calcination for 5 h at 550 °C, yielding the solid **S0**.

- **Synthesis of S1**

In order to functionalize the outer surface of **S0**, an excess of (3-glycidyloxypropyl)trimethoxysilane (500 μL , 2.26 mmol) was added to 100 mg of **S0**, and the suspension was stirred for 5.5 h at room temperature. The resulting solid was isolated by centrifugation, washed with acetonitrile and toluene, and dried at room temperature overnight. Then, the previously prepared solid and 154

mg (1.13 mmol) of 3-aminophenyl boronic acid were dispersed in 15 mL of toluene and was stirred for 24h. Afterward, the nanoparticles were isolated by centrifugation, washed with toluene and acetonitrile and dried at room temperature, which yielded the solid **S0-I**. Next, 100 mg of solid **S0-I** and 150 mg of [Ru(bpy)₃]Cl₂ were suspended in 15 mL of acetonitrile and stirred for 24 h at room temperature in order to load the pores. Finally, the solid was isolated by centrifugation, washed with toluene and dried, yielding the functionalized and loaded nanoparticles **S1**.

- **Synthesis of S2**

In order to cap the nanoparticles with the enzyme acetylcholinesterase, 5 mg of **S1** were mixed with 0.5 mg of enzyme in 500 μL of phosphate buffer pH 7.5 (50 mM). The mixture was stirred overnight at 4 °C. Then, the resulting solid (**S2**) was isolated by centrifugation, exhaustively washed with phosphate buffer, and kept in the refrigerator (4 °C) in phosphate buffer until use.

- **Synthesis of S2_{dox}**

For cells experiments, we prepared **S2_{dox}** (a solid like **S2** but loaded with the cytotoxic drug doxorubicin). In this case, the loading process was performed in water. Briefly, 5 mg of the boronic functionalized solid (S0-I) was dispersed in 500 μL of phosphate buffer pH 7.5 (50 mM) containing 2.5 mg of doxorubicin, and the mixture was stirred overnight. Then, 0.5 mg of enzyme were added and the solution was further stirred for 24 h at 4 °C. Then, the **S2_{dox}** was isolated by centrifugation, exhaustively washed with phosphate buffer, aliquoted, and kept in the freezer until use.

Materials characterization

• Solid-state NMR

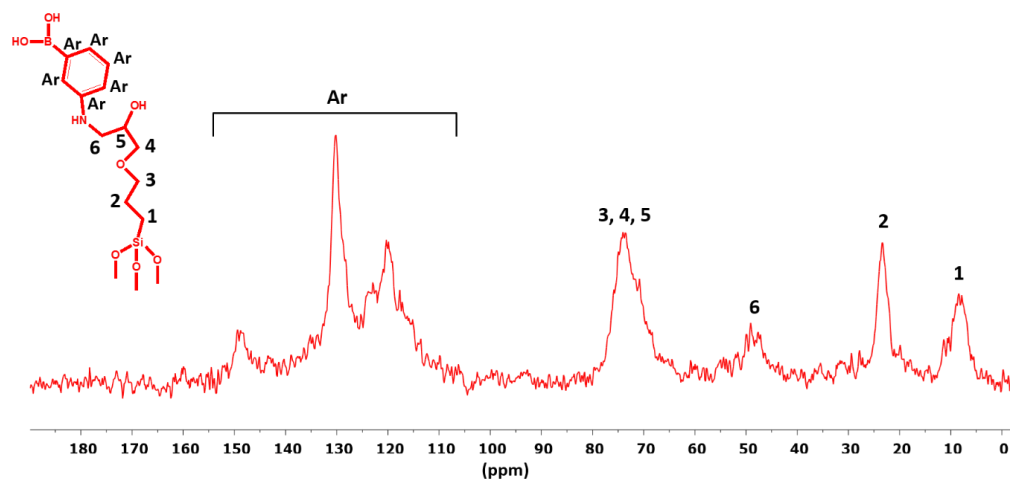


Figure S1. Solid-state ^{13}C -NMR of the 3-aminophenylboronic-functionalized nanoparticles (**S0-I**), showing the corresponding carbon signals from the organic functionalization.

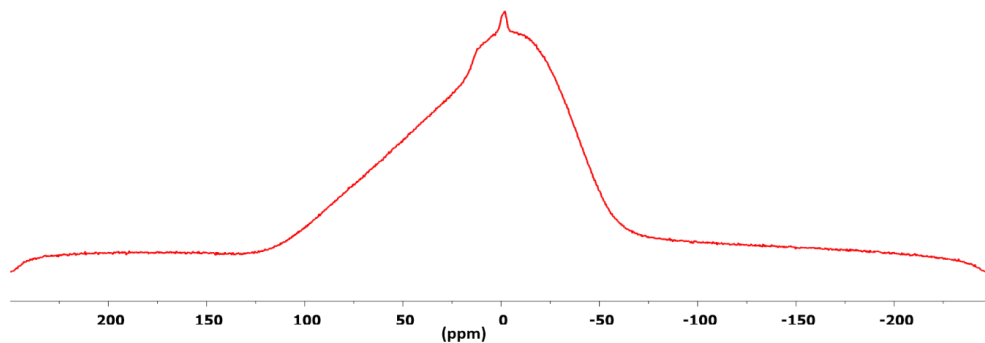


Figure S2. Solid-state ^{11}B -NMR of the 3-aminophenylboronic-functionalized nanoparticles (**S0-I**), confirming the presence of B.

- FTIR

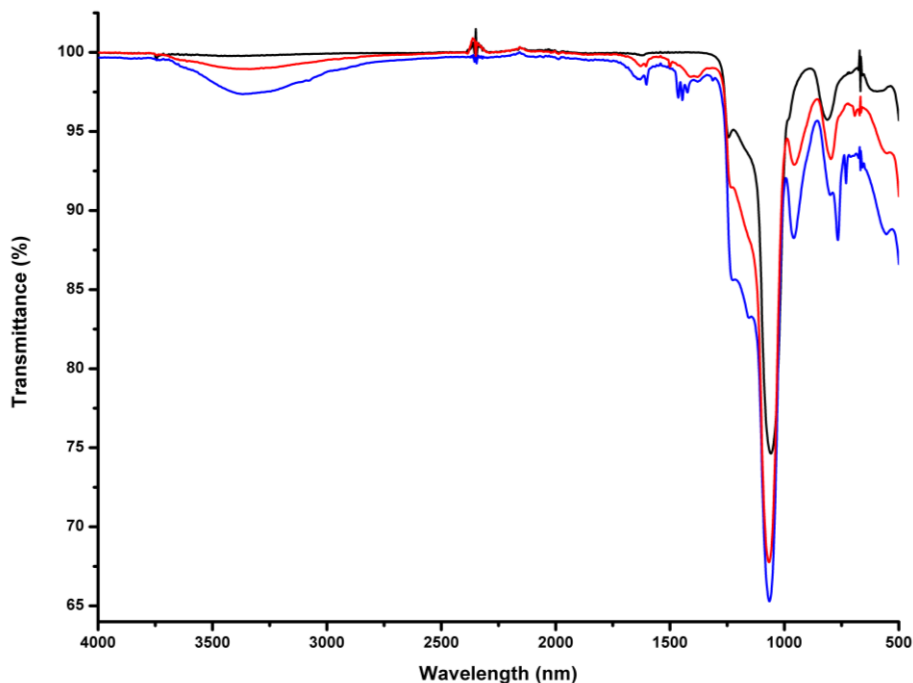


Figure S3. FTIR spectra of the MS nanoparticles (**S0**, black line), 3-aminophenylboronic-functionalized nanoparticles (**S0-I**, red line), and cargo-loaded nanoparticles (**S1**, blue line).

Figure SI-3 showed the FTIR spectrum of **S0**, **S0-I** and **S1** nanoparticles. As could be seen, the FTIR spectrum of **S0** showed the typical appearance for MSNs with a major band at ca. 1050 cm^{-1} corresponding to the Si-O stretching vibrations. After functionalization with 3-aminophenylboronic moieties, new peaks appear at around 3300 cm^{-1} , $1650\text{--}1350\text{ cm}^{-1}$, and 955 cm^{-1} which can be ascribed to the vibration of hydroxyl groups, C-C aromatic bonds and aliphatic C-C bonds, respectively. After cargo ($[\text{Ru}(\text{bpy})_3]\text{Cl}_2$) loading, new peaks corresponding to bipyridine rings between $1400\text{--}1470\text{ cm}^{-1}$ are observed.

- **UV-Vis**

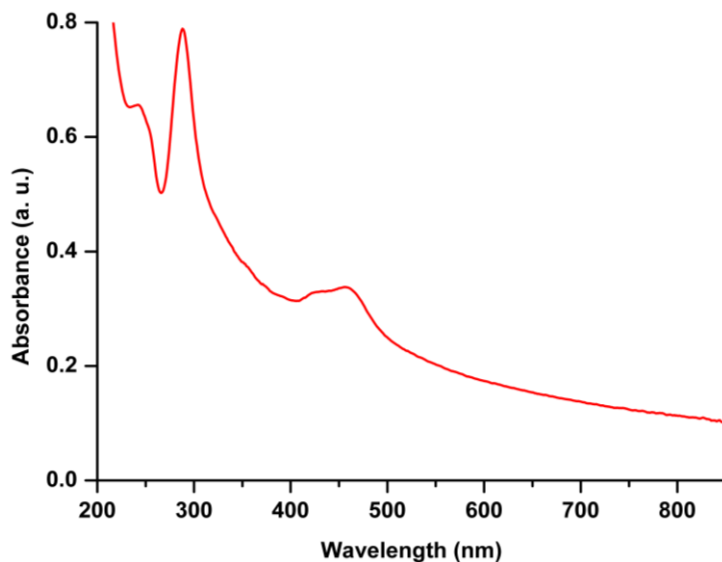


Figure S4. UV-visible spectrum of the final nanodevice **S2** (0.2 mg mL^{-1} in aqueous solution, pH 7.5), which shows a peak at 453 nm corresponding to the encapsulated dye.

- **Dynamic light scattering (DLS) studies**

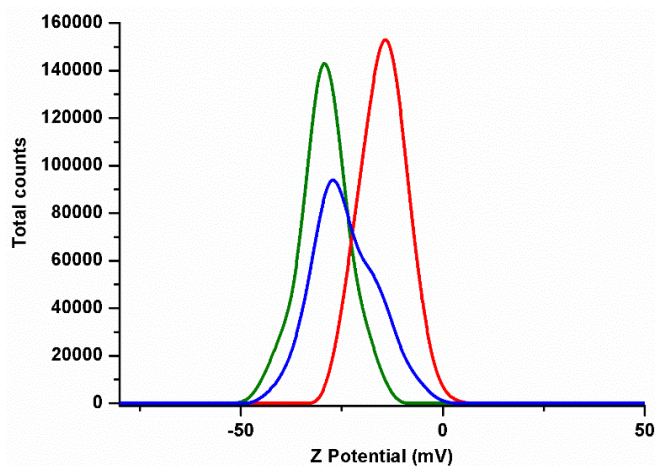


Figure S5. Z-potential curves for **S0** (green, -30.5 mV), **S1** (red, -12.7 mV) and **S2** (blue, -24.1 mV).

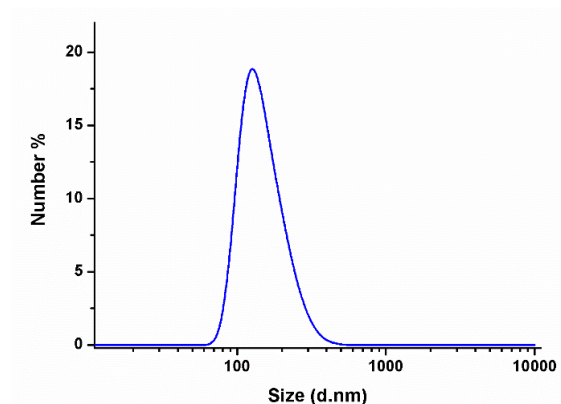


Figure S6. Hydrodynamic diameter distribution of the final nanodevice **S2** determined by DLS.

- **Elemental analysis**

Solid	%C	%H	%N
S0-I	3.63	1.72	0.54
S1	18.90	2.68	4.08

$$\text{Boronic ligand content} = \frac{0.545 \text{ g of N}}{100 \text{ g of solid}} * \frac{1 \text{ g of ligand}}{0.102 \text{ g of N}} = \frac{0.053 \text{ g of ligand}}{\text{g of solid}}$$

$$\text{Cargo content} = \frac{3.54 \text{ g of N}}{100 \text{ g of solid}} * \frac{1 \text{ g of [Ru(bpy)}_3\text{]Cl}_2}{0.131 \text{ g of N}} = \frac{0.27 \text{ g of [Ru(bpy)}_3\text{]Cl}_2}{\text{g of solid}}$$

- **Enzymatic activity assay**

Acetylcholinesterase activity on **S2** was measured based on the Ellman's assay.¹ An enzymatic unit (U) transforms 1 μmol of substrate per minute. Acetylcholinesterase is capable of hydrolysing acetylthiocholine into thiocholine and acetic acid. The generated thiocholine reacts with the Ellman's reagent (5,5'-dithiobis(2-nitrobenzoic acid), DTNB), cleaving its disulfide bond to give 2-nitro-5-thiobenzoate (TNB^{2-}) which has a characteristic yellow colour. In this assay, the formation of TNB^{2-} as a function of time is followed by monitoring absorbance at 412 nm during 2 minutes using a UV-visible spectrophotometer. The rate of transformation is directly proportional to the enzymatic activity of the sample.

In a typical assay, 900 μL of 100 mM sodium phosphate buffer (pH 7.5), 30 μL of 10 mM DTNB solution and 12 μL of acetylthiocholine (75 mM) were placed in a quartz cuvette. Then, 5 μL of either buffer (for blank) or **S2** nanoparticles (1 $\text{mg}\cdot\text{mL}^{-1}$) were added. The mixture was shaken and absorbance at 412 nm was monitored (Figure SI-7). When **S2** was added, the solution turned yellow quickly as a consequence of TNB^{2-} formation due to **S2**'s enzymatic activity.

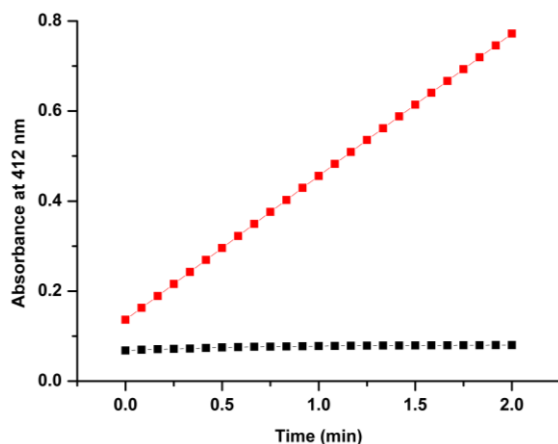


Figure S7. Monitoring of TNB^{2-} formation due to acetylcholinesterase activity upon addition of buffer (black points) and upon addition of **S2** (red points).

The acetylcholinesterase activity on **S2** was estimated to be $4784 \text{ U}\cdot\text{g}^{-1}$, by applying the following formula:

$$\frac{\text{Enzymatic Units}}{\text{g}} = \frac{(\Delta - \Delta_{\text{blank}}) * V_{\text{T}}}{\epsilon_{\text{TNB}} * l * V_{\text{NPs}} * C_{\text{NPs}}}$$

Where,

Δ is the slope of the graph (min^{-1})

Δ_{blank} is the slope of the graph for the blank (min^{-1})

V_{T} is the total volume in the cuvette

ϵ_{TNB} is the molar extinction of TNB^{2-} at 412 nm ($13.7 \text{ mM}^{-1} \cdot \text{cm}^{-1}$)

l is the optical path in the cuvette (1 cm)

V_{NPs} is the volume of nanoparticles added (mL)

C_{NPs} is the concentration of nanoparticles suspension added ($\text{g}\cdot\text{mL}^{-1}$).

- **Bradford protein assay**

For quantification of the protein content on the nanoparticles, using the Bradford method,² we followed the technical procedure suggested by the provider.³ For obtaining the calibration line, different concentrations of commercial acetylcholinesterase were prepared by dilution of a 0.1 mg mL^{-1} stock solution in phosphate buffer (50 mM) and mixed with 200 μL of Bradford dye reagent concentrate (final volume 1 mL). For sample analysis, 10 μL of a suspension of nanoparticles (10 mg mL^{-1}) were diluted in 790 μL of phosphate buffer and mixed with 200 μL of Bradford dye reagent concentrate. The solutions were vortexed, and stirred at 25 °C for 45 min. Then, the absorbance at 595 nm was measured with the spectrophotometer.

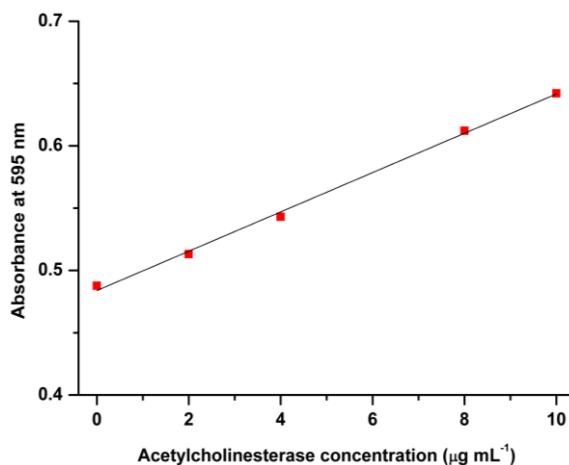


Figure SI-8. Bradford assay calibration for different concentrations of acetylcholinesterase.

From the equation of the calibration line ($y = 0.0158x + 0.4839$, $r^2 = 0.998$) and the signal of the sample assay, the amount of protein on the nanodevice **S2** was quantified as $58.5 \mu\text{g mg}^{-1}$.

• STEM-EDX

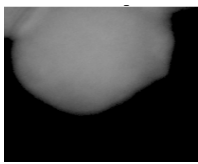
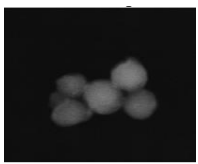
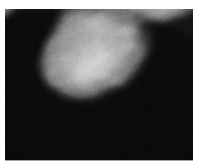
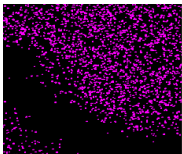
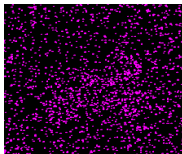
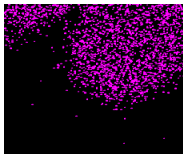
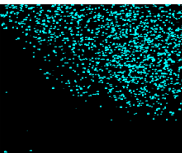
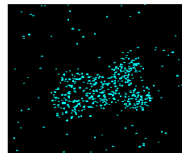
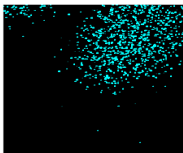
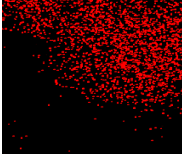
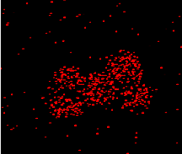
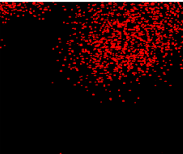
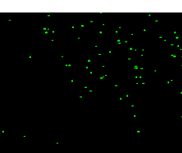
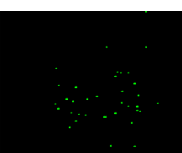
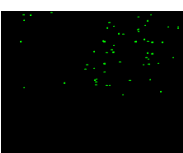
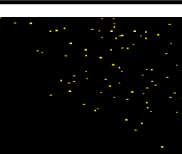
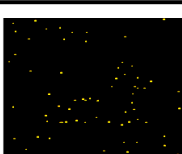
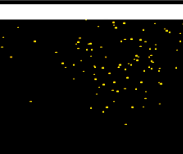
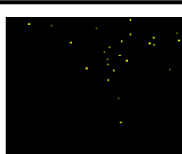

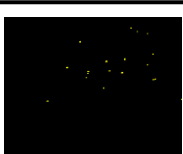
ELEMENT	S2 SAMPLES		
			
C			
O			
Si			
N			
B			
S			

Figure SI-9. Additional images of STEM-EDX mapping of S2.

- **Release experiments**

For the release experiments indicated in the manuscript, **S2** nanoparticles were taken from a refrigerated stock solution of 10 mg mL^{-1} , washed three times by centrifugation with an aqueous solution at pH 7.5 ($20 \text{ mM Na}_2\text{SO}_4$), re-suspended and brought to a concentration of 2 mg mL^{-1} in aqueous solution containing the corresponding concentration of ACh or other neurotransmitters (for selectivity studies). The samples were stirred at $25 \text{ }^\circ\text{C}$. At the programmed times, aliquots were taken in 1.5 mL tubes and centrifuged for 2 min at 12000 rpm (to precipitate the solid) and the fluorescence of the supernatant corresponding to the released $[\text{Ru}(\text{bpy})_3]\text{Cl}_2$ dye was measured ($\lambda_{\text{em}} = 595 \text{ nm}$, $\lambda_{\text{exc}} = 453 \text{ nm}$). Amount of cargo released was calculated from a calibration line and maximum release efficiency (total amount of loaded cargo) was calculated by via several extractions of the dye content in water at acidic pH (3).

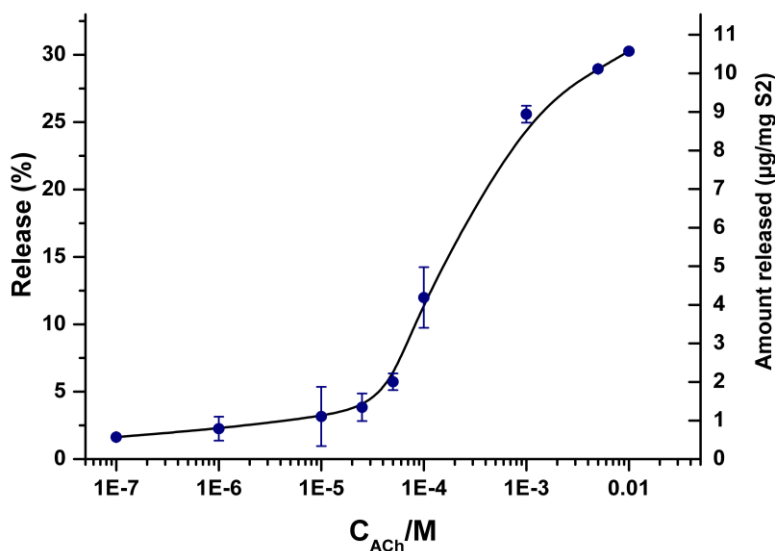


Figure SI-10. Cargo release from **S2** (2 mg mL^{-1}) in aqueous media (pH 7.5) as a function of ACh concentration after 10 min.

Furthermore, we also conducted an additional experiment using a higher concentration of **S2** (6.6 mg mL^{-1}) in order to test if the difference could be seen to the naked-eye (see Figure S11).

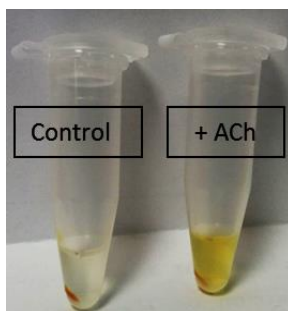


Figure S11. Visualization of $[\text{Ru}(\text{bpy})_3]\text{Cl}_2$ released from **S2** nanoparticles in the absence (left) and in the presence (right) of ACh after 10 min. It can be noted that nanoparticles form a pellet at the bottom after centrifugation, and that there is a remarkable release of dye in the supernatant for the sample in medium containing ACh.

For evaluating the acetylcholinesterase activity on **S2** after the release, nanoparticles were collected after 10 min in the absence or presence of ACh, washed 3 times with phosphate buffer and redispersed. Then, the enzymatic assay was conducted as explained above. As can be observed in **Figure S12**, the remaining acetylcholinesterase activity on **S2** (or increase in absorbance at 412 nm) was much lower (0.4 U mg^{-1}) when **S2** had been in the presence of ACh (red line) compared to when it had been stirred in the absence of ACh (4.5 U mg^{-1}).

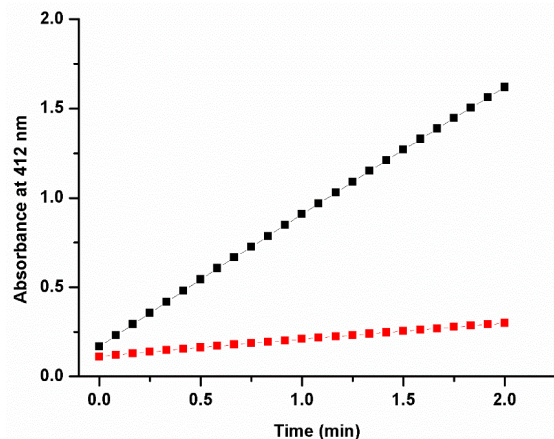


Figure S12. Enzymatic assay (monitoring of TNB^{2-} formation) for evaluating the remaining acetylcholinesterase activity on **S2** after a release experiment. Plotted lines for the sample that had been exposed to ACh (red) and for the control (black, stirred in the absence of ACh).

- **Gating mechanism experiments**

In a first step, in order to confirm that the enzyme is attached through the phenylboronic linker and not through simple physical adsorption to the silica surface, we carried out additional control experiments. To this end, we compared the amount of enzyme that attaches to phenylboronic-functionalized-MSNs *versus* the amount of enzyme that attaches to non-functionalized-MSNs. First, non-functionalized-MSNs were loaded with the ruthenium dye (following the same procedure as described above). Then, 1 mg mL⁻¹ of enzyme solution were added to the different solids: (i) phenylboronic-functionalized-MSNs (**S1**) and (ii) non-functionalized-MSNs. Following the procedure as described above for preparing **S2**, after 24 h of incubation, the solids were isolated by centrifugation and exhaustively washed with phosphate buffer.

In the second case (without the linker), a much lower amount of enzyme was found on the nanoparticles as measured by acetylcholinesterase-specific assay and by protein (Bradford) assay. In particular, ca. 10-times less AChE-activity was found when nanoparticles are non-functionalized with the ligand (**see Figure S13**). Additionally, whereas the amount of protein attached to phenylboronic-functionalized-MSNs was found to be 58.5 µg·mg⁻¹ (according to the Bradford protein assay quantification), the amount for the non-functionalized-MSNs was below the LOD of the method. Furthermore, after the enzyme-attachment procedure, a significant larger cargo leakage is observed for the solution of non-functionalized nanoparticles (**see Figure S14**), which is ascribed to the absence of enzyme molecules blocking the pores.

These results support the formation of ester linkages between diol/saccharide-groups (of the enzyme) and phenyl boronic ligands, as previously reported by other authors (see reference 19 in the manuscript).

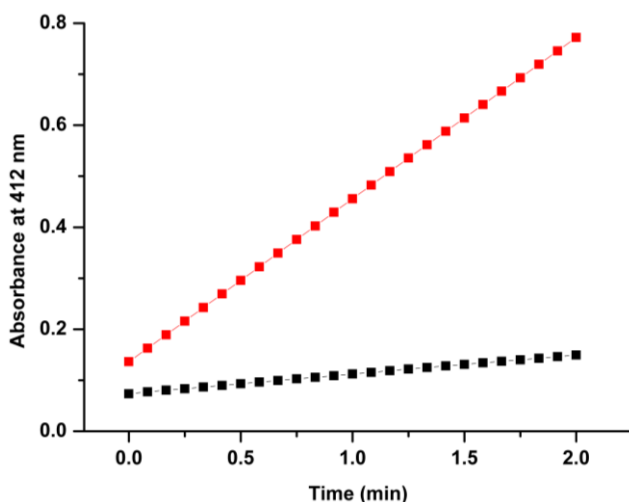


Figure S13. Acetylcholinesterase activity assay on the different solids (after enzyme attachment procedure) for: (i) non-functionalized-MSNs (black), and (ii) phenyl-boronic-functionalized-MSNs (red).

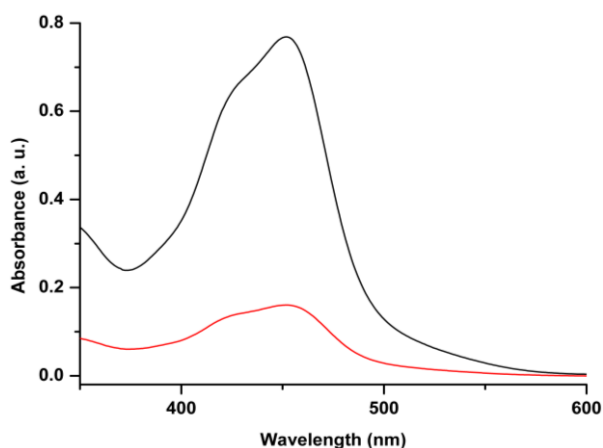


Figure S14. Absorbance of the cargo leakage from nanoparticles after enzyme attachment procedure for: (i) non-functionalized-MSNs (black), and (ii) phenyl-boronic-functionalized-MSNs (red).

In a further step, we checked the pH variation after release experiments using an indicator solution of methyl red. Methyl red is a pH indicator that turns red in pH under 4.4, yellow in pH over 6.2 and orange in between. 10 μL of a saturated solution of methyl red (1 mg in 0.3 mL of ethanol and 0.2 mL of DI water) were added to the supernatant of aliquots (200 μL) after release experiments (10 min)

in the presence and in the absence of ACh. A clear difference was observed (see **Figure S15**), showing the acidification of the solution to pH below 4.4 after the release in the presence of ACh. This observation correlates with the formation of acetic acid by the enzyme.

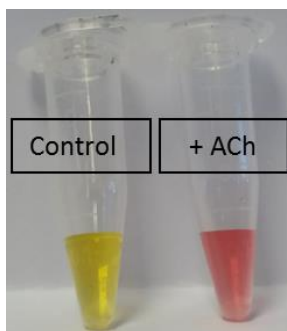


Figure S15. Measurement of the pH of the supernatant solution after the release experiments (10 min) using methyl red indicator. It can be noted that for the control (absence of ACh) the pH of the solution remains neutral, whereas it is acidified to below 4.4 in the presence of ACh due to the enzyme-mediated formation of acetic acid.

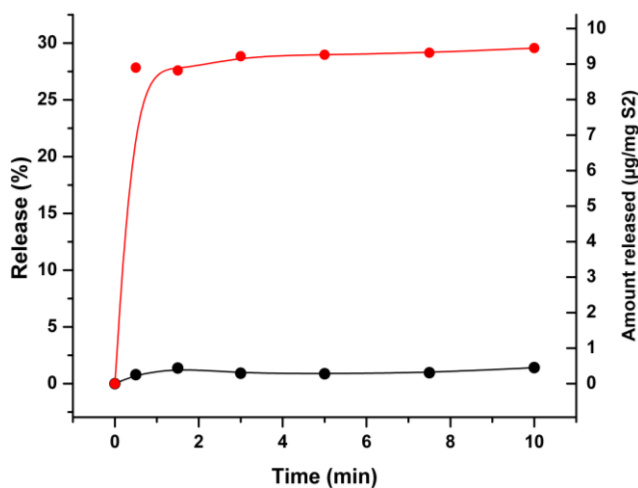


Figure S16. Cargo release from **S2** in aqueous media at pH 7.5 (black) and at pH 4.5 (red).

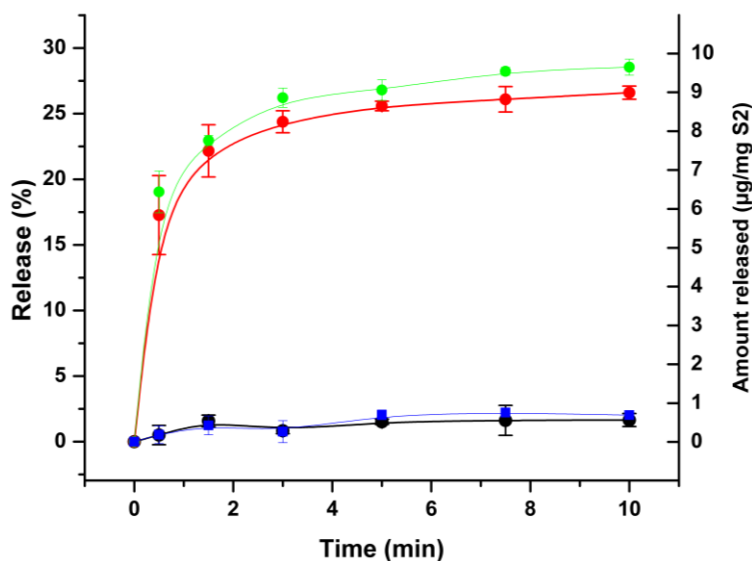


Figure S17. Cargo release from **S2** in aqueous media under different conditions: pH 7.5 in the absence of ACh (black), pH 6.5 in the absence of ACh (blue), pH 7.5 in the presence of ACh (1 mM, red), and pH 6.5 in the presence of ACh (1 mM, green).

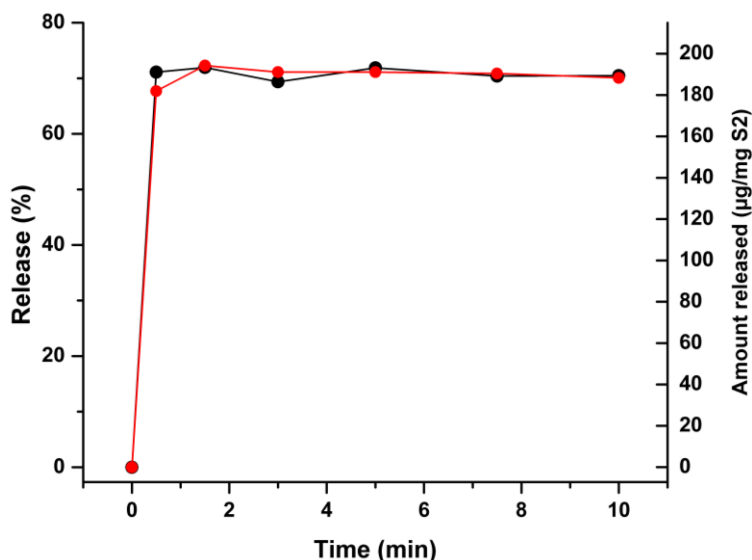


Figure S18. Cargo release from **S1** in the absence (black) and in the presence (1 mM, red) of ACh.

In order to confirm the cleavage of the linker under acidic conditions, we also carried out $^1\text{H-NMR}$ experiments using a model system (see **Figure S19**). First, we recorded the spectra in D_2O of pure 3-aminophenylboronic acid (APB) and APB

with *D*-glucose (model saccharide) after 24 h incubation. As showed in Figure SI-19-A-B, new signals appear due to the linkage of APB with *D*-glucose. However, upon addition of acetic acid (10 μ L) to these samples, only the signals corresponding to the free (protonated) APB are observed which indicates the cleavage of the boronic ester linker.

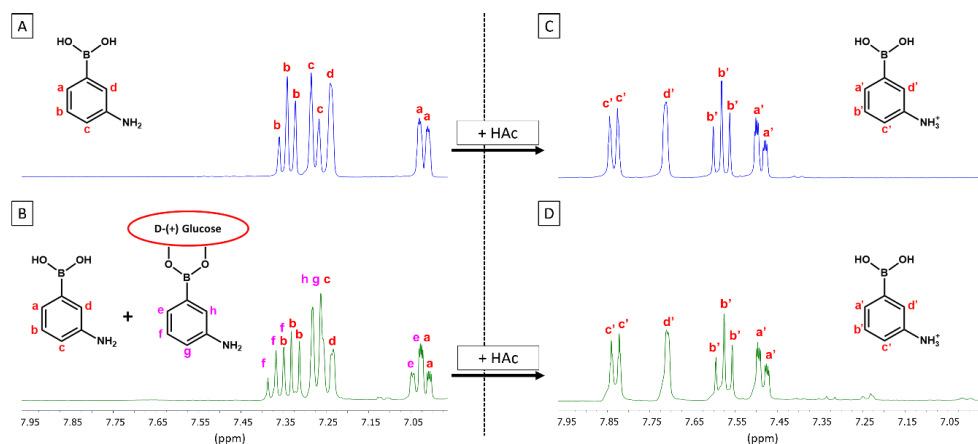


Figure S19. $^1\text{H-NMR}$ study of a model system in order to confirm the cleavage of the linker under acidic conditions. Samples containing (A) pure APB and (B) APB incubated with glucose, and corresponding spectra upon addition of acetic acid (C-D).

• Cell experiments

In vitro release of the cytotoxic drug doxorubicin

Release experiments with $S2_{\text{dox}}$ were carried out as explained above for $S2$. In this case, the amount of released cargo was determined by measuring the absorption of doxorubicin at 485 nm with the spectrophotometer.

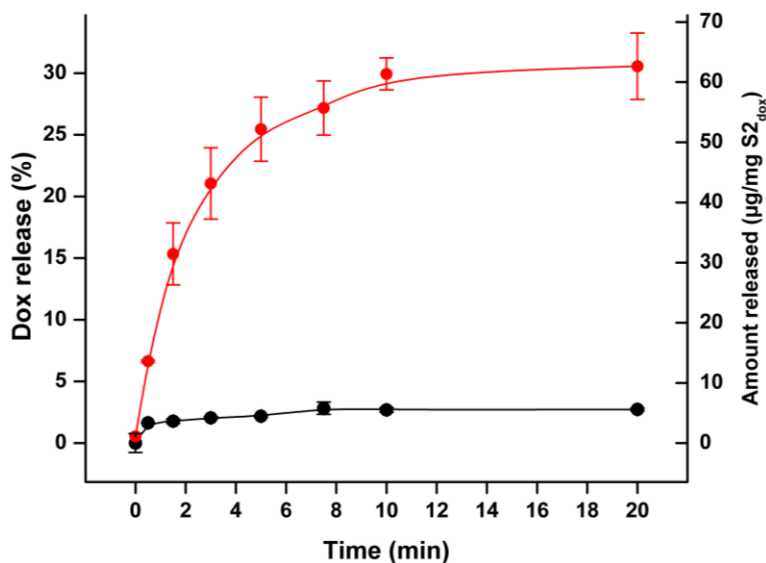


Figure S20. Kinetics of doxorubicin release from $S2_{\text{dox}}$ in aqueous media (pH 7.5) in the absence (black curve) and in the presence of ACh (1 mM, red curve).

Cell culture conditions

HeLa human cervix adenocarcinoma cells were purchased from the German Resource Centre for Biological Materials-DSMZ and were grown in DMEM supplemented with 10% FBS. Cells were incubated at 37 °C in an atmosphere of 5% carbon dioxide and 95% air and underwent passage twice a week.

Cell viability assays

HeLa cells were seeded in a 24-well plate at 50000 cells per well and incubated at 37 °C for 24 h. Then, cells were incubated with $S2_{\text{dox}}$ ($50 \mu\text{g}\cdot\text{mL}^{-1}$) for 30 min, washed with PBS, and further incubated for 24 h in DMEM medium supplemented with 10% FBS in the absence or in the presence of ACh (50 mM). Finally, cell viability was assessed by incubation with the cell

proliferation WST-1 reagent for 1 h and measuring the absorbance at 595 nm in the Wallac Workstation. Three independent experiments containing triplicates were carried out. Similar experiments with the equivalent amount of doxorubicin (16 μM) were also carried out.

Confocal microscopy imaging

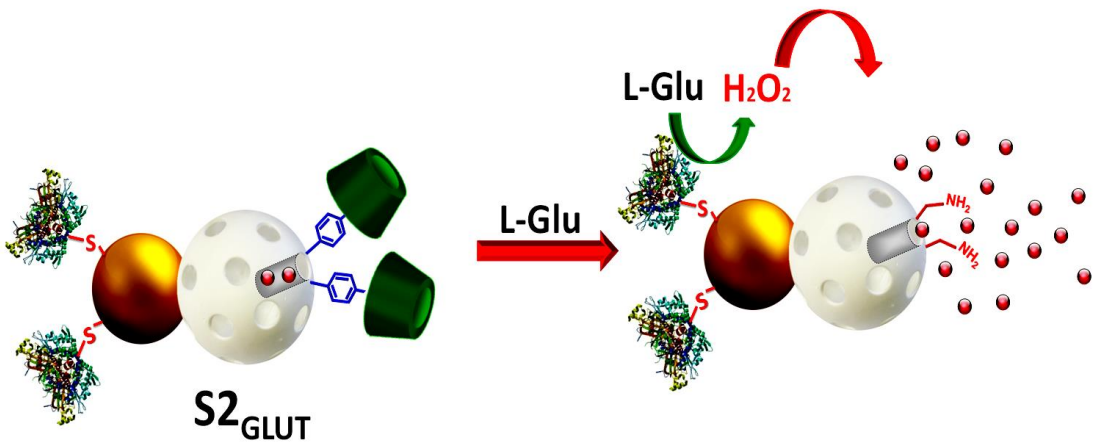
HeLa cells were seeded on glass coverslips at 300000 cells·mL⁻¹ in 6-well culture plates and incubated at 37 °C for 24 h. Then, cells were incubated with **S2_{dox}** (75 $\mu\text{g}\cdot\text{mL}^{-1}$) for 30 min, washed with PBS, and further incubated for 2 h in the absence or in the presence of ACh (50 mM). Then, cells were washed several times with PBS, stained with DNA marker Hoechst 33342 by addition at 2 $\mu\text{g}\cdot\text{mL}^{-1}$, and placed in fresh media. Finally, samples were visualized using a confocal microscope Leica TCS SP8 AOBS.

• **References**

1. G. L. Ellman, K. D. Courtney, V. Andres and R. M. Featherstone, *Biochem. Pharmacol.*, 1961, **7**, 88.
2. M. Bradford, *Anal. Biochem.*, 1976, **72**, 248.
3. <http://www.bio-rad.com/webroot/web/pdf/lsr/literature/LIT33.pdf>

Chapter 4: Part 2

L-Glutamate-Responsive Delivery System Based on Enzyme-Controlled Self- Immolative Arylboronate-Gated Nanoparticles



L-Glutamate-Responsive Delivery System Based on Enzyme-Controlled Self- Immolative Arylboronate-Gated Nanoparticles

Tania M. Godoy-Reyes^{abc}, Antoni Llopis-Lorente^{abc}, Alba García-Fernández^{ab}, Pablo Gaviña^{abd}, Ana M. Costero^{*abd}, Reynaldo Villalonga^e, Félix Sancenón^{abc} and Ramón Martínez-Mañez^{*abc}

^a Instituto Interuniversitario de Investigación de Reconocimiento Molecular y Desarrollo Tecnológico (IDM), Universitat Politècnica de València-Univeritat de València, Spain

^b CIBER de Bioingeniería, Biomateriales y Nanomedicina (CIBER-BBN), Spain.

^c Departamento de Química, Universitat Politècnica de València, Camino de Vera s/n, 46022, Valencia, Spain. E-mail: rmaez@qim.upv.es

^d Departamento de Química Orgánica, Universitat de Valencia, Doctor Moliner 50, Burjassot, 46100, Valencia, Spain. E-mail: ana.costero@uv.es

^e Nanosensors & Nanomachines Group, Department of Analytical Chemistry, Faculty of Chemistry, Complutense University of Madrid, 28040 Madrid, Spain. E-mail: rvillalonga@quim.ucm.es

Published online: 11 March 2019

(Reprinted with permission from *Org. Chem. Front.*, 2019, 6, 1058)

Abstract

We report herein a L-glutamate (L-Glu)-responsive delivery system. It consists of Janus Au–mesoporous silica nanoparticles (MSNs) functionalized with L-glutamate oxidase on the Au face and with self-immolative arylboronate derivatives as caps on the MSNs face. The MSNs face is additionally loaded with a cargo. The delivery paradigm is based on the recognition of L-Glu by the enzyme and the subsequent formation of H₂O₂, which induces the cleavage of the self-immolative gate and the uncapping of the pores. Given the importance of L-Glu as a key neurotransmitter, we hope that these findings will help in designing new therapeutic strategies for nervous system diseases.

Introduction

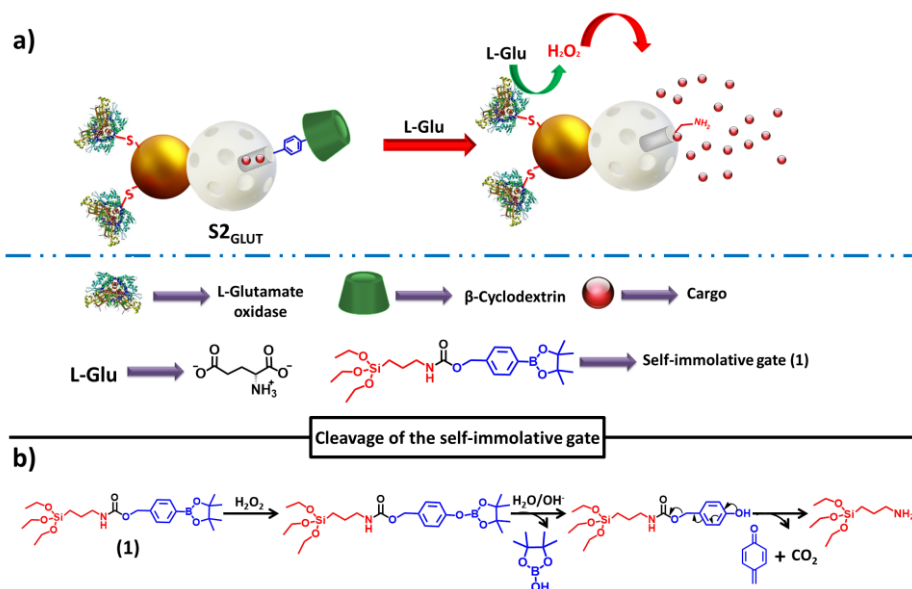
The amino acid L-glutamate (**L-Glu**) is the major excitatory neurotransmitter in the central nervous system (CNS).¹ It is synthesized in brain cells from local precursors and released to transmit excitatory signals by activating **L-Glu** receptors on neighbouring neurons.² Due to its crucial role in the CNS physiology,³ any alteration in glutamatergic activity may cause psychological and neurodegenerative disorders.⁴ In particular, high concentrations of **L-Glu** produced by an excessive release from presynaptic nerve terminals into the extracellular space induce a process known as neuronal excitotoxicity, which is the damage and death of neurons due to the overactivation of **L-Glu** receptors.⁵ **L-Glu** excitotoxicity is involved in the neuronal injury observed in several CNS disorders such as Huntington's disease, Alzheimer's disease, sclerosis, Parkinson's disease, epilepsy and brain cancer.⁶ In brain tumours, glioblastoma cells grow at an uncontrolled rate producing excessive **L-Glu** and inducing neuronal death during proliferation.⁷

On the other hand, the design of stimuli-responsive delivery systems has recently attracted significant attention due to their potential applications in the biomedical field.⁸ Among potential drug nanocarriers,⁹ MSNs have appealing properties such as high loading capacity, low cost and biocompatibility.¹⁰ Furthermore, the outer surface of MSNs can be functionalized with gating ensembles, which control the payload delivery by blocking the outlets of pores until a certain stimulus is applied.¹¹ A variety

of gated mesoporous materials that respond to physical or chemical stimuli have been reported.¹² However, as far as we know, no **L-Glu**-responsive delivery system has been reported yet.

The so-called self-immolative molecules (SIMs) are organic entities that fragment from head to tail into their building blocks in response to a certain trigger.¹³ A typical SIM structure is composed of a protecting group linked to an aromatic ring with a good leaving substituent in the *ortho* or *para* position.¹⁴ The trigger initiates the cleavage of the protecting group, which transmits an electron pair to the aromatic ring resulting in a cascade of electronic elimination processes. These interesting molecules have found several applications such as the design of chromo-fluorogenic sensors, prodrugs and polymeric carriers.¹⁵ For these applications, the selection of the protecting group is the key, since it controls the initial trigger recognition. For instance, several H₂O₂ probes based on arylboronate esters linked to a reporter have been reported, the emission of which is activated after the self-immolation process.¹⁶

Given the relevance of **L-Glu** in the CNS and given our interest in the development of smart nanodevices for cargo release, we report herein a **L-Glu**-responsive delivery system based on enzyme-controlled Janus Au-MSNs. The design and performance of the system are illustrated in **Scheme 1**. The MSNs face is loaded with a model cargo ([Ru(bpy)₃]Cl₂), functionalized on its external surface with H₂O₂-sensitive self-immolative arylboronate derivatives and capped by host-guest complexation with β -cyclodextrin (β -CD). The Au face is used for anchoring the enzyme L-glutamate oxidase (L-GluOx) which performs as a “biocomputing unit”. Thus, the biocomputing unit acts as: (i) a recognition agent, able to detect the presence of **L-Glu**; (ii) an anti-glutamatergic agent¹⁷ that eliminates **L-Glu** by oxidation to 2-oxoglutarate, NH₃ and H₂O₂; and (iii) a mediator agent, which produces H₂O₂ molecules and induces the well-known self-immolation reaction of arylboronate derivatives (**see Scheme 1b**),¹⁶ which results in the uncapping of the MSNs pores. In turn, the MSNs face acts as a cargo transporter and delivery unit, which after receiving the chemical messenger (H₂O₂) sent by the Au face releases the payload.



Scheme 1 (a) Representation of the design and performance of the L-glutamate-responsive nanocarrier ($S2_{GLUT}$). Janus nanoparticles are functionalized with the enzyme L-GluOx (on the Au face) and with the self-immolative (β -CD)-arylboronate gate (on the MSNs face). (b) Mechanism of cleavage of the self-immolative derivative 1.

In order to prepare the L-Glu-responsive nanodevice, firstly compound **1** was synthesized, by coupling reaction (see Figure S1) between 4-(hydroxymethyl) phenylboronic acid pinacol ester and (3-isocyanatopropyl)triethoxysilane in the presence of Na^+ as a catalyst. **1** was characterized by 1H -NMR, ^{13}C -NMR and HRMS (see Figure S2 and S3). In the second step, MSNs with an MCM-41-type structure were prepared following a standard procedure based on the use of cetyltrimethylammonium bromide (CTABr) as a structure-directing agent and tetraethyl orthosilicate (TEOS) as a silica precursor. The as-made MSNs were calcined using an oxidant atmosphere in order to remove the surfactant to yield the starting mesoporous support (**S0**). Next, gold nanoparticles (AuNPs) were prepared based on the Turkevich–Frens method,¹⁸ by reduction of Au^{+3} using sodium citrate. In a further step, MSNs were partially functionalized with (3-mercaptopropyl)trimethoxysilane by confinement at an interface between paraffin wax and water. Then, AuNPs were attached to MSNs by the formation of Au–S bonds and the paraffin was removed through washing with $CHCl_3$, which yielded Janus nanoparticles (**S1**).¹⁹ Afterwards, the

Au face was functionalized with carboxylic groups by treatment with 3-mercaptopropionic acid for 1 hour. Thereafter, the Janus particles were suspended in an acetonitrile solution containing $[\text{Ru}(\text{bpy})_3]\text{Cl}_2$ in order to load the pores by stirring at room temperature overnight. Then, derivative **1** was anchored on the external silica surface and capped nanoparticles (**S2**) were obtained by further stirring with β -CD which forms inclusion complexes with the boronate pinacol ester.²⁰ Finally, the oxidoreductase L-GluOx enzyme from *Streptomyces* sp.²¹ was immobilized by coupling lysine residues from the enzyme with the carboxylic groups on the Au surface using the well-known crosslinking reagents NHS and EDC,²² to give the final nanodevice **S2**_{GLUT}.

The prepared materials were characterized by different standard techniques. Transmission electron microscopy (TEM) of Janus nanoparticles **S1** confirmed the size and correct attachment between spherical MSNs (ca. 100 nm) and spherical AuNPs (ca. 20 nm) (see **Figure 1A** and **Figure S4**). The visible spectrum of the as-synthesized AuNPs showed an absorption band at 520 nm (see **Figure S5**), whereas for **S1**, there was a red-shift caused by the increase in the refractive index around Au due to silica attachment.²³ Powder X-ray diffraction (PXRD) patterns (see **Figure 1B**) at low angles of the starting mesoporous support (**S0**) and Janus nanoparticles **S1** showed the presence of the (100) reflection peak around 2.4° characteristic of MCM-41-type mesoporous materials.²⁴ The preservation of this characteristic peak in **S2** indicated that the cargo loading and surface functionalization processes had not damaged the 3-D mesoporous structure. Moreover, the diffraction patterns of **S1** and **S2** at high angles showed the characteristic cubic gold nanocrystal (111), (200), (220), and (311) peaks, thus confirming the Au-MSNs architecture observed by TEM. N_2 adsorption-desorption isotherms of the starting **S0** and Janus nanoparticles **S1** (see **Figure S6**) showed an adsorption step at intermediate P/P_0 values (0.1–0.3), indicating the presence of mesopores with a pore size of ca. 2.4 nm (see **Figure S7**). A BET specific surface area of $1365 \text{ m}^2 \text{ g}^{-1}$ and a pore volume of $0.946 \text{ m}^3/\text{g}$ were determined for **S0**, whereas these values decreased for **S1** to $1001 \text{ m}^2 \text{ g}^{-1}$ and $0.589 \text{ cm}^3 \text{ g}^{-1}$, respectively, due to the attachment of non-porous AuNPs (see **Table S1**). Using elemental analysis and UV-vis spectrophotometry, the content of $[\text{Ru}(\text{bpy})_3]\text{Cl}_2$, arylboronate derivative (**1**) and β -CD in mmol per 100 g of **S2** was calculated to be 7.94 (5.08 wt%), 10.22 (4.91 wt%) and 10.71 (12.16 wt%), respectively (see **Supplementary Equation (1) and (2)**). From

dynamic light scattering (DLS) measurements, the hydrodynamic diameter and zeta potential of the final nanodevice (**S2_{GLUT}**) were determined to be 185 ± 41 nm and -42.3 ± 4.9 mV, respectively (see **Figure S8**). The L-GluOx activity of **S2_{GLUT}** was determined to be $40889 \text{ mU} \cdot \text{g}^{-1}$, by performing an enzymatic specific assay (see **Figure S9**). Finally, **Figure 1C** and **Figure S10** show the STEM-EDX mapping of several atoms on **S2_{GLUT}** attributed to the different components: Si, O and Au (Janus scaffold), N (cargo, self-immolative gate and enzyme), and P (phosphate groups of the enzyme).

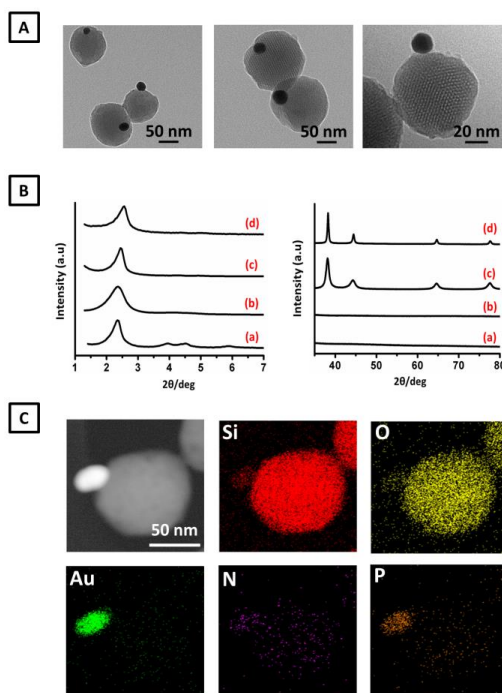


Figure 1. (A) TEM images of the Janus Au-MSNs (**S1**). (B) PXRD at low (left) and high (right) angles of the (a) as-made MSNs, (b) calcined MSNs (**S0**), (c) Janus Au-MSNs (**S1**) and (d) functionalized nanoparticles (**S2**). (C) STEM image and STEM-EDX mapping of different atoms on the final nanodevice **S2_{GLUT}**.

In order to test the ability of the nanodevice to recognize **L-Glu**, we performed release experiments in which **S2_{GLUT}** was brought to a concentration of 3.0 mg mL^{-1} in physiological buffer (PBS, pH 7.5) in the absence and presence of **L-Glu** (10 mM). Samples were stirred at room temperature and, at scheduled times, aliquots were taken, centrifuged to remove nanoparticles, and then cargo release was evaluated by measuring the emission band of $[\text{Ru}(\text{bpy})_3]\text{Cl}_2$ at 595 nm ($\lambda_{\text{exc}} = 453 \text{ nm}$). As can be

observed in **Figure 2**, in the absence of **L-Glu**, the nanocarrier **S2_{GLUT}** is capped and cargo release was negligible. In contrast, a remarkable payload release was observed in the presence of **L-Glu** in less than one hour. The observed cargo delivery is ascribed to the recognition of the neurotransmitter and its transformation to give 2-oxoglutarate, NH_3 and H_2O_2 by the enzyme **L-GluOx**. Subsequently, hydrogen peroxide (H_2O_2) acts as a chemical messenger sent by the enzymatic control unit (Au face) to the MSNs face. H_2O_2 induces the cleavage of the self-immolative arylboronate derivative **1**, resulting in the payload delivered from the nanoparticles. The production of this chemical messenger was also confirmed by the enzymatic assay in which the **L-GluOx**-generated H_2O_2 reacts with an indicator in the presence of peroxidase (see **Supplementary Equation (3) and Figure S8**).

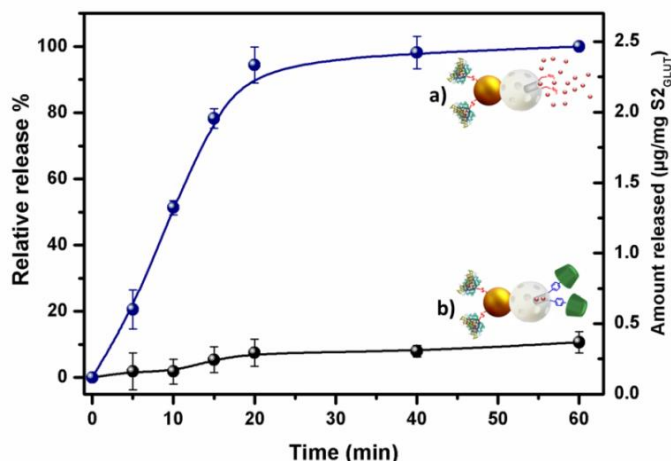


Figure 2. Kinetics of cargo release from the nanodevice **S2_{GLUT}** (3 mg mL^{-1}) in physiological buffer (PBS, pH 7.5) in the absence (a) and in the presence of **L-Glu** (10 mM) determined by measuring the $[\text{Ru}(\text{bpy})_3]\text{Cl}_2$ fluorescence at 595 nm ($\lambda_{\text{exc}} = 453 \text{ nm}$). Error bars correspond to the s. d. from three independent experiments.

In the second step, we evaluated the response of the nanoparticles **S2_{GLUT}** (3 mg mL^{-1}) in physiological buffer (PBS, pH 7.5) towards other important amino acid neurotransmitters (at a concentration of 10 mM). Like **L-Glu**, these amino acids play a key role in brain metabolism and function: gamma-aminobutyric acid (GABA) is the primary inhibitory neurotransmitter known to counterbalance the action of **L-Glu**, glycine (Gly) acts as an inhibitory neurotransmitter and is a co-agonist at **L-Glu**

receptors, and L-aspartate (L-Asp) exerts excitatory actions in the ventral spinal cord. As shown in **Figure 3A**, despite having a chemical structure very similar to **L-Glu**, GABA and Gly did not induce any cargo delivery. A slight delivery (20%) was observed in the presence of 10 mM L-Asp, which was ascribed to a certain activity of L-GluOx enzyme towards L-Asp as previously reported.²⁵ Additionally, we also tested the response of **S2_{GLUT}** in the presence of glucose (Glc) and D-glutamate (D-Glu) (10 mM). These molecules were unable to trigger cargo release from **S2_{GLUT}**. The ability of the nanodevice **S2_{GLUT}** to discriminate between the D and L forms of glutamate is noteworthy.

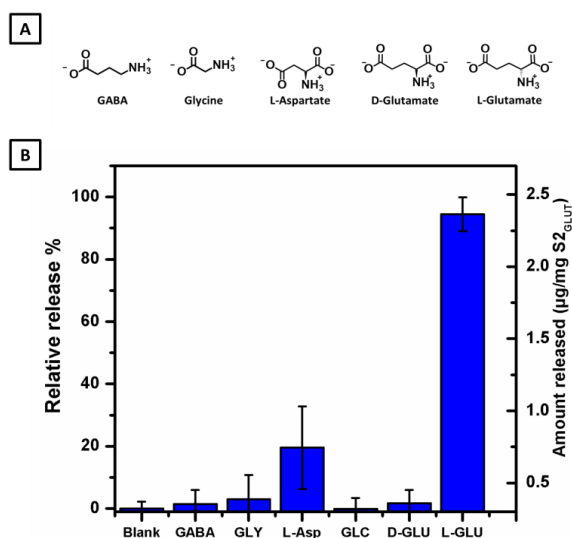


Figure 3. (A) Chemical structure of **L-Glu** and the amino acid neurotransmitters used as potential interferents. (B) Cargo release from the nanodevice **S2_{GLUT}** (3 mg mL^{-1}) after 20 min in physiological buffer (PBS, 7.5) in the presence of selected molecules (10 mM).

Regarding the physiological levels of **L-Glu**, it has been reported that **L-Glu** concentrations are 0.05–0.1 mM in plasma.²⁶ In the brain, **L-Glu** concentrations are *ca.* 5–12 mM in neurons and glial cells. However, brain tumours and other CNS diseases can increase the **L-Glu** concentration in the extracellular environment 100–500 times.^{7,27} Bearing this in mind, it is noteworthy that when we evaluated the delivery from **S2_{GLUT}** in the presence of **L-Glu** plasma levels (0.075 mM), the response was negligible (**Figure 4**). Although this is a preliminary proof-of-concept study and the road

from these results to the *in vivo* use of similar nanocarriers remains long and uncertain, these findings suggest that this nanosystem or similar nanodevices could potentially be suitable drug delivery systems that would remain capped in plasma, but would deliver the cargo in sites where the concentrations of **L-Glu** are overexpressed, such as in the brain of patients.

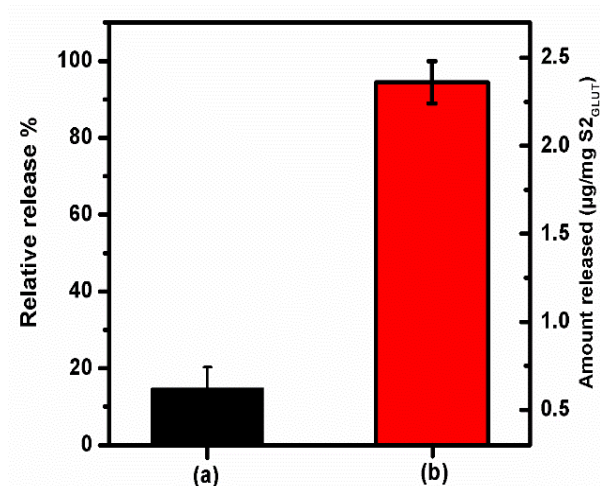


Figure 4. Cargo release from the nanodevice S2_{GLUT} (3 mg mL^{-1}) after 20 min in physiological buffer (PBS, pH 7.5) in the presence of (a) **L-Glu** plasma concentrations ($75 \mu\text{M}$) and (b) **L-Glu** brain concentrations (10 mM).

Finally, encouraged by these findings, we decided to evaluate the performance of the nanodevice in a brain cancer cell line (LN-18 glioblastoma). For this, we prepared nanoparticles similar to S2_{GLUT} but loaded with the cytotoxic anticancer drug doxorubicin (S3_{GLUT}). Different concentrations of doxorubicin-loaded nanoparticles (S3_{GLUT}) were added to glioblastoma cell culture media, and the cell viability after 24 h was evaluated by means of the WST-1 assays. Three independent experiments containing triplicate were carried out. As depicted in **Figure 5A**, a S3_{GLUT} concentration-dependent reduction in cancer cell viability was observed. In order to confirm that cell death was due to the recognition of **L-Glu**, we also carried out viability experiments with **S3** (lacking the enzyme L-GluOx). In this case, no significant reduction in cell viability was observed when cells were treated with **S3**.

This fact points out the key role played by the enzyme L-GluOx in the performance of the nanodevice and discards any toxic effect due to the Janus scaffold. Additionally, to

directly image the release of doxorubicin, we conducted confocal microscopy experiments. For these experiments, cells were incubated with $50 \mu\text{g mL}^{-1}$ solid (**S3**_{GLUT} or **S3**) for 2 hours, washed to remove non-internalized particles, and stained with DNA-marker Hoechst 3342 before image acquisition. As shown in **Figure 5B**, a clear doxorubicin-associated red fluorescence was observed when cells were treated with **S3**_{GLUT}.

In contrast, the doxorubicin fluorescence was significantly weaker in the case of cells treated with nanoparticles lacking the enzyme **S3**. Altogether, the experiments with cells indicate that despite the presence of a large amount of potential interferents and biomolecules present in cell media, the enzyme-controlled nanodevice retained the capability to recognize L-Glu and release the payload (doxorubicin) inducing the death of glioblastoma cells.

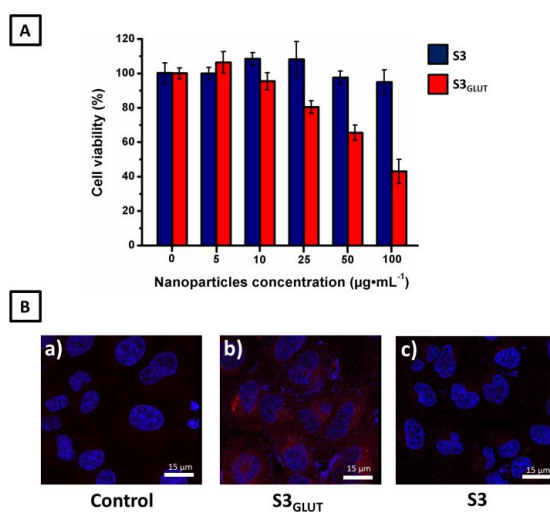


Figure 5. Experiments in cell culture media (LN-18 glioblastoma cell line). (A) Glioblastoma cell viability in the presence of different concentrations of **S3** (blue) and **S3**_{GLUT} (red). Error bars correspond to the s. d. from three independent experiments containing triplicate. (B) Confocal microscopy images of glioblastoma cells for (a) control experiment (without nanoparticles), (b) cells incubated with **S3**_{GLUT} ($50 \mu\text{g mL}^{-1}$) and (c) cells incubated with **S3** ($50 \mu\text{g mL}^{-1}$), showing nuclei-marker fluorescence in blue and dox-fluorescence in red.

Conclusions

In conclusion, we have designed, synthesized and characterized a novel **L-Glu**-responsive nanocarrier based on enzyme-controlled Janus nanoparticles. The nanodevice is functionalized with the L-GluOx enzyme (on the Au face) and with a self-immolative (β -CD)-arylboronate gate (on the MSNs face). The nanocarrier is able to recognize **L-Glu** *via* an enzyme-mediated transformation to H_2O_2 , which induces the cleavage of the self-immolative cap and results in payload delivery. Release studies in physiological buffer showed that in the presence of **L-Glu**, the nanocarrier was able to selectively deliver the cargo in less than one hour, whereas it remained closed in the absence of the neurotransmitter. Furthermore, the nanodevice exhibited a negligible release at **L-Glu** plasma concentrations, but was capable of recognising **L-Glu** in brain cancer cells. The selective recognition of **L-Glu** by the enzyme-controlled nanoparticles loaded with doxorubicin in glioblastoma cell culture media induced a nanoparticle-concentration dependent reduction in cell viability. Bearing in mind the key role played by this neurotransmitter in the CNS, we hope the results presented here can help in developing better therapies for nervous system-related diseases.

Acknowledgements

T. Godoy-Reyes is grateful to Generalitat Valenciana for her Santiago Grisolíá fellowship. A. Llopis-Lorente thanks “La Caixa” Foundation for his PhD grant. A. García-Fernández is grateful to the Spanish Government for her FPU fellowship. The authors gratefully acknowledge the financial support from the Spanish Government (Projects MAT2015-64139-C4-1-R, MAT2015-64139-C4-4-R and AGL2015-70235-C2-2-R) and the Generalitat Valenciana (Project PROMETEO2018/024).

References

1. (a) A. N. V. Den Pol, J. P. Wuarin and F. E. Dudek, *Science*, 1990, **250**, 1276; (b) M. Jamal, M. Hasan, A. Mathewson, and K. M. Razeeb, *Biosens. Bioelectron.*, 2013, **40**, 213.
2. (a) J. Aoto, P. Ting, B. Maghsoodi, N. Xu, M. Henkemeyer and L. Chen, *J. Neurosci.*, 2007, **27**, 7508; (b) L. Hertz, *Front. Endocrinol.*, 2013, **4**, 59.

3. (a) W. J. McEntee and T. H. Crook, *Psychopharmacology*, 1993, **111**, 391; (b) G. Riedel, B. Platt and J. Micheau, *Behav. Brain Res.*, 2003, **140**, 1.
4. D. W. Choi, *Neuron.*, 1988, **1**, 623.
5. (a) J. G. Greene and J. T. Greenamyre, *Prog Neurobiol.*, 1996, **48**, 613; (b) X. X. Dong, Y. Wang and Z. H. Qin, *Acta Pharmacol. Sin.*, 2009, **30**, 379; (c) A. Doble, *Pharmacol. Ther.*, 1999, **81**, 163. (d) Y. Wang, and Z. H. Qin, *Apoptosis*, 2010, **15**, 1382.
6. (a) P. R. Sanberg and G. A. Johnston, *Med. J. Aust.*, 1981, **2**, 460; (b) D. J. Benos, B. H. Hahn, J. K. Bubien, S. K. Ghosh, N. A. Mashburn, M. A. Chaikin, J. M. Shaw and E. N. Benveniste, *Proc. Natl. Acad. Sci. U. S. A.*, 1994, **91**, 494; (c) J. Gazulla, and M. Cavero-Nagore, *Rev. Neurol.*, 2006, **42**, 427; (d) M. R. Hynd, H. L. Scott, and P. R. Dodd, *Neurochem. Int.*, 2004, **45**, 583; (e) J. D. Rothstein, L. J. Martin and R. W. Kuncl, *N. Engl. J. Med.*, 1992, **326**, 1464; (f) D. Pitt, P. Werner and C. S. Raine, *Nat. Med.*, 2000, **6**, 67; (g) A. Camacho and L. Massieu, *Arch. Med. Res.*, 2006, **37**, 11; (h) A. G. Chapman, *J. Nutr.*, 2000, **130**, 1043S.
7. (a) Z.-C. Ye and H. Sontheimer, *Cancer Res.*, 1999, **59**, 4383; (b) H. Sontheimer, *J. Neurochem.*, 2008, **105**, 287; (c) E. Noch and K. Khalili, *Cancer Biol. Ther.*, 2009, **8**, 1791.
8. (a) S. Mura, J. Nicolas and P. Couvreur, *Nature Mater.*, 2013, **12**, 911; (b) M. Karimi, A. Ghasemi, P. S. Zangabad, R. Rahighi, S. M. M. Basri, H. Mirshekari, M. Amiri, Z. S. Pishabad, A. Aslani, M. Bozorgomid, D. Ghosh, A. Beyzavi, A. Vaseghi, A. R. Aref, L. Haghani, S. Bahrami and M. R. Hamblin, *Chem. Soc. Rev.*, 2016, **45**, 1457.
9. (a) W. H. De Jong and P. J. Borm, *Int. J. Nanomedicine.*, 2008, **3**, 133; (b) A. Samad and Y. Sultana, M. Aqil, *Curr. Drug Deliv.*, 2007, **4**, 297; (c) M. Elsabahy, G. S. Heo, S.-M. Lim and K. L. Wooley, *Chem. Rev.*, 2015, **115**, 10967; (d) E. C. Dreaden, M. A. Mackey, X. Huang, B. Kang and M. A. El-Sayed, *Chem. Soc. Rev.*, 2011, **40**, 3391, (e) N. Zhao, L. Yan, X. Zhao, X. Chen, A. Li, D. Zheng, X. Zhou, X. Dai and F. J. Xu, *Chem. Rev.*, 2019, **119**, 1666.
10. (a) Z. Li, J. C. Barnes, A. Bosoy, J. F. Stoddart and J. I. Zink, *Chem. Soc. Rev.*, 2012, **41**, 2590; (b) F. Tang, L. Li and D. Chen, *Adv. Mater.*, 2012, **24**, 1504; (c) D. Tarn, C. E. Ashley, M. Xue, E. C. Carnes, J. I. Zink and C. J. Brinker, *Acc. Chem. Res.*

- 2013, **46**, 792; (d) J. G. Croissant, Y. Fatieiev, A. Almalik and N. Khashab, *Adv. Healthcare Mater.*, 2018, **7**, 1700831.
11. (a) J. Wen, K. Yang, F. Liu, H. Liu, Y. Xu and S. Sun, *Chem. Soc. Rev.*, 2017, **46**, 6024; (b) C. Coll, A. Bernardos, R. Martínez-Máñez and F. Sancenón, *Acc. Chem. Res.*, 2013, **46**, 339.
12. (a) E. Aznar, M. Oroval, L. Pascual, J. R. Murguía, R. Martínez-Máñez and F. Sancenón, *Chem. Rev.*, 2016, **116**, 561; (b) A. Llopis-Lorente, B. Lozano-Torres, A. Bernardos, R. Martínez-Máñez and F. Sancenón, *J. Mater. Chem. B*, 2017, **5**, 3069; (c) B. Rühle, P. Saint-Cricq and J. I. Zink, *ChemPhysChem*, 2016, **17**, 1769; (d) N. Song and Y.-W. Yang, *Chem. Soc. Rev.*, 2015, **44**, 3474.
13. A. Alouane, R. LabruHre, T. Le Saux, F. Schmidt and L. Jullien, *Angew. Chem. Int. Ed.*, 2015, **54**, 7492.
14. (a) M. Gisbert-Marzán, M. Manzano and M. Vallet-Regí, *Chem. Eng. J.*, 2018, **340**, 24; (b) L. A. Juárez, E. Añón, C. Giménez, F. Sancenón, R. Martínez-Máñez, A. M. Costero, P. Gaviña, M. Parra and A. Bernardos, *Chem. Eur. J.*, 2016, **22**, 14126.
15. (a) M. Shamis, H. N. Lode and D. Shabat, *J. Am. Chem. Soc.*, 2004, **126**, 1726; (b) R. J. Amir, M. Popkov, R. A. Lernes, C. F. Barbas III and D. Shabat, *Angew. Chem. Int. Ed.*, 2005, **44**, 4378; (c) S. Gnaim and D. Shabat, *Acc. Chem. Res.*, 2014, **47**, 2970; (d) M. Gisbert-Garzarán, D. Lozano, M. Vallet-Regí and M. Manzano, *RSC Adv.*, 2017, **7**, 132; (e) Z. Deng, Y. Qian, Y. Yu, G. Liu, J. Hu, G. Zhang and S. Liu, *J. Am. Chem. Soc.*, 2016, **138**, 10452.
16. (a) H. Chen, Z. He, M. Su, W. Zhai, H. Zhang and C. Li, *J. Am. Chem. Soc.*, 2017, **139**, 10157; (b) E. Sella and D. Shabat, *Chem. Commun.*, 2008, **0**, 5701; (c) L.-C. Lo and C.-Y. Chu, *Chem. Commun.*, 2003, **0**, 2728; (d) C. Li, T. Wu, C. Hong, G. Zhang and S. Liu, *Angew. Chem. Int. Ed.* 2012, **51**, 455.
17. (a) V. Coric, S. Milanovic, S. Wasylink, P. Paterl, R. Malison and J. H. Krystal, *Psychopharmacology*, 2003, **167**, 219; (b) J.-E. Kim, D.-S. Kim, S.-E. Kwak, H.-C. Thoi, H. K. Song, S.-Y. Choi, O.-S. Kwon, Y.-I. Kim and T.-C. Kang, *Neuroscience*, 2007, **147**, 136; (c) P. Carrillo-Mora, D. Silva-Adaya and K. Viallaseñor-Aguayo, *Basal Ganglia*, 2013, **3**, 147.

18. (a) P. Zhao, N. Li and D. Astruc, *Coord. Chem. Rev.*, 2013, **257**, 638; (b) J. Turkevich, P. C. Stevenson and J. Hillier, *Discuss. Faraday Soc.*, 1951, **11**, 55; (c) G. Frens, *Nature-Phys Sci.*, 1973, **241**, 20.
19. (a) P. Díez, A. Sánchez, M. Gamella, P. Martínez-Ruíz, E. Aznar, C. de la Torre, J. R. Murguía, R. Martínez-Máñez, R. Villalonga and J. M. Pingarrón, *J. Am. Chem. Soc.* 2014, **136**, 9116; (b) A. Llopis-Lorente, P. Díez, A. Sánchez, M. D. Marcos, F. Sancenón, P. Martínez-Ruíz, R. Villalonga and R. Martínez-Máñez, *Nature Commun.*, 2017, **8**, 15511; (c) A. Llopis-Lorente, B. de Luis, A. García-Fernández, S. Jiménez-Falcao, M. Orzáez, F. Sancenón, R. Villalonga and R. Martínez-Máñez, *Appl. Mater. Interfaces*, 2018, **10**, 26494.
20. S. Y. Tan, C. Teh, C. Y. Ang, M. Li, P. Li, V. Korzh and Y. Zhao, *Nanoscale*, 2017, **9**, 2253.
21. J. Arima, C. Sasaki, C. Sakaguchi, H. Mizuno, T. Tamura, A. Kashima, H. Kusakabe, S. Sugio and K. Inagaki, *FEBS J.*, 2009, **276**, 3894.
22. (a) J. Conde, P. V. Baptista, Y. Hernández, V. Sanz and J. M. de la Fuente, *Nanomedicine (Lond.)*, 2012, **7**, 1657; (b) J. Conde, A. Ambrosone, V. Sanz, Y. Hernández, F. Tian, H. Child, C. C. Berry, M. R. Ibarra, P. V. Baptista, C. Tortiglione and J. M. de la Fuente, *ACS Nano*, 2012, **6**, 8316; (c) P. Tengvall, E. Jansson, A. Askendal, P. Thomsen and C. Gretzer, *Colloids Surf., B*, 2003, **28**, 261-272.
23. (a) K. L. Kelly, E. Coronado, L. L. Zhao, G. C. Schatz, *J. Phys. Chem. B*, 2003, **107**, 668; (b) I. Pastoriza-Santos, J. Pérez-Juste and L. M. Liz-Marzán, *Chem. Mater.*, 2006, **18**, 2465.
24. C. T. Kresge and W. K. Roth, *Chem. Soc. Rev.*, 2013, **42**, 3663.
25. H. Kusakabe, Y. Midorikawa, T. Fujishima, A. Kuninaka and H. Yoshino, *Agric. Biol. Chem.*, 1983, **47**, 1323.
26. R. A. Hawkins, *Am. J. Clin. Nutr.* 2009, **90**, 867S.
27. A. A. Farooqui, W. Y. Ong and L. A. Horrocks, *Neurochemical Aspects of Excitotoxicity*, Springer, New York, 2008.

Supporting information

• Chemicals

Tetraethyl orthosilicate (TEOS), n-cetyltrimethylammonium bromide (CTABr), sodium hydroxide (NaOH), tris(2,2'-bipyridyl)dichlororuthenium(II) hexahydrate ($[\text{Ru}(\text{bpy})_3]\text{Cl}_2$), hydrogen tetrachloroaurate(III) ($\text{HAuCl}_4 \cdot 3\text{H}_2\text{O}$), sodium citrate tribasic dihydrate, paraffin wax, (3-mercaptopropyl)-triethoxysilane, 3-(triethoxysilyl)propyl isocyanate, 4-(Hydroxymethyl) phenyl boronic acid pinacol ester, sodium, L-Glutamate Oxidase from *Streptomyces sp.*, N-(3-dimethylaminopropyl)-N'-ethylcarbodiimide hydrochloride (EDC), N-hydroxysuccinimide (NHS), L-glutamic acid, D-glutamic acid, L-aspartic acid, γ -aminobutyric acid, glycine, glucose, 2,2'-azino-bis(3-ethylbenzothiazoline-6-sulfonic acid) diammonium salt (ABTS), peroxidase from horseradish (HRP), and doxorubicin were purchased from Sigma-Aldrich and used without purification. Sodium chloride, potassium chloride, sodium phosphate dibasic, potassium phosphate monobasic, hydrochloric acid and solvents were provided by Scharlau. Doxorubicin hydrochloride was purchased from Sequoia Research Products. For cell experiments, LN-18 glioblastoma cells were purchased from the German Resource Centre for Biological Materials-DSMZ, Dulbecco's Modified Eagle's Medium (DMEM) was acquired from Life Technologies (Grand Island, NY), and cell proliferation reagent WST-1 was purchased from Roche Applied science.

• General methods

Powder X-ray diffraction (PXRD), transmission electron microscopy (TEM), N_2 adsorption-desorption isotherms, elemental analysis, dynamic light scattering (DLS), UV-visible and fluorescence spectrophotometry techniques were employed for materials characterization. PXRD measurements were performed on a Seifert 3000TT diffractometer using $\text{CuK}\alpha$ radiation. TEM images were acquired using a JEOL TEM-1010 Electron microscope working at 100 kV. N_2 adsorption-desorption isotherms were recorded on a Micromeritics TriStar II Plus automated analyzer. Elemental analysis was performed in a CE Instrument LECO CHN-932 Elemental Analyzer. DLS studies were performed using a ZetaSizer Nano ZS (Malvern).

Fluorescence measurements were carried out in a JASCO FP-8500 Spectrophotometer. UV-visible spectra were recorded with a JASCO V-650 Spectrophotometer. Scanning transmission electron microscopy coupled with energy dispersive X-ray spectroscopy (STEM-EDX) was carried out using a JEM 2100F instrument. ^1H -NMR and ^{13}C -NMR spectra were recorded with a Bruker DRX-300 Spectrometer (300 MHz, 128 scans). Chemical shifts are reported in ppm with tetramethylsilane as an internal standard. High resolution mass spectra (HRMS) were recorded in the positive ion mode on a VG-AutoSpec Mass Spectrometer. Confocal microscopy imaging was performed employing a Leica TCS SP8 inverted laser scanning confocal microscope. Cell viability measurements were carried out with a Wallac 1420 workstation.

• **Synthesis of self-immolative arylboronate derivative (1)**

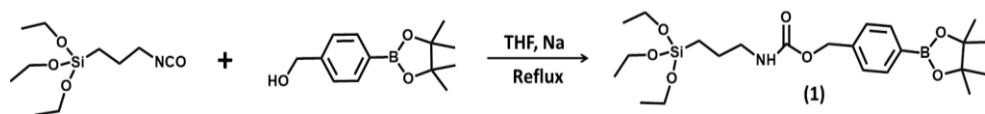


Figure S1. Synthesis of self-immolative arylboronate derivative (1).

4-(Hydroxymethyl) phenyl boronic acid pinacol ester (235 mg, 1.01 mmol) was dissolved in anhydrous THF (8 mL) and a small piece of Na (ca. 1 mg) was added. After stirring 10 min under argon at room temperature, (3-isocyanatopropyl)triethoxysilane (249 μL , 1.01 mmol) was added dropwise and the mixture was stirred under reflux for 48 h. Evaporation of the solvent gave the self immolative molecule **1** with an 90% yield as a dark yellow oil.

^1H NMR (300 MHz, CDCl_3) δ 7.78 (d, 2H), 7.33 (d, 2H), 5.10 (s, 2H), 3.79 (m, 6H), 3.18 (m, 2H), 1.62 (m, 2H), 1.34 (s, 12H), 1.21 (m, 9H), 0.62 (m, 2H). ^{13}C NMR (75 MHz, CDCl_3) δ 134.80, 127.06, 99.167, 83.71, 66.35, 57.81, 43.40, 25.00, 23.09, 18.21, 18.12. HRMS (ESI): m/z ($[\text{M}+\text{H}]$): calc. for $\text{C}_{23}\text{H}_{40}\text{BNO}_7\text{Si}$ 481,46; Found 482.27 (100%).

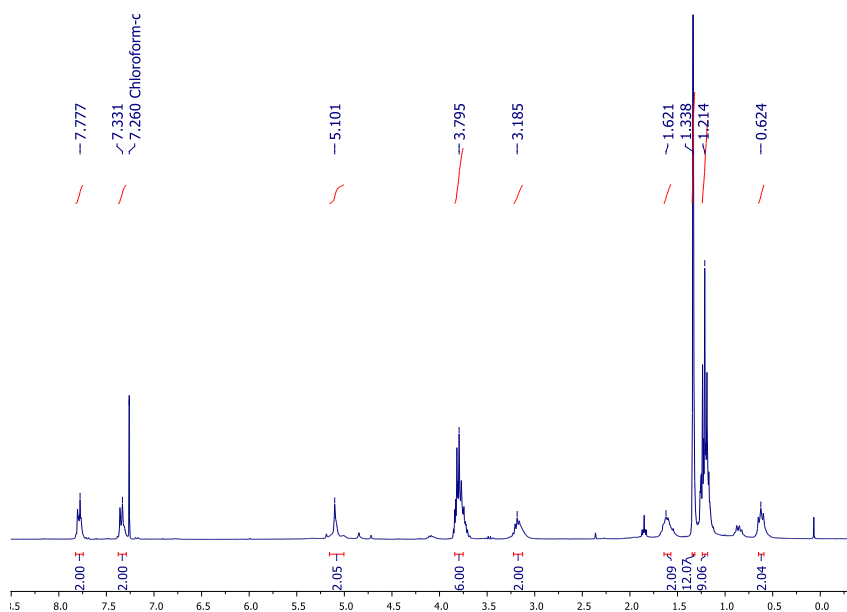


Figure S2. ^1H NMR in CDCl_3 at 300 MHz of self-immolative arylboronate derivative (**1**).

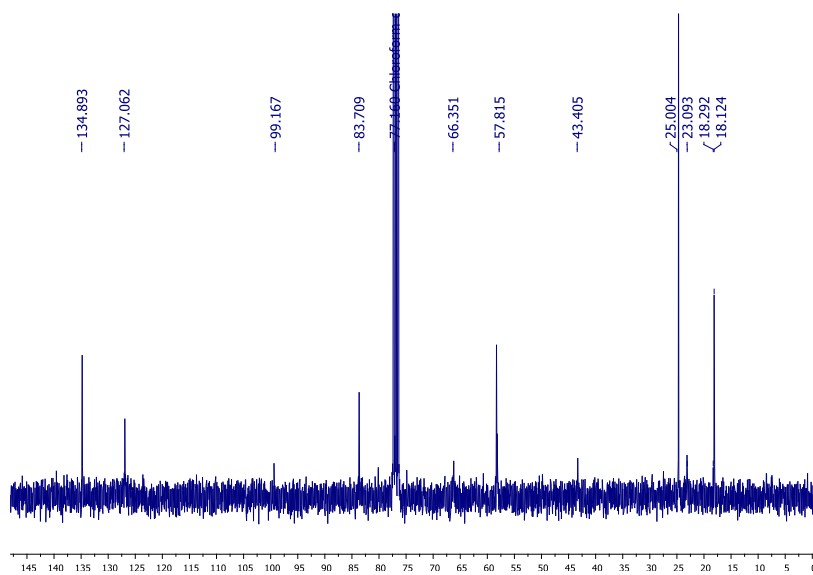


Figure S3. ^{13}C NMR in CDCl_3 at 300 MHz of self-immolative arylboronate derivative (**1**).

- **Synthesis of mesoporous silica nanoparticles (S0)**

In order to synthesize the mesoporous silica nanoparticles (MSNs), 1.00 g of n-cetyltrimethylammonium bromide (CTABr) was dissolved in 480 mL of distilled water. When the CTABr solution reached 40 °C, a solution of NaOH (2.0 M, 3.5 mL) was added and the solution was kept stirring until reaching 80 °C. Then, TEOS (5.00 mL, 22.4 mmol) was added dropwise to the surfactant solution under vigorous stirring. The mixture was kept stirred for 2 h. The white precipitate was isolated by centrifugation and washed several times with distilled water until the washing waters reached a pH of 7.5. The solid was dried at 70 °C overnight. Finally, in order to remove the template phase, the as-synthesized solid was calcined in an oxidant atmosphere for 5 h at 550 °C, yielding the calcined nanoparticles (S0).

- **Synthesis of gold nanoparticles**

Citrate-capped AuNPs with a diameter ca. 20 nm were synthesized based on the Turkevich-Frens method. Firstly, 100 mL of 3 μM HAuCl₄·3H₂O were heated under refluxing conditions. Then, 1.5 mL of a 1 % sodium citrate solution was added and the resulting solution was refluxed for 15 min until a red solution was obtained. Finally, the synthesized AuNPs solution was let to cool at room temperature. This process was repeated four times.

- **Preparation of Janus Au-MS nanoparticles (S1)**

180 mg of MSNs were added to an aqueous solution (6.7 % ethanol) of n-cetyltrimethylammonium bromide (CTABr) (9 mL, 1 μM). Then, the mixture was heated at 75 °C and 1 g of paraffin wax was added. After the paraffin wax was melted, the mixture was vigorously mixed using an Ultra-Turrax T-25 homogenizer (IKA) for 15 minutes. Thereafter, the mixture was further stirred for 1 h at 1500 rpm and 75 °C using a magnetic stirrer. Then, the obtained Pickering emulsion was cooled at room temperature mixed with methanol (9 mL), and treated with 180 μL of (3-mercaptopropyl) trimethoxysilane for 3 h under magnetic stirring. The solid was isolated by centrifugation and washed with methanol. In order to assemble the Janus particles, the partially mercapto-functionalized MSNs were dispersed in 75 mL of methanol and added over 300 mL of the as-synthesized

AuNPs. After stirring overnight, the solid was isolated by filtration and exhaustively washed with ethanol and chloroform. Finally, the Janus Au-MSNs (**S1**) were dried at room temperature.

- **Preparation of solid S2**

In order to prepare the solid **S2**, firstly 50 mg of **S1** (50 mg) were suspended in 5 mL of acetonitrile and treated with 50 μ L of 3-mercaptopropionic to functionalize the gold face. The solution was stirred for 1 hour and then nanoparticles were isolated by centrifugation and washed by centrifugation with fresh acetonitrile for 5 times. Once dried, these nanoparticles (25 mg) were loaded by stirring for 24 h under argon atmosphere in 5 mL of anhydrous acetonitrile containing 25 mg of tris(2,2'-bipyridyl)dichlororuthenium(II) hexahydrate ($[\text{Ru}(\text{bpy})_3]\text{Cl}_2$). Then, self immolative molecule **1** (70 mg, 0.14 mmol) was dissolved in 700 μ L of acetonitrile and added dropwise to the nanoparticle suspension. The mixture was let to react for 5.5 h under stirring at room temperature. Afterwards, the solid was isolated by centrifugation, washed twice with acetonitrile and twice with PBS buffer (pH 7.5), and dried at 70 °C overnight. Finally, 21 mg of the resulting nanoparticles and 90 mg of β -cyclodextrin were mixed in 5 mL of PBS buffer (pH 7.5) in order to cap the mesopores and avoid the delivery of the loaded cargo. After 24 of stirring, the nanoparticles were isolated by centrifugation, washed 3 times with PBS buffer (pH 7.5) and dried at 70 °C for 5 h. This process finally yielded the solid **S2**.

- **Preparation of solid S2_{GLUT}**

In order to prepare the final nanodevice **S2_{GLUT}**, 7.2 mg of **S2_{GLUT}**, 0.35 mg of the enzyme L-glutamate oxidase, 2.5 mg of EDC and 2.5 mg of NHS were suspended in a final volume of 1600 μ L of 50 mM sodium phosphate buffer (pH 7.5) and stirred at 4 °C overnight. Finally, the nanoparticles were isolated by centrifugation and exhaustively washed by repeated centrifugation with fresh sodium phosphate buffer (pH 7.5). This process finally yielded the nanocarrier **S2_{GLUT}**, which was kept in refrigeration until use.

- Preparation of solid **S3**_{GLUT}

In order to prepare nanoparticles loaded with the cytotoxic anticancer drug doxorubicin, the process was the same as described above but using doxorubicin instead of ([Ru(bpy)₃]Cl₂). Subsequently, nanoparticles **S3** (without enzyme) and enzyme-functionalized **S3**_{GLUT} were obtained.

- Materials characterization

Transmission electron microscopy (TEM)

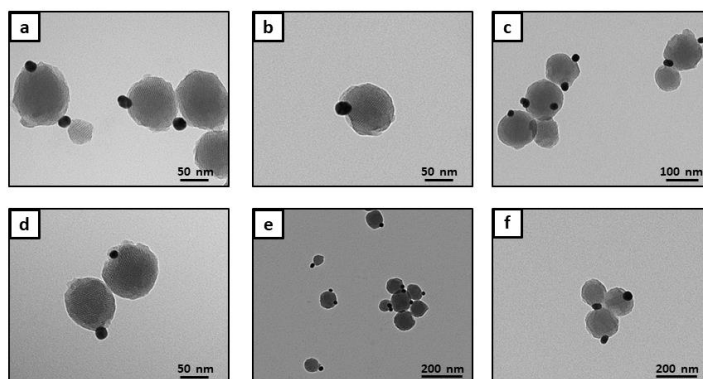


Figure S4. TEM images of the Janus Au-MSNs (**S1**).

UV-visible spectra

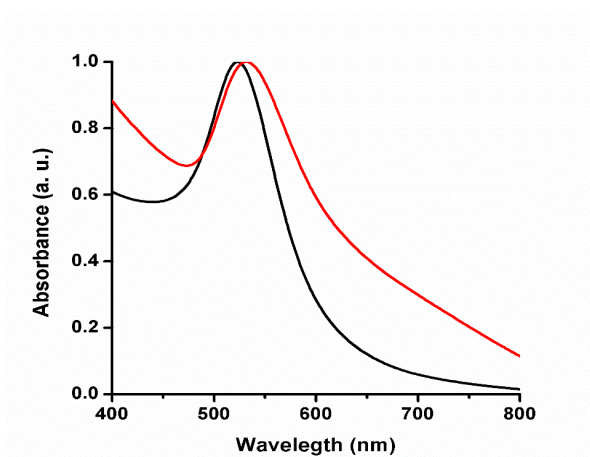


Figure S5. Normalized absorbance spectra of the as-synthesized AuNPs (black curve) **S1** (red curve).

N₂ adsorption-desorption isotherms

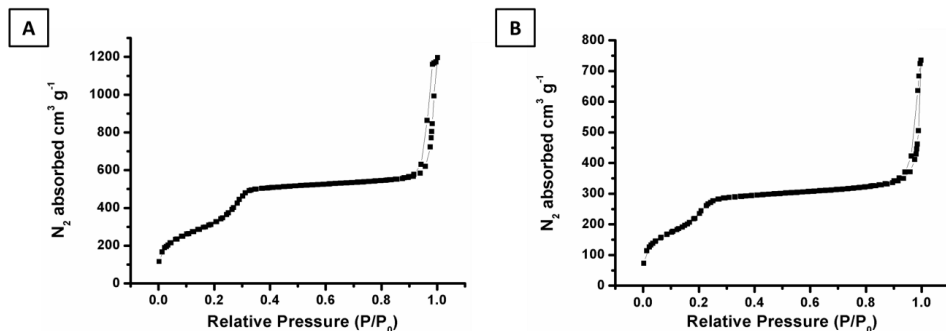


Figure S6. N₂ adsorption-desorption isotherms for (A) MSNs (S0) and (B) Janus Au-MSNs (S1).

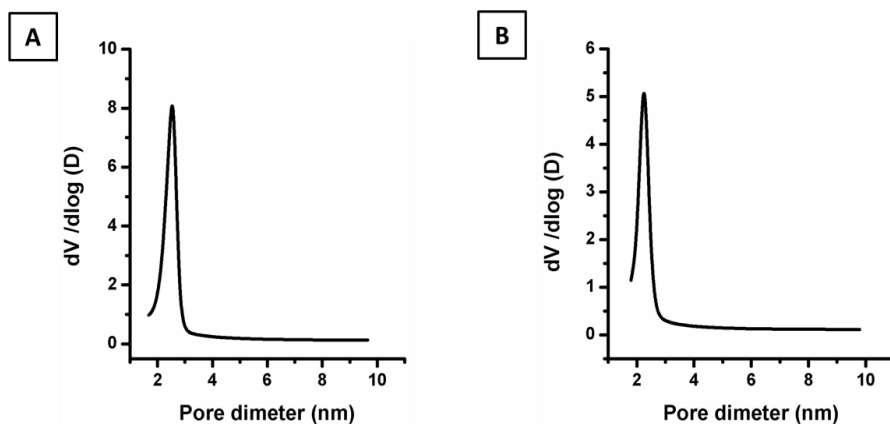


Figure SI-7. Pore diameter distribution for (A) MSNs (S0) and (B) Janus Au-MSNs (S1), as determined by applying the BJH model on the adsorption branch of the isotherm for P/P₀ < 0.8, which is associated with the surfactant generated mesopores.

Table S1. BET specific surface values, pore volumes and pore sizes calculated from N₂ adsorption-desorption isotherms of MSNs (S0) and Janus Au-MSNs (S1).

Nanoparticles	BET Surface	Pore size	Pore volume
MS (S0)	1365.39 m ² /g	2.47 nm	0.946 cm ³ /g
Au-MS (S1)	1000.78 m ² /g	2.38 nm	0.589 cm ³ /g

Elemental analysis

Table S2. Mass percentage of C, H, and N from **S2** determined with the elemental analysis instrument.

Solid	%C	%H	%N
S2	11.08	2.43	0.81

- The content of dye (**Ru(bpy)₃Cl₂**) was determined to be 7.9 mmol per 100 g of **S2** by dissolving the silica scaffold with 20% NaOH aqueous solution, and measuring the absorbance of the solution at 453 nm with the spectrophotometer.
- Calculation of self-immolative derivative **1** content (**Supplementary Equation 1**):

$$\left(\frac{0.81 \text{ g of N (total)}}{100 \text{ g of S2}} - \frac{0.6669 \text{ g of N (from [Ru(bpy)}_3\text{]Cl}_2)}{100 \text{ g S2}} \right) * \frac{1 \text{ mol of derivative 1}}{14 \text{ g of N}}$$

$$= \frac{0.01022 \text{ mol of derivative 1}}{100 \text{ g of S2}}$$

- Calculation of β -CD content (**Supplementary Equation 2**):

$$\left(\frac{11.08 \text{ g of C (total)}}{100 \text{ g of S2}} - \frac{2.8584 \text{ g of C (from [Ru(bpy)}_3\text{]Cl}_2)}{100 \text{ g S2}} - \frac{2.8199 \text{ g of C (from derivative 1)}}{100 \text{ g S2}} \right)$$

$$* \frac{1 \text{ mol of } \beta\text{-CD}}{504 \text{ g of C}} = \frac{0.01072 \text{ mol of } \beta\text{-CD}}{100 \text{ g of S2}}$$

Dynamic light scattering (DLS)

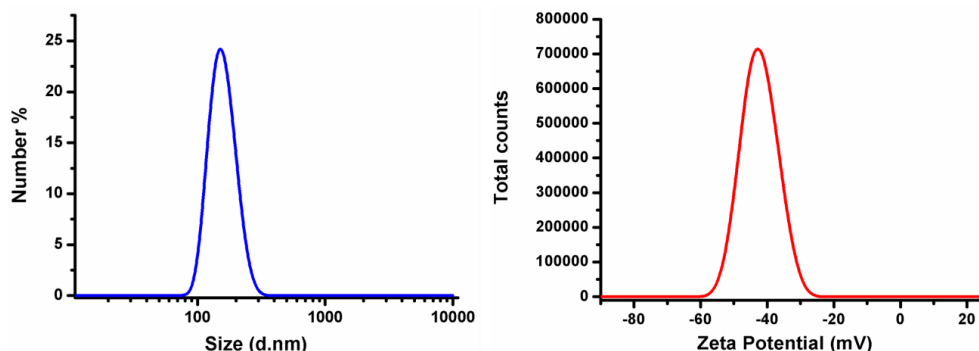
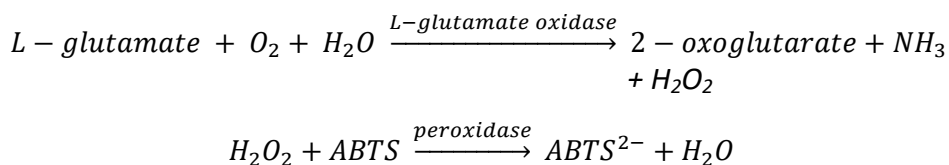


Figure S8. Hydrodynamic diameter and zeta potential distributions of the final nanodevice **S2_{GLUT}** determined by DLS.

• Enzymatic assay

One unite of L-glutamate oxidase transforms one μmol of substrate (L-glutamate) per minute at pH 7.4 at room temperature. The enzymatic reaction gives 2-oxoglutarate, ammonia and hydrogen peroxide. In the enzymatic assay, hydrogen peroxide reacts with ABTS in the presence of peroxidase (HRP) to form a yellow product (ABTS^{2-}) that can be monitored by measuring its absorption at 418 nm with a spectrophotometer. Thus, the method is based on the following set of reactions (**Supplementary Equation 3**):



In order to carry out the assay, 250 μL of L-glutamate (10 mM), 250 μL of ABTS (1 $\text{mg}\cdot\text{mL}^{-1}$), and 50 μL of HRP (2 $\text{mg}\cdot\text{mL}^{-1}$) were placed in a quart cuvette. These solutions were freshly prepared in PBS buffer (pH 7.4). Then, 20 μL of either buffer (for blank) or **S2_{GLUT}** solution (3 $\text{mg}\cdot\text{mL}^{-1}$) were added. The mixture was shaken and absorbance at 420 nm was monitored as a function of time. Whereas no change was observed in the absence of nanoparticles, a strong yellow colour appeared in

the presence of those. The increase in absorbance (ABTS²⁻ formation) as a function of time in the presence of S₂GLUT is depicted in Figure S9:

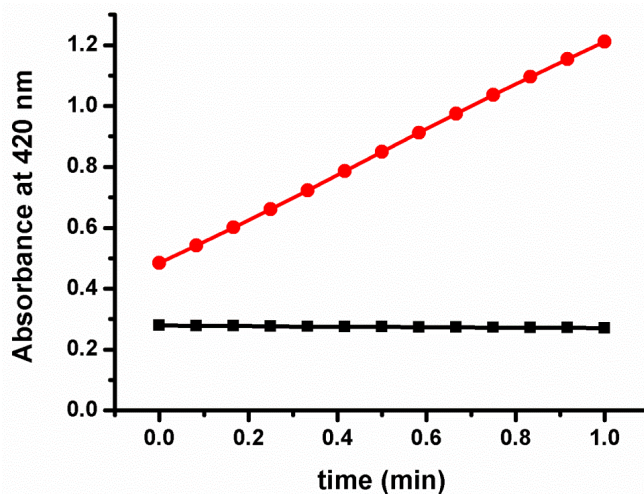


Figure S9. Monitoring of absorbance at 420 nm due to substrate transformation during the enzymatic assay, upon addition of buffer (black points) and upon addition of S₂GLUT (red points).

The units of L-glutamate oxidase on S₂GLUT were estimated to be 40889 mU·g⁻¹, by applying the following formula (**Supplementary Equation 4**):

$$\frac{\text{Enzymatic Units}}{\text{g}} = \frac{(\Delta - \Delta_{\text{blank}}) * V_T * F_D}{\epsilon_{\text{ABTS}} * l * V_{\text{NPs}} * C_{\text{NPs}}}$$

Where,

Δ is the slope of the graph (min⁻¹)

Δ_{blank} is the slope of the graph for the blank (min⁻¹)

V_T is the total volume in the cuvette (mL)

ϵ_{ABTS} is the molar extinction of ABTS²⁻ at 420 nm (36 mM⁻¹ · cm⁻¹)

l is the optical path in the cuvette (1 cm)

V_{NPs} is the volume of nanoparticles added (mL)

C_{NPs} is the concentration of nanoparticle solution added (g·mL⁻¹).

STEM-EDX

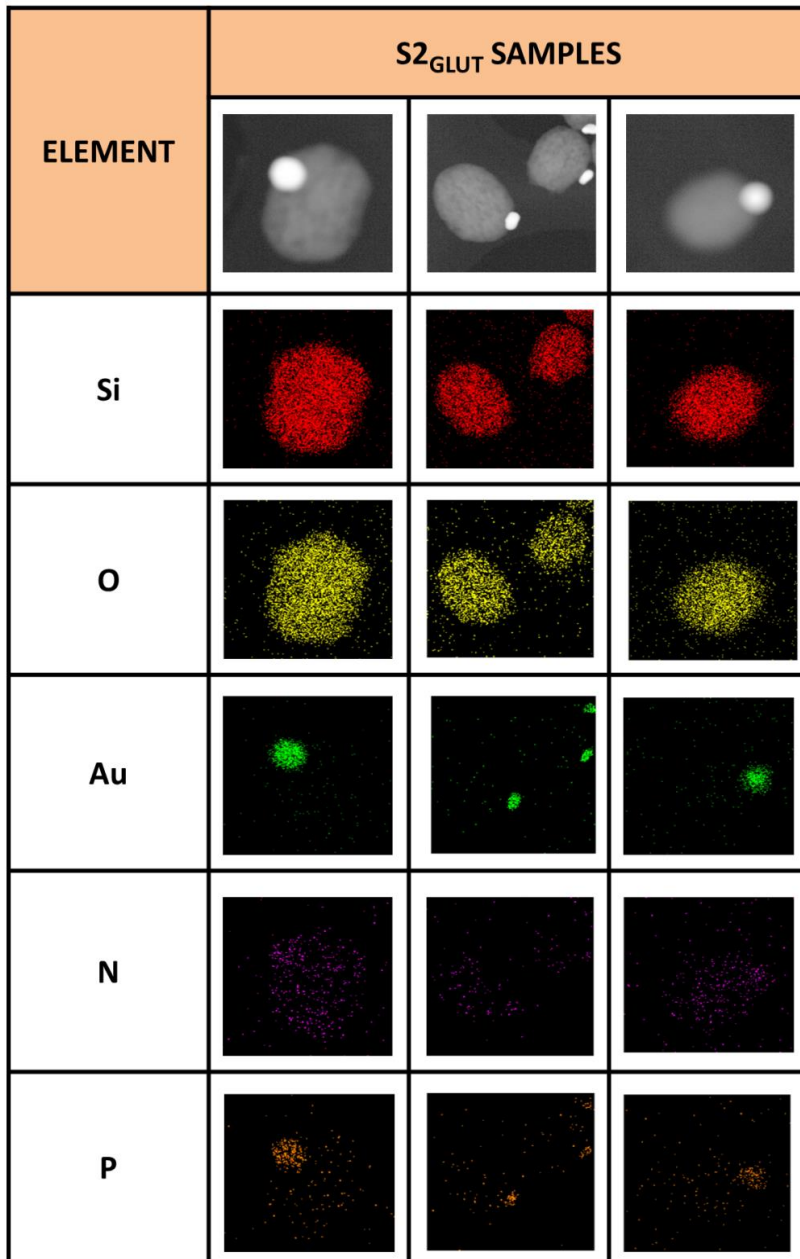


Figure S10. Additional images of STEM-EDX mapping of different atoms on S2_{GLUT}.

- **Release experiments**

For the release experiments mentioned in the manuscript, refrigerated stock solutions of nanoparticles (**S2_{GLUT}**) (10 mg mL^{-1}), were aliquoted, washed a couple of times with PBS buffer (pH 7.5) and placed at concentration of 3 mg mL^{-1} in PBS buffer (pH 7.5) containing the corresponding concentration of **L-Glu** or other neurotransmitters (for selectivity studies). The samples were stirred at $25 \text{ }^\circ\text{C}$. At programmed times, aliquots were taken, centrifuged for 2 min at 12000 rpm (to precipitate the solid) and then the fluorescence of the supernatant corresponding to the released $[\text{Ru}(\text{bpy})_3]\text{Cl}_2$ dye was measured ($\lambda_{\text{em}} = 595 \text{ nm}$, $\lambda_{\text{exc}} = 453 \text{ nm}$).

- **Cell experiments**

Cell culture conditions

LN-18 glioblastoma cells line were purchased from the German Resource Centre for Biological Materials-DSMZ and were grown in Dulbecco's Modified Eagle's Medium (DMEM) supplemented with 10% fetal bovine serum (FBS). Cells were incubated at $37 \text{ }^\circ\text{C}$ in an atmosphere of 5% carbon dioxide and 95% air and underwent passage twice a week.

Cell viability assays

Cells were seeded in a 24-well plate at 50000 cells/well and incubated at $37 \text{ }^\circ\text{C}$ for 24 h. Afterwards, cells were incubated separately with **S3** and **S3_{GLUT}** at concentrations of 5, 10, 25, 50 and $100 \text{ mg}\cdot\text{mL}^{-1}$ for 60 min, washed with PBS, and further incubated for 24 h in DMEM medium. Finally, cell viability was assessed by incubation with the cell proliferation WST-1 reagent ($15 \text{ } \mu\text{L}$) for 1 h, followed measuring the absorbance at 595 nm in the Wallac Workstation. Three independent experiments containing triplicates were carried out.

Confocal microscopy imaging

Glioblastoma cells seeded on glass coverslips at $300000 \text{ cells}\cdot\text{mL}^{-1}$ in 6-well culture plates and incubated at $37 \text{ }^\circ\text{C}$ for 24 h. Then, cells were incubated separately with **S3** and **S3_{GLUT}** ($50 \text{ } \mu\text{g}\cdot\text{mL}^{-1}$) for 2 hours, washed with PBS, and further incubated for 2 h. Afterwards, cells were washed several times with

PBS, stained with DNA marker Hoechst 33342 by addition at $2 \mu\text{g}\cdot\text{mL}^{-1}$, and placed in fresh media. Finally, samples were visualized using a confocal microscope Leica TCS SP8 AOBS.

Chapter 5:

Conclusions

The development of tools for the detection of neurotransmitters and the development of neurotransmitter-responsive delivery systems are current topics of interest due to their potential to help in the earlier diagnosis and treatment of neurological diseases. In this context, the use of chemistry and nanotechnology allow the design and preparation of smart nanodevices able to perform different kind of functionalities, to provide solutions to these challenges.

The present thesis has been focused on the design, preparation, characterization and evaluation of nanodevices for the colorimetric sensing of neurotransmitters and controlled delivery systems responsive to neurotransmitters based on gold nanoparticles and mesoporous silica nanoparticles equipped with organic ligands, enzymatic effectors, molecular gates and chromo-fluorogenic species or drugs.

First of all, a general introduction has been included in the first chapter of this thesis. The main aspects about the types, characteristics and functions and related disorders of neurotransmitters were exposed. In addition, the principal aspects of nanotechnology regarding: (i) the chemistry behind the synthesis, functionalization and optical properties of gold nanoparticles, in order to understand the basis of the colorimetric sensing strategy of the sensors prepared; and (ii) the development of hybrid organic-inorganic mesoporous materials, in particular, the application of stimuli-responsive hybrid materials as controlled delivery systems, were emphasized. Moreover, a brief description of some significant examples of gated nanodevices based on mesoporous silica supports for controlled delivery applications has been presented.

In chapter 3, three different colorimetric sensors for the detection of neurotransmitters were developed. The designs were based on the double functionalization of gold nanoparticles with different organic ligands, which were (i) able to recognize specific functional groups of each neurotransmitter and (ii) able to stabilize the gold nanoparticles. The sensing mechanism consisted in neurotransmitter triggered aggregation of the gold nanoparticles, leading to a

bathochromic shift of the SPRB in the UV-vis spectrum of the probe and a clear change in the color of the solution from red to blue.

In the first part, a sensor for the colorimetric detection of serotonin (5-HT) using 15 nm AuNPs bifunctionalized with dithiobis(succinimidylpropionate) (DSP) and N-Acetyl-L-Cysteine (NALC) was developed. The prepared sensor was able to detect the presence of 5-HT in aqueous media, thanks the recognition of the amino and hydroxyl groups by DSP and NALC, respectively. Selectivity assays evidenced a remarkable selectivity of the sensor in presence of other neurotransmitters. Moreover, a similar behaviour was observed in simulated blood serum with a linear response within the 0-3 μM 5-HT concentration range and with a LOD as low as 0.12 μM . Finally, the probe was capable of detecting 5-HT in human blood samples and of distinguishing between normal 5-HT levels and 5-HT levels that are indicative of disease.

In the second part, a colorimetric sensor for the detection of norepinephrine (NE) was prepared. The preparation of this sensor consisted on the use of spherical gold nanoparticles functionalized with benzaldehyde and boronic acid-terminated moieties. A double molecular recognition involving on one hand the aromatic aldehyde and the aminoalcohol group of NE, and on the other hand the boronic acid and the catechol moiety of the neurotransmitter, results in a aggregation of the gold nanoparticles and the subsequent change in color. This double functionalization conferred to the sensing system a significative selectivity in the presence of other similar catecholamines such as dopamine and epinephrine. The optimization of the sensing methodology allowed the achievement of higher sensitivity with a LOD in this medium of 0.09 μM in synthetic urine.

In the third part, the double functionalization of gold nanoparticles with benzaldehyde-terminated ligand and N-Acetyl-Cysteine allowed the selective and sensitive detection of the metabolite normetanephrine, an O-methylated metabolite of NE. The developed probe recognized the presence of normetanephrine in spite of the presence of other neurotransmitters'

metabolites. Regarding the sensibility, the optimized probe achieved a LOD of 0.52 μM in synthetic urine.

Accordingly, the results obtained from this chapter is worth to point out that, the double functionalization of gold nanoparticles with specific organic ligands has proven to be an interesting approach to the design and development of more selective and sensitive detection systems.

In chapter 4, two different nanodevices for enzymatic controlled delivery in response to neurotransmitters were developed. In the first part, a delivery system able to respond to the neurotransmitter acetylcholine (ACh) was prepared. The design was based on the incorporation of the enzyme acetylcholinesterase as recognition and bulky capping unit on the surface of silica mesoporous nanoparticles. Acetylcholinesterase mediated the transformation of ACh into acetic acid and choline, locally lowering the pH and opening the molecular gate by the hydrolysis of the boronic ester bonds. The nanodevice showed a remarkable payload delivery in the presence of ACh in less than 5 min. Regarding the selectivity of the system, it remains closed in the presence of other relevant neurotransmitters, responding selectively to Ach. Moreover, the cargo release was negligible at ACh concentrations present in human blood, whereas a significant payload delivery is observed in the 0.025–10 mM range, which coincides with typical concentration of ACh in synaptic vesicles, neuromuscular junctions and synaptic clefts in Parkinson's patients. Finally, *in vitro* assays performed in complex biological environments such as HeLa cells, demonstrated that the designed system was able to respond to the presence of ACh and deliver a model drug.

Regarding the second part, it was shown that is possible to develop a delivery system in response to L-glutamate based on the utilization of enzymes and self-immolative molecular gates. In this particular case, the Janus nanodevice was functionalized with a self-immolative arylboronate molecular gate on the mesoporous face, whereas the gold face was functionalized with the enzyme L-

glutamate oxidase. The nanodevice was able to recognize L-glutamate via enzyme-mediated transformation to H_2O_2 , which induced the cleavage of the self-immolative cap and resulting in payload delivery. Moreover, the nanodevice exhibited a negligible release at L-glutamate plasma concentrations, but was capable of recognising L-glutamate in brain cancer cells. As far as we know, this delivery system was the first example in the literature for specific enzymatic-controlled delivery in presence of L-glutamate.

Therefore, from this chapter is worth to point out that the incorporation of enzymes as functional components of controlled delivery systems have allowed performing certain functions that would be very difficult or impossible to achieve using artificial components. Moreover, the use of enzymes as functional components can provide gated hybrid nanodevices with high specific recognition capabilities toward selected neurotransmitters. In addition, the results obtained on the cellular media assays indicated the biocompatibility of the nanodevices under the conditions studied.

Finally, as a general conclusion that can be extracted from this thesis results is that the use of inorganic nanoparticles equipped with organic or enzymatic components has successfully achieved the recognition of neurotransmitters with high selectivity, giving rise to the design of versatile detection and controlled release systems. Therefore, we expect that the findings exposed on this PhD thesis could help to develop innovative tools for early point-of-care or personalized diagnosis applications and developing better therapies for nervous system-related diseases.

*Gracias a la Generalitat Valenciana por concederme
una beca SANTIAGO GRISOLÍA.*